catalysts

Commemorative Issue in Honor of Professor Emeritus Calvin H. Bartholomew in Anticipation of His 75th Birthday

Edited by
Morris D. Argyle

Printed Edition of the Special Issue Published in *Catalysts*

www.mdpi.com/journal/catalysts

MDPI

Commemorative Issue in Honor of Professor Emeritus Calvin H. Bartholomew in Anticipation of His 75th Birthday

Commemorative Issue in Honor of Professor Emeritus Calvin H. Bartholomew in Anticipation of His 75th Birthday

Special Issue Editor

Morris D. Argyle

MDPI • Basel • Beijing • Wuhan • Barcelona • Belgrade

Special Issue Editor
Morris D. Argyle
Brigham Young University
USA

Editorial Office
MDPI
St. Alban-Anlage 66
4052 Basel, Switzerland

This is a reprint of articles from the Special Issue published online in the open access journal *Crystals* (ISSN 2073-4352) from 2017 to 2018 (available at: https://www.mdpi.com/journal/catalysts/special_issues/Calvin_Bartholomew)

For citation purposes, cite each article independently as indicated on the article page online and as indicated below:

LastName, A.A.; LastName, B.B.; LastName, C.C. Article Title. *Journal Name* **Year**, *Article Number*, Page Range.

ISBN 978-3-03897-531-1 (Pbk)
ISBN 978-3-03897-532-8 (PDF)

Contents

About the Special Issue Editor

Morris D. Argyle, Associate Professor of Chemical Engineering at Brigham Young University, became interested in catalysis while working as a bachelor's level process engineer for one of the fluid catalytic cracking units at Exxon Company USA's Baytown, Texas Refinery. After earning his PhD at the University of California, Berkeley in 2003, he joined the Department of Chemical and Petroleum Engineering at the University of Wyoming, ultimately becoming Associate Professor and Department Head, before moving to the Chemical Engineering faculty at Brigham Young University in 2009. His research interests include energy and related carbon dioxide capture, plasma reactions, and reactor engineering, but his primary focus is on heterogeneous catalysis, including metal oxides and carbides for partial oxidation, hydrogen production, and Fischer—Tropsch synthesis. He also shares Professor Bartholomew"s interest in catalyst deactivation. He has co-authored 46 journal articles, one book chapter, and six patents, and co-edited one book.

Preface to "Commemorative Issue in Honor of Professor Emeritus Calvin H. Bartholomew in Anticipation of His 75th Birthday"

Sir Isaac Newton said that if he had seen further than others, it was because he was standing on the shoulders of giants. Within the field of heterogeneous catalysts, Calvin H. Bartholomew, Professor Emeritus of Chemical Engineering at Brigham Young University (BYU), is one of those giants. As a few selected highlights from his career, Dr. Bartholomew has authored several definitive reviews on catalyst deactivation, with special emphasis on sulfur poisoning, carbon deposition, and sintering, for which he championed the use of generalized power law expressions (GPLE) to model the deactivation. GPLE's contain a limiting, steady-state value of activity that is more accurate compared tothan the more common assumption of a simple power law expression, which takes the final activity of the catalyst as zero. He has been active in both cobalt and iron based Fischer—Tropsch catalyst research. More recently, he developed the slit pore model to characterize the pore size distribution of mesoporous catalytic support materials, that which is more accurate than conventional models. Finally, as a major contribution to the field, he published a leading handbook and textbook, Fundamentals of Industrial Catalytic Processes, with his long-time collaborator, Dr. Robert Farrauto.

This compilation highlights and complements many of Professor Bartholomew's contributions to the field. The nine chapters comprising the book were written by former students, collaborators, colleagues, and respected peers. Keyvanloo et al.'s study on Fischer—Tropsch catalysis (Chapter 1) honors Professor Bartholomew's extensive contributions to this area. Hallac et al.'s spectroscopic study on iron-based water gas shift catalysts (Chapter 2) hearkens back to Professor Bartholomew's graduate work with iron. Ha et al.'s contribution on nickel catalysts for (dry) methane reforming and carbon deactivation (Chapter 3) go back relate to Dr. Bartholomew's early work on both nickel and methane reforming. Türks et al.'s work on carbon dioxide methanation on nickel catalysts (Chapter 4) builds on these major themes. Martinelli et al.'s study (Chapter 5) continues the steam reforming theme, but with methanol as the reactant on platinum catalysts supported on sodium-modified yttrium stabilized zirconia. The contribution by Xiang et al. (Chapter 6), whose corresponding author is Dr. Bartholomew's friend, Bob Farrauto, echoes some of his earliest work on environmental catalysts. Tu et al.'s contribution on palladium catalysts supported on titania for hydrogen peroxide production (Chapter 7) also touches onrelates to themes of this metal and support in Dr. Bartholomew's research. Finally, Seeburg et al.'s paper on methane combustion catalyst stability (Chapter 8) and Ruelas-Leyva and Fuentes work on chiral catalyst deactivation (Chapter 9) fit with Dr. Bartholomew's consistent theme of catalyst deactivation. In summary, this book covers much of the breadth and points to the depth of Professor Bartholomew's illustrious career. Dr. Bartholomew has taught and mentored students at both BYU and across the world in catalysis, materials, and catalyst deactivation for 45 years. After graduating with his bachelor's degree from BYU, he performed his PhD research on the "Surface Composition and Chemistry of Supported Platinum—Iron Alloy Catalysts" at Stanford University under the direction of the incomparable Michel Boudart. Upon graduation from Stanford, he worked for Corning Glass Works as a Senior Chemical Engineer in Automotive Emissions Control and Surface Chemistry Research. He then began his career as a professor in the Chemical Engineering Department at BYU in 1973, where he built the Catalysis Laboratory while advising over 34 graduate students and dozens more undergraduates in

his research. As part of hisIn professional service, he served as president of the Central Utah Section of the American Chemical Society and the California Catalysis Society, remains active in the American Institute of Chemical Engineers, and was a founder of both the Rocky Mountain Fuel Society and the Western States Catalysis Club, which currently exists as the Rocky Mountain Catalysis Society. He received the Karl G. Maeser Research Award, which is the highest honor awarded annually to a researcher at BYU and was chosen as the Engineering College Outstanding Faculty member. Most recently, he was named as the Honorary Chair of the North American Catalysis Society Meeting held in Denver, CO in 2017. Since receiving emeritus status in 2009, Professor Bartholomew has continued his premier research and mentoring of faculty, graduate students, and undergraduates. He continues to be active in the field of heterogeneous catalysis as a recognized authority on Fischer—Tropsch synthesis and catalyst deactivation. He is also noted for his work with Mössbauer spectroscopy, NOx decomposition with automotive catalysts, and authoritative works on supported nickel catalysts and their poisoning by sulfur. He has co-authored over 140 journal articles, which have received over 10,000 citations; 20 chapters/reviews; six books; and six patents. In addition to his employment at Corning Inc., he has also worked for UnoCal, Sandia National Labs, and Lawrence Livermore Laboratory and consulted with more than 80 company clients, including more than a dozen plus start-up gas-to-liquids companies. Further, he whas been the principal motivator for development of advanced supports and Fischer—Tropsch catalysts at Cosmas Inc.

Finally, in addition to teaching countless university courses on kinetics, catalysis, catalyst deactivation, air pollution control, creativity, and engineering materials, Professor Bartholomew has taught short courses on "Heterogeneous Catalysis," "Fischer—Tropsch Synthesis," and "Catalyst Deactivation" to more than 750 professionals from industry and academiae. In down times during these courses, he is known to break into song in his beautiful, resonant voice. He is a scholar, a gentleman, and a friend. The other authors who contributed to this book and I wish him and his family (as of this writing, Cal and his wife Karen have five5 children, nine9 grandchildren and two2 great- grandchildren) many more years of happiness and scholarly productivity. We thank him for his kind example and honor him for his lasting contributions.

Morris D. Argyle
Special Issue Editor

catalysts

MDPI

Editorial

Commemorative Issue in Honor of Professor Calvin H. Bartholomew's 75th Birthday

Morris D. Argyle

Brigham Young University, Chemical Engineering Department, Provo, UT 84602, USA; mdargyle@byu.edu; Tel.: +1-801-422-6293

Received: 6 November 2018; Accepted: 8 November 2018; Published: 9 November 2018

Abstract: This editorial is written to recognize Professor Emeritus Calvin H. Bartholomew, who celebrated his 75th birthday in 2018, and to introduce the commemorative issue of *Catalysts* compiled in his honor. Following a brief biography that celebrates the career and contributions of Professor Bartholomew, the nine articles that make up the special issue are briefly reviewed. Dr. Bartholomew is an eminent researcher, an outstanding educator, mentor, and friend.

Keywords: Calvin H. Bartholomew; heterogeneous catalyst deactivation; Fischer-Tropsch

1. Introduction

Serving as editor of this special issue in honor of Professor Calvin H. Bartholomew (see Figure 1) truly has been a privilege. Professor Bartholomew, or Dr. B as he is known to his students, is continuing his distinguished career in heterogeneous catalysis. He has been a mentor and a friend to multitudes. This special issue is a small token of the respect he has gained from his peers and students.

Figure 1. Professor Emeritus Calvin H. Bartholomew.

2. Brief Biography

Calvin H. Bartholomew, Professor Emeritus of Chemical Engineering at Brigham Young University (BYU), has taught and mentored students at both BYU and across the world in catalysis, materials, and catalyst deactivation for 45 years. After graduating with his bachelor's degree from BYU, he performed his PhD research on "Surface Composition and Chemistry of Supported Platinum-Iron Alloy Catalysts" [1] at Stanford University under the direction of the incomparable Michel Boudart.

Upon graduation from Stanford, he worked for Corning Glass Works as Senior Chemical Engineer in Automotive Emissions Control and Surface Chemistry Research. He then began his career as a professor in the Chemical Engineering Department at BYU in 1973, where he built the Catalysis Laboratory while advising over 34 graduate students and dozens more undergraduates in his research. In professional service, he served as president of the Central Utah Section of the American Chemical Society and the California Catalysis Society, is active in the American Institute of Chemical Engineers, and was a founder of both the Rocky Mountain Fuel Society and the Western States Catalysis Club, which currently exists as the Rocky Mountain Catalysis Society. He received the Karl G. Maeser Research Award, which is the highest honor awarded annually to a researcher at BYU, and was chosen as the Engineering College Outstanding Faculty member. Most recently, he was named as the Honorary Chair of the North American Catalysis Society Meeting held in Denver, CO in 2017.

Since receiving emeritus status in 2009, Professor Bartholomew has continued his premier research and mentoring of faculty, graduate students, and undergraduates. He continues to be active in the field of heterogeneous catalysis as a recognized authority on Fischer–Tropsch synthesis and catalyst deactivation. He is also noted for his work with Mössbauer spectroscopy, NO_x decomposition with automotive catalysts, and authoritative works on supported nickel catalysts and their poisoning by sulfur. He has co-authored over 140 journal articles, which have received over 10,000 citations; 20 chapters/reviews; six books; and six patents. In addition to his employment at Corning Inc., he has also worked for UnoCal, Sandia National Labs, and Lawrence Livermore Laboratory and consulted with more than 80 company clients, including a dozen plus start-up gas-to-liquids companies. Furthermore, he has been the principal motivator for the development of advanced supports and Fischer–Tropsch catalysts at Cosmas Inc.

Finally, in addition to teaching countless university courses over 36 years on kinetics, catalysis, catalyst deactivation, air pollution control, creativity, and engineering materials (see Figure 2), Professor Bartholomew has taught short courses on "Heterogeneous Catalysis", "Fischer–Tropsch Synthesis", and "Catalyst Deactivation" to more than 750 professionals from industry and academe. In down times during these courses, he is known to break into song in his beautiful, resonant voice. He is a scholar, a gentleman, and a friend. The other authors who contributed to this special issue and I wish him and his family (Cal and his wife Karen have five children, nine grandchildren and two great grandchildren) many more years of happiness and scholarly productivity.

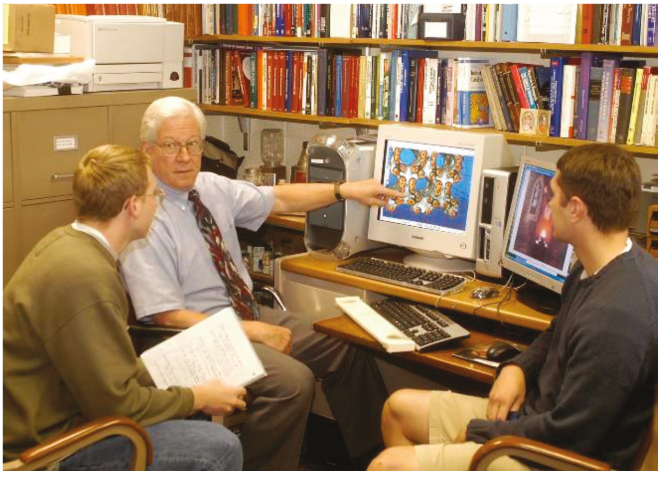

Figure 2. Professor Bartholomew with students.

3. Highlights of Professor Bartholomew's Research

As a few selected highlights from his most-cited published works, Dr. Bartholomew has authored several definitive reviews on catalyst deactivation [2,3], with special emphasis on sulfur poisoning [4], carbon deposition [5], and sintering [6,7], for which he championed the use of generalized power law expressions (GPLE) to model the deactivation. GPLE's contain a limiting, steady-state value of activity that is more accurate compared to the more common assumption of a simple power law expression, which takes the final activity of the catalyst as zero. He has been active in both cobalt [8] and iron [9] based Fischer–Tropsch catalyst research. More recently, he developed the slit pore model to characterize the pore size distribution of mesoporous catalytic support materials that is more accurate than conventional models [10]. Finally, as a major contribution to the field, he published a leading handbook and textbook, *Fundamentals of Industrial Catalytic Processes*, with his long-time collaborator, Dr. Robert Farrauto [11].

4. The Contents of the Special Issue

The nine contributions to this special issue come from former students, collaborators, colleagues, and respected peers. Keyvanloo et al.'s paper on Fischer–Tropsch catalysis [12] honors Professor Bartholomew's extensive contributions to this area. Hallac et al.'s spectroscopic study on iron-based water gas shift catalysts [13] hearkens back to Professor Bartholomew's graduate work with iron. Seeburg et al.'s paper on methane combustion catalyst stability [14] and Ruelas–Leyva and Fuentes work on chiral catalyst deactivation [15] fit with the constant theme of catalyst deactivation in Dr. Bartholomew's work. Tu et al.'s contribution on palladium catalysts supported on titania for hydrogen peroxide production [16] also touches on themes of this metal and support in Dr. Bartholomew's work. Ha et al.'s paper on nickel catalysts for (dry) methane reforming and carbon deactivation [17] go back to Dr. Bartholomew's early work on both nickel and methane reforming. Türks et al.'s work on CO_2 methanation on nickel catalysts builds on these major themes of Dr. Bartholomew's research [18]. Finally, the contribution by Xiang et al. [19], whose corresponding author is Dr. Bartholomew's long-time collaborator, Bob Farrauto [20], echoes some of his earliest work on environmental catalysts. In summary, this special issue covers much of the breadth and points to the depth of Professor Emeritus Calvin H. Bartholomew's illustrious career. We thank him for his admirable example and honor him for his lasting contributions.

Conflicts of Interest: The author declares no conflict of interest.

References

1. Bartholomew, C.H. Surface Composition and Chemistry of Supported Platinum-Iron Alloy Catalysts. Ph.D. Thesis, Stanford University, Palo Alto, CA, USA, 1972.
2. Bartholomew, C.H. Mechanisms of catalyst deactivation. *Appl. Catal. A* **2001**, *212*, 17–60. [CrossRef]
3. Argyle, M.D.; Bartholomew, C.H. Heterogeneous catalyst deactivation and regeneration: A review. *Catalysts* **2015**, *5*, 145–269. [CrossRef]
4. Bartholomew, C.H. Carbon Deposition in Steam Reforming and Methanation. *Catal. Rev. Sci. Eng.* **1992**, *24*, 67–112. [CrossRef]
5. Bartholomew, C.H.; Agrawal, P.K.; Katzer, J.R. Sulfur Poisoning of Metals. *Adv. Catal.* **1982**, *31*, 135–242. [CrossRef]
6. Bartholomew, C.H. Sintering kinetics of supported metals: New perspectives from a unifying GPLE treatment. *Appl. Catal. A* **1993**, *107*, 1–57. [CrossRef]
7. Bartholomew, C.H. Sintering Kinetics of Supported Metals: Perspectives from a Generalized Power Law Approach. In *Studies in Surface Science and Catalysis*; Delmon, B., Froment, G.F., Eds.; Elsevier: Amsterdam, The Netherlands, 1994; Volume 88, pp. 1–18. ISBN 978-0-444-81682-5. [CrossRef]
8. Reuel, R.C.; Bartholomew, C.H. The stoichiometries of H_2 and CO adsorptions on cobalt: Effects of support and preparation. *J. Catal.* **1984**, *85*, 78–88. [CrossRef]

9. Xu, J.; Bartholomew, C.H. Temperature-programmed hydrogenation (TPH) and in situ Mössbauer spectroscopy studies of carbonaceous species on silica-supported iron Fischer-Tropsch catalysts. *J. Phys. Chem. B* **2005**, *109*, 2392–2403. [CrossRef] [PubMed]
10. Huang, B.; Bartholomew, C.H.; Woodfield, B.F. Improved calculations of pore size distribution for relatively large, irregular slit-shaped mesopore structure. *Microporous Mesoporous Mater.* **2014**, *184*, 112–121. [CrossRef]
11. Bartholomew, C.H.; Farrauto, R. *Fundamentals of Industrial Catalytic Processes*, 2nd ed.; Wiley: Hoboken, NJ, USA, 2006; pp. 1–966. ISBN 978-047145713-8.
12. Keyvanloo, K.; Huang, B.; Okeson, T.; Hamdeh, H.H.; Hecker, W.C. Effect of Support Pretreatment Temperature on the Performance of an Iron Fischer–Tropsch Catalyst Supported on Silica-Stabilized Alumina. *Catalysts* **2018**, *8*, 77. [CrossRef]
13. Hallac, B.B.; Brown, J.C.; Stavitski, E.; Harrison, R.G.; Argyle, M.D. In Situ UV-Visible Assessment of Iron-Based High-Temperature Water-Gas Shift Catalysts Promoted with Lanthana: An Extent of Reduction Study. *Catalysts* **2018**, *8*, 63. [CrossRef]
14. Seeburg, D.; Liu, D.; Radnik, J.; Atia, H.; Pohl, M.-M.; Schneider, M.; Martin, A.; Wohlrab, S. Structural Changes of Highly Active Pd/MeOx (Me = Fe, Co, Ni) during Catalytic Methane Combustion. *Catalysts* **2018**, *8*, 42. [CrossRef]
15. Ruelas-Leyva, J.P.; Fuentes, G.A. Chiral Catalyst Deactivation during the Asymmetric Hydrogenation of Acetophenone. *Catalysts* **2017**, *7*, 193. [CrossRef]
16. Tu, R.; Li, L.; Zhang, S.; Chen, S.; Li, J.; Lu, X. Carbon-Modified Mesoporous Anatase/TiO_2(B) Whisker for Enhanced Activity in Direct Synthesis of Hydrogen Peroxide by Palladium. *Catalysts* **2017**, *7*, 175. [CrossRef]
17. Ha, Q.L.M.; Armbruster, U.; Atia, H.; Schneider, M.; Lund, H.; Agostini, G.; Radnik, J.; Vuong, H.T.; Martin, A. Development of Active and Stable Low Nickel Content Catalysts for Dry Reforming of Methane. *Catalysts* **2017**, *7*, 157. [CrossRef]
18. Türks, D.; Mena, H.; Armbruster, U.; Martin, A. Methanation of CO_2 on Ni/Al_2O_3 in a Structured Fixed-Bed Reactor—A Scale-Up Study. *Catalysts* **2017**, *7*, 152. [CrossRef]
19. Martinelli, M.; Jacobs, G.; Graham, U.M.; Davis, B.H. Methanol Steam Reforming: Na Doping of Pt/YSZ Provides Fine Tuning of Selectivity. *Catalysts* **2017**, *7*, 148. [CrossRef]
20. Xiang, W.; Han, X.; Astorsdotter, J.; Farrauto, R. Catalysts Promoted with Niobium Oxide for Air Pollution Abatement. *Catalysts* **2017**, *7*, 144. [CrossRef]

catalysts

MDPI

Article

Effect of Support Pretreatment Temperature on the Performance of an Iron Fischer–Tropsch Catalyst Supported on Silica-Stabilized Alumina

Kamyar Keyvanloo [1,*], Baiyu Huang [2], Trent Okeson [1], Hussein H. Hamdeh [3] and William C. Hecker [1]

[1] Department of Chemical Engineering, Brigham Young University, Provo, UT 84602, USA; okesontj@gmail.com (T.O.); hecker@byu.edu (W.C.H.)
[2] Department of Chemistry and Biochemistry, Brigham Young University, Provo, UT 84602, USA; baiyu.huang@gmail.com
[3] Department of Physics, Wichita State University, Wichita, KS 67260, USA; hussein.hamdeh@wichita.edu
* Correspondence: kamyar.keyvanloo@yahoo.com

Received: 12 December 2017; Accepted: 29 January 2018; Published: 12 February 2018

Abstract: The effect of support material pretreatment temperature, prior to adding the active phase and promoters, on Fischer–Tropsch activity and selectivity was explored. Four iron catalysts were prepared on silica-stabilized alumina (AlSi) supports pretreated at 700 °C, 900 °C, 1100 °C or 1200 °C. Addition of 5% silica to alumina made the AlSi material hydrothermally stable, which enabled the unusually high support pretreatment temperatures (>900 °C) to be studied. High-temperature dehydroxylation of the AlSi before impregnation greatly reduces $FeO{\cdot}Al_2O_3$ surface spinel formation by removing most of the support-surface hydroxyl groups leading to more effectively carbided catalyst. The activity increases more than four-fold for the support calcined at elevated temperatures (1100–1200 °C) compared with traditional support calcination temperatures of <900 °C. This unique pretreatment also facilitates the formation of ε'-$Fe_{2.2}C$ rather than χ-$Fe_{2.5}C$ on the AlSi support, which shows an excellent correlation with catalyst productivity.

Keywords: Fischer–Tropsch synthesis; supported iron catalyst; silica-stabilized alumina; support pretreatment temperature; iron carbide

1. Introduction

Fisher–Tropsch synthesis (FTS) is a catalytic process that converts carbon sources like natural gas, coal and biomass into more valuable hydrocarbon fuels. Traditionally, the FTS industry uses supported cobalt and unsupported iron catalysts [1,2]. Iron catalysts are preferred over cobalt for FTS from coal or biomass because of their low cost, low methane selectivity and high water–gas shift (WGS) activity; WGS activity is needed for internal production of H_2 during FTS because of inherently low H_2/CO ratios of syngas produced from coal or biomass. Unsupported iron FT catalysts are limited by their weak mechanical strength making them a poor option for slurry-bubble column reactors, the most thermally efficient and economical FT reactors [3]. Unfortunately, supported iron FT catalysts have historically had poor activities and selectivities making them commercially unavailable [4–6]. Potassium and copper are structural promoters often used in industrial iron FT catalysts. It is widely accepted that potassium suppresses methane formation and increases the formation rate of heavy hydrocarbons [7–9]. On the other hand, copper reduces the temperature required for the reduction of iron oxides through enhanced H_2 dissociation [7,8,10].

The relatively poor performance of supported iron FTS catalysts is primarily attributed to the strong Fe oxide-support interactions [6,11]. The effect of inorganic oxide supports (Al_2O_3, SiO_2, TiO_2

and ZrO_2) have been tested for iron based FTS [12–14]; it was shown that catalysts' activity and selectivity are greatly affected by support-surface acidity and catalyst-support interaction. To decrease Fe oxide–support interactions a variety of carbon supports (for example carbon nanotubes, nanofibers, carbon spheres or activated carbon), which provide inert surface chemistry, have also been studied [15–20].

Of all the studies on supported Fe catalyst, there has been limited focus on the effects of support pretreatment methods, prior to adding the active phase and promoters [12]. On the other hand, some studies have been undertaken on the effect of support type and support pore sizes [11,18,21,22]. Among the few studies on the effect of support pretreatment, Xu and Bartholomew prepared 10% Fe/silica catalyst via non-aqueous evaporative impregnation of a silica support, where the support was dehydroxylated at 600 °C before Fe impregnation [6]. This was done using a non-aqueous solvent to decrease any further metal oxide–support interactions. Even with the careful catalyst preparation, interaction of metal oxide and the silica support was high which resulted in low catalyst activity. It could be expected that the supports with high interaction with metals could provide higher stability by preventing the agglomeration of metal particles [21]. On the other hand, strong metal oxide–support interaction could lead to inactive species which are very difficult to reduce or to carbidize [11]. Weak interactive supports such as activated carbon have been also modified with functional surface groups to increase interaction between support and iron species [23].

Calcination of supports at high temperatures is a pathway to make reducible iron catalysts. However, the calcination temperature is usually limited to 500–800 °C due to the limited hydrothermal stability of typical supports, such as alumina and silica. Qu et al. showed higher dispersion of Ag on silica and, subsequently, higher CO oxidation activity as the support was pretreated at 550–700 °C [24]. Higher calcination temperatures (900–950 °C) of the support resulted in an agglomeration of Ag particles due to a drastic decrease in surface area and pore volume of the support with calcination temperature. However, our group has recently reported a hydrothermally stable γ-alumina doped with 5 wt % silica. Silica enters the tetrahedral vacancies in the defect spinel structure of alumina and forms Si–Al spinel phase, which significantly postpones the alumina phase transition from γ to α even at temperatures as high as 1200 °C [25,26]. This unique feature enables pretreatment of the AlSi support at much higher temperatures than conventionally practiced for catalyst preparation and makes it a unique support for FT iron catalyst [27].

In this paper, we explore the effect of support pretreatment temperature on the catalytic performance of iron catalysts supported on AlSi. The hydrothermal stability of the AlSi support enabled us, for the first time, to pretreat the support at high temperatures (1100–1200 °C) while still maintaining the γ-alumina phase with high surface area and large pore volume. High-temperature dehydroxylation of the AlSi facilitates the formation of ε′-$Fe_{2.2}C$, which resulted in a very active supported iron catalyst.

2. Results

2.1. Physical Properties

2.1.1. Nitrogen Adsorption

Nitrogen adsorption measurements were conducted on both the supports and final catalysts to determine the pore properties. Table 1 summarizes the surface areas, pore volumes and average pore diameters, while their pore size distributions are shown in Figure 1. As shown in Table 1, surface area and pore volume of the supports decrease as the pretreatment temperature increases from 700 °C to 1200 °C, i.e., surface area decreases from 331 m^2/g to 76 m^2/g and pore volume decreases from 1.75 cm^3/g to 0.52 cm^3/g. Similarly, the same trend for surface area is observed for the final catalysts. However, drastic differences for pore volume of the supports and the corresponding catalysts are found. The pore volumes of the catalysts in which the supports were pretreated at 700 °C and 900 °C are less than that of the catalysts with supports pretreated at 1100 °C. The pore size distribution of each support is very similar and the average pore diameter is about 22 nm, as shown in Figure 1a. However,

once Fe was loaded on to each support, the pore size distribution was quite different for the final catalysts (Figure 1b). Average pore diameter is decreased significantly for Fe/700AlSi and Fe/900AlSi by 72% and 51%, respectively, while the average pore diameter is decreased for Fe/1100AlSi and Fe/1200AlSi by only 10% and 12%, respectively. Moreover, the pore diameters of the final catalysts, by which the support was calcined at lower temperatures (Fe/700AlSi and Fe/900AlSi), were much lower than those catalysts calcined at higher temperatures (Fe/1100AlSi and Fe/1200AlSi) (5–11 nm vs. 21 nm).

Table 1. Surface area, pore volume and pore diameter of supports and catalysts after pretreatment for 2 h at four different temperatures.

Supports' Pretreatment Temperature, °C	Brunauer–Emmett–Teller (BET) Surface Area, m^2/g		Total Pore Volume, cm^3/g		Average Pore Diameter, nm	
	Support	Catalyst	Support	Catalyst	Support	Catalyst
700	331	180	1.75	0.16	20.2	5.6
900	276	164	1.53	0.26	21.5	10.7
1100	163	117	0.99	0.53	23.3	21.0
1200	76	63	0.52	0.25	23.5	20.6

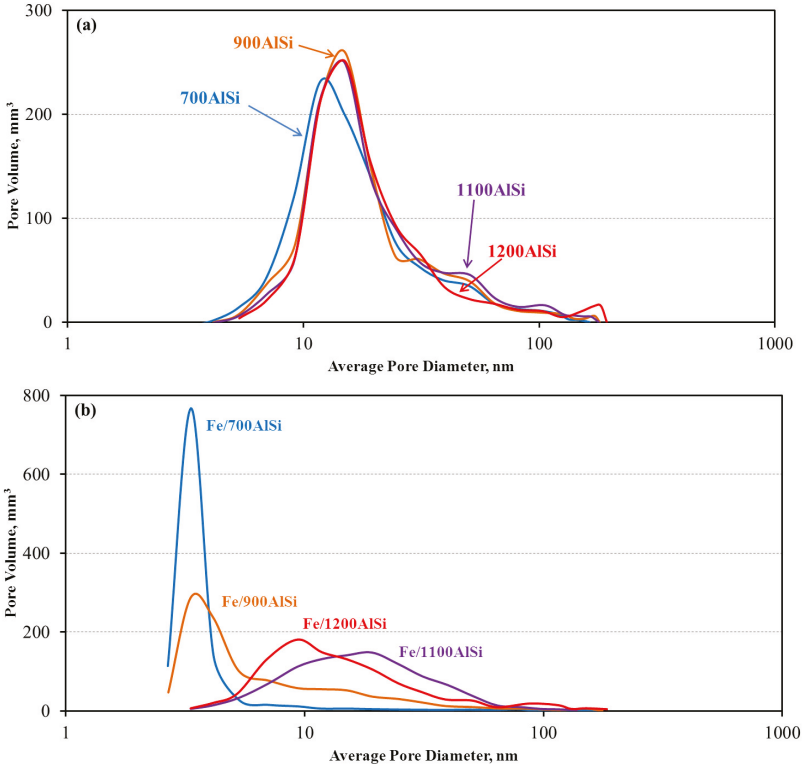

Figure 1. Brunauer–Emmett–Teller (BET) results of (**a**) supports calcined at different temperatures and (**b**) catalysts with supports calcined at different temperatures.

2.1.2. X-ray Diffraction (XRD)

Figure 2 shows the X-ray diffraction (XRD) patterns of the freshly reduced and carbided catalysts. Fe_3O_4 and Fe metal are present in the freshly reduced catalysts (Figure 2a); however, the peak intensities are different for each catalyst. Fe/1100AlSi has the lowest Fe_3O_4/Fe ratio, while the highest ratio

of Fe_3O_4/Fe is observed in Fe/700AlSi. Particle sizes for Fe_3O_4 and Fe^0 were calculated based on peaks at 2θ = 37.6° and 45.8°, respectively (Table 2). Iron particle sizes are relatively large (>35 nm) when the support is calcined at 700–900 °C; however, the lowest particles sizes (4–8 nm) result with 1100AlSi support. The iron particle sizes are slightly increased when the support is calcined at higher temperatures of 1200 °C. The iron carbide phase is the prevailing phase of the carbided catalysts for Fe/1100AlSi and Fe/1200AlSi, while Fe_3O_4 is the major phase observed for the other two catalysts supported on AlSi support calcined at lower temperatures, as shown in Figure 2b.

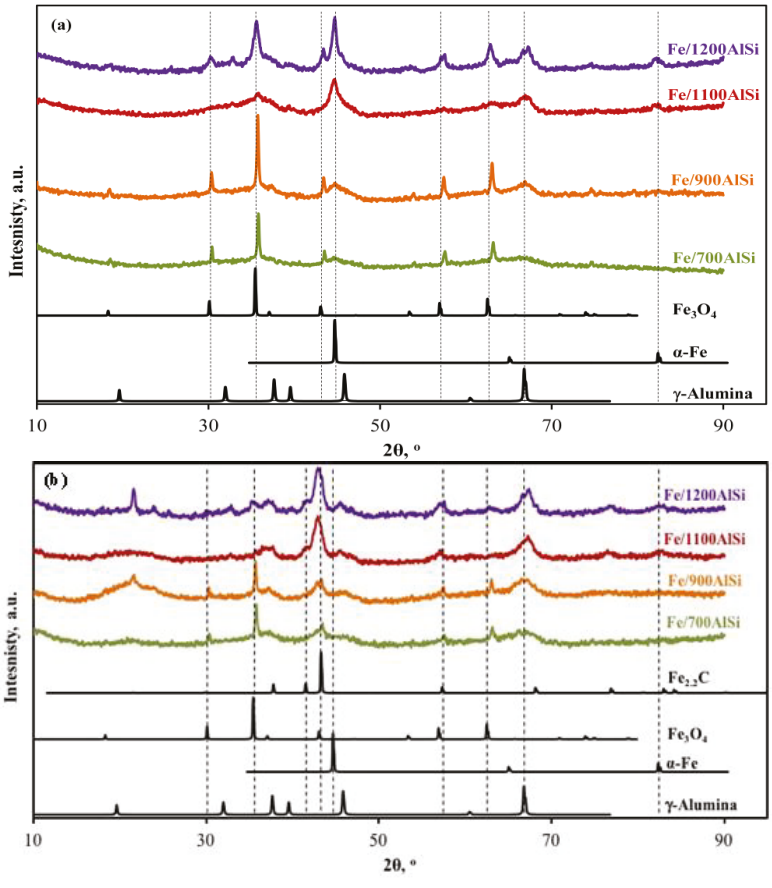

Figure 2. X-ray diffraction (XRD) results for different support calcination temperatures of (**a**) reduced and (**b**) carbided catalysts. The catalysts reduced in H_2 at 320 °C for 16 h and then passivated in 1% O_2 in He. The passivated reduced catalysts were carbided at 280 °C in H_2/CO = 1.

Table 2. Crystallite size of reduced catalysts calculated from XRD.

Catalyst	Particle Size, nm	
	Fe	Fe_3O_4
Fe/700AlSi	38.9	33.0
Fe/900AlSi	40.1	41.4
Fe/1100AlSi	8.4	4.6
Fe/1200AlSi	13.6	13.9

2.2. Chemical Properties

2.2.1. H_2 Temperature-Programmed Reduction (TPR)

The effect of support calcination temperature on the reducibility of the final catalyst was studied using H_2 temperature-programmed reduction (TPR). As shown in Figure 3, the reduction of each catalyst begins with (1) transformation of Fe_2O_3 to Fe_3O_4 and FeO happening between 150 and 350 °C; followed by (2) reduction of FeO and Fe_3O_4 to Fe metal from 250–500 °C; and (3) Fe metal formation from FeO. Al_2O_3 spinel in the temperature range of 500–550 °C. The results show that the peak temperatures for each of these transformations decrease with increasing support pretreatment temperature, implying a more reducible catalyst when the AlSi support is calcined at higher temperatures. For example, a difference of 70 °C in the reduction temperature of the first stage for Fe/700AlSi and Fe/1200AlSi is observed. Extent of reduction (EOR) was determined by dividing the actual weight loss by the theoretical weight loss corresponding to the conversion of Fe_2O_3 to Fe and of CuO to Cu. Values for EOR are reported in Table 3 for stage 1, stage 2, and overall reduction. Support calcination temperature had a significant impact on EOR; EOR is increased by 43% when the support calcined at 1200 °C (Fe/1200AlSi) compared to 700 °C (Fe/700AlSi).

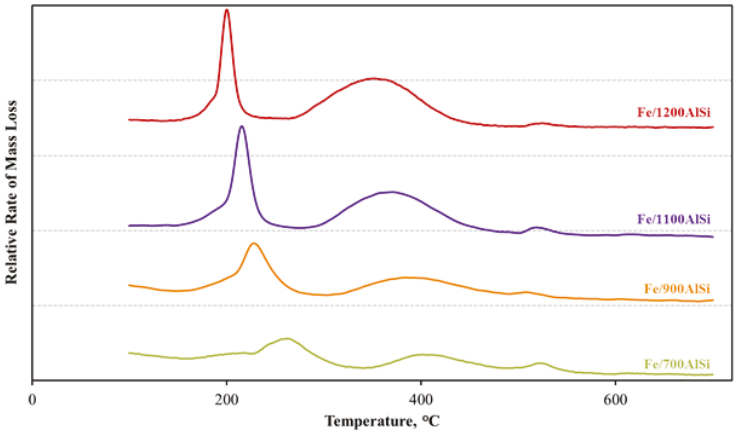

Figure 3. H_2-TPR profiles of Fe catalysts supported on supports calcined at different temperatures.

Table 3. Extent of reduction (EOR) from temperature programmed reduction (TPR) weight loss.

Catalyst	Extent of Reduction, %			
	First Stage [a]	Second Stage	Third Stage	Total
Fe/700AlSi	4.89	6.88	4.85	16.6
Fe/900AlSi	15.5	19.8	1.78	37.1
Fe/1100AlSi	22.2	31.3	1.15	54.7
Fe/1200AlSi	18.8	39.2	1.38	59.4

[a] The first stage of weight loss consists of two peaks, the reduction of Fe_2O_3 to FeO and Fe_3O_4.

2.2.2. Syngas-TPR

In addition to H_2-TPR, syngas-TPR was also implemented to obtain information for carbiding properties of the catalysts. The calcined catalysts were exposed to syngas to form iron carbides which are apparently the active phase in FT [28–32]. Syngas-TPR results are shown in Figure 4. The observed weight changes under a H_2/CO atmosphere are a combination of several competing

reactions including: (1) reduction of Fe_2O_3 to lower iron oxides or iron metal (150–280 °C); and (2) carbiding of the iron oxides or iron metal to iron carbides (260–400 °C). The observed net changes for these two stages are weight losses (reported in Table 4). For the reduction step (first stage), increasing support pretreatment temperature increases the amount of Fe_2O_3 reduced to lower iron oxides or iron metals, with the weight loss of Fe/1200AlSi being the highest followed by Fe/1100AlSi. Most importantly, increasing support pretreatment temperature increases the conversion of iron oxides or iron metals to iron carbides (second stage). Fe/700AlSi had a broad carbiding stage, which barely showed any weight loss compared to Fe/1200AlSi with a distinct peak around 310 °C. Furthermore, increasing support pretreatment temperature also decreases the temperature at which these catalysts are carbided (easier carbiding); the peak temperature of the carbiding stage is decreased by 40 °C for Fe/1200AlSi compared to Fe/900AlSi. Theoretical weight losses for reduction of Fe_2O_3 to Fe_3O_4, FeO, Fe, and ε'-$Fe_{2.2}C$ are approximately: 3.3%, 10%, 30% and 23%, respectively. The experimental weight losses vary greatly but suggest all the catalysts (except Fe/700AlSi) are reduced beyond FeO on the first stage. In addition, the carbiding of Fe/1100AlSi and Fe/1200AlSi catalysts are complete or close to completion because their weight losses are beyond the theoretical weight loss of 23% (Fe_2O_3 to ε'-$Fe_{2.2}C$).

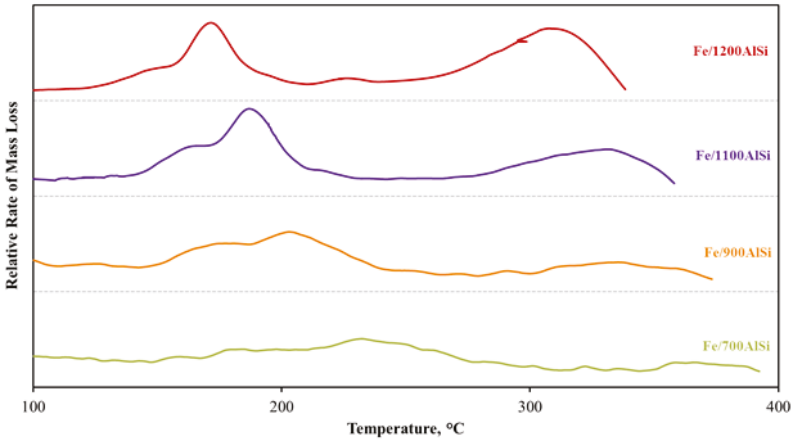

Figure 4. Syngas-TPR for Fe catalysts with different support calcination temperatures focused on two stages of weight loss (inverted).

Table 4. Weight losses of Fe catalysts supported on AlSi calcined at different temperatures during reduction and carbiding stage.

Catalyst	Extent of Reduction/Carbiding [a], %		
	First Stage	Second Stage	Total
Fe/700AlSi	1.9	3.7	5.6
Fe/900AlSi	12.8	5.4	18.2
Fe/1100AlSi	18.5	7.5	26.0
Fe/1200AlSi	15.3	10.4	25.7

[a] This was calculated based on the assumption of Fe_2O_3 to FeO for the first stage and FeO to $Fe_{2.2}C$ for the second stage.

2.2.3. Hydroxyl Group Content Measurement

The hydroxyl group content of the support pretreated at different temperatures was determined using thermogravimetric analysis (TGA). The previously calcined supports at different temperatures

were heated in TGA with a ramp rate of 10 °C/min in an inert gas flow. The weight loss can be divided into two stages: (1) removal of physisorbed water (dehydration) in the temperature range 25–130 °C; and (2) removal of surface hydroxyl groups (dehydroxylation) in the form of water in the temperature range 130–1100 °C, as reported by Ek et al. [33]. It is well known that alumina dehydroxylates during phase transition from gamma to alpha when temperature increases. In the present study, as shown in Figure 5, 700AlSi exhibits the highest dehydration and dehydroxylation rate and its weight decreases up to 1100 °C. In contrast, the other three samples show a mass loss up to 700 °C and then remained almost constant up to 1100 °C.

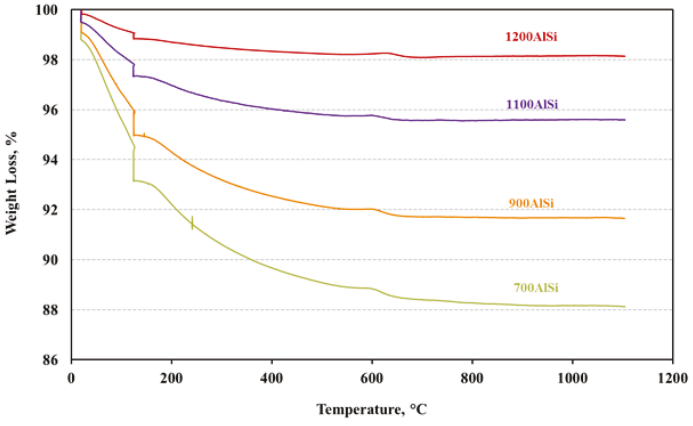

Figure 5. Thermogravimetric analysis (TGA) curves of supports calcined at different temperatures.

Based on the values of concentrations of physisorbed water and OH groups (Table 5) for supports pretreated at different temperatures, it is clear that the higher the support pretreatment temperature, the lower the physisorbed water and hydroxyl group content of the corresponding support. Consequently, 700AlSi has the highest hydroxyl group concentration (5.6 mmol/g) while 1200AlSi has the lowest (0.8 mmol/g). Due to the hydrophilic nature of calcined alumina, 700AlSi also has the highest physisorbed water concentration (3.7 mmol/g) while 1200AlSi has the lowest (0.6 mmol/g).

Table 5. Concentrations of physisorbed water and OH groups for supports pretreated at different temperatures.

	700AlSi	900AlSi	1100AlSi	1200AlSi
First [a] mass loss, %	6.8	5.0	2.6	1.2
Second [b] mass loss, %	5.0	3.3	1.4	0.7
Physisorbed water, mmol/g_{Al2O3}	3.7	2.7	1.4	0.6
OH group content, mmol/g_{Al2O3}	5.6	3.7	1.6	0.8

[a] Weight loss up to 130 °C. [b] Weight loss between 130–1100 °C.

2.2.4. Mossbauer Spectroscopy

Mossbauer spectroscopy gives quantitative information about the iron phase present in the reduced and carbided catalysts. The Mossbauer spectra are shown in Figure 6 and the results are summarized in Table 6. For the reduced catalysts, Fe_3O_4 contents are almost the same. However, Fe/700AlSi and Fe/900AlSi have the lowest Fe0 content, while the other two catalysts exhibit three- to four-fold more metallic Fe. In addition, Fe/700AlSi and Fe/900AlSi have the highest $FeO{\cdot}Al_2O_3$ surface

spinel as suggested by higher Fe^{2+} and Fe^{3+} species, while Fe/1100AlSi and Fe/1200AlSi have the lowest spinel content. This means that support pretreatment temperature increases the percentage of Fe0 in the reduced samples at the expense of $FeO{\cdot}Al_2O_3$ surface spinel. Increasing support pretreatment temperature also increases iron carbide formation by lowering $FeO{\cdot}Al_2O_3$ surface spinel in carbided samples. Carbided Fe/1100AlSi and Fe/1200AlSi have more than 55% carbides, whereas the carbide contents for Fe/700AlSi and Fe/900AlSi are 22% and 29%, respectively. Carbided Fe/1100AlSi and Fe/1200AlSi also have much less spinel content (6% and 3%, respectively) than that of Fe/700AlSi and Fe/900AlSi (48% and 31%, respectively). Both ε'-$Fe_{2.2}C$ and χ-$Fe_{2.5}C$ are observed in carbided samples; however, their distribution changes significantly with pretreating the support at different temperatures, as shown in Figure 7. The content of χ-$Fe_{2.5}C$ slightly increases (8–18%) by raising the pretreating temperature from 700 °C to 900 °C, but is constant at higher temperatures. On the other hand, the content of ε'-$Fe_{2.2}C$ is increased three-fold (14% to 43%) when the pretreatment temperature increases from 700 °C to 1200 °C.

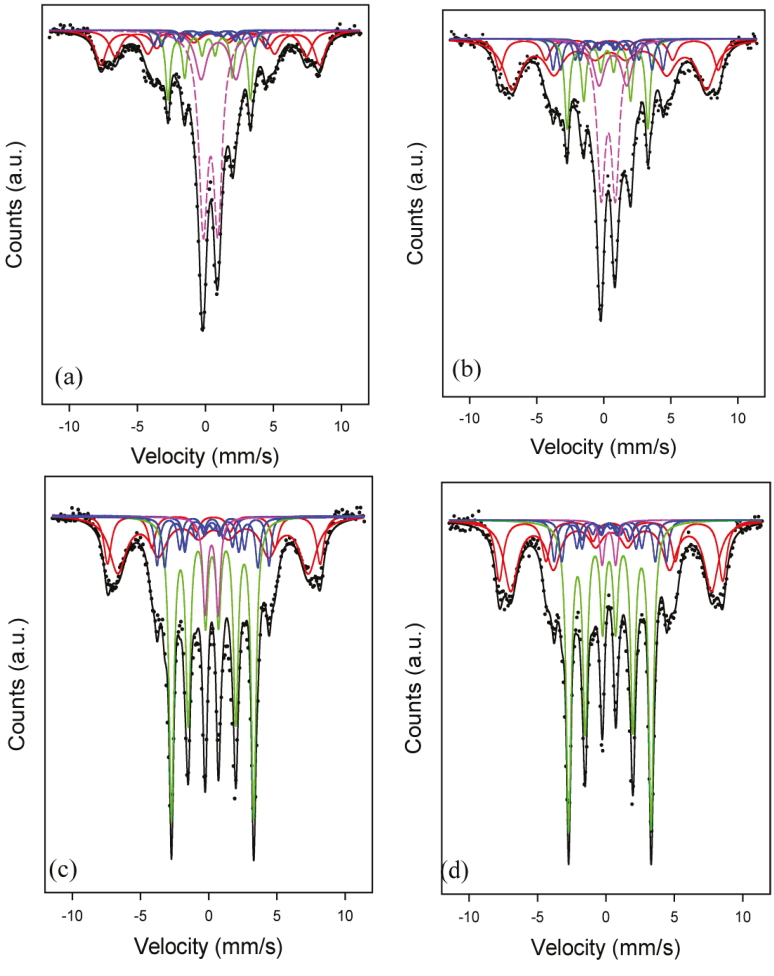

Figure 6. Mossbauer spectra of carbided (**a**) Fe/700AlSi, (**b**) Fe/900AlSi, (**c**) Fe/1100AlSi, and (**d**) Fe/1200AlSi. Spectra were recorded at 20 K. The passivated reduced catalysts were carbided at 280 °C in $H_2/CO = 1$.

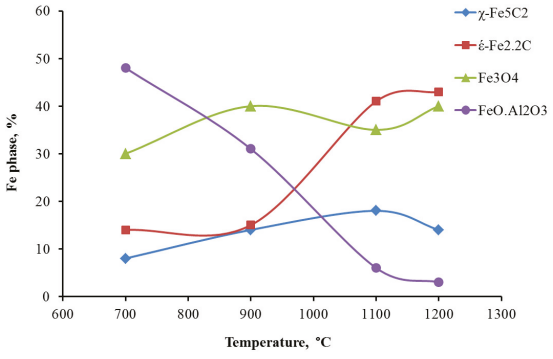

Figure 7. The change in distribution of the iron phases as the function of support pretreatment temperature.

Table 6. Phase identification of iron from Mossbauer spectroscopy analysis at 20 K for reduced or carbided catalysts with support calcination at different temperatures.

Catalyst	Iron Species, %						
	Reduced			Carbided			
	Fe_3O_4	Fe	Fe^{2+} or Fe^{3+}	Fe_3O_4	ε′-$Fe_{2.2}C$	χ-$Fe_{2.5}C$	Fe^{2+} or Fe^{3+}
Fe/700AlSi	63	7	30	30	14	8	48
Fe/900AlSi	60	8	32	40	15	14	31
Fe/1100AlSi	68	22	10	35	41	18	6
Fe/1200AlSi	68	28	4	40	43	14	3

2.3. Fisher–Tropsch Synthesis (FTS) Performance

The activity and selectivity data were obtained at low CO conversions (X_{CO}) of 18–22%, temperature of 260 °C, and H_2/CO of 1. The catalysts' preparation was uniform except for the support pretreatment temperature. The rate, productivity, CO_2 selectivity, and hydrocarbon selectivity for each of the catalysts are shown in Table 7. The support pretreatment temperature does affect performance. The rates for Fe/700AlSi and Fe/900 AlSi are significantly lower than the rate of Fe/1100AlSi, while Fe/1200AlSi only has a marginally better rate than Fe/1100 AlSi. The rate increases by more than four-fold as the support pretreatment temperature increases from 700 °C to 1200 °C (Fe/700AlSi: 24.3 mmol $CO/g_{cat}/h$ vs. Fe/1200AlSi: 110.9 mmol $CO/g_{cat}/h$). The same trend is also observed in productivity which includes the selectivity, with the productivity of Fe/1200AlSi being 0.80 $g_{HC}/g_{cat}/h$ and Fe/700AlSi being only 0.20 $g_{HC}/g_{cat}/h$. Surprisingly, all four catalysts show similar methane selectivity (CO_2-free basis), between 13% and 14%. The authors acknowledge that the methane selectivity for the supported materials is undesirably high since they have not yet been optimized for selectivity. Thus, a future study is needed to reduce methane selectivity for supported Fe catalysts.

Table 7. Performance of four catalysts with different support temperatures in fixed bed reactor. T = 260 °C, H_2/CO = 1, P = 20 bar.

Catalyst	Rate, mmol $(CO + H_2)/g_{cat}/h$	X_{CO} [a], %	$X_{CO} + H_2$ [a], %	Productivity, $g_{HC}/g_{cat}/h$	CO_2 Selectivity %	H. C. Selectivity [b], %		
						CH_4	C_2	C_3+
Fe/700AlSi	24.3	19.8	21.7	0.196	34.1	13.3	11.2	75.5
Fe/900AlSi	37.7	21.8	25.5	0.316	31.5	13.3	8.95	77.7
Fe/1100AlSi	93.8	18.6	20.9	0.763	33.0	14.1	8.99	76.9
Fe/1200AlSi	110.9	22.4	22.7	0.796	40.9	14.0	9.76	76.3

[a] X_{CO} = CO conversion, X_{CO} +H_2 = CO and H_2 conversion. [b] Hydrocarbon selectivity on a CO_2-free basis.

3. Discussion

This work demonstrates that the support pretreatment temperature, before precursor loading, has a significant impact on the final catalyst morphology and FTS catalytic performance. The effect of pretreatment temperature of the support was studied, for the first time, over a wider range of temperatures, 700–1200 °C; higher than typically practiced by previous authors. This was made possible by incorporation of a unique silica-stabilized alumina support of high thermal stability [25,26]. The catalyst preparation and activation procedures used in this study led to the significant formation of ε'-$Fe_{2.2}C$, which had a great correlation with steady-state activity of the catalyst.

3.1. Effects of Support Pretreatment Temperature on Catalyst Physical Properties

Support pretreatment temperature affects both the support and final catalyst pore properties, i.e., surface area, pore volume and pore size distribution. It is well known that γ-alumina is a metastable transition phase. When calcined at elevated temperatures, γ-alumina loses surface area and pore volume due to sintering and finally undergoes phase transition into α-phase with a lower surface area and pore volume. This trend is also observed in the present study, i.e., 700AlSi and 900AlSi have large surface areas (more than 250 m^2/g) and pore volumes (more than 1.5 cm^3/g), while 1100AlSi and 1200AlSi show relatively low surface areas (<170 m^2/g) and pore volumes (<1 cm^3/g). However, it should be mentioned that even at high-temperature pretreatment of 1200 °C, the AlSi support is still in γ-alumina phase with desirable surface area and pore volume. From the pore property point of view, 700AlSi and 900AlSi should be able to accommodate more Fe and be more suitable as catalyst supports. However, a drastic reduction in surface area, pore volume and pore size is observed in the final catalysts of Fe/700AlSi and Fe/900AlSi when Fe is loaded, as reported in Table 1. Nucleation of FeO crystallites is favored on hydroxylated alumina surfaces [34]. Therefore, much lower pore volume (0.16–0.26 cm^3/g) and pore diameter (5.6–10.7 nm) of Fe/700AlSi and Fe/900AlSi with higher hydroxyl group concentrations (Table 5) suggest pore blockage of the support due to the presence of large Fe and Fe_3O_4 particles (>30 nm calculated from XRD).

High-temperature dehydroxylation of Fe/1100AlSi and Fe/1200AlSi results in relatively uniform distribution of Fe_2O_3 and Fe_3O_4 crystallites inside the pores and, consequently, higher dispersion as evidenced by narrower iron carbide peaks observed in XRD. Although small by comparison, the pore volume and pore size of 1100AlSi and 1200AlSi are still remarkably large, especially when treated at such high temperatures to remove most of the hydroxyl groups. It should also be noted that the support pretreatment temperature up to 1100 °C improves the dispersion of iron particles as evidenced by decreasing iron particle sizes from ~40 nm to 4 nm (700–900 °C vs. 1100 °C support pretreatment temperature). However, higher support pretreatment temperatures (>1100 °C) further decreases the surface area and pore volume of the support, which consequently results in slightly lower dispersion and larger particle sizes (~8 nm). These results are in agreement with Qu et al. who found higher dispersion of Ag on silica as the calcination temperature increased to 700 °C, while lower dispersion resulted at higher calcination temperatures [24].

3.2. Effects of Support Pretreatment Temperature on Catalyst Chemical Properties

The results in this work provide correlations between support pretreatment temperature and the catalyst reducibility and extent of carbiding. Figure 8 shows the correlations between the support pretreatment temperature and hydroxyl groups (Table 5), and the extent of reduction from TPR (Table 3) and ε'-$Fe_{2.2}C$ from Mossbauer spectroscopy (Table 6). Higher dehydroxylation temperature of the support for Fe/1100AlSi and Fe/1200AlSi leads to highly reducible Fe_2O_3 and Fe_3O_4, and subsequently a higher extent of reduction due to weaker FeO-support interactions. This observation is confirmed by H_2-TPR and CO-TPR data shown in Figures 3 and 4. Lower temperature and higher area of the reduction and carbiding peaks clearly support higher reducibility and carbiding extent as the calcination temperature of the support increases. This observation is further evidenced by a much

lower Fe^{2+}/Fe^{3+} percentage from iron aluminate spinel in Fe/1100AlSi and Fe/1200AlSi than that of Fe/700AlSi and Fe/900AlSi measured by Mossbauer spectroscopy. Brenner et al. reported that oxidation of Fe^0 to Fe^{3+} occurs on the hydroxyl groups of alumina supports and a high density of FeO crystallites, which are difficult to reduce or carbide, are produced [35]. Therefore, highly reducible Fe_2O_3 and Fe_3O_4 clusters are formed in the near absence of surface OH groups. That likely explains why Fe/700AlSi and Fe/900AlSi with higher concentrations of surface hydroxyl groups have lower extents of reduction and a lower iron carbide phase.

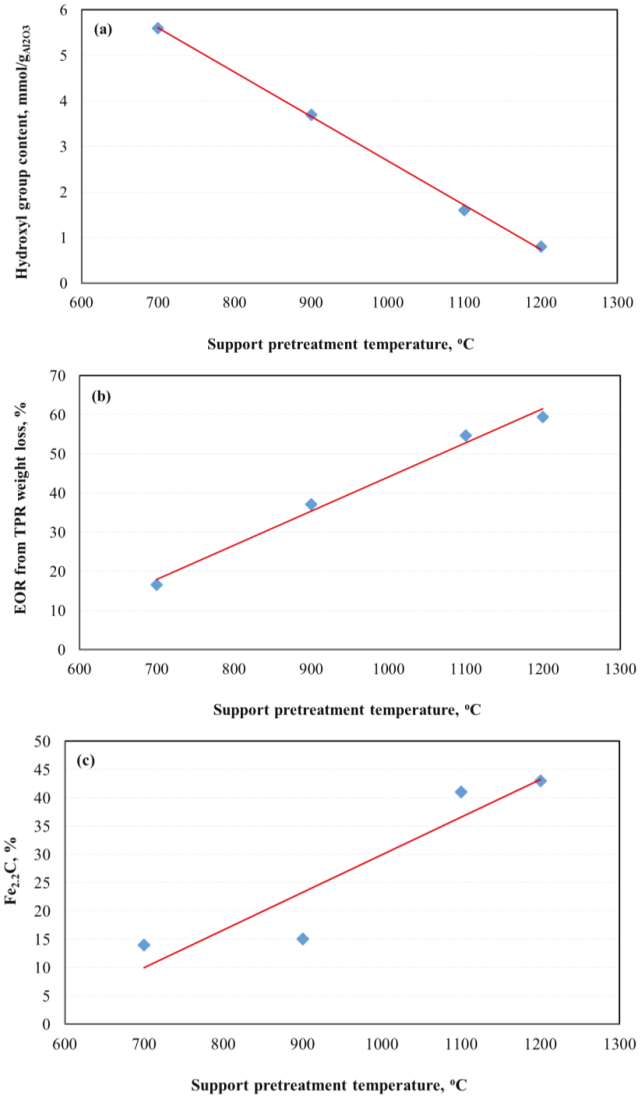

Figure 8. Correlation between support treatment temperature and (**a**) hydroxyl groups, (**b**) extent of reduction, and (**c**) iron carbide phase.

Degree of carbidization can also be affected by iron particle size. Generally, larger iron oxide crystallites are easier to carbidize than smaller iron oxide counterparts [21]. However, this is only true if the surface chemistry of the support in supported iron catalyst would be relatively the same. For example, large iron particle sizes on Fe/700AlSi and Fe/900AlSi have the lowest degree of carbidization because of high metal oxide–support interaction at lower support dehydroxylation temperatures.

3.3. Effects of Support Pretreatment Temperature on Catalyst Performance

A positive correlation between the extent of reduction to Fe metal (from TPR data) following reduction in H_2 and Fe carbide content is evident (Figure 8). This means that highly reducible Fe_2O_3 and Fe_3O_4 clusters result in a higher concentration of carbides, which are believed to be the active phase for FTS. The concentration of carbides increases significantly as the support pretreatment temperature increases, but it stays constant for pretreatment temperatures of 1100 °C and 1200 °C. This observation is consistent with syngas-TPR results, which show the carbiding of Fe/1100AlSi and Fe/1200AlSi is almost complete. In the present study, these iron carbide phases are identified as both ε'-$Fe_{2.2}C$ and χ-$Fe_{2.5}C$ by Mossbauer spectroscopy. The χ-$Fe_{2.5}C$ is only increased from 8% to 14–18% by higher pretreatment temperature of the support while the formation of ε'-$Fe_{2.2}C$ is significantly enhanced. In addition, the catalyst activity is also increased five-fold as the support pretreatment temperature increased from 700 °C to 1200 °C. The positive correlation between catalyst activity and ε'-$Fe_{2.2}C$ content is shown in Figure 9.

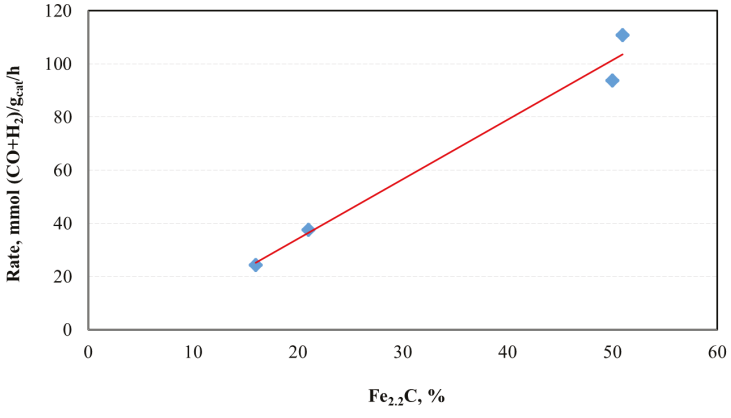

Figure 9. Correlation of catalyst activity with iron carbide content.

It has been reported that the formation of χ-$Fe_{2.5}C$ is favored over unsupported Fe catalysts under typical FT conditions and identified as an active iron carbide phase [36,37]. Nevertheless, the catalysts used in most of those studies are unsupported, whereas the catalyst in the present study is supported with pretreated silica-stabilized alumina. In the study by de Smit et al. using chemical potentials calculated by statistical thermodynamics, ε'-$Fe_{2.2}C$ formation is more favored for small particle sizes with less diffusion resistance and in the presence of a support material [38]. One can expect higher dispersion of active sites using supports, especially highly dehydroxylated supports used in this study which lower the metal oxide-support interaction and produce highly reducible and well dispersed iron oxides. On the other hand, the formation of ε'-$Fe_{2.2}C$ is more favored at low temperatures followed by its conversion to χ-$Fe_{2.5}C$ at higher temperatures (>250 °C). In this study, the calcined Fe/AlSi catalysts were activated under syngas at 20 atm by increasing the temperature from 180 °C and holding every 10 °C up to 280 °C, while keeping conversion less than 60% in each step. The highly dispersed ε'-$Fe_{2.2}C$ particles formed at low temperatures might have been stabilized on the support and their conversion

to χ-$Fe_{2.5}C$ was not completed at higher temperatures of the activation process. This finding is in accordance with Niemantsverdriet et al. who reported the formation of ε′-$Fe_{2.2}C$ over iron supported on TiO_2/CaO after FT reaction at 240 °C [39]. Raupp et al. also observed ε′-$Fe_{2.2}C$ on Fe/SiO_2 exposed to FTS at 250 °C for 6 h [40].

The activity of Fe/AlSi, in this study, is among the highest in the literature for both unsupported and supported iron catalysts, and the catalyst is stable over 800 h time on stream. In addition, the significant correlation of the catalyst activity with the amount of ε′-$Fe_{2.2}C$ clearly show that ε′-$Fe_{2.2}C$ on AlSi support can be as active as χ-$Fe_{2.5}C$ on unsupported Fe catalysts. Thus, historically ε′-$Fe_{2.2}C$ was not considered the active phase due to a lack of evidence on unsupported iron catalysts. This is an important finding because the supported iron catalysts reported in the literature prior to this study were usually much less active than unsupported iron catalysts due to their high metal oxide–support interaction, and thus careful characterization of supported catalysts is scarce in the literature.

4. Materials and Methods

4.1. Catalyst Preparation

A series of iron catalysts supported on BYU alumina supports (Brigham Young University, Provo, UT, USA) pretreated at different temperatures were investigated in this study. The alumina support was doped with 5% SiO_2 to increase the thermal stability, as described previously [25]. The supports were sieved to 250–595 µm (30–60 mesh size) and calcined in air at 700 °C, 900 °C, 1100 °C or 1200 °C for 4 h prior to impregnation. The supports were named starting with their calcination temperature, e.g., the support calcined at 700 °C was named 700AlSi. All four catalysts were prepared by incipient wetness using an aqueous solution containing desired amounts of ferric nitrate, copper nitrate and potassium bicarbonate in four steps. In each step, 10 wt % Fe with the desired amount of Cu and K were dissolved in sufficient water for incipient wetness and mixed into the catalyst support. The catalysts were sat at room temperature for 4 h, dried in an oven at 80 °C for 16 h, and finally calcined for 16 h at 300 °C in air. Nominal compositions (on a relative mass basis) of reduced catalysts were 100Fe/7.5Cu/4K/150Al_2O_3 for an iron loading of 40%. The final catalysts were named Fe/xAlSi, where "x" was the calcination temperature. For example, Fe/700AlSi was the Fe/Cu/K catalyst supported on the support calcined at 700 °C.

The samples were reduced at 280–320 °C in 10% H_2/He for 10 h followed by 100% H_2 for 6 h for characterization of reduced catalysts. Reduced catalysts were carefully passivated by first exposing each to flowing air in He (<1%) at room temperature followed by gradually increasing concentrations of air in helium while monitoring the temperature of the catalyst bed. The passivated reduced catalysts were carbided at 280 °C, 20 atm, and H_2/CO = 1 for 24 h for characterization of carbided samples.

4.2. Catalyst Characterization

4.2.1. Nitrogen Adsorption/Desorption

Surface area, pore volume, and pore size distribution were calculated by nitrogen adsorption/desorption isotherms measured using a Micromeritics TriStar 3000 instrument (Norcross, GA, USA). The samples (0.3 g) were degassed at 120 °C for 12 h before measurement. Surface area was calculated by the BET model using P/P0 ranging from 0.05 to 0.2. Pore volume was measured by the single point method using P/P0 = 0.990. Pore size distribution was calculated using the desorption branch of the isotherm according to a newly developed slit pore-geometry model [41].

4.2.2. XRD

To determine the presence of different iron phases, X-ray diffraction patterns were collected for all the catalysts using a PANalytical X'Pert Pro diffractometer (Almelo, The Netherlands) with a Cu source and a Ge monochromator tuned to the Cu-Kα1 wavelength (λ = 1.54 Å). Samples (reduced and

passivated) were scanned from 10–90° using a step size of 0.016° and a step time of 350 s. Diffraction patterns were compared to standard patterns in the database.

4.2.3. TPR

TPR experiments were performed in a Mettler Toledo TGA/DSC 1 equipped with an automated GC 200 gas controller (Columbus, OH, USA) to understand the reduction/carbiding behavior of the catalysts. 10–20 mg of calcined samples were exposed to a reducing gas mixture of 10% H_2/He (H_2-TPR) or 10% syngas (H_2:CO = 1) in He (syngas-TPR), while the temperature was increased at 3 °C/min from ambient to 700 °C.

4.2.4. Hydroxyl Group Content Measurement

TGA was performed for alumina samples in the same TGA equipment (Columbus, OH, USA) described in Section 2.2.3 to determine hydroxyl group content. Pre-calcined alumina samples were heated at a rate of 5 °C/min from room temperature to 1100 °C in He flow of 80 mL/min and held for 2 h. The weight loss between 130 °C and 1100 °C was used to determine the hydroxyl group content.

4.2.5. Mossbauer Spectroscopy

Mossbauer measurements were taken in transmission mode, with a ^{57}Co source in Rh matrix mounted in a standard constant acceleration drive unit. Samples were placed inside a closed-cycle refrigerator for low-temperature measurements. All measurements were calibrated with respect to alpha-Fe. Analysis of measured spectra was carried out by using defined functions within the PeakFit program (version 4.12) using the least-squares-fitting routine. The parameters for each sub-spectrum in the fit consisted of the position, width and height of the first peak, the hyperfine magnetic field and the quadrupole electric field. Initially, the hyperfine magnetic fields of known FexC ($2.2 \leq x \leq 3$) were constrained but all other parameters could vary freely. Subsequently, the carbides' hyperfine magnetic fields for the intense-distinct peaks could vary to obtain the best fit to the experimental data. The percentages of Fe in the different phases were determined from the areas under the peaks of the different sub-spectra. Calculated carbide sub-spectra of Fe percentages less than the experimental error of about $\pm$ 3% were then removed from the fitting procedure and data was fitted for the final results.

4.3. FTS Performance Measurement

FTS was conducted in a fixed-bed reactor (stainless steel, 3/8 inch OD) described previously [34]. Each sample (0.25 g, 250–590 μm) was diluted with 1 g silicon carbide to improve heat distribution in the catalytic zone.

Before FTS, the samples were reduced in situ at 280–320 °C in 10% H_2/He for 10 h followed by 100% H_2 for 6 h. After cooling to 180 °C, the system was then pressurized to 20 atm in syngas (H_2:CO = 1), and the catalysts were activated by ramping and holding every 10 °C up to 280 °C, while keeping conversion less than 60% in each step. Activity and stability data were then obtained over the next 200–700 h as reaction temperatures were varied from 220 °C to 260 °C.

After leaving the reactor, the exit gas and liquid effluent passed through a hot trap (90 °C) and a cold trap (0 °C) to collect heavy hydrocarbons and liquid products. The effluent gaseous product was analyzed using an HP5890 gas chromatograph (Santa Clara, CA, USA) equipped with a thermal conductivity detector and 60/80 carboxene-1000 column. CO conversion and selectivities were determined with the use of an internal standard (Ar).

5. Conclusions

In summary, the results of this work demonstrate that support pretreatment temperature has a significant impact on the properties (physical and chemical) and catalytic performance of silica-stabilized alumina (AlSi) supported iron FTS catalysts. The high thermal stability of the AlSi

support prepared in this study compared with the traditional alumina supports enabled us to study the effect of support pretreatment temperature at much higher temperatures than traditional practice (500–800 °C). Pretreating AlSi material at higher temperatures (i.e., 1100–1200 °C) before catalyst loading significantly removes support surface hydroxyl groups and reduces the iron oxide–support interaction. Therefore, the Fe/AlSi catalyst where the support calcined at 1100–1200 °C is (1) more reduced and more easily reduced, (2) more effectively carbided, and (3) significantly more active and productive. In addition, the results of this work show an excellent correlation of the catalyst activity and ε'-$Fe_{2.2}C$ content, which provide new insights into the active phase for supported FTS catalysts.

Acknowledgments: We thank Stacey Smith for her assistance in powder X-ray diffraction data analysis. This work is supported by members of the Brigham Young University Fischer–Tropsch Consortium and the University of Wyoming Clean Coal Technologies program.

Author Contributions: K.K. designed and performed the experiments and contributed to the writing of the manuscript; B.H. and T.O. performed catalyst characterizations, analyzed data, and wrote the paper; H.H. performed and analyzed Mossbauer spectroscopy tests; W.C.H. directed the research and contributed to the writing of the manuscript.

Conflicts of Interest: The authors declare no conflict of interest.

References

1. Botes, F.G.; Niemantsverdriet, J.W.; van de Loosdrecht, J. A comparison of cobalt and iron based slurry phase fischer–tropsch synthesis. *Catal. Today* **2013**, *215*, 112–120. [CrossRef]
2. Xu, J.; Yang, Y.; Li, Y.-W. Fischer–tropsch synthesis process development: Steps from fundamentals to industrial practices. *Curr. Opin. Chem. Eng.* **2013**, *2*, 354–362. [CrossRef]
3. Bukur, D.B.; Lang, X.; Mukesh, D.; Zimmerman, W.H.; Rosynek, M.P.; Li, C. Binder/support effects on the activity and selectivity of iron catalysts in the fischer-tropsch synthesis. *Ind. Eng. Chem. Res.* **1990**, *29*, 1588–1599. [CrossRef]
4. Bukur, D.B.; Sivaraj, C. Supported iron catalysts for slurry phase fischer–tropsch synthesis. *Appl. Catal. A Gen.* **2002**, *231*, 201–214. [CrossRef]
5. O'Brien, R.J.; Xu, L.; Bao, S.; Raje, A.; Davis, B.H. Activity, selectivity and attrition characteristics of supported iron fischer–tropsch catalysts. *Appl. Catal. A Gen.* **2000**, *196*, 173–178. [CrossRef]
6. Xu, J.; Bartholomew, C.H.; Sudweeks, J.; Eggett, D.L. Design, synthesis, and catalytic properties of silica-supported, pt-promoted iron fischer–tropsch catalysts. *Top. Catal.* **2003**, *26*, 55–71. [CrossRef]
7. Li, S.; Li, A.; Krishnamoorthy, S.; Iglesia, E. Effects of Zn, Cu, and K promoters on the structure and on the reduction, carburization, and catalytic behavior of iron-based fischer–tropsch synthesis catalysts. *Catal. Lett.* **2001**, *77*, 197–205. [CrossRef]
8. Chernavskii, P.A.; Kazak, V.O.; Pankina, G.V.; Perfiliev, Y.D.; Li, T.; Virginie, M.; Khodakov, A.Y. Influence of copper and potassium on the structure and carbidisation of supported iron catalysts for fischer-tropsch synthesis. *Catal. Sci. Technol.* **2017**, *7*, 2325–2334. [CrossRef]
9. Li, T.; Virginie, M.; Khodakov, A.Y. Effect of potassium promotion on the structure and performance of alumina supported carburized molybdenum catalysts for fischer-tropsch synthesis. *Appl. Catal. A Gen.* **2017**, *542*, 154–162. [CrossRef]
10. Ma, W.; Kugler, E.L.; Dadyburjor, D.B. Promotional effect of copper on activity and selectivity to hydrocarbons and oxygenates for fischer−tropsch synthesis over potassium-promoted iron catalysts supported on activated carbon. *Energy Fuels* **2011**, *25*, 1931–1938. [CrossRef]
11. Wan, H.; Wu, B.; Xiang, H.; Li, Y. Fischer-tropsch synthesis: Influence of support incorporation manner on metal dispersion, metal-support interaction, and activities of iron catalysts. *ACS Catal.* **2012**, *2*, 1877–1883. [CrossRef]
12. Pansanga, K.; Lohitharn, N.; Chien, A.C.Y.; Lotero, E.; Panpranot, J.; Praserthdam, P.; Goodwin, J.G. Copper-modified alumina as a support for iron fischer-tropsch synthesis catalysts. *Appl. Catal. A Gen.* **2007**, *332*, 130–137. [CrossRef]
13. Kang, S.-H.; Bae, J.W.; Sai Prasad, P.S.; Jun, K.-W. Fischer–tropsch synthesis using zeolite-supported iron catalysts for the production of light hydrocarbons. *Catal. Lett.* **2008**, *125*, 264–270. [CrossRef]

14. Suo, H.; Wang, S.; Zhang, C.; Xu, J.; Wu, B.; Yang, Y.; Xiang, H.; Li, Y.-W. Chemical and structural effects of silica in iron-based fischer–tropsch synthesis catalysts. *J. Catal.* **2012**, *286*, 111–123. [CrossRef]
15. Malek Abbaslou, R.M.; Soltan, J.; Dalai, A.K. Iron catalyst supported on carbon nanotubes for fischer-tropsch synthesis: Effects of mo promotion. *Fuel* **2011**, *90*, 1139–1144. [CrossRef]
16. Ma, W.; Ding, Y.; Yang, J.; Liu, X.; Lin, L. Study of activated carbon supported iron catalysts for the fischer-tropsch synthesis. *React. Kinet. Catal. Lett.* **2005**, *84*, 11–19. [CrossRef]
17. Torres Galvis, H.M.; Bitter, J.H.; Davidian, T.; Ruitenbeek, M.; Dugulan, A.I.; de Jong, K.P. Iron particle size effects for direct production of lower olefins from synthesis gas. *J. Am. Chem. Soc.* **2012**, *134*, 16207–16215. [CrossRef] [PubMed]
18. Cheng, K.; Ordomsky, V.V.; Virginie, M.; Legras, B.; Chernavskii, P.A.; Kazak, V.O.; Cordier, C.; Paul, S.; Wang, Y.; Khodakov, A.Y. Support effects in high temperature fischer-tropsch synthesis on iron catalysts. *Appl. Catal. A Gen.* **2014**, *488*, 66–77. [CrossRef]
19. Chen, Q.; Liu, G.; Ding, S.; Chanmiya Sheikh, M.; Long, D.; Yoneyama, Y.; Tsubaki, N. Design of ultra-active iron-based fischer-tropsch synthesis catalysts over spherical mesoporous carbon with developed porosity. *Chem. Eng. J.* **2018**, *334*, 714–724. [CrossRef]
20. Qin, H.; Wang, B.; Zhang, C.; Zhu, B.; Zhou, Y.; Zhou, Q. Lignin based synthesis of graphitic carbon-encapsulated iron nanoparticles as effective catalyst for forming lower olefins via fischer-tropsch synthesis. *Catal. Commun.* **2017**, *96*, 28–31. [CrossRef]
21. Cheng, K.; Virginie, M.; Ordomsky, V.V.; Cordier, C.; Chernavskii, P.A.; Ivantsov, M.I.; Paul, S.; Wang, Y.; Khodakov, A.Y. Pore size effects in high-temperature fischer–tropsch synthesis over supported iron catalysts. *J. Catal.* **2015**, *328*, 139–150. [CrossRef]
22. Xie, J.; Torres Galvis, H.M.; Koeken, A.C.J.; Kirilin, A.; Dugulan, A.I.; Ruitenbeek, M.; de Jong, K.P. Size and promoter effects on stability of carbon-nanofiber-supported iron-based fischer–tropsch catalysts. *ACS Catal.* **2016**, *6*, 4017–4024. [CrossRef] [PubMed]
23. Kang, J.; Zhang, S.; Zhang, Q.; Wang, Y. Ruthenium nanoparticles supported on carbon nanotubes as efficient catalysts for selective conversion of synthesis gas to diesel fuel. *Angew. Chem.* **2009**, *121*, 2603–2606. [CrossRef]
24. Qu, Z.; Huang, W.; Zhou, S.; Zheng, H.; Liu, X.; Cheng, M.; Bao, X. Enhancement of the catalytic performance of supported-metal catalysts by pretreatment of the support. *J. Catal.* **2005**, *234*, 33–36. [CrossRef]
25. Mardkhe, M.K.; Huang, B.; Bartholomew, C.H.; Alam, T.M.; Woodfield, B.F. Synthesis and characterization of silica doped alumina catalyst support with superior thermal stability and unique pore properties. *J. Porous Mater.* **2016**, *23*, 475–487. [CrossRef]
26. Mardkhe, M.K.; Keyvanloo, K.; Bartholomew, C.H.; Hecker, W.C.; Alam, T.M.; Woodfield, B.F. Acid site properties of thermally stable, silica-doped alumina as a function of silica/alumina ratio and calcination temperature. *Appl. Catal. A Gen.* **2014**, *482*, 16–23. [CrossRef]
27. Keyvanloo, K.; Mardkhe, M.K.; Alam, T.M.; Bartholomew, C.H.; Woodfield, B.F.; Hecker, W.C. Supported iron fischer-tropsch catalyst: Superior activity and stability using a thermally stable silica-doped alumina support. *ACS Catal.* **2014**, *4*, 1071–1077. [CrossRef]
28. Blanchard, J.; Abatzoglou, N.; Eslahpazir-Esfandabadi, R.; Gitzhofer, F. Fischer-tropsch synthesis in a slurry reactor using a nanoiron carbide catalyst produced by a plasma spray technique. *Ind. Eng. Chem. Res.* **2010**, *49*, 6948–6955. [CrossRef]
29. Deng, C.-M.; Huo, C.-F.; Bao, L.-L.; Feng, G.; Li, Y.-W.; Wang, J.; Jiao, H. Co adsorption on Fe4c (100), (110), and (111) surfaces in fischer-tropsch synthesis. *J. Phys. Chem. C* **2008**, *112*, 19018–19029. [CrossRef]
30. Ning, W.; Koizumi, N.; Chang, H.; Mochizuki, T.; Itoh, T.; Yamada, M. Phase transformation of unpromoted and promoted fe catalysts and the formation of carbonaceous compounds during fischer-tropsch synthesis reaction. *Appl. Catal. A Gen.* **2006**, *312*, 35–44. [CrossRef]
31. Ordomsky, V.V.; Legras, B.; Cheng, K.; Paul, S.; Khodakov, A.Y. The role of carbon atoms of supported iron carbides in fischer-tropsch synthesis. *Catal. Sci. Technol.* **2015**, *5*, 1433–1437. [CrossRef]
32. Zhao, S.; Liu, X.-W.; Huo, C.-F.; Li, Y.-W.; Wang, J.; Jiao, H. Surface morphology of haegg iron carbide (χ-Fe5c2) from ab initio atomistic thermodynamics. *J. Catal.* **2012**, *294*, 47–53. [CrossRef]
33. Ek, S.; Root, A.; Peussa, M.; Niinisto, L. Determination of the hydroxyl group content in silica by thermogravimetry and a comparison with 1h mas nmr results. *Thermochim. Acta* **2001**, *379*, 201–212. [CrossRef]

34. Keyvanloo, K.; Horton, J.B.; Hecker, W.C.; Argyle, M.D. Effects of preparation variables on an alumina-supported fecuk fischer-tropsch catalyst. *Catal. Sci. Technol.* **2014**, *4*, 4289–4300. [CrossRef]
35. Brenner, A.; Hucul, D.A. Catalysts of supported iron derived from molecular complexes containing one, two, and three iron atoms. *Inorg. Chem.* **1979**, *18*, 2836–2840. [CrossRef]
36. Pendyala, V.R.R.; Graham, U.M.; Jacobs, G.; Hamdeh, H.H.; Davis, B.H. Fischer-tropsch synthesis: Deactivation as a function of potassium promoter loading for precipitated iron catalyst. *Catal. Lett.* **2014**, *144*, 1704–1716. [CrossRef]
37. Xu, J.; Bartholomew, C.H. Temperature-programmed hydrogenation (TPH) and in situ mössbauer spectroscopy studies of carbonaceous species on silica-supported iron fischer−tropsch catalysts. *J. Phys. Chem. B* **2005**, *109*, 2392–2403. [CrossRef] [PubMed]
38. de Smit, E.; Cinquini, F.; Beale, A.M.; Safonova, O.V.; van Beek, W.; Sautet, P.; Weckhuysen, B.M. Stability and reactivity of ε-χ-θ iron carbide catalyst phases in fischer-tropsch synthesis: Controlling μc. *J. Am. Chem. Soc.* **2010**, *132*, 14928–14941. [CrossRef] [PubMed]
39. Niemantsverdriet, J.W.; Van der Kraan, A.M.; Van Dijk, W.L.; Van der Baan, H.S. Behavior of metallic iron catalysts during fischer-tropsch synthesis studied with moessbauer spectroscopy, X-ray diffraction, carbon content determination, and reaction kinetic measurements. *J. Phys. Chem.* **1980**, *84*, 3363–3370. [CrossRef]
40. Raupp, G.B.; Delgass, W.N. Moessbauer investigation of supported iron and iron-nickel (FeNi) catalysts. Ii. Carbides formed by fischer-tropsch synthesis. *J. Catal.* **1979**, *58*, 348–360. [CrossRef]
41. Huang, B.; Bartholomew, C.H.; Woodfield, B.F. Improved calculations of pore size distribution for relatively large, irregular slit-shaped mesopore structure. *Microporous Mesoporous Mater.* **2014**, *184*, 112–121. [CrossRef]

catalysts

MDPI

Article

In Situ UV-Visible Assessment of Iron-Based High-Temperature Water-Gas Shift Catalysts Promoted with Lanthana: An Extent of Reduction Study

Basseem B. Hallac [1,†], Jared C. Brown [1,‡], Eli Stavitski [2], Roger G. Harrison [3] and Morris D. Argyle [1,*]

1 Department of Chemical Engineering, Ira A. Fulton School of Engineering and Technology, Brigham Young University, 350 CB, Provo, UT 84602, USA; basseem_h03@hotmail.com (B.B.H.); jaredcbrown@yahoo.com (J.C.B.)
2 Brookhaven National Laboratory, NSLS-II Building 743, Upton, NY 11973, USA; istavitski@bnl.gov
3 Department of Chemistry and Biochemistry, College of Physical and Mathematical Sciences, Brigham Young University, C209 BNSN, Provo, UT 84602, USA; rgharris@chem.byu.edu
* Correspondence: mdargyle@byu.edu; Tel.: +1-801-422-6239
† Current address: Phillips 66, US Highway 60 & State Highway 123, Bartlesville, OK 74003, USA.
‡ Current address: Micron Technology, 8000 S. Federal Way, P.O. Box 6, Boise, ID 83707, USA.

Received: 22 December 2017; Accepted: 29 January 2018; Published: 4 February 2018

Abstract: The extent of reduction of unsupported iron-based high-temperature water-gas shift catalysts with small (<5 wt %) lanthana contents was studied using UV-visible spectroscopy. Temperature- programmed reduction measurements showed that lanthana content higher than 0.5 wt % increased the extent of reduction to metallic Fe, while 0.5 wt % of lanthana facilitated the reduction to Fe_3O_4. *In situ* measurements on the iron oxide catalysts using mass and UV-visible spectroscopies permitted the quantification of the extent of reduction under temperature-programmed reduction and high-temperature water-gas shift conditions. The oxidation states were successfully calibrated against normalized absorbance spectra of visible light using the Kubelka-Munk theory. The normalized absorbance relative to the fully oxidized Fe_2O_3 increased as the extent of reduction increased. XANES suggested that the average bulk iron oxidation state during the water-gas shift reaction was $Fe^{+2.57}$ for the catalyst with no lanthana and $Fe^{+2.54}$ for the catalysts with 1 wt % lanthana. However, the UV-vis spectra suggest that the surface oxidation state of iron would be $Fe^{+2.31}$ for the catalyst with 1 wt % lanthana if the oxidation state of iron in the catalyst with 0 wt % lanthana were $Fe^{+2.57}$. The findings of this paper emphasize the importance of surface sensitive UV-visible spectroscopy for determining the extent of catalyst reduction during operation. The paper highlights the potential to use bench-scale UV-visible spectroscopy to study the surface chemistry of catalysts instead of less-available synchrotron X-ray radiation facilities.

Keywords: iron water gas shift catalysts; extent of reduction; UV-visible spectroscopy; XANES

1. Introduction

The water-gas shift (WGS) reaction is a critical industrial process for hydrogen production and for controlling carbon monoxide to hydrogen ratio in multiple chemical processes [1,2]. The reaction can be written as:

$$CO + H_2O_{(g)} \rightleftharpoons CO_2 + H_2 \qquad \Delta H^\circ_{298K} = -41 \text{ kJ/mol} \tag{1}$$

The exothemicity and reversibility of the WGS reaction lead it to be performed in 2 steps in industrial reactors: (1) high-temperature (HT) at ~400 °C and (2) low-temperature (LT) at ~220 °C,

in order to minimize the CO concentration in the effluent gas stream. Industrial high-temperature (HT) WGS catalysts are typically 92 wt % Fe_3O_4/8 wt % Cr_2O_3 that serve as active and stable catalysts at reaction temperatures close to 400 °C [2]. Numerous research studies have been conducted on enhancing the stability and activity of these catalysts through the addition of promoters (such as Cu, Ce, Hg, Ag and Rh) that can stabilize the iron-chromium structure and provide additional active sites for the chemical reaction [3–13]. A previous study has shown that the addition of lanthana to Fe/Cr/Cu high-temperature (HT) water-gas shift (WGS) catalysts changes their temperature-programmed reduction profiles, generally causing more consumption of the reducing agent [10]. Previous studies also showed that lanthana increases the thermal stability and rate activity of perovskite-like unsupported chromium-free iron-based catalysts for the water-gas shift reaction and Co-based catalysts for the Fischer-Tropsch synthesis reaction [11–13]. Determining the oxidation states of metals on the surface of such catalysts is crucial for understanding the activity and stability patterns observed with variable promoters.

Operando spectroscopic techniques for surface analysis are critical characterization methods in the field of heterogeneous catalysis due to their sensitivity to changes in the surface chemistry of catalysts under operating conditions [14,15]. Applying UV-visible spectroscopy to characterize and quantify the extent of iron reduction (or the amount of active Fe_3O_4 phase) will help explain the activity pattern of the catalysts reported previously [10]. Previous UV-visible studies on vanadium-oxide catalysts for oxidative dehydrogenation of propane were performed and a calibration curve was formulated for extent of reduction as a function of normalized absorbance [16,17]. Weckhuysen and co-workers studied the dehydrogenation of isobutane over supported chromium oxide catalysts and were able to quantify surface reduced centers (Cr^{3+}/Cr^{2+}) using *in situ* UV-visible spectroscopy and relate them to the dehydrogenation activity [14]. Absorption bands in the UV region were observed due to ligand-to-metal charge transfer (LMCT) in which the metal cations were reduced by electron transfer from oxygen (O^{2-}) species. Therefore, despite iron-based WGS catalysts appearing dark and unchanged in color to the unaided eye, absorbance of light over the visible (380–750 nm) and UV (<380 nm) regions are still responsive to electronic changes in oxidation states, or electronic occupation of d-orbitals, of surface Fe domains.

UV-visible diffuse reflectance spectroscopy is one technique that can be used to determine the extent of reduction of fully-oxidized catalysts by exposing them to a broad spectrum of UV and visible wavelengths [14,16–22]. While XANES/EXAFS studies require high-energy X-rays from synchrotron sources, UV-visible spectroscopy is easily performed in the lab at much lower cost. *Operando* UV-visible spectroscopy can provide new insight on surface electronic configurations that has potential as a new method to determine the extent of reduction of a fully oxidized catalyst, which affects the absorbance of light by the catalyst surface [14–18]. From previous work examining the edge and pre-edge absorption regions in UV-visible spectra, the pre-edge region is extremely sensitive to changes in oxidation state, while the edge region is not [16,17,19,23]. Determining the extent of reduction from near-edge features of the XANES spectra of these same catalysts was rendered unsuccessful due to overlapping features of the cationic spectra [16,17]. Therefore, the absorbance of UV-visible diffusely reflected light over the pre-edge region is used in this work to characterize the surface oxidation states of Fe. In addition, this technique can be used for other catalysts that undergo an oxidation-reduction cycle. The physical theory behind this phenomenon is that different oxidation states of the same metal have different band gaps and thus absorb light of different quantized energies [24–28]. The band gap for some iron oxide minerals falls in the range 2.0–2.5 eV (2.2 eV for hematite and 2.3 eV for wüstite), while that for magnetite is only 0.1 eV. (Conductive metals, including Fe, have no band bap because the Fermi level lies within the conduction band) [28–30]. The O(2p) → Fe^{3+}(3d) charge transfer requires 4.2–4.7 eV of energy [31].

Diffuse reflectance UV-visible data are frequently analyzed using a normalized absorbance, which is referred to as the Kubelka-Munk function, f(R_∞), as shown in Equation (2) [32,33],

$$f(R_\infty) = \frac{(1 - R_\infty)^2}{2R_\infty} = \frac{K}{S} \quad (2)$$

where R_∞ is the infinite reflectance (assuming the sample is infinitely thick) relative to a reference perfect reflector (powdered magnesium oxide or Teflon®), K is proportional to the absorbance coefficient (k) and S is proportional to the scattering coefficient (s). For this study, the reference was chosen as the fully oxidized catalyst to permit sensitive detection of changes in the oxidation state of the catalyst relative to this fully oxidized reference. The Kubelka-Munk function is based on scattering and absorption theory and is obtained by performing a shell balance on the flux of light moving in the downward direction (I) and in the upward direction (J) through differential distance dx and solving the resulting coupled differential equations shown below [34–36]:

$$\frac{dI}{dx} = -(k + s)I + sJ \quad (3)$$

$$\frac{dJ}{dx} = (k + s)J - sI \quad (4)$$

Kubelka-Munk theory assumes a continuous infinite medium and does not account for changes in particle size. A study by Christy et al. has modified the Kubelka-Munk equation to account for the inverse relationship with the size of particles [32]. Particle size distribution affects both scattering and absorbance terms [37,38].

Qualitatively, Kubelka-Munk values increase with increasing absorbance, which corresponds to a higher extent of reduction. $F(R_\infty)$ can be correlated to the number of reduced centers by measuring the amount of oxygen required to return the catalyst to its fully oxidized state after it has been reduced.

Another powerful spectroscopic technique is X-ray absorption near edge structure (XANES) from which extent of metal reduction can be quantified by exposing the sample to highly energetic X-ray photons that are absorbed by core electrons, causing photoelectrons to be emitted at characteristic energies. The multiple scattering of the excited electrons specifies the spatial configuration of the atoms using extended X-ray absorption fine structure (EXAFS) analysis. Any changes in the distribution of charge around an atom of a given element produce shifts to the absorption edge regions caused by variations in the binding energies of the electrons [23,39]. Such methods, however, deemed to be complex and expensive to run when compared to bench-scale spectroscopic techniques.

In this paper, we show how ultraviolet-visible (UV-visible) spectroscopy can be used to augment and potentially replace XANES to evaluate oxidation states of heterogeneous catalysts. This technique is applied to characterizing the extent of reduction of HT WGS Fe/Cr/Cu catalysts with varying lanthana contents and is compared with XANES analysis of the same catalysts. This paper presents temperature-programmed reduction (TPR) profiles of iron WGS catalysts with varying amounts of lanthana and correlates them to *in situ* UV-visible absorbance measurements. The Kubelka-Munk function was used to calibrate the UV-visible response to extent of reduction (or oxidation state of iron) determined by the TPR profiles. The resultant calibration curves were applied to scans performed on operating WGS catalysts to determine the effect of lanthana on the extent of reduction of these catalysts. The conclusive results are compared with data acquired from XANES.

2. Results and Discussion

2.1. Temperature-Programmed Reduction and Oxidation (TPR and TPO)

The full TPR profiles as functions of time for the five iron oxide WGS catalysts with varying quantities of La (0 to 5 wt %) are shown in Figure 1. Two peaks were observed during the reduction of the catalysts with H_2, in which the first peak corresponds to the reduction of Fe_2O_3 to Fe_3O_4, CuO to

Cu and possibly Cr^{6+} to Cr^{3+}, while the second peak is attributed to the reduction of Fe_3O_4 to FeO and metallic Fe [40–42]. The second peak is much larger than the first peak because it requires 8 times more H_2 to reduce Fe_3O_4 to Fe than to reduce Fe_2O_3 to Fe_3O_4. The temperature was not increased beyond 450 °C during the TPR experiments to fully characterize the second peak due to limitations on the heater used. The reduction temperature for the second peak typically extends to 650–700 °C for Fe/Cr/Cu catalysts [3]. Consistent with our previous study, the 0.5La catalyst was the easiest to reduce of the catalysts containing La, as determined by the maximum of the first reduction peak occurring at the lowest temperature (approximately 219 °C) [10].

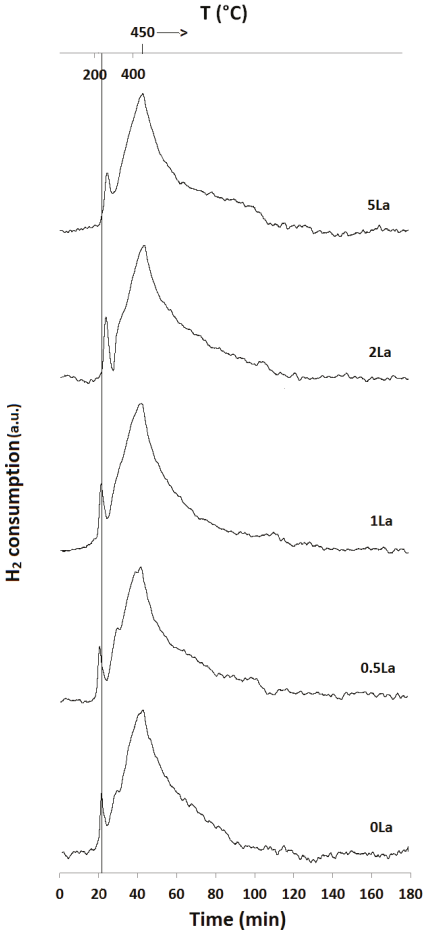

Figure 1. First temperature-programmed reduction profiles of all the catalysts (TPR 1, 10 mol % H_2/Ar, total flow = 50 sccm, ramp rate = 10 °C/min). 0.5La catalyst starts reducing at the lowest temperature.

The maxima of the second peaks occur at almost the same times (temperature) for all the catalysts due to stopping the heating at 450 °C. Table 1 shows the extent of reduction (EOR) for each of the catalysts. EOR is defined as the fraction of iron that has been reduced from Fe_2O_3 to either Fe_3O_4 (in the second column of Table 1) or to metallic iron (in the third and fourth columns of Table 1) as quantified by the integrated hydrogen consumption from the TPR peaks. The listed values have been corrected by subtracting the small amount of hydrogen expected to be consumed by the other

reducible catalyst components, CuO to Cu and Cr^{6+} to Cr^{3+}, which are reported to reduce near the temperature range of the first peak [40–42]. Hydrogen consumption increases with La content for the first reduction phase and is approximately the same for the second reduction phase (within the ±5% error for this experiment).

Table 1. Extent of reduction of catalysts for TPR 1 and TPR 2 (10 mol % H_2/Ar, total flow = 50 sccm).

Catalyst ID	TPR 1 (First Peak) % EOR to Fe_3O_4 [a]	TPR 1 (Both Peaks) % EOR to Fe [a]	TPR 2 % EOR to Fe
0La	42	82	42
0.5La	53	78	72
1La	67	85	53
2La	79	89	N/A
5La	82	89	57

[a] EOR is Extent of Reduction.

However, even considering the uncertainty, 2La and 5La appear to consume more hydrogen than 0.5La. This is explained in terms of the stabilized iron-chromium spinel that is formed in the 0.5La catalyst after it is reduced to the active magnetite form [10]. Therefore, the 0.5La catalyst has a higher extent of reduction to magnetite than the 0La catalyst but a lower extent of reduction to Fe than the 1La, 2La and 5La catalysts. Furthermore, the 2La and 5La catalysts start consuming hydrogen with the second peak later (i.e., at higher temperatures) possibly due to lanthana covering iron domains making them less accessible. The 2La and 5La catalysts consume more hydrogen than the 0.5La catalyst, possibly due to a disrupted spinel structure and loss of strong interaction between Fe and other elements (such as Cr), which make the catalysts more reducible in terms of hydrogen consumption [10].

Following an intervening full oxidation, the overall extents of reduction during TPR 2 show a different trend. The maximum hydrogen consumption is now observed for the 0.5La catalyst, while 0La consumes the least amount and 1La and 5La consume less than 0.5La. The TPR 2 profiles, plotted in Figure 2, show that the peaks appear at higher temperatures (>300 °C for the first peak and >400 °C for the second peak), with the second much smaller than the first peak as the heating does not go beyond 450 °C, suggesting that the catalysts have been stabilized after the first TPR/TPO cycle. The 0.5La and 1La catalysts start consuming H_2 at 30–40 °C lower temperatures (3–4 min earlier) than the other catalysts. However, the 0.5La catalyst ends up consuming more hydrogen than the other samples by the time the temperature reaches 450 °C (at approximately 43 min). This ease and extent of reducibility is correlated to the overall WGS reaction rates previously reported for these catalysts [10].

The results of TPR 2 are significant because the 0.5La catalyst is a better catalyst candidate for re-use, as it has been deactivated the least. In fact, the extent of reduction for the 0.5La catalyst calculated from TPR 2 is 8% lower than that calculated from TPR 1, while those of the other catalysts are approximately 35–50% lower. The decreased reducibility of the catalyst comes as result of possible sintering and deactivation of the catalyst after TPR 1 treatment at 450 °C for 3 h. Qualitatively, these results agree very well with what has been reported previously on the stability of the catalysts, where the WGS reaction rate decreased by 11% for the 0.5La catalyst after 120 h under reaction conditions and 20–25% for the other catalysts [10]. The promoting effect of lanthana in lowering the reduction temperature observed with the first and second peaks in TPR 1 is attributed to a stabilized spinel that starts forming at lower temperatures in the 0.5La catalyst and continues to consume H_2 until the hematite is reduced to magnetite. Further addition of lanthana appears to disrupt the spinel once formed and possibly cover the surface, making the Fe domains less accessible to H_2, thus requiring higher temperatures for the catalysts to be reduced [10].

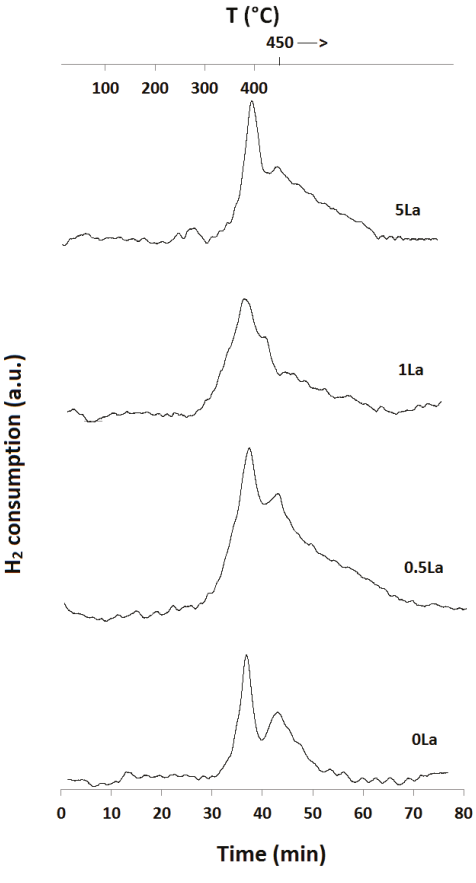

Figure 2. Second temperature-programmed reduction profiles of most of the catalysts (TPR 2, 10 mol % H2/Ar, total flow = 50 sccm, ramp rate = 10 °C/min). 0.5La catalyst has the highest hydrogen consumption.

Extent of reduction was also checked with TPO profiles. Figure 3 shows the oxygen consumption and water formation for the initial oxidation and TPO 1 profiles for the 0La catalyst obtained by mass spectra (MS) (similar plots were obtained for the other catalysts). Previous XRD analysis showed that the iron phase in the fresh calcined catalysts is ferrihydrite [10]. Therefore, water is produced during the oxidation of iron to hematite and ferrihydrite. Oxygen is consumed during TPO 1 to form hematite after the catalysts have been reduced during TPR 1. The amount of oxygen consumed during TPO 1 for the 0La catalyst is 80% of the hypothetical value for full oxidation of metallic Fe to Fe_2O_3, which is in good agreement with the extent of reduction calculated from TPR 1 (82%).

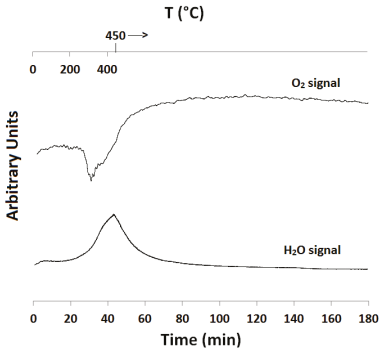

Figure 3. H_2O release during initial oxidation of the 0La catalyst and O_2 consumption during the temperature-programmed oxidation following TPR 1. Oxygen is consumed as metallic Fe and other reduced forms of iron oxides oxidize to Fe_2O_3.

2.2. Powder X-ray Diffraction (XRD) Analysis

XRD spectra were collected for a specific set of samples post reduction/oxidation treatment, as shown in Figures 4 and 5. The spectra in Figure 4 qualitatively show that the major iron phases in the catalysts post TPR 1 and TPR 2 are a mixture of metallic Fe and magnetite, based on comparison with the International Centre for Diffraction Data (ICDD) database. However, the peak at 44.7°, which is representative of metallic Fe, is much less intense and essentially negligible for the samples post TPR 2, when compared to the other samples post TPR 1. These results are in good agreement with the TPR trends discussed in the previous section, where the extent of reduction for TPR 2 is 50% lower than that for TPR 1 for the 0La and 5La samples. No peaks for FeO were detected in the XRD patterns. Fe_3O_4 and Fe are more thermodynamically stable than FeO at 400–450 °C for these shift catalysts [43]. The peaks for the samples post TPR 2 are not intense compared to the peaks observed with samples post TPR 1, indicating a lower content of Fe and hence a lower extent of reduction. There are slight shifts to the left in the peaks at 57° and 62.5° for the 1La and 2La catalysts post TPR 1 and a clear left shift in the peaks at 35.5°, 57° and 62.5° for the 5La catalyst post TPR 2, indicating larger lattice parameters and therefore larger unit cells for Fe_3O_4. This suggests incorporation of the larger La^{3+} ions. This trend is similar to that observed with the samples post WGS reaction [10].

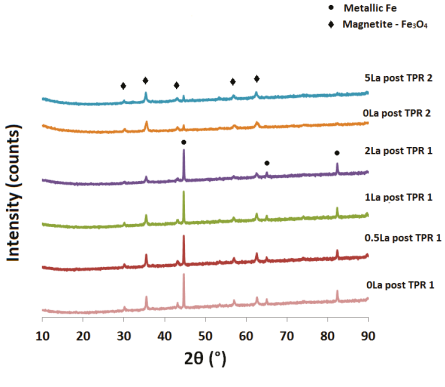

Figure 4. XRD of catalysts after temperature-programmed reduction treatments (TPR 1 and TPR 2). Metallic Fe is the major form of iron in samples after TPR 1. The peaks for metallic Fe are less intense for samples after TPR 2.

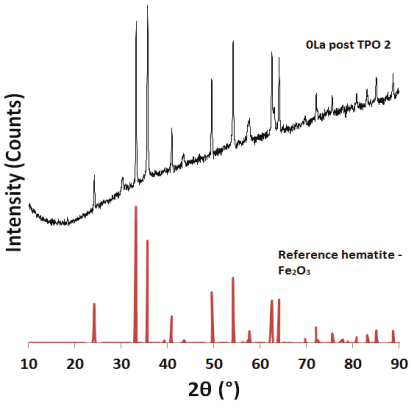

Figure 5. XRD of 0La catalyst after the final temperature-programmed oxidation. The catalyst is oxidized with Fe_2O_3 as the major bulk phase of iron.

Figure 5 compares the XRD spectrum for the 0La catalyst post TPO 2 with the reference hematite spectrum from the ICDD database. Clearly, the major iron oxide phase in the bulk of the catalyst is hematite, thus iron is in the +3 oxidation state after full oxidation of the catalyst. However, a small peak at 30.2° indicates that Fe_3O_4 is still present in the bulk but its intensity is negligible compared to the peaks of hematite.

2.3. In Situ UV-Visible Spectroscopy

2.3.1. Absorption vs. Time Spectra

The diffuse reflectance light absorption signals from the UV-visible spectrophotometer and mass spectrometer change simultaneously at the same temperature during the first reduction process. Figure 6 shows the absorption signal response at 12,500 cm^{-1} as a function of time for the 0La, 0.5La and 1La catalysts from the beginning of the reduction processes (TPR 1 and TPR 2) at room temperature to the maximum temperature of 450 °C, which was reached at about 43 min. For TPR 1, the jump in the UV-vis absorption occurs in 2 steps, for which the first step starts at around 21 min (about 230 °C), while step 2 starts at around 28 min (about 300 °C). The timings of steps 1 and 2 match with the times at which the H_2 signal from the mass spectrometer starts to show hydrogen consumption for the first and second reduction phases, respectively. On the other hand, only a long 1-step jump is observed at around 32 min (about 340 °C) for the 0La catalyst and around 28 min (about 300 °C) for the 0.5La and 1La catalysts during TPR 2, which corresponds to the large hydrogen consumption peaks shown by the mass spectrometer shown in Figure 2. The second peaks are smaller and some are overlapped by the first larger peak (as is the case for the 1La catalyst). The absorbance is clearly insensitive to the second peaks due their overlapping nature. Compared to TPR 1, the absorbance signal for TPR 2 increases over a broader range of time, unlike that for TPR 1, which is sharper. The increase in the absorbance signal at 12,500 cm^{-1} is apparently due to the combined effect of reduction of Fe_2O_3 to Fe_3O_4 and metallic Fe, both of which species have smaller or no band gaps and more oxygen vacancies than hematite.

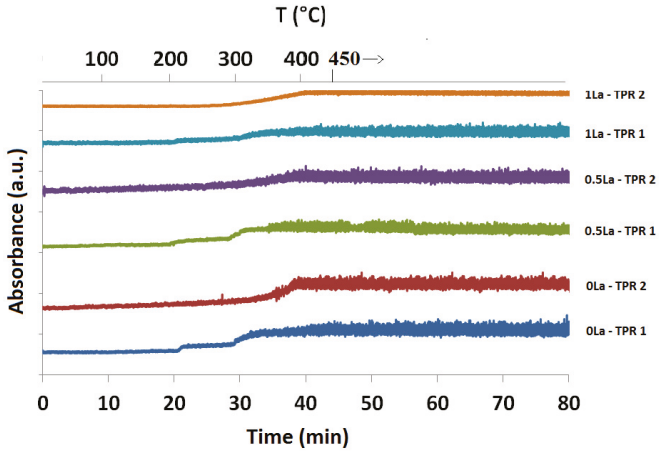

Figure 6. UV-vis absorbance vs. time for the 0La, 0.5La and 1La catalysts during TPR 1 and TPR 2. The absorbance signal increases simultaneously with the increase of the hydrogen consumption signal from the mass spectrometer.

Figure 7 shows the UV-visible absorbance as a function of time for the 0La catalyst post TPR 1, TPO and TPR 2 on the same graph. The absorbance signal increases during the TPR experiments, while it decreases as the catalyst is oxidized during TPO. The asymptotic absorbance attained during TPR 2 is lower than that reached during TPR 1, indicating a lower extent of reduction. However, the absorbance signal starts with a lower value for TPR 2 compared to that for TPR 1. A possible explanation for this behavior is sintering of the particles due to thermal effects of the initial TPR and TPO. Furthermore, the absorbance at which TPO 1 ends is not the same as the signal at which TPR 2 starts (see Figure 7) due to temperature effects which are depicted in Figure 8. The same effect is observed for the signals at the end of TPR 1 and beginning of TPO 1. The effect of temperature is discussed in more detail in the following section.

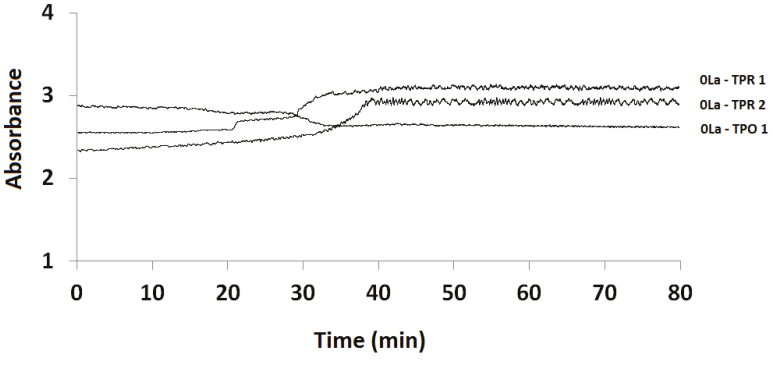

Figure 7. Kinetic spectra (absorbance vs. time) for the 0La catalyst during TPR 1, TPO 1 and TPR 2 combined on the same coordinates.

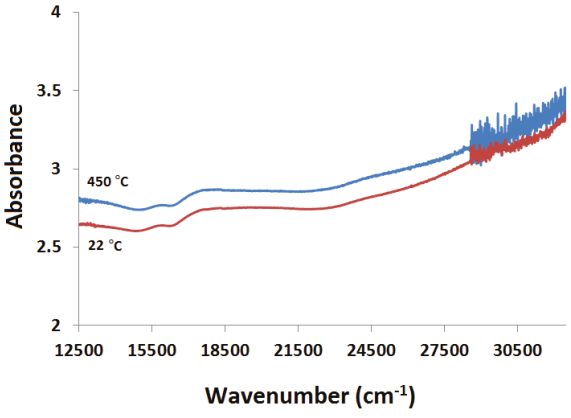

Figure 8. Absorbance scans of a fully oxidized 1La sample obtained at 22 °C and 450 °C. Higher temperatures cause the absorbance signal to increase.

2.3.2. Kubelka-Munk Scans and Calibration

The UV-visible spectroscopic analysis discussed in this section and the sections that follow has been performed primarily on the 0La, 0.5La and 1La catalysts because they produced the highest WGS activities and showed significant chemical and physical and chemical changes among them in previous results [10].

The previous results show that light absorbance at 12,500 cm^{-1} is affected by the extent of reduction of the WGS catalysts. Scans across the UV-visible spectrum (modified Kubelka-Munk (K-M) function values vs. wavenumber) are plotted in Figure 9 for the 0La, 0.5La and 1La catalysts. The reference for the modified K-M scan is a fully oxidized sample of each catalyst. The values of the normalized absorbance are the same as the K-M values when the catalysts are scanned under normalized absorbance scans, suggesting that the scattering term has minimal effect on the K-M function during the TPR and TPO experiments. The values of the Kubelka-Munk function (F(R)) are higher for the more reduced catalysts and nearly zero for the fully oxidized ones.

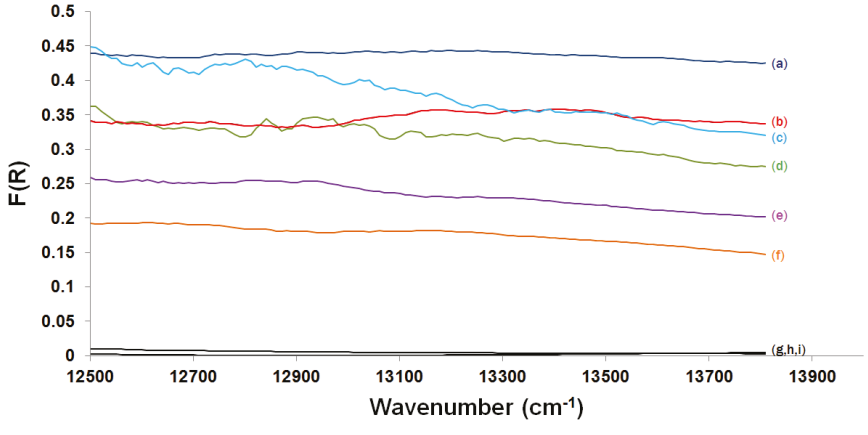

Figure 9. Kubelka-Munk scans for: (**a**) 0.5La catalyst post TPR 1; (**b**) 0La catalyst post TPR 1; (**c**) 1La catalyst post TPR 1; (**d**) 0.5La catalyst post TPR 2; (**e**) 1La catalyst post TPR 2; (**f**) 0La catalyst post TPR 2; (**g**) 0La catalyst post TPO 1; (**h**) 0.5La catalyst post TPO 1; (**i**) 1La catalyst post TPO 1.

These spectra are interpreted as follows. Figure 8 shows the temperature dependence of the spectra, with a lower absorbance signal at room temperature than that at 450 °C. Higher temperatures increase the molecular vibration and rotation movements and therefore increase the absorbance [44]. In order to avoid temperature effects on the absorbance signal, all K-M and baseline scans were acquired at room temperature for analysis. Furthermore, according to Figure 8, there is an absorption band centered around 17,500 cm^{-1} for the oxidized catalyst. This band around 17,500 cm^{-1}, or 2.2 eV, is due to the band gap in Fe_2O_3 [30,45–47]) Since the K-M function is proportional to absorbance, the K-M value for each catalyst post TPR 1 is higher than those post TPR 2, which correlates to the differences in the extents of reduction from Fe_2O_3 to metallic Fe, as shown in Figure 9 and which is in agreement with the TPR results presented in Section 3.1. Furthermore, the 0La catalyst post TPR 2 has the lowest K-M value of the reduced catalysts, which corresponds to the least extent of reduction. The K-M values for the reduced 0.5La catalyst fall in between, while the K-M value post TPO for the 0La catalyst is essentially zero, especially near 12,500 cm^{-1}, confirming that the catalyst returned to the fully oxidized state that was used as the reference in the K-M function. Absorbance is highest, which produces the largest K-M value for each specific spectrum, at 12,500 cm^{-1} (1.5 eV), because the reduced catalysts (primarily Fe or Fe_3O_4) absorb more light at this energy relative to the reference of the fully oxidized catalyst (primarily hematite).

A linearly regressed calibration line was generated (Figure 10) to correlate K-M function (independent variable) and Fe oxidation state acquired from quantification of MS H_2 consumption peaks (dependent variable) on the surfaces of each of the three catalysts.

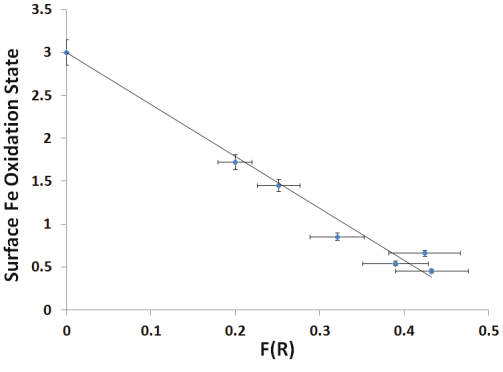

Figure 10. Calibration curve of surface Fe oxidation state as a function of Kubelka-Munk values with 10% error bars at 12,500 cm^{-1} and using TPR 1 and TPR 2 K-M values for the 0La, 0.5La and 1La catalysts.

The slope and intercept of the calibration line with 95% confidence intervals are given in Table 2, along with the coefficient of determination (r^2) value to evaluate the quality of the data fit. The intercept is 3.0, which corresponds to the oxidation state of hematite (the fully oxidized phase of the samples, with a corresponding K-M value of zero due to the fully oxidized catalyst reference). The results show that the UV-visible technique is sensitive to and can be directly calibrated with extent of catalyst reduction.

Table 2. Slope, intercept and coefficient of determination for the oxidation states vs. K-M calibration curve.

Slope	Intercept	r^2
-6.05 ± 0.39	3.00 ± 0.13	0.977

2.3.3. Water-Gas Shift Reaction: In Situ and Ex Situ Analysis

In-situ analysis on the 1La catalyst under varying times of HT WGS shift reaction is shown in Figure 11, with the scans performed at the reaction temperature of 400 °C. The K-M values are much higher (80% more) than those post TPR 1, even after accounting for the temperature effect on the absorbance signal (as seen in Figure 8). The K-M values increase significantly with time as the WGS reaction proceeds. Prior kinetic results with these and similar catalysts indicate that they do not approach a steady state activity for about 100 h [10,48]. This change during the initial 24 h is likely associated with sintering, which has been linked to decreasing catalytic rate during this initial time.

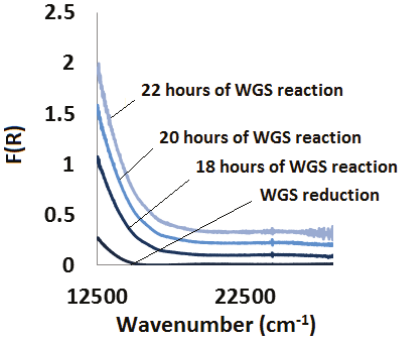

Figure 11. *In situ* Kubelka-Munk spectra for the 1La catalyst under WGS reaction. The Kubelka-Munk values are higher than the values obtained during TPR experiments.

Ex situ analysis, presented in Figure 12, was performed at room temperature on the 0La and 1La catalysts after 10 days under high-temperature WGS reaction and show similar results: the normalized absorbance values are higher than those for TPR 1 and TPR 2 of either catalyst.

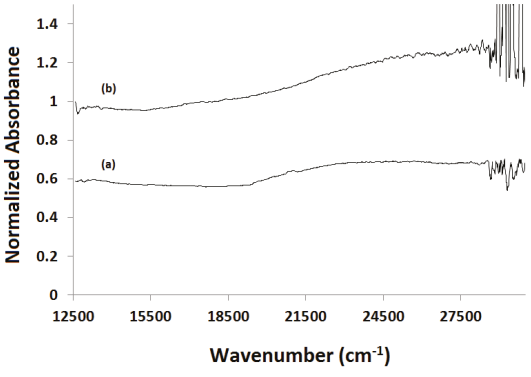

Figure 12. *Ex situ* analysis after 240 h of WGS reaction. The spectra shown are normalized absorbance for (**a**) used 0La catalyst; (**b**) used 1La catalyst.

Although carbon deposition on the catalyst surface is a potential explanation for the increased absorbance signal as a function of the WGS reaction time, this possibility has been discounted. No CO or CO_2 signals were detected during a TPO of the used catalysts in flowing air and no iron carbide phase was observed in the XRD and EDS results. Therefore, catalyst carbiding or formation of surface carbon species (e.g., graphite or coke) does not appear to occur.

The apparent explanation is that there are morphological changes to the catalysts once steam is introduced in the feed. This was manifested by physical change to the catalysts, which expands and fractures when exposed to water during WGS conditions. SEM analysis, shown in Figure 13, demonstrates the change in the particle size distribution after WGS treatment, suggesting that introduction of water physically alters the shapes of the particles of the catalysts. In contrast, the particle size distribution after the TPR treatments remains almost the same (figures not shown). Since the K-M function is an absorbance to scattering ratio, morphological changes likely change the ratio of the absorbed and scattered (or diffusely reflected) light off the surface of the catalyst, which accounts for the increase in the K-M values.

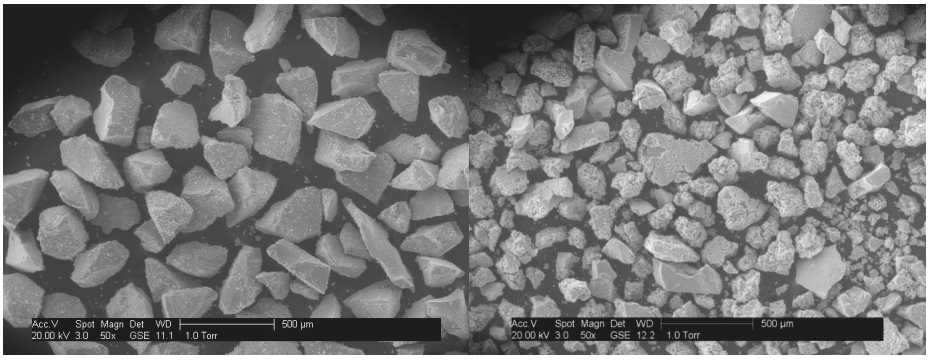

Figure 13. SEM images of calcined fresh (**left**) and used (**right**) 0La catalyst. The images show a change in particle size distribution after the catalyst was exposed to reaction conditions.

Although the direct correlation between reduced centers and absorbance was not possible due to the morphological changes to the catalyst, the use of UV-visible spectroscopy to quantify extent of reduction should be applicable to more physically stable catalysts. These studies will be presented in future papers.

However, in order to use of the calibration curve in Figure 10 and to apply it to quantify the reduced centers of the catalysts post WGS treatment, the ratio of normalized absorbance (which is the ratio of the K-M values excluding the scattering term) for both catalysts after WGS reaction has been compared with the slope of the calibration curve. This ratio of absorbance between two catalysts is an attempt to cancel out the disturbance to the signal caused by the smaller particle size distribution. This analysis presumes that the same morphological changes occur for all of the catalysts during the WGS reaction, which appears to be the case based on analysis of the SEM images. Taking the ratio of the normalized absorbances yields,

$$\frac{(3 - y_1)}{(3 - y_0)} = \frac{x_1}{x_0} \tag{5}$$

where y_0 and y_1 are the oxidation states of Fe in the 0La and 1La catalysts, respectively and x_0 and x_1 are the K-M values for the 0La and 1La catalysts (which are equal to normalized absorbance values for which these calibration lines were derived), respectively. The ratio of the normalized absorbance at 12,500 cm^{-1}, $\frac{x_1}{x_0}$, post WGS treatment gives a value of 1.6 ± 0.16. Figure 14 correlates the ratio on the left-hand side of Equation (5) to different ratios of normalized absorbance within the 95% confidence of the fitted slope for both catalysts.

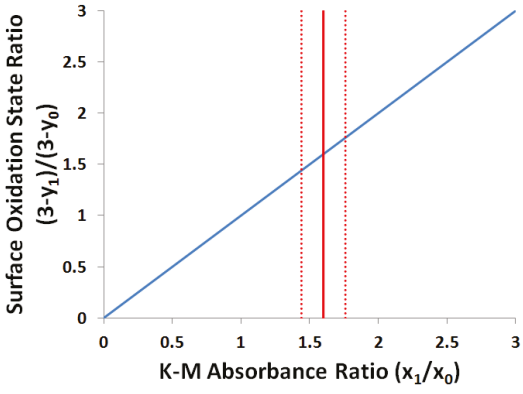

Figure 14. The ratio of surface Fe oxidation states in 1La to the oxidation state in 0La as a function of the ratio of the normalized absorbance. The figure shows the 95% upper and lower bounds of the regression.

Although these results do not give full quantification for the oxidation state of Fe on the surface during the WGS reaction, they correlate the oxidation state of Fe on the surface of the 1La catalyst to that on the surface of the 0La catalyst.

These findings are consistent with the activity pattern observed previously [10]. The 0.5La catalyst had highest WGS activity, which in this study also displayed higher extent of reduction from Fe_2O_3 to Fe_3O_4 than the 0La catalyst and the lower extent of reduction from Fe_2O_3 to Fe than the 1La, 2La and 5La catalysts, presumably because its spinel structure was better maintained and stabilized [10]. This suggests that addition of 0.5 wt % of lanthana maximizes the content of the active magnetite phase under reaction conditions.

2.4. X-ray Absorption Near Edge Structure (XANES) Spectra Compared to UV-Visible Results

The XANES spectra of the 0La and 1La samples after WGS reaction, along with those of reference compounds, iron (II, III) oxides and metallic iron, are shown in the Figure 15.

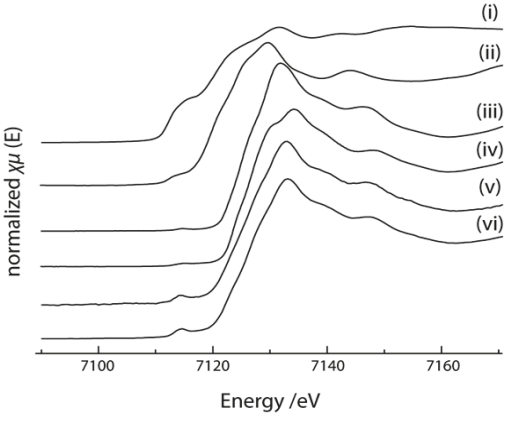

Figure 15. XANES region of the XAS spectra for (**i**) metal Fe foil; (**ii**) ferrous oxide, FeO; (**iii**) magnetite, Fe_3O_4; (**iv**) hematite, Fe_2O_3; (**v**) 0La sample after WGS reaction; (**vi**) 1La sample after WGS reaction. The pre-edge energies for both samples are close to the energy of magnetite.

Inspection of the spectral features, in particular, the position of the pre-edge feature and the position of the main edge suggest that oxidation state of iron in the samples is close to that of magnetite (+2.66), which is consistent with previous reports on iron oxide catalysts during the WSG reaction [49]. An attempt to fit the XANES spectra of the samples as linear combination of reference spectra was unsuccessful, which is not uncommon for non-stoichiometric iron oxides. Hence, to establish the oxidation state of iron in the samples, the approach of Wilke has been applied [50]. In this method, the position of the pre-edge features is determined for the reference compounds and plotted as a function of a formal oxidation state (or oxidation state measured independently, e.g., by Mössbauer spectroscopy, as demonstrated by Wilke et al. [50]) and fitting is used to obtain the chemical state for the unknown material. Figure 16 shows the position of the pre-edge peaks for all materials plotted as a function of Fe^{3+}/Fe total. This ratio is zero when the all iron is Fe^{2+} and 1 when the all iron is Fe^{3+}. Any number between zero and 1 is a combination of the +2 and +3 oxidation states. From the interpolation of this data, the Fe oxidation in the used 0La sample is +2.57, while that in 1La is +2.54.

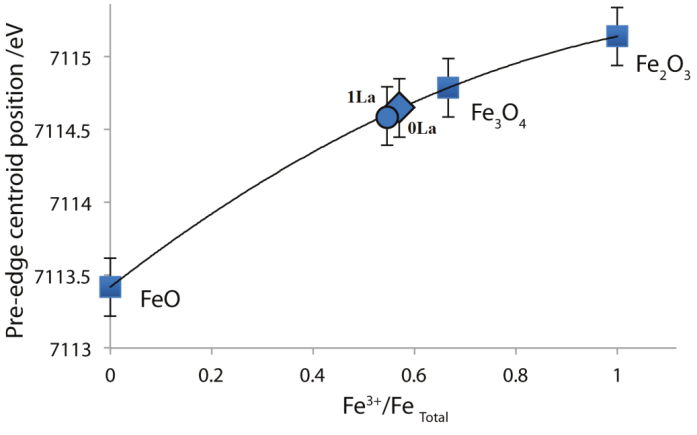

Figure 16. Interpolation of Fe oxidation state in 0La and 1La samples as a combination of Fe^{3+} and Fe^{2+}, which is predicted to be around +2.57.

If the correlation in Equation (5) is used to calculate the oxidation state of 1La from that of the 0La, then the predicted value for the oxidation state of Fe in 1La is +2.31 $\pm$ 0.07 for an oxidation state of +2.57 for the 0La. Results obtained from the XANES spectra show the used 1La sample is slightly more reduced than the used 0La sample, which is consistent with the UV-visible analysis. However, the UV-visible results suggest a greater difference between the oxidation states of Fe near the surface, which is not unexpected, considering that XANES detects bulk properties, while UV-visible spectroscopy is more sensitive to the surface conditions. Cations near the surface tend to be more reduced (lower oxidation state) than those in the bulk of partially reduced metal oxide catalysts [51]. Given the UV-visible absorbance data, the penetration depth of light with a wavelength of 800 nm is estimated to be close to 200 µm. Therefore, although the XANES analysis indicates that the bulk oxidation state of Fe is nearly the same in both samples, they are likely slightly different near the surface, as suggested by the UV-visible results. As shown in the previous section, if the oxidation state of Fe near the surface is +2.57 for the 0La sample, then the results from the UV-visible spectra calibration suggest an oxidation state between +2.24 and +2.38 for the 1La sample with an average of +2.31. We hypothesize that UV-visible spectroscopy is a more precise technique to use for characterizing extent of reduction of cations near the surface, as they are more relevant to describe surface kinetics and catalysis.

3. Materials and Methods

3.1. Temperature-Programmed Reduction and Oxidation (TPR and TPO)

The catalysts, prepared by co-precipitation as reported elsewhere [10] contain varying amounts of lanthana at the expense of iron(III) oxide. The five catalysts have (88 − x) wt % Fe_2O_3, 8 wt % Cr_2O_3, 4 wt % CuO and x wt % lanthana, where x = 0, 0.5, 1, 2 and 5 and are designated as 0La, 0.5La, 1La, 2La and 5La, respectively. Initially, 40 mg of catalyst were fully oxidized in flowing air (Zero Air, Airgas, Radnor, PA, USA) at 30 sccm for 60 to 90 min at 450 °C and then cooled to room temperature. The flow rate of air was controlled by a calibrated 100 sccm rotameter (OMEGA Engineering, Norwalk, CT, USA). TPR's were performed in 10 mol % H_2/Ar (5 sccm of H_2 (99.95%, Airgas, Radnor, PA, USA) and 45 sccm of Ar (99.997%, Airgas, Radnor, PA, USA)) for 3 h and a temperature ramp of 10 °C/min from room temperature to 450 °C. The flow rates of H_2 and Ar were controlled using calibrated mass flow controllers (Porter Instruments 201, Parker Hannifin Corp., Hatfield, PA, USA). Hydrogen consumption was quantified via concomitant mass spectrometry (MKS Cirrus 100, MKS Instruments, Andover, MA, USA). Following the first TPR (TPR 1), the samples were reoxidized (TPO 1) in flowing air at 30 sccm for three hours at a temperature ramp of 10 °C/min from room temperature to 450 °C. A similar procedure was followed by a second TPR (TPR 2) to check the cyclic reducibility of the catalysts. All experiments were performed at atmospheric pressure. Hydrogen consumption was quantified by integrating the areas under the peaks from the mass spectrometer data relative to a calibrated baseline. Reactions (6) and (7) were used to quantify the iron reduction due to hydrogen consumption, corrected by subtracting the calculated amount of hydrogen required to reduce the Cu and Cr^{6+} components of the catalysts according to Reactions (8) and (9):

$$3Fe_2O_{3(s)} + H_{2(g)} \rightarrow 2Fe_3O_{4(s)} + H_2O_{(g)} \quad (6)$$

$$Fe_2O_{3(s)} + 3H_{2(g)} \rightarrow 2Fe_{(s)} + 3H_2O_{(g)} \quad (7)$$

$$CuO_{(s)} + H_{2(g)} \rightarrow Cu_{(s)} + H_2O_{(g)} \quad (8)$$

$$2CrO_{3(s)} + 3H_{2(g)} \rightarrow Cr_2O_{3(s)} + 3H_2O_{(g)} \quad (9)$$

3.2. In Situ UV-Visible Experiments

A diffuse reflectance UV-visible spectrophotometer (Varian Cary 4000, Agilent Technologies, Santa Clara, CA, USA) with a high-temperature reaction chamber (Praying Mantis™ model HVC-VUV-4, Harrick Scientific Products Inc., Pleasantville, NY, USA) was used. A 40-mg sample of catalyst, sieved to 100–250 μm agglomerate pellet size, was placed in a cup holder and supported on a quartz frit with 100 μm porosity to allow for uniform flow. The intensity of light collected from the sample surface was normalized relative to that of a fully oxidized surface of the same sample at room temperature in the Kubelka-Munk function. The absorbance vs. time data were obtained at 12,500 cm^{-1} (800 nm), which was where the most sensitive signal changes were observed during prior scans across the light spectrum from 12,500 cm^{-1} to 50,000 cm^{-1} (200 nm). Subsequent scans collected Kubelka-Munk absorbance vs. light energy over the 12,500 to 50,000 cm^{-1} (800 nm to 200 nm with 2 nm per second steps) spectrum after the temperature cooled to room temperature. Kubelka-Munk values were calibrated against quantified extents of reduction obtained during simultaneous TPR measurements, as described in the previous section. Statistical analysis was performed on the parameters of the calibration using non-linear fitting tools available in R™ programming language (R Development Core Team, v. 2.13.0) with 1000 points to acquire and plot the 95% confidence regions.

3.3. High-Temperature Water-Gas Shift Reaction

UV-visible scans were collected for reduced samples under high-temperature water-gas shift conditions at 400 °C and atmospheric pressure after different reaction times. The CO/Ar reactant

mixture (CO (99.995%, Airgas) at 2.1 sccm and Ar at 25 sccm) was saturated with distilled water prior to entering the UV-visible reaction chamber. The partial pressure of water was assumed to be 3.2 kPa, which is the water saturation pressure at room temperature.

3.4. Powder X-ray Diffraction (XRD)

Powder X-Ray Diffraction (XRD) analysis (X'Pert Pro PANalaytical with X-Celerator detector, Malvern Panalytical B.V., Eindhoven, The Netherlands) was performed on used catalyst samples to determine the major phase of iron oxide in the catalysts post TPR or TPO. The instrument was operated at 45 kV and 40 mA, using Cu Kα1 radiation and a graphite monochromator. The results were obtained over the 2θ range of 10°–90° with 1° divergence and receiving slits and 400 s per step.

3.5. Energy Dispersive X-ray Spectroscopy (EDS) and Scanning Electron Microscopy (SEM)

An environmental scanning electron microscope (Philips, XL30, Thermo Fischer Scientific FEI, Hillsboro, OR, USA) was used to determine the elemental compositions in the catalysts and to evaluate the distribution of the components across the catalyst surface. The scans were taken at 20 keV and in low-vacuum mode, which did not require coating the non-conductive catalysts with sputtered gold or palladium. Each scan took 50 s. Scanning electron micrographs (SEM) of the fresh and used catalysts were also taken using the same microscope at 50× and 400× magnifications with a 20 keV beam voltage.

3.6. X-ray Absorption Near Edge Structure (XANES)

X-ray absorption spectroscopy (XAS) experiments were performed on the X18A beamline at the NSLS at Brookhaven National Laboratory (Upton, NY, USA). Beamline X18A is a bending magnet line, which uses a Si {1 1 1} channel-cut monochromator and a rhodium-coated toroidal focusing mirror to provide a ~1.0 mm (horizontal) and ~0.5 mm (vertical) spot size with a flux of ~2.5×10^{11} photons/s at 10 keV. After alignment using the spectra obtained from the Fe foil in the reference ion chamber, three consecutive scans were averaged and recorded simultaneously with those of the sample. Samples and reference compounds were diluted with boron nitride to achieve an edge jump of ~1 and encapsulated between two Kapton foil sheets.

4. Conclusions

A thorough study on the extent of reduction of iron-based high-temperature water-gas shift catalysts using different characterization techniques has been presented in this paper. Temperature-programmed reduction studies using mass spectrometry showed that 0.5 wt % addition of lanthana as a promoter to iron-chromium-copper oxide water-gas shift catalysts enhances the reducibility of the catalysts in terms of both total hydrogen consumption and reduction temperature. However, further additions of lanthana cause the catalysts to reduce at higher temperatures and to consume more hydrogen (i.e., over-reduce), possibly due to disruption of the catalytically active Fe_3O_4 spinel structures by incorporation of the larger La^{3+}. A second temperature-programmed reduction was performed on each catalyst after they were fully reoxidized to examine the re-reducibility of the catalysts. The catalyst with the 0.5 wt % lanthana appeared to be the most reducible with only an 8% decrease in extent of reduction, as opposed to a 35–45% decrease in total hydrogen consumption from the first reduction experiment for the other catalysts. Analysis via UV-visible spectrometry showed that the absorbance of light at 800 nm is very sensitive during the reduction processes of these catalysts due to alterations in the band gaps of the different iron oxide phases and could be calibrated to extent of reduction as determined during concomitant TPR. *Ex situ* analysis on the used catalysts also showed similar trends with the Kubelka-Munk values. The ratio of normalized absorbance correlated to the ratio of Fe oxidation states acquired from the calibration curve for the used catalysts with 0 wt % and 1 wt % lanthana. This showed that the extent of reduction for the 1 wt % catalyst was 1.1 times lower than for the 0 wt % catalyst, suggesting that the catalyst with more lanthana reduced to a larger extent

during water-gas shift treatment than the one with no lanthana, resulting in lower content of the active Fe_3O_4 phase due to over-reduction. XANES spectra showed nearly equal extents of reduction (+2.54 for 1La and +2.57 for 0La), suggesting that UV-visible spectroscopy is a highly sensitive tool to analyze extent of reduction of cations near the surface.

Acknowledgments: The authors gratefully acknowledge funding from the Wyoming Clean Coal initiative and Brigham Young University. Use of the X18A beamline at the National Synchrotron Light Source, Brookhaven National Laboratory, was supported by the U.S. Department of Energy, Office of Science, Office of Basic Energy Sciences, under Contract No. DE-AC02-98CH10886.

Author Contributions: B.B. Hallac and J.C. Brown conceived and designed the experiments; B.B. Hallac, J.C. Brown, and E. Stavitski performed the experiments; B.B. Hallac, J.C. Brown, and E. Stavitski analyzed the data; B.B. Hallac wrote the paper, with R.G. Harrison providing editorial and senior authorship, and M.D. Argyle providing editorial, senior, and corresponding authorship.

Conflicts of Interest: The authors declare no conflict of interest.

References

1. Twigg, M.V. *Catalyst Handbook*, 2nd ed.; Wolfe: London, UK, 1989.
2. Bartholomew, C.H.; Farrauto, R.J. *Fundamentals of Industrial Catalytic Processes*, 2nd ed.; Wiley-InterScience: New York, NY, USA, 2005.
3. Rhodes, C.; Hutchings, G.J. Studies of the Role of the Copper Promoter in the Iron-Chromia High Temperature Water Gas Shift Catalyst. *Phys. Chem. Chem. Phys.* **2003**, *5*, 2719–2723. [CrossRef]
4. Rhodes, C.; Williams, B.P.; King, F.; Hutchings, G.J. Promotion of Fe_3O_4/Cr_2O_3 High Temperature Water Gas Shift Catalyst. *Catal. Commun.* **2002**, *3*, 381–384. [CrossRef]
5. Edwards, M.A.; Whittle, D.M.; Rhodes, C.; Ward, A.M.; Rohan, D.; Shannon, M.D.; Hutchings, G.J.; Kiely, C.J. Microstructural Studies of the Copper Promoted Iron Oxide/Chromia Water-Gas Shift Catalyst. *Phys. Chem. Chem. Phys.* **2002**, *4*, 3902–3908. [CrossRef]
6. Lei, Y.; Cant, N.W.; Trimm, D.L. Activity Patterns for the Water Gas Shift Reaction over Supported Precious Metal Catalysts. *Catal. Lett.* **2005**, *103*, 133–136. [CrossRef]
7. Andreev, A.; Idakiev, V.; Mihajlova, D.; Shopov, D. Iron-based Catalysts for the Water-Gas Shift Reaction Promoted by First-Row Transition Metal Oxides. *Appl. Catal.* **1986**, *22*, 385–387. [CrossRef]
8. Júnior, I.; Lima, M.; Jean-Marc, M.; Aouine, M.; Do Carmo, M.R. The Role of Vanadium on the Properties of Iron Based Catalysts for the Water Gas Shift Reaction. *Appl. Catal. A Gen.* **2005**, *283*, 91–98. [CrossRef]
9. Hu, Y.; Jin, H.; Liu, J.; Hao, D. Reactive Behaviors of Iron-Based Shift Catalyst Promoted by Ceria. *Chem. Eng. J.* **2000**, *78*, 147–152. [CrossRef]
10. Hallac, B.B.; Brown, J.C.; Baxter, L.L.; Argyle, M.D. A Kinetic Study on the Structural and Functional Roles of Lanthana in Iron-Based High-Temperature Water-Gas Shift Catalysts. *Int. J. Hydrogen Energy* **2014**, *39*, 7306–7317. [CrossRef]
11. Sun, Y.; Hla, S.S.; Duffy, G.J.; Cousins, A.J.; French, D.; Morpeth, L.D.; Edwards, J.H.; Roberts, D.G. Effect of Ce on the Structural Features and Catalytic Properties of $La_{(0.9-X)}Ce_XFeO_3$ Perovskite-Like Catalysts for the High Temperature Water-Gas Shift Reaction. *Int. J. Hydrogen Energy* **2011**, *36*, 79–86. [CrossRef]
12. Hla, S.S.; Sun, Y.; Duffy, G.J.; Morpeth, L.D.; Ilyuschechkin, A.; Cousins, A.; Edwards, J.H. Kinetics of the Water-Gas Shift Reaction Over a $La_{0.7}Ce_{0.2}FeO_3$ Perovskite-Like Catalyst Using Simulated Coal-Derived Syngas at High Temperature. *Int. J. Hydrogen Energy* **2011**, *36*, 518–527. [CrossRef]
13. Wang, T.; Ding, Y.; Lü, Y.; Zhu, H.; Lin, L. Influence of Lanthanum on the Performance of Ze-Co/Activated Carbon Catalysts in Fischer-Tropsch Synthesis. *J. Nat. Gas Chem.* **2008**, *17*, 153–158. [CrossRef]
14. Weckhuysen, B.M.; Verberckmoes, A.A.; Debaere, J.; Ooms, K.; Langhans, I.; Schoonheydt, R.A. *In Situ* UV-Vis Diffuse Reflectance Spectroscopy—On Line Activity Measurements of Supported Chromium Oxide Catalysts: Relating Isobutane Dehydrogenation Activity With Cr-Speciation Via Experimental Design. *J. Mol. Catal. A Chem.* **2000**, *151*, 115–131. [CrossRef]
15. Wachs, I.E. Recent Conceptual Advances in the Catalysis Science of Mixed Metal Oxide Catalytic Materials. *Catal. Today* **2005**, *100*, 79–94. [CrossRef]
16. Argyle, M.D.; Chen, K.; Resini, C.; Krebs, C.; Bell, A.T.; Iglesia, E. *In Situ* UV-vis Assessment of Extent of Reduction During Oxidation Reactions on Oxide Catalysts. *Chem. Commun.* **2003**, 2082–2083. [CrossRef]

17. Argyle, M.D.; Chen, K.; Iglesia, E.; Bell, A.T. *In Situ* UV-vis Spectroscopic Measurements of Kinetic Parameters and Active Sites for Catalytic Oxidation of Alkanes on Vanadium Oxides. *J. Phys. Chem. B* **2005**, *109*, 2414–2420. [CrossRef] [PubMed]
18. Ovsister, O.; Maymol, C.; Angelika, B.; Evgenii, K.V. Dynamics of Redox Behavior of Nano-Sized VO_x Species Over Ti–Si-MCM-41 from Time-Resolved *in Situ* UV/Vis Analysis. *J. Catal.* **2009**, *265*, 8–18.
19. Gao, X.; Jehng, J.M.; Wachs, I.E. *In Situ* UV-Vis-NIR Diffuse Reflectance and Raman Spectroscopic Studies of Propane Oxidation over ZrO_2-Supported Vanadium Oxide Catalysts. *J. Catal.* **2002**, *209*, 43–50. [CrossRef]
20. Sayah, E.; La Fontaine, C.; Briois, V.; Brouri, D.; Massiani, P. Silver Species Reduction upon Exposure of Ag/Al_2O_3 Catalyst to Gaseous Ethanol: An *In Situ* Quick-XANES Study. *Catal. Today* **2012**, *189*, 55–59. [CrossRef]
21. Singh, P.; Das, A.K.; Sarkar, B.; Niemeyer, M.; Roncaroli, F.; Olabe, J.A.; Fiedler, J.; Zalis, S.; Kaim, W. Redox Properties of Ruthenium Nitrosyl Porphyrin Complexes with Different Axial Ligation: Structural, Spectroelectrochemical (IR, UV-Visible, and EPR), and Theoretical Studies. *Inorg. Chem.* **2008**, *47*, 7106–7113. [CrossRef] [PubMed]
22. Daughtry, K.D.; Xiao, Y.; Stoner-Ma, D.; Cho, E.; Orville, A.M.; Liu, P.; Allen, K.N. Quaternary Ammonium Oxidative Demethylation: X-ray Crystallographic, Resonance Raman, and UV-Visible Spectroscopic Analysis of a Rieske-Type Demethylase. *J. Am. Chem. Soc.* **2012**, *134*, 2823–2834. [CrossRef] [PubMed]
23. Gunter, K.K.; Miller, L.M.; Aschner, M.; Eliseey, R.; Depuis, D.; Gavin, C.E.; Gunter, T.E. XANES Spectroscopy: A Promising Tool for Toxicology: A Tutorial. *Neurotoxicology* **2002**, *23*, 127–146. [CrossRef]
24. Atkins, P.; Shriver, D. *Inorganic Chemistry*; Oxford University Press: New York, NY, USA, 2006.
25. Rao, C.N.R. *Ultra-Violet and Visible Spectroscopy: Chemical Applications*; Butterworth-Heinemann: London, UK, 1974.
26. Clark, B.J.; Frost, T.; Russell, M.A. *UV Spectroscopy: Techniques, Instrumentation, Data Handling*; Chapman & Hall: London, UK, 1993.
27. Tossell, J.A.; Vaughan, D.; Johnson, K.H. The Electronic Structure of Rutile, Wustite and Hematite from Molecular Orbital Calculations. *Am. Mineral.* **1974**, *59*, 319–334.
28. Cornell, R.M.; Schwertmann, U. *The Iron Oxides: Structure, Properties, Reactions, Occurrences and Uses*, 2nd ed.; Wiley-VCH: New York, NY, USA, 2003.
29. Zhang, Z.; Boxall, C.; Kelsall, G.H. Photoelectropheresis of Colloidal Iron Oxides. Part 2.—Magnetite (Fe_3O_4). *J. Chem. Soc. Faraday Trans.* **1996**, *92*, 791–802.
30. Sherman, D.M. Electronic Structures of Iron(III) and Manganese(IV) (Hydr)oxide Minerals: Thermodynamics of Photochemical Reductive Dissolution in Aquatic Environments. *Geochim. Cosmochim. Acta* **2005**, *69*, 3249–3255. [CrossRef]
31. Sherman, D.M. Electronic Stuctures of Fe^{3+} Coordination Sites in Iron Oxides: Applications to Spectra, Bonding, and Magnetism. *Phys. Chem. Miner.* **1985**, *12*, 161–175. [CrossRef]
32. Christy, A.A.; Kvalheim, O.M.; Velapoldi, R.A. Quantitative Analysis in Diffuse Reflectance Spectrometry: A Modified Kubelka-Munk Equation. *Vib. Spectrosc.* **1995**, *9*, 19–27. [CrossRef]
33. Džimbeg-Malčić, V.; Barbarić-Mikočević, Ž.; Itrić, K. Kubelka-Munk Theory in Describing Optical Properties of Paper (I). *Tech. Gazette* **2011**, *18*, 117–124.
34. Kubelka, P.; Munk, F. Ein Beitrag zur Optik der Farbanstriche (A Contribution to the Optics of Paint). *Z. Tech. Phys.* **1931**, *12*, 593–601.
35. Schuster, A. Radiation Through a Foggy Atmosphere. *Astrophys. J.* **1905**, *21*, 1–22. [CrossRef]
36. Wyszecki, G.; Stiles, W.S. *Color Science*, 2nd ed.; John Wiley & Sons: New York, NY, USA, 2000.
37. Doak, J.; Gupta, R.K.; Manivannan, K.; Ghosh, K.; Kahol, P.K. Effect of Particle Size Distributions on Absorbance Spectra of Gold Nanoparticles. *Physica E* **2010**, *42*, 1605–1609. [CrossRef]
38. Van de Hulst, H.C. *Light Scattering by Small Particles*; John Wiley & Sons: New York, NY, USA, 1957.
39. Koningsberger, D.C.; Prins, R. *X-ray Absorption: Principles Applications Techniques of EXAFS SEXAFS and XANES, Chemical Analysis*; John Wiley & Sons: New York, NY, USA, 1988.
40. Puig-Molina, A.; Cano, F.M.; Janssens, T.V.W. The Cu Promoter in an Iron-Chromium-Oxide Based Water-Gas Shift Catalyst under Industrial Conditions Studied by *In-Situ* XAFS. *J. Phys. Chem. C* **2010**, *114*, 15410–15416. [CrossRef]
41. Gonzalez, J.C.; Gronzalez, M.G.; Laborde, M.A.; Moreno, N. Effect of Temperature and Reduction on the Activity of High Temperature Water Gas Shift Catalysts. *Appl. Catal.* **1986**, *20*, 3–13. [CrossRef]

42. Kundakovic, L.; Flytzani-Stephanopoulos, M. Reduction Characteristics of Copper Oxide in Cerium and Zirconium Oxide Systems. *Appl. Catal. A* **1998**, *171*, 13–29. [CrossRef]
43. Greenwood, N.N.; Earnshaw, A. *Chemistry of the Elements*; Butterworth-Heinemann: London, UK, 1997.
44. Li, X.; Wang, Y.; Xu, P.; Zhang, Q.; Nie, K.; Hu, X.; Kong, B.; Li, L.; Chen, J. Effects of Temperature and Wavelength Choice on *In-Situ* Dissolution Test of Cimetidine Tablets. *J. Pharm. Anal.* **2013**, *3*, 71–74. [CrossRef]
45. Zhu, Y.; Sun, D.; Huang, Q.; Jin, X.; Liu, H. UV-vis Spectra of Perovskite Iron-Doped $Ba_{0.72}Sr_{0.28}TiO_3$. *Mater. Lett.* **2008**, *62*, 407–409. [CrossRef]
46. Kim, J.Y.; Magesh, G.; Youn, D.H.; Jang, J.; Kubota, J.; Domen, K.; Lee, J.S. Single-Crystalline, Wormlike Hematite Photoanodes for Efficient Solar Water Splitting. *Sci. Rep.* **2013**, *3*, 2681. [CrossRef] [PubMed]
47. Sherman, D.M.; Waite, T.D. Electronic Spectra of Fe^{3+} Oxides and Oxide Hydroxides in the Near-IR to Near-UV. *Am. Mineral.* **1985**, *70*, 1262–1269.
48. Popa, T.; Xu, G.; Barton, T.F.; Argyle, M.D. High Temperature Water Gas Shift Catalysts with Alumina. *Appl. Catal. A Gen.* **2010**, *379*, 15–23. [CrossRef]
49. Patlolla, A.; Carino, E.V.; Ehrlich, S.N.; Stavitski, E.; Frenkel, A.I. Application of *Operando* XAS, XRD, and Raman Spectroscopy for Phase Speciation in Water Gas Shift Reaction Catalysts. *ACS Catal.* **2012**, *2*, 2216–2223. [CrossRef]
50. Wilke, M.; Hahn, O.; Woodland, A.B.; Rickers, K. The Oxidation State of Iron Determined by Fe K-Edge XANES—Application to Iron Gall Ink in Historical Manuscripts. *J. Anal. At. Spectrom.* **2009**, *24*, 1364–1372. [CrossRef]
51. Labinger, J.A.; Ott, K.C. Is There a Difference Between Surface and Bulk Oxidation Levels in Partially Reduced Metal Oxide Catalysts? Evidence from Methane Oxidative Coupling Kinetics. *Catal. Lett.* **1990**, *4*, 245–250. [CrossRef]

catalysts

MDPI

Article

Development of Active and Stable Low Nickel Content Catalysts for Dry Reforming of Methane

Quan Luu Manh Ha [1,2], Udo Armbruster [1,*], Hanan Atia [1], Matthias Schneider [1], Henrik Lund [1], Giovanni Agostini [1], Jörg Radnik [3], Huyen Thanh Vuong [1] and Andreas Martin [1]

1 Department Heterogeneous Catalytic Processes, Leibniz-Institut für Katalyse e.V., Albert-Einstein-Str. 29a, 18059 Rostock, Germany; quan.ha@catalysis.de (Q.L.M.H.); hanan.atia@catalysis.de (H.A.); matthias.schneider@catalysis.de (M.S.); henrik.lund@catalysis.de (H.L.); giovanni.agostini@catalysis.de (G.A.); huyen.vuong@catalysis.de (H.T.V.); andreas.martin@catalysis.de (A.M.)

2 Vietnam Petroleum Institute, 167 Trung Kinh, Cau Giay, Hanoi 100000, Vietnam

3 Division 6.1, Surface Analysis and Interfacial Chemistry, Federal Institute for Materials Research and Testing, Richard-Willstätter-Str. 12, 12489 Berlin, Germany; joerg.radnik@bam.de

* Correspondence: udo.armbruster@catalysis.de; Tel.: +49-381-1281-257

Academic Editor: Morris D. Argyle

Received: 30 March 2017; Accepted: 12 May 2017; Published: 16 May 2017

Abstract: Methane dry reforming (DRM) was investigated over highly active Ni catalysts with low metal content (2.5 wt %) supported on Mg-Al mixed oxide. The aim was to minimize carbon deposition and metal sites agglomeration on the working catalyst which are known to cause catalyst deactivation. The solids were characterized using N_2 adsorption, X-ray diffraction, temperature-programmed reduction, X-ray photoelectron spectroscopy, and UV-Vis diffuse reflectance spectroscopy. The results showed that MgO-Al_2O_3 solid solution phases are obtained when calcining Mg-Al hydrotalcite precursor in the temperature range of 550–800 °C. Such phases contribute to the high activity of catalysts with low Ni content even at low temperature (500 °C). Modifying the catalyst preparation with citric acid significantly slows the coking rate and reduces the size of large octahedrally coordinated NiO-like domains, which may easily agglomerate on the surface during DRM. The most effective Ni catalyst shows a stable DRM course over 60 h at high weight hourly space velocity with very low coke deposition. This is a promising result for considering such catalyst systems for further development of an industrial DRM technology.

Keywords: dry reforming of methane; carbon dioxide; nickel; MgO-Al_2O_3 solid solution

1. Introduction

The dry reforming of methane (DRM), which is the strong endothermic reaction of methane with carbon dioxide to syngas (Equation (1)), has gained increasing interest in recent years:

$$CH_4 + CO_2 \rightarrow 2CO + 2H_2 \quad (1)$$

This reaction cannot only be effectively applied for natural gas conversion into liquid fuels via the syngas route, but also may contribute to reducing the emission of CO_2 and CH_4 greenhouse gases to our atmosphere [1–4]. The syngas from DRM with a low ratio of H_2/CO is suitable for subsequent syntheses of oxygenated chemicals [5] and hydrocarbons via the Fischer-Tropsch synthesis [6]. However, DRM requires a high reaction temperature [7]. This leads to several catalyst deactivation processes resulting in catalytic sites' agglomeration and coke formation [8]. The deposited carbon is formed during the DRM reaction through CH_4 decomposition (Equation (2)) and Boudouard (Equation (3)) reactions [4,9,10]:

$$CH_4 \rightarrow C + 2H_2 \quad (2)$$

$$2CO \rightarrow CO_2 + C \quad (3)$$

Therefore, the great challenge for the development of a DRM process is the development of catalysts with high activity for the conversion of CO_2 and CH_4 and strong ability in suppressing the formation of carbon deposits [8]. Ni based catalysts were most frequently reported in DRM studies due to their high activity, availability, and lower price compared to other transition and noble metals [11–13]. In those studies, efforts were focused on improving the activity and stability of Ni active sites in the following aspects: screening and modifying the properties of the support, selecting the support and catalyst preparation methods, and the addition of promoters [13].

Suitable supports play a key role in the enhancement of catalytic activity and the suppression of carbon deposition for the DRM reaction [4]. γ-Al_2O_3 has been widely employed as a support for DRM catalysts because of its high availability and low price [4,14]. It was also suggested that an improvement of the support properties for the adsorption and activation of CO_2 would accelerate the gasification of the deposited carbons and prevent the rapid deactivation of the catalyst [13]. In order to achieve that, certain alkaline-earth metal oxides were incorporated into alumina to increase the basicity of the support [13]. MgO was reported to improve the catalytic performance of Ni/Al_2O_3 because of the strong interaction between Ni and the supports and the basic property of the metal oxide could suppress carbon formation in the dry reforming process [15,16]. The cooperation of Mg and Al oxides in same support material can result in many structures, such as $MgAl_2O_4$ spinel, which is the well-studied support structure for Ni catalysts in several types of reactions due to its good chemical stability and mechanical strength [13,17]. Other structures of MgO and Al_2O_3 mixed oxides could also serve as supports for DRM catalysts in order to disperse and stabilize the metallic Ni species and promote the coking resistance behavior [18–20]. However, only a few DRM studies have focused on low Ni content catalysts with such mixed oxide supports, probably due to the partial formation of stable but poorly active phases, such as $NiAl_2O_4$ spinel or NiO-MgO solid solution [17]. However, Ni catalysts with low metal content are potentially one of the solutions for overcoming the abovementioned problems of DRM. This is due to higher catalyst stability and lower carbon deposition achieved by forming highly dispersed and smaller sized Ni particles [21,22].

Chelating agents are molecules with two or more electron-pair donor atoms which can act as a ligand and attach themselves to metal ions [23]. This causes the formation of metal complexes, which were also studied to modify the preparation route for supported catalysts using the impregnation method [23]. In such studies, uniform distribution and high dispersion of the active component over the support were achieved. Those beneficial properties arise from the diffusion-controlled homogeneous distribution of metal atoms in the precursor structure as well as the enhanced viscosity of the gel-like material inhibiting redistribution of the impregnated species during subsequent drying. Citric acid (CA) is the most common and promising compound among the chelating agents because it is cheap, highly soluble, and environmentally harmless [24].

The aim of this study is to explore the potential of catalysts with low Ni content, according to the literature review [8], on Mg-Al mixed oxide supports (Mg-Al) that can be both stable and active in DRM at high weight hourly space velocity (WHSV). Modifications of the support and catalyst preparation were investigated to enhance the stability of the catalyst without deteriorating the DRM activity. Thus, various Ni catalysts with different supports were prepared via modified routes and tested in a continuous fixed bed reactor. Long-term experiments together with the characterization of fresh and spent catalysts using various techniques, including inductively coupled plasma-optical emission spectroscopy and atomic adsorption spectroscopy (ICP-OES resp. AAS), N_2 physisorption, X-ray powder diffraction (XRD), X-ray photoelectron spectroscopy (XPS), Temperature-programmed reduction (TPR), and UV-Vis diffuse reflectance spectroscopy (UV-Vis-DRS), indicated important attributes that contribute to catalyst activity and stability.

2. Results

2.1. Characterization of the Catalysts

First of all, the crystalline structures of the supports and catalysts can be revealed by X-ray diffraction. Figure 1 depicts the XRD patterns of $MgO{\cdot}Al_2O_3$ mixed oxides (denoted as Mg.Al.X with X indicating the calcination temperature) obtained from hydrotalcite material with different calcination temperatures (550, 700, 800, 1000 °C). The patterns of MgO and Al.550 (boehmite calcined at 550 °C) are also displayed as references. When hydrotalcite samples are calcined at temperatures between 550 °C and 800 °C, the XRD patterns of the resulting Mg.Al.X samples show broad reflections at about 2θ = 43° and 63° which have 2θ values higher than those of periclase (cubic form of magnesium oxide, ICDD (International Centre for Diffraction Data) file No. 01-071-1176) but lower than those of γ-Al_2O_3 (ICDD file No. 00-010-0425). The patterns of periclase and γ-Al_2O_3 structures are clearly observed in MgO and Al.550 samples, respectively. This highlights the incorporation of smaller Al^{3+} cations into the bulk of the periclase (MgO) structure lattice, establishing a solid solution between MgO and Al_2O_3 (Mg-Al-O) [25,26]. A higher calcination temperature modifies such an incorporation which can be observed as a shift of reflections to lower 2θ values. Up to 800 °C, the pattern of such a solid solution is still observable. Besides, Mg.Al.700 and Mg.Al.800 show reflections (2θ = 31.3°; 37°; 45°; 55.5°; 59°; 65°) assigned to the formation of the $MgAl_2O_4$ phase (ICDD file No. 00-021-1152) at higher calcination temperatures [27]. At 1000 °C, no reflection of the solid solution can be observed while peaks assigned to periclase MgO and $MgAl_2O_4$ phases are sharp and characteristic, indicating the high crystallinity of those phases. Those results are in accordance with other studies [25,28,29] focusing on the thermal decomposition behavior of hydrotalcite, producing Mg-Al oxides and mixed oxides in solid solution or spinel structures, particularly when a low heating rate was applied.

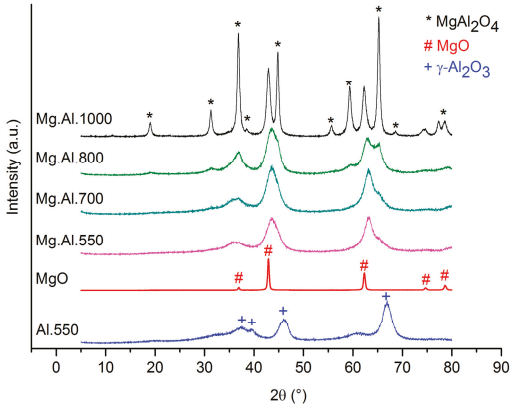

Figure 1. XRD patterns of the MgO, γ-Al_2O_3, and Mg.Al supports.

The XRD patterns of impregnated low content Ni samples (not shown) show no significant differences from those of their corresponding supports. This reflects the formation of well-dispersed Ni^{2+} species leading to very small Ni particles that were not detected by the XRD measurements [30,31]. This might be also due to Ni diffusion into the bulk of the supports, especially when a high calcination temperature was applied during the preparation [31].

The XRD patterns of spent Ni catalysts are presented in Figure 2. Ni metal species (Ni^0), which are the result of the pre-reduction process before DRM, can be detected with reflections at 2θ = 44.5° and 51.8° (ICDD file No. 01-071-3740). Spent Ni/Al.550 (Figure 2b) shows a pattern with additional reflections at the mentioned 2θ values compared to the fresh one. This is assigned to the formation of highly crystalline Ni^0 domains due to agglomeration during the reaction. On the other hand, the XRD

pattern of spent Ni/Mg.Al.550 (Figure 2a) displays a similar profile as the fresh sample, proving the stability of the material during the reaction. This result is probably due to the incorporation of Ni into the solid solution or/and the $MgAl_2O_4$ spinel framework since such stable phases prevent the structural transformation at the high reaction temperature [17,18,21].

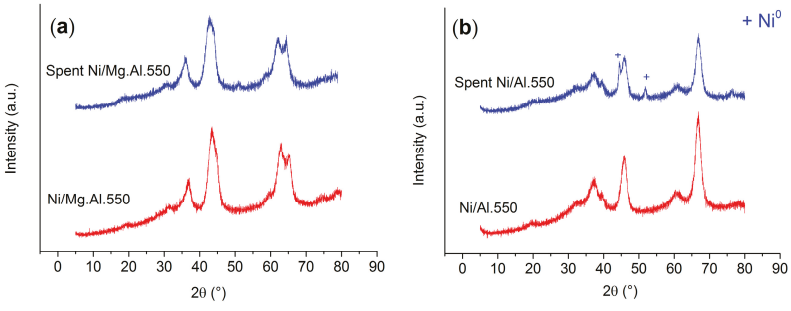

Figure 2. XRD patterns of fresh and spent samples of Ni supported (**a**) on Mg.Al.550 and (**b**) on Al_2O_3 (DRM (dry reforming of methane) conditions: 700 °C, 1 bar, CH_4:CO_2 = 1, WHSV (weight hourly space velocity) = 85 L/(g_{cat} × h), TOS (time-on stream) = 8 h).

The N_2 adsorption-desorption isotherms together with the BJH (Barrett-Joyner-Halenda) pore size distributions (PSD) of the Mg.Al.550.800 support and corresponding Ni catalysts are shown in Figures 3 and 4, respectively. All isotherms exhibit type II curves with H3 type hysteresis loops according to the IUPAC (International Union of Pure and Applied Chemistry) classification, which reflects the contribution of the mesopores in the materials.

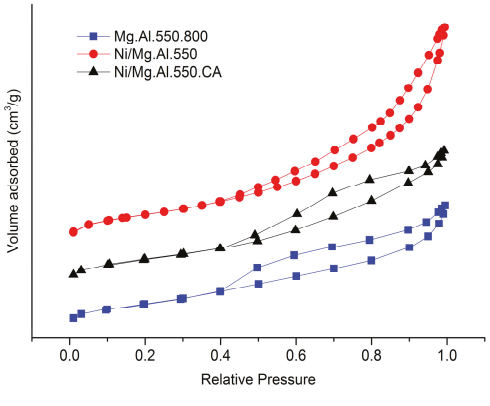

Figure 3. N_2 physisorption isotherms of fresh catalysts and their support Mg.Al.550.800.

Regarding the pore size distribution (Figure 4), both the Ni samples show a shift toward higher pore diameter compared to their support. This feature most likely indicates the re-structuring of the support material in the impregnation step. However, in both cases, no limitation by internal diffusion is expected for the feed molecules, which are small compared to the size of the pores.

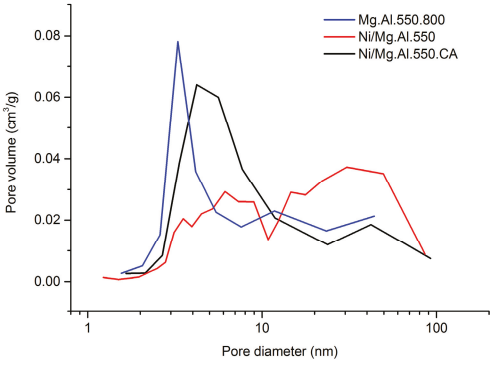

Figure 4. Pore size distribution of fresh catalysts and their support Mg.Al.550.800.

The textural parameters of the calcined Ni samples and the supports are summarized in Table 1.

Table 1. Textural properties of calcined catalysts and their supports.

Catalyst	S_{BET} (m^2/g)	Total Pore Volume (cm^3/g)
Mg.Al.550	180	0.24
Mg.Al.550.800 [1]	147	0.24
Mg.Al.1000	85	0.37
Al.550	234	0.54
MgO	50	0.35
Ni/Mg.Al.550	174	0.40
Ni/Mg.Al.550.CA [2]	156	0.27
Ni/Mg.Al.1000	82	0.36
Ni/Al.550	178	0.47
Ni/MgO	45	0.33

[1] Mg.Al.550 calcined again at 800 °C; [2] Citric acid was used during impregnation.

While all bare supports were calcined once at 550 °C and the resulting catalysts at 800 °C, one particular sample denoted as Mg.Al.550.800 was calcined at 550 and 800 °C as a reference support without impregnation.

Support Al.550 displays the highest surface area and pore volume among the studied supports. However, Ni/Mg.Al.550 and Ni/Al.550 show similar texture parameters. Both Ni/Mg.Al.550 and Ni/Mg.Al.550.CA expose larger surface areas than their corresponding support (Mg.Al.550.800) which might be explained by the mentioned re-structuring of the support surface due to the dissolution of alumina and magnesia into the acidic solution (containing Ni^{2+} and/or citric acid) during the impregnation step [30]. Ni/Mg.Al.1000 possesses relatively low surface area because its support was calcined at high temperature. Ni/Al.550 and Ni/MgO show textural parameters which are in agreement with their supports' attributes.

The reducibility of the materials was examined by TPR measurements. It should be noted that Ni^{2+} species are the predominant reducible ones in those samples. The TPR profile of the unsupported NiO sample as the reference is exhibited in Figure 5 with an intense peak at 350 °C, illustrating the bulk NiO reduction. Generally, all studied supported Ni samples display poor reducibility, possibly due to their low Ni loading and high sample calcination temperature. Those effects might cause strong interaction of Ni^{2+} and the support, suppressing free NiO that can otherwise easily react with hydrogen [32,33]. On Al_2O_3, the Ni^{2+} species show high-temperature reduction peaks at 700 °C and the reduction is incomplete below 1000 °C (Figure 5). This behavior is typical for the reduction of nickel aluminate species. The mentioned samples were prepared at high calcination temperature

(800 °C) and low Ni content (2.5 wt %), leading to unavoidable poor reducibility due to the diffusion of Ni^{2+} into the Al_2O_3 lattice, suppressing the formation of bulk NiO species [34]. The TPR profile of Ni/MgO discloses peaks at somewhat lower temperatures mainly assigned to the reduction of Ni^{2+} species in the outer face or subsurface layers of the MgO lattice. The remaining shoulder at higher temperature of the profile is related to the reduction of the species in solid solution, resulting from the diffusion of Ni^{2+} species into the periclase lattice due to high calcination temperature (800 °C) [32]. Ni/Mg.Al.550 shows a broad peak starting at 600 °C, reflecting the reduction of Ni^{2+} species mainly in the solid solution [35] and/or in the spinel structure when Ni is embedded in Mg and Al mixed oxides prepared from the hydrotalcite precursor [36]. The reducibility of that sample is slightly better than that for Ni/MgO or Ni/Al.550. Indeed, Ni/Mg.Al.550 displays a weak band at 500 °C in its TPR profile, attributed to the reduction of NiO species formed on the surface that have weak interaction with the support [37]. Additionally, it shows higher H_2 consumption than the single oxide supported samples (Table 2). This is similar to literature reports [20] concluding that the availability of Mg in Ni-Al containing samples facilitates the solid solution formation and stabilizes the Ni species on the surface. This benefit avoids the Ni diffusion into the alumina lattice, and therefore suppresses the formation of the poorly reducible $NiAl_2O_4$ spinel structure.

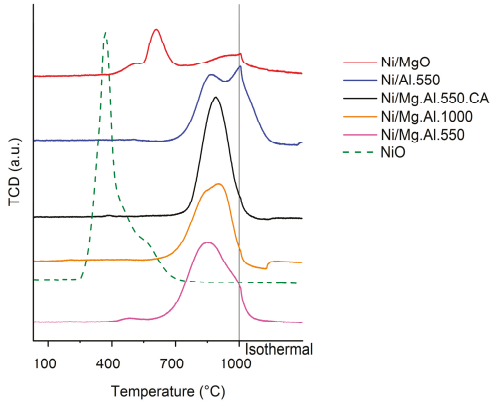

Figure 5. TPR (temperature-programmed reduction) profiles of several supported Ni catalysts and NiO.

In comparison to Ni/Mg.Al.550, both Ni/Mg.Al.550.CA and Ni/Mg.Al.1000 show a shift in reduction peak maxima in their TPR profiles to higher temperature (900 °C) (Figure 5). Besides, they consume less hydrogen in the TPR experiment (Table 2), illustrating the formation of poorly reducible Ni^{2+} species that have higher interaction with the support frameworks [35,38].

Table 2. H_2 consumption in TPR for the catalysts.

Sample	H_2 Consumption (μmol/g)
Ni/Al.550	397
Ni/MgO	181
Ni/Mg.Al.550	480
Ni/Mg.Al.1000	404
Ni/Mg.Al.550.CA	437

XPS measurements were carried out to characterize the surface composition of the materials. The binding energy (BE) values were also measured to verify the oxidation states of the atoms as well as their chemical and physical environments. All of the samples show binding energies (BE) corresponding to the Ni $2p_{3/2}$ region within the range around 855–857 eV (Table 3) [39]. Those are

slightly higher than the values for free NiO (854.5 eV) [39,40] and close to that observed for Ni_2O_3 (856 eV) [35,39], $NiAl_2O_4$ (856 eV) [35,39], NiO-MgO solution (855.7 eV [40] or 856 eV [41]), and solid solution Mg(Ni.Al)O (855.5 eV) [35].

Table 3. XPS (X-ray photoelectron spectroscopy) and ICP-AES (Inductively coupled plasma atomic emission spectroscopy) results for the catalysts.

Sample	Binding Energy (eV)	Surface Molar Ratio [1]		Bulk Molar Ratio [2]	
	Ni $2p_{3/2}$	Ni/(Mg + Al)	Mg/Al	Ni/(Mg + Al)	Mg/Al
Ni/Al.550	855.5	0.029	-	0.022	0
Ni/MgO	- [3]	- [3]	- [3]	0.017	-
Ni/Mg.Al.550	856.9	0.063	0.4	0.019	1.3
Ni/Mg.Al.1000	856.1	0.057	0.3	0.019	1.3
Ni/Mg.Al.550.CA	855.2	0.071	1.6	0.019	1.3
Mg.Al.550	-	-	1.2	-	1.3
Mg.Al.550.800	-	-	1.1	-	1.3
Mg.Al.1000	-	-	1.5	-	1.3

[1] XPS results; [2] ICP results; [3] Ni content is below the XPS detection limit.

In any case, it could be suggested that the transfer of electrons from nickel to electron-poor magnesium and/or aluminum species in the structure causes the BE to shift to a higher value than that of free NiO [35]. Those results indicate a strong interaction of Ni with the supports, as seen in the TPR results, lowering their reducibility compared to pure NiO (Figure 5).

Regarding the Mg/Al surface ratio (Table 3) of samples with the Mg.Al support, there are differences between the Ni catalysts and their corresponding supports, suggesting the mentioned alumina and magnesia dissolution and re-dispersion of the surface components after preparation in some cases. On one side, impregnating Ni^{2+} onto the support in the presence of CA slightly increases the Mg/Al ratio from 1.1 to 1.6, but still maintains the Mg-rich surface. On the other hand, Ni/Mg.Al.550 and Ni/Mg.Al.1000 show Al-rich surfaces. Those observations are not fully understood, but are probably due to the Mg and Al leaching rate and re-dispersion in different precursor solutions during catalyst preparation. However, the surface Ni concentrations of those samples are still comparable.

Comparison of the surface Ni/(Mg + Al) ratio (from XPS) and bulk composition (from ICP) (Table 3) highlights the preferred location of Ni in different supports. Regarding the reference samples, Ni/MgO exposes almost no Ni on the surface and Ni/Al.550 shows a slightly higher surface Ni/(Mg + Al) ratio (0.029) compared to the bulk values (0.022). On the other hand, Ni/Mg.Al.550, Ni/Mg.Al.1000, and Ni/Mg.Al.550.CA expose Ni on the surface with significantly higher atom ratios (0.063, 0.057, and 0.071) compared to their bulk values (0.017–0.019). These data reflect the ability of Mg.Al supports to augment active Ni species on the outer shell of materials. Such an effect contributes to the higher reducibility of the Mg.Al supported samples compared to Ni/MgO and Ni/Al.550, as shown in the TPR profiles (Figure 5). Increasing the support calcination temperature from 550 to 1000 °C produces samples with less Ni^{2+} domains on the surface available for reduction [38]. As a result, Ni/Mg.Al.1000 provides poorer reducibility compared to Ni/Mg.Al.550 (Figure 5). This illustrates the ability of the Mg.Al.550 support with Mg-Al-O solid solution domains to enrich the surface Ni species and thus to enhance sample reducibility.

Introduction of CA during preparation increases the fraction of surface Ni^{2+} species. However, the reducibility of Ni/Mg.Al.550.CA as mentioned is not as high as that of Ni/Mg.Al.550 (Figure 5). The sample shows a sharp and symmetric reduction peak with a maximum temperature around 900 °C. These observations suggest that the low reducibility of Ni/Mg.Al.550.CA is primarily due to the higher dispersion of Ni species on the support surface [23], leading to a strong interaction with the Mg.Al material.

The coordination of the nickel (mostly Ni^{2+}) species in the samples was examined by UV-Vis-DRS (Diffuse reflection spectroscopy). This technique is helpful for the identification of the nickel phases. No absorption can be seen in the support samples (not shown), suggesting that only Ni^{2+} species are sensitive at the chosen analysis conditions. The UV-Vis-DRS spectra of the Ni impregnated samples on different supports are shown in Figure 6. Those spectra show intense signals in the UV region of 250–350 nm, which relate to the $O^{2-} \rightarrow Ni^{2+}$ charge transfer (CT) in the octahedral NiO lattice [42]. NiO shows strong absorption over the whole mentioned range which can be assigned to nonstoichiometric NiO containing some Ni^{3+} domains [42]. Mg.Al supported samples show shoulders in the range of 250–350 nm which cannot be found in the spectra of Ni/MgO and Ni/Al.550, suggesting weaker interaction of Ni species with the Mg.Al supports [30]. In comparison to Ni/Mg.Al.550.CA and Ni/Mg.Al.1000, a red-shift of the CT band of NiO is observed for Ni/Mg.Al.550, which points to the weakest interaction of Ni species and support among the studied samples. This explains the TPR results, which proved that Ni/Mg.Al.550.CA and Ni/Mg.Al.1000 have lower reducibility compared to Ni/Mg.Al.550 (Figure 5).

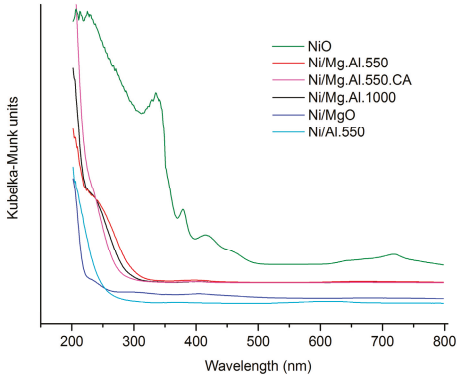

Figure 6. UV-Vis-DRS spectra of supported Ni catalysts and NiO.

A magnification of the UV-Vis-DRS spectra in the visible region (350–800 nm) of the mentioned samples can be seen in Figure 7. The signals in this region represent d-d transitions of Ni^{2+} ions mainly in octahedral (O_h) and tetrahedral coordination (T_d) [43]. Pure NiO presents intense signals at 380, 420, and 720 nm which illustrate the Ni^{2+} (O_h) in the cubic (rock-salt) NiO lattice [44]. Ni/Al.550, on the other hand, shows a doublet signal at 600–650 nm which is related to the Ni^{2+} (T_d) species in the nickel aluminate spinel lattice [44,45]. Besides, small absorption bands at 380 nm can be assigned to Ni^{2+} (O_h) in the $NiAl_2O_4$ spinel [46]. Ni/MgO displays a spectrum similar to that of the pure NiO sample. It shows an intense signal at 410 nm and a wide band at 650–800 nm which suggests a majority of Ni^{2+} (O_h) species. Those bands belong to the solid solution of Ni and Mg when Ni species migrate into the MgO parent lattice, which has a cubic rock-salt structure as well [47]. The absence of intense signals at 380 nm and 720 nm is probably due to the lack of bulk NiO in Ni/MgO [46]. This suggestion is supported by the XRD pattern of Ni/MgO (not shown), in which no crystalline structure other than periclase MgO can be seen. Indeed, the low content of Ni in the sample and the strong interaction between NiO and MgO results in the high dispersion of Ni species, thus suppressing the agglomeration of NiO in the calcination process. Ni/Mg.Al.550 shows a wide band from 380 nm to 410 nm with the highest intensity at around 400 nm, which is located between the corresponding signals of Ni/MgO and Ni/Al.550. This reveals the formation of octahedral coordination of the Ni domains which diffuse into the support framework of the solid solution Mg-Al-O. This kind of structure containing the three elements was also discussed in other studies [29,48] in which Ni^{2+} and Al^{3+} were substituted for the Mg^{2+} site in the parent MgO (periclase) structure (denoted as Mg(Ni,Al)O). Furthermore, it should

be noted that the presence of Ni^{2+} (O_h) in the $NiAl_2O_4$ spinel can be stated for the Ni/Mg.Al.550 sample. In [30], the authors claimed the formation of Ni^{2+} (O_h) species in $NiAl_2O_4$-like "surface spinel", identified by bands in the range of 405–410 nm. These surface spinel species were suggested to more likely exist in the samples with higher nickel content on the surface, similar to the surface features revealed by XPS in this study (Table 3). Briefly, Ni^{2+} (O_h) species are formed in both types of structures but the individual species are hard to identify and localize because of their overlapping absorption ranges in the UV-Vis-DRS spectra.

No significant difference between the spectra of Ni/Mg.Al.550.CA and Ni/Mg.Al.550 in the range of 350–800 nm can be found. However, the intensity of the broad signal at 720 nm in the spectrum of Ni/Mg.Al.550.CA (Figure 7b) is lower than that of Ni/Mg.Al.550, indicating less Ni^{2+} species in the domains of bulk NiO-like species which are reducible at low temperature (475 °C, Ni/Mg.Al.550, Figure 5). This suggests that higher dispersion of Ni species can be obtained when CA is added during the preparation. Compared to Ni/Mg.Al.550, a red-shift of the band at around 403 nm can be seen in the Ni/Mg.Al.1000 spectrum (Figure 7b). This shift toward the position of the corresponding intense signal of Ni/MgO illustrates the behavior of the NiO-MgO solid solution. Such a phase formation might be in accordance with the blue-shift of the CT band of the NiO lattice in this sample, displaying the higher stability of the Ni species (Figure 6).

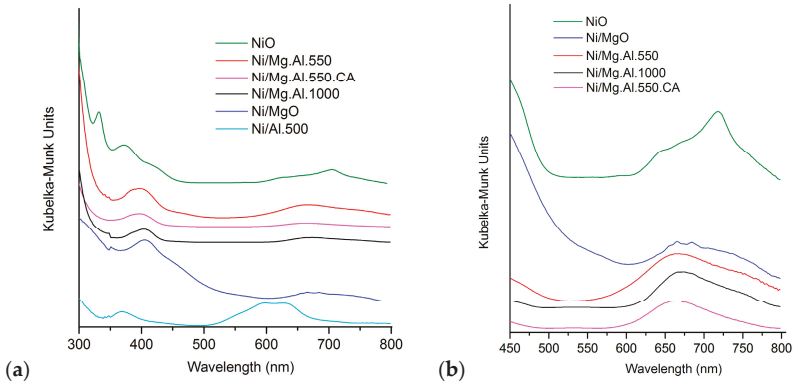

Figure 7. Magnification of complete UV-Vis-DRS spectrum (Figure 6) for supported Ni catalysts and NiO to (**a**) 300-800 nm and (**b**) from 450–800 nm regions.

2.2. Catalyst Performance in the DRM Reaction

Blank tests were carried out in the absence of catalysts or only with the supports in the inert material bed (not shown). No conversion of the feed gases was observed at the favored conditions. Figure 8 shows the CH_4 and CO_2 conversions in DRM during 8 h on stream over the supported Ni catalysts at 650 °C with various supports. The reaction conditions (650 °C, 1 bar, CH_4:CO_2 = 1, WHSV = 85 L/(g_{cat} × h)) were chosen to differentiate the activity of the catalysts. Higher activity can be obtained with Mg.Al supported Ni catalysts compared to the single oxide supported samples. Addition of CA during preparation plays a minor role regarding the activity. In contrast, supporting Ni^{2+} on Mg.Al.1000 causes a deterioration of conversion compared to Ni/Mg.Al.550. The latter catalyst exposed the highest activity with the conversions of CH_4 and CO_2 being very close to the thermodynamic limitations for CH_4 (71%) and CO_2 (82%) [49].

In order to verify such high activity of Ni/Mg.Al.550, additional DRM tests at lower temperature with the same WHSV were investigated. Figure 9 shows the excellent performance of Ni/Mg.Al.550 in comparison with the thermodynamic limitations [49]. The catalyst activates CH_4 and CO_2 already around 500 °C. It should be noted that DRM requires high temperatures to convert the reactants to

syngas. According to the literature, the reaction starts at 350 °C, referred to by the thermodynamic calculations [49,50]. Moreover, remarkable conversions of methane and CO_2 were observed only above 500 °C [13]. Some studies claimed the catalysts to be active in DRM at very low temperature (400 °C [51] or 450 °C [50]). However, in those studies more beneficial conditions for high catalytic activity compared to this study were applied (lower WHSV, higher content of active sites, or usage of noble metals). Therefore, the activity of Ni/Mg.Al.550 in this study is outstanding at low temperature considering its low Ni content and the high WHSV (85 L/(g_{cat} × h)) in comparison with other investigations [3,8,52]. Figure 9 displays the effect of temperature on the H_2/CO ratio. This ratio is always lower than unity at any set reaction temperature, which indicates the occurrence of the reverse water gas shift (RWGS) reaction, lowering H_2 selectivity through the reaction with CO_2 to form CO and H_2O [1]. This reaction plays a more important role at lower temperature due to the thermodynamic equilibrium [1].

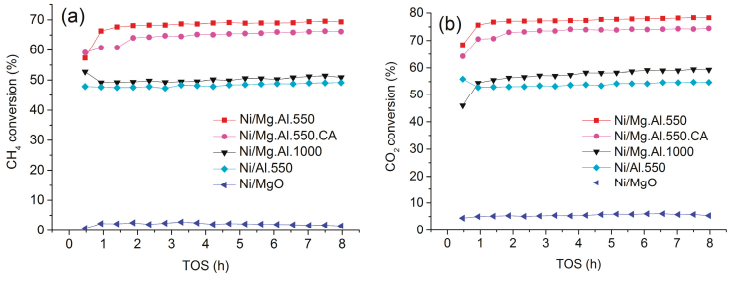

Figure 8. DRM performance of supported Ni catalysts: conversion of (**a**) CH_4 and (**b**) CO_2 (650 °C, 1 bar, CH_4:CO_2 = 1, WHSV = 85 L/(g_{cat} × h), TOS = 8 h).

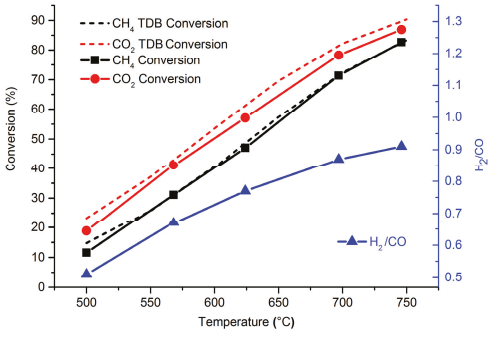

Figure 9. Catalytic performance of Ni/Mg.Al.550 in comparison with the thermodynamic balance (TDB) (1 bar, CH_4:CO_2 = 1, WHSV = 85 L/(g_{cat} × h)). Activity data were collected after 2 h stabilization at each temperature.

The coke deposition behavior in DRM was examined for the Ni catalysts by analyzing the carbon content in the catalysts after 8 h on stream (Figure 10). According to a previous DRM review [49], carbon formation occurs due to methane decomposition (MD) above 550 °C as well as the Boudouard (BD) reaction below 700 °C. Therefore, the reaction temperature in this study was set to 600 °C to study the coking behavior, which is one of the DRM main issues. Carbon deposition during DRM is known to cause catalyst deactivation and reactor plugging [53]. High WHSV (170 L/(g_{cat} × h)) was applied to clearly discriminate the coking resistance among the catalysts. Longer catalyst pre-reduction time (1.5 h) was applied in order to avoid the instant deactivation due to re-oxidation of Ni at a high flowrate of CO_2. The carbon amount found on spent Ni/Mg.Al.550 is higher than that of Ni/Mg.Al.1000 and

Ni/Al.550 (Figure 10). Those amounts appear to be proportional to the conversions in DRM (Figure 8). The addition of CA during the preparation significantly contributes to designing a coking resistant catalyst. Indeed, the carbon amount on Ni/Mg.Al.550.CA is almost 8 times lower than that on Ni/Mg.Al.550 at the same reaction conditions and with similar activity. After 8 h on stream, the carbon content is as low as 0.77 wt % of the sample mass, which is in the range of carbonaceous remainders from the hydrotalcite precursor after calcination. This indicates the high coking resistance of the sample, which is a remarkable result compared to previous research [17,54], especially considering the Ni, Al, and Mg containing catalyst systems.

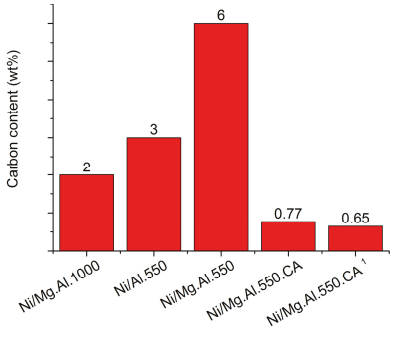

Figure 10. Carbon deposition on spent catalysts after DRM (600 °C, 1 bar, CH_4:CO_2 = 1, WHSV = 170 L/(g_{cat} × h), TOS = 8 h). All the catalysts were in situ pre-reduced for 1.5 h prior to the reaction. [1] Carbon deposition on spent Ni/Mg.Al.550.CA after long term DRM (T = 700 °C, p = 1 bar, CH_4:CO_2 = 1, WHSV = 170 L/(g_{cat} × h), TOS = 60 h).

Long-term DRM was also carried out with Ni/Mg.Al.550.CA (Figure 11). The reaction was implemented at a considerably high WHSV of 170 L/(g_{cat} × h) compared to the literature data [6]. The conversions of CH_4 and CO_2 are very close to the thermodynamic limitations for CH_4 (82%) and CO_2 (86%) [49]. The catalytic performance is almost unchanged after 60 h on-stream, representing high stability of the catalyst in the reaction. At any TOS, the CO_2 conversion is about 8% higher than the CH_4 conversion, illustrating the contribution of the RWGS reaction. The CO selectivity achieves a constant value around 100% (not shown) which is consistent with negligible carbon deposition (<1 wt %) measured after the reaction (Figure 10).

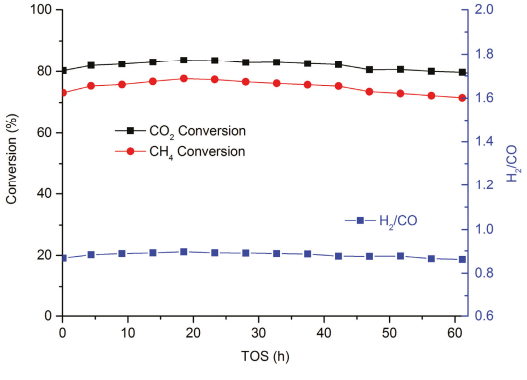

Figure 11. Catalytic performance of Ni/Mg.Al.550.CA in long-term DRM (T = 700 °C, p = 1 bar, CH_4:CO_2 = 1, WHSV = 170 L/(g_{cat} × h)).

3. Discussion

3.1. Activity of Mg.Al Supported Catalysts

Mg.Al supported catalysts show higher activity compared to single oxide supported samples. This is related mainly to their excellent reducibility and Ni enriched surface. This behavior has been also studied elsewhere [20,55], reporting that the coexistence of both Mg and Al in the supports reduces the formation of inactive species (NiO-MgO solid solution, $NiAl_2O_4$ spinel), stabilizes the Ni species on the surface, and subsequently enhances the DRM performance.

Ni/Mg.Al.550 is the most active catalyst for DRM among the studied samples because it possesses a high surface concentration of Ni in combination with the large surface of the support, forming species that are well reduced by H_2. Those active sites are proposed to be Ni^{2+} (O_h) in cooperation with the solid solution of MgO and Al_2O_3 (periclase structure) or surface $NiAl_2O_4$. Such phases are formed and stabilized at high calcination temperature (800 °C), but are still active at high WHSV and low temperature conditions even with low loading of Ni. The modification of such samples by using more severely calcined Mg.Al.1000 or adding CA during impregnation causes poorer reducibility and thus lower CH_4 and CO_2 conversions.

3.2. Coking Resistance and Stability of Mg.Al Supported Catalysts

It is well-known that coking during DRM is related to the large metal particles [4,56]. This is the result of the metal mobility on the surface and the subsequent agglomeration leading to less dispersed particles or clusters [49]. Ni/Mg.Al.550 presents the highest carbon deposition after 8 h on stream (Figure 10). However, the conversion is almost the same, the H_2/CO ratio is constant at 0.78, and the CO selectivity is almost 100% over the complete TOS. Therefore, such carbon deposition can be considered as negligible for catalyst performance. This high coking resistance can also be correlated to the low Ni content and high surface area of the support, by which both the metal and carbon species can be highly dispersed. Such dispersion results in less formation of big Ni particles and lower pore plugging by coke deposition, suppressing fast catalyst deactivation [53].

Ni/Mg.Al.550.CA shows the lowest carbon deposit amount after 8 h and even after 60 h, which is likely to be due to the stable dispersion of Ni species on the support surface. It was suggested above that the Ni/Mg.Al.550.CA sample has a stronger metal-support interaction and less NiO-like domains on the surface, contributing to a better coking resistance of the sample. This strong interaction also contributes to maintaining the catalyst performance in the long-term DRM experiment (Figure 11), by preventing Ni agglomeration and the loss of active sites.

There is another possible explanation for the coke resistance of Ni/Mg.Al.550.CA when comparing the Ni $3p_{3/2}$ BE in the XPS results. The BE values, which are recorded at 856.91 eV and 855.18 eV (Table 3, Figure 12), are assigned to the surface $NiAl_2O_4$ in the Ni/Mg.Al.550 sample and the Ni-Mg-O solid solution in Ni/Mg.Al.550.CA.

Additionally, the surface atom Mg/Al ratio of Ni/Mg.Al.550 (Table 3) exposes an excess amount of Al species on the surface, also suggesting surface $NiAl_2O_4$ formation in Ni/Mg.Al.550 [38]. In contrast, the surface Mg concentration is highest in Ni/Mg.Al.550.CA, revealing the possibility of preferable Ni-Mg interactions on the surface. Our current explanation is that most of the Ni species on the surface of Ni/Mg.Al.550.CA might interact with Mg in the support, providing an effective carbon gasification by CO_2 (reverse Boudouard reaction) and thus coke deposition is suppressed [20], especially at high reaction temperatures (Figure 10). Therefore, Ni/Mg.Al.500.CA may show two beneficial effects that help to suppress coking during DRM: one correlates with the stable physicochemical properties and the other associates with the carbon gasification behavior.

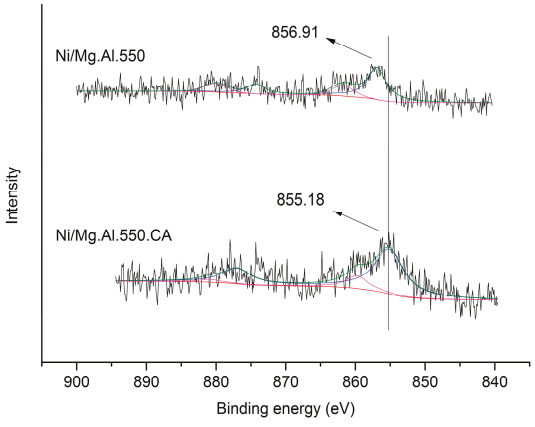

Figure 12. Ni $2p_{3/2}$ XPS spectra of Ni/Mg.Al.550 and Ni/Mg.Al.550.CA (coloured lines: deconvoluted signals; blue = Ni $2p_{3/2}$ and Ni $2p_{1/2}$, magenta = corresponding satellite signals, green = averaged raw data).

4. Materials and Methods

4.1. Catalyst Preparation

Mg-Al mixed oxide (calcined Mg-Al hydrotalcite, Pural MG, Sasol) supported Ni catalysts were prepared by wet impregnation. $Ni(NO_3)_2{\cdot}6H_2O$ (Carl Roth, Karlsruhe, Germany) was used as the precursor for Ni. The Mg-Al hydrotalcite precursor possesses an Mg/Al ratio = 1.3 (data from ICP-OES and AAS measurement). Prior to impregnation, the precursor samples were calcined at different temperatures (550 °C, 700 °C, 800 °C, 1000 °C) for 6 h in air to obtain the corresponding bare supports which are denoted as Mg.Al.X, in which X represents the support calcination temperature. The calculated amount of Ni precursor was dissolved in deionized water and the solution was stirred for 4 h. The supports were then put into the solution and the slurry was kept stirring at 60 °C for 15 h. Water was removed by a rotary evaporator and the samples were dried overnight and calcined at 400 °C for 3 h and then at 800 °C for 6 h, both in air. The final catalysts are symbolized as Ni/Mg.Al.X. Citric acid (CA) was added simultaneously to the Ni precursor solution in the case of Ni/Mg.Al.550.CA preparation to study the influence of the chelating agent on impregnation. The nominal content of Ni in all supported Ni-containing catalysts was 2.5 wt %. Other materials were used as reference materials; those are MgO (FLUKA) and Al_2O_3 (boehmite calcined at 550 °C, Pural SB, Sasol) as well as their corresponding 2.5 wt % Ni samples (Ni/MgO and Ni/Al.550). One Mg-Al hydrotalcite sample was calcined first at 550 °C for 6 h and then at 800 °C for 6 h to obtain a material that provides properties similar to the support of Ni/Mg.Al.550.CA and Ni/Mg.Al.550, because those catalysts were calcined at 800 °C. That material is denoted as Mg.Al.550.800. Pure NiO was prepared by calcining $Ni(NO_3)_2{\cdot}6H_2O$ (Alfa Aesar) at 800 °C.

4.2. Catalyst Characterization

The metal (Ni, Mg, Al) contents of the samples were determined by inductively coupled plasma-optical emission spectroscopy (ICP-OES) using a 715-ES device (Varian, Inc., Palo Alto, CA, USA) and atomic adsorption spectroscopy (AAS) using an Analyst 300 apparatus (PerkinElmer, Inc., Waltham, MA, USA), respectively. The carbon deposition on spent catalysts was analyzed using a Truespace CHNS analyzer (LECO Corporation, Saint Joseph, MI, USA). After the reaction, the reactor was cooled to room temperature under Ar flow. Then the spent catalysts were separated from the inert material by sieving and transferred to the CHNS device.

The nitrogen physisorption method was used to calculate the specific surface area and pore volume distribution according to the BET theory and BJH calculation, respectively. The measurements were performed on a Micromeritics ASAP 2010 apparatus (Micromeritics GmbH, Aachen, Germany) at −196 °C. The samples were degassed at 200 °C in vacuum for 4 h before the analysis.

The XRD powder patterns were recorded either on a Panalytical X'Pert diffractometer (Almelo, The Netherlands) equipped with a X'celerator detector or on a Panalytical Empyrean diffractometer (Almelo, The Netherlands) equipped with a PIXcel 3D detector system using Cu $K\alpha_1/\alpha_2$ radiation (40 kV, 40 mA) in both cases. Cu beta-radiation was excluded by using a nickel filter foil. The Cu K alpha2 radiation contribution was removed arithmetically using the Panalytical HighScore Plus software package (V. 3.0e, Panalytical, Almelo, The Netherlands). The peak positions and profile were fitted with the Pseudo-Voigt function using the WinXPow software package (V3.0.2, Stoe, Darmstadt, Germany). Phase identification was done by using the PDF-2 database of the International Center of Diffraction Data (ICDD).

XPS measurements were carried out with a VG ESCALAB 220iXL instrument (Thermo Fisher Scientific, Inc., Waltham, MA, USA) with monochromatic AlKα radiation (E = 1486.68 eV). The peak areas were determined after background subtraction and fitting with Gaussian-Lorentzian curves. The amount of each component in the near-surface region can be calculated based on these peak areas with division by the element-specific Scofield factor and the transmission function of the spectrometer.

For the H_2-TPR experiments, the measurement was done using a Autochem II 2920 instrument (Micromeritics, Aachen, Germany). A 300 mg sample was loaded into a U-shaped quartz reactor and heated from room temperature (RT) to 400 °C at 20 K/min in 5% O_2/He (50 mL/min) for 30 min at 400 °C, and was then cooled to RT and the sample was flushed with Ar. The TPR run was carried out from RT to 1000 °C in a 5% H_2/Ar flow (50 mL/min) with a heating rate of 10 K/min and was then held at the final temperature for 30 min before being cooled to RT. The hydrogen consumption peaks, indicating the reduction, were recorded using a TCD detector. The amount of hydrogen consumed was calculated based on the peak areas.

UV-Vis-DR spectra were measured over the wavelength range of 200–800 nm using a Cary 5000 spectrometer (Agilent Technologies, Petaling Jaya, Malaysia) equipped with a diffuse reflectance accessory (praying mantis, Harrick). In normal experiments, $BaSO_4$ is used as a reference white standard and dilute material for pure NiO measurement because of its high Ni content.

4.3. Catalytic Tests

DRM was carried out in a fixed bed continuous flow quartz reactor (ambient pressure, WHSV = 85 or 170 L/(g_{cat} × h); T = 500–700 °C). All volumetric flow rates given in this study are related to 25 °C and atmospheric pressure. After in situ pre-reduction in H_2 (700 °C, 100% H_2, 50 mL/min) for 1 h (used in the activity and stability tests) or 1.5 h (used for the coking test), the temperature was adjusted and maintained for 8 or 72 h and the reactant mixture (45 vol % CH_4, 45 vol % CO_2, 10 vol % He) was fed to the reactor. Helium was used as the internal standard for volume change estimation in the reaction. The gas compositions were then analyzed by an on-line Agilent 6890 gas chromatograph (Agilent Technologies, Santa Clara, CA, USA) equipped with a flame ionization detector (HP Plot Q capillary, 15 m × 0.53 mm × 40 μm) and a thermal conductivity detector (Carboxene packed, 4.572 m × 3.175 mm) for the analysis of hydrocarbons and permanent gases, respectively. Pure components were used as references for peak identification and calibration. Carbon balances were calculated from the gas products reaching more than 95% in this work. Conversions (X) and the H_2/CO ratio were calculated using the formulas given below:

$$X_{CH_4}\ (\%) = \frac{\text{moles of converted } CH_4 \times 100\%}{\text{moles of } CH_4 \text{ in feed}} \quad (4)$$

$$X_{CO_2}\ (\%) = \frac{\text{moles of } CO_2 \text{ converted} \times 100\%}{\text{moles of } CO_2 \text{ in feed}} \quad (5)$$

$$H_2/CO\ \text{ratio} = \frac{\text{moles of } H_2 \text{ produced}}{\text{moles of CO produced}} \quad (6)$$

Acknowledgments: The authors gratefully acknowledge financial support from the German Academic Exchange Service (DAAD). We want to thank R. Eckelt, A. Simmula, and A. Lehmann (LIKAT) for their analytical support.

Author Contributions: Q.L.M.H., A.M., and U.A. conceived and designed the experiments; Q.L.M.H. performed the experiments and analyzed the data; H.A. performed the TPR measurements; H.L. and M.S. performed the XRD measurements; G.A. and J.R. performed the XPS measurements; H.T.V. analyzed the UV-Vis-DRS data; Q.L.M.H. and U.A. wrote the paper.

Conflicts of Interest: The authors declare no conflict of interest.

References

1. Havran, V.; Duduković, M.P.; Lo, C.S. Conversion of Methane and Carbon Dioxide to Higher Value Products. *Ind. Eng. Chem. Res.* **2011**, *50*, 7089–7100. [CrossRef]
2. Rostrupnielsen, J.R.; Hansen, J.H.B. CO_2-Reforming of Methane over Transition Metals. *J. Catal.* **1993**, *144*, 38–49. [CrossRef]
3. Fan, M.-S.; Abdullah, A.Z.; Bhatia, S. Catalytic Technology for Carbon Dioxide Reforming of Methane to Synthesis Gas. *Chemcatchem* **2009**, *1*, 192–208. [CrossRef]
4. Bradford, M.C.J.; Vannice, M.A. CO_2 Reforming of CH_4. *Catal. Rev.* **1999**, *41*, 1–42. [CrossRef]
5. Wurzel, T.; Malcus, S.; Mleczko, L. Reaction engineering investigations of CO_2 reforming in a fluidized-bed reactor. *Chem. Eng. Sci.* **2000**, *55*, 3955–3966. [CrossRef]
6. Oyama, S.T.; Hacarlioglu, P.; Gu, Y.; Lee, D. Dry reforming of methane has no future for hydrogen production: Comparison with steam reforming at high pressure in standard and membrane reactors. *Int. J. Hydrog. Energy* **2012**, *37*, 10444–10450. [CrossRef]
7. Albarazi, A.; Gálvez, M.E.; Da Costa, P. Synthesis strategies of ceria–zirconia doped Ni/SBA-15 catalysts for methane dry reforming. *Catal. Commun.* **2015**, *59*, 108–112. [CrossRef]
8. Usman, M.; Wan Daud, W.M.A.; Abbas, H.F. Dry reforming of methane: Influence of process parameters—A review. *Renew. Sustain. Energy Rev.* **2015**, *45*, 710–744. [CrossRef]
9. Paksoy, A.I.; Caglayan, B.S.; Aksoylu, A.E. A study on characterization and methane dry reforming performance of Co–Ce/ZrO_2 catalyst. *Appl. Catal. B Environ.* **2015**, *168–169*, 164–174. [CrossRef]
10. Yu, M.; Zhu, Y.-A.; Lu, Y.; Tong, G.; Zhu, K.; Zhou, X. The promoting role of Ag in Ni-CeO_2 catalyzed CH_4-CO_2 dry reforming reaction. *Appl. Catal. B Environ.* **2015**, *165*, 43–56. [CrossRef]
11. Ma, J.; Sun, N.; Zhang, X.; Zhao, N.; Xiao, F.; Wei, W.; Sun, Y. A short review of catalysis for CO_2 conversion. *Catal. Today* **2009**, *148*, 221–231. [CrossRef]
12. Liu, C.-J.; Ye, J.; Jiang, J.; Pan, Y. Progresses in the Preparation of Coke Resistant Ni-based Catalyst for Steam and CO_2 Reforming of Methane. *ChemCatChem* **2011**, *3*, 529–541. [CrossRef]
13. Gao, J.; Hou, Z.; Lou, H.; Zheng, X. Chapter 7—Dry (CO_2) Reforming. In *Fuel Cells: Technologies for Fuel Processing*; Elsevier: Amsterdam, The Netherlands, 2011; pp. 191–221.
14. Edwards, J.H.; Maitra, A.M. The chemistry of methane reforming with carbon dioxide and its current and potential applications. *Fuel Process. Technol.* **1995**, *42*, 269–289. [CrossRef]
15. Tang, S.B.; Qiu, F.L.; Lu, S.J. Effect of supports on the carbon deposition of nickel catalysts for methane reforming with CO_2. *Catal. Today* **1995**, *24*, 253–255. [CrossRef]
16. Roh, H.-S.; Jun, K.-W. Carbon Dioxide Reforming of Methane over Ni Catalysts Supported on Al_2O_3 Modified with La_2O_3, MgO, and CaO. *Catal. Surv. Asia* **2008**, *12*, 239–252. [CrossRef]
17. Guo, J.; Lou, H.; Zhao, H.; Chai, D.; Zheng, X. Dry reforming of methane over nickel catalysts supported on magnesium aluminate spinels. *Appl. Catal. A Gen.* **2004**, *273*, 75–82. [CrossRef]
18. Habibi, N.; Arandiyan, H.; Rezaei, M. Mesoporous MgO·Al_2O_3 nanopowder-supported meso-macroporous nickel catalysts: A new path to high-performance biogas reforming for syngas. *RSC Adv.* **2016**, *6*, 29576–29585. [CrossRef]

19. Abdollahifar, M.; Haghighi, M.; Babaluo, A.A.; Talkhoncheh, S.K. Sono-synthesis and characterization of bimetallic Ni–Co/Al_2O_3–MgO nanocatalyst: Effects of metal content on catalytic properties and activity for hydrogen production via CO_2 reforming of CH_4. *Ultrason. Sonochem.* **2016**, *31*, 173–183. [CrossRef] [PubMed]
20. García-Diéguez, M.; Herrera, C.; Larrubia, M.Á.; Alemany, L.J. CO_2-reforming of natural gas components over a highly stable and selective NiMg/Al_2O_3 nanocatalyst. *Catal. Today* **2012**, *197*, 50–57. [CrossRef]
21. Zhang, J.; Wang, H.; Dalai, A.K. Effects of metal content on activity and stability of Ni-Co bimetallic catalysts for CO_2 reforming of CH_4. *Appl. Catal. A Gen.* **2008**, *339*, 121–129. [CrossRef]
22. Kim, J.-H.; Suh, D.J.; Park, T.-J.; Kim, K.-L. Effect of metal particle size on coking during CO_2 reforming of CH_4 over Ni–alumina aerogel catalysts. *Appl. Catal. A Gen.* **2000**, *197*, 191–200. [CrossRef]
23. Suárez-Toriello, V.A.; Santolalla-Vargas, C.E.; de los Reyes, J.A.; Vázquez-Zavala, A.; Vrinat, M.; Geantet, C. Influence of the solution pH in impregnation with citric acid and activity of Ni/W/Al_2O_3 catalysts. *J. Mol. Catal. Chem.* **2015**, *404–405*, 36–46. [CrossRef]
24. Van Dillen, A.J.; Terörde, R.J.A.M.; Lensveld, D.J.; Geus, J.W.; de Jong, K.P. Synthesis of supported catalysts by impregnation and drying using aqueous chelated metal complexes. *J. Catal.* **2003**, *216*, 257–264. [CrossRef]
25. Prescott, H.A.; Li, Z.-J.; Kemnitz, E.; Trunschke, A.; Deutsch, J.; Lieske, H.; Auroux, A. Application of calcined Mg-Al hydrotalcites for Michael additions: An investigation of catalytic activity and acid-base properties. *J. Catal.* **2005**, *234*, 119–130. [CrossRef]
26. Ono, Y.; Hattori, H. Preparation and Catalytic Properties of Solid Base Catalysts—II. Specific Materials for Solid Bases. In *Solid Base Catalysis*; Springer: Berlin/Heidelberg, Germany, 2011; pp. 157–218.
27. Kumar, P.A.; Reddy, M.P.; Hyun-Sook, B.; Phil, H.H. Influence of Mg Addition on the Catalytic Activity of Alumina Supported Ag for C_3H_6-SCR of NO. *Catal. Lett.* **2009**, *131*, 85–97. [CrossRef]
28. Stanimirova, T.; Vergilov, I.; Kirov, G.; Petrova, N. Thermal decomposition products of hydrotalcite-like compounds: Low-temperature metaphases. *J. Mater. Sci.* **1999**, *34*, 4153–4161. [CrossRef]
29. Takehira, K.; Kawabata, T.; Shishido, T.; Murakami, K.; Ohi, T.; Shoro, D.; Honda, M.; Takaki, K. Mechanism of reconstitution of hydrotalcite leading to eggshell-type Ni loading on MgAl mixed oxide. *J. Catal.* **2005**, *231*, 92–104. [CrossRef]
30. Escobar, J.; De Los Reyes, J.A.; Viveros, T. Nickel on TiO_2-modified Al_2O_3 sol–gel oxides: Effect of synthesis parameters on the supported phase properties. *Appl. Catal. A Gen.* **2003**, *253*, 151–163. [CrossRef]
31. Damyanova, S.; Pawelec, B.; Arishtirova, K.; Fierro, J.L.G. Ni-based catalysts for reforming of methane with CO_2. *Int. J. Hydrog. Energy* **2012**, *37*, 15966–15975. [CrossRef]
32. Jafarbegloo, M.; Tarlani, A.; Mesbah, A.W.; Muzart, J.; Sahebdelfar, S. NiO–MgO Solid Solution Prepared by Sol–Gel Method as Precursor for Ni/MgO Methane Dry Reforming Catalyst: Effect of Calcination Temperature on Catalytic Performance. *Catal. Lett.* **2016**, *146*, 238–248. [CrossRef]
33. Li, C.; Chen, Y.-W. Temperature-programmed-reduction studies of nickel oxide/alumina catalysts: Effects of the preparation method. *Thermochim. Acta* **1995**, *256*, 457–465. [CrossRef]
34. Rogers, J.L.; Mangarella, M.C.; D'Amico, A.D.; Gallagher, J.R.; Dutzer, M.R.; Stavitski, E.; Miller, J.T.; Sievers, C. Differences in the Nature of Active Sites for Methane Dry Reforming and Methane Steam Reforming over Nickel Aluminate Catalysts. *ACS Catal.* **2016**, *6*, 5873–5886. [CrossRef]
35. Lucrédio, A.F.; Bellido, J.D.A.; Assaf, E.M. Effects of adding La and Ce to hydrotalcite-type Ni/Mg/Al catalyst precursors on ethanol steam reforming reactions. *Appl. Catal. A Gen.* **2010**, *388*, 77–85. [CrossRef]
36. Jiang, Z.; Su, J.; Jones, M.O.; Shi, H.; Xiao, T.; Edwards, P.P. Catalytic Partial Oxidation of Methane over Ni-Based Catalysts Derived from Ni-Mg/Al Ternary Hydrotalcites. *Energy Fuels* **2009**, *23*, 1634–1639. [CrossRef]
37. Sánchez-Sánchez, M.C.; Navarro, R.M.; Fierro, J.L.G. Ethanol steam reforming over Ni/M_xO_y-Al_2O_3 (M = Ce, La, Zr and Mg) catalysts: Influence of support on the hydrogen production. *Int. J. Hydrog. Energy* **2007**, *32*, 1462–1471. [CrossRef]
38. Özdemir, H.; Öksüzömer, M.A.F.; Gürkaynak, M.A. Effect of the calcination temperature on Ni/$MgAl_2O_4$ catalyst structure and catalytic properties for partial oxidation of methane. *Fuel* **2014**, *116*, 63–70. [CrossRef]
39. NIST X-ray Photoelectron Spectroscopy Database: Version 3.4 (Web Version). Available online: http://srdata.nist.gov/xps/ (accessed on 6 February 2017).

40. Cimino, A.; Gazzoli, D.; Indovina, V.; Moretti, G.; Occhiuzzi, M.; Pepe, F. High and low surface area NiO–MgO and CoO–MgO solid solutions: A study of XPS surface composition and CO oxidation activity. *Top. Catal.* **1999**, *8*, 171–178. [CrossRef]
41. Ruckenstein, E.; Hu, Y.H. Methane partial oxidation over NiO/MgO solid solution catalysts. *Appl. Catal. A Gen.* **1999**, *183*, 85–92. [CrossRef]
42. Scheffer, B.; Heijeinga, J.J.; Moulijn, J.A. An electron spectroscopy and X-ray diffraction study of nickel oxide/alumina and nickel-oxide-tungsten trioxide/alumina catalysts. *J. Phys. Chem.* **1987**, *91*, 4752–4759. [CrossRef]
43. Boukha, Z.; Jiménez-González, C.; de Rivas, B.; González-Velasco, J.R.; Gutiérrez-Ortiz, J.I.; López-Fonseca, R. Synthesis, characterisation and performance evaluation of spinel-derived Ni/Al_2O_3 catalysts for various methane reforming reactions. *Appl. Catal. B Environ.* **2014**, *158–159*, 190–201. [CrossRef]
44. Heracleous, E.; Lee, A.F.; Wilson, K.; Lemonidou, A.A. Investigation of Ni-based alumina-supported catalysts for the oxidative dehydrogenation of ethane to ethylene: Structural characterization and reactivity studies. *J. Catal.* **2005**, *231*, 159–171. [CrossRef]
45. Jiménez-González, C.; Boukha, Z.; de Rivas, B.; González-Velasco, J.R.; Gutiérrez-Ortiz, J.I.; López-Fonseca, R. Behavior of Coprecipitated $NiAl_2O_4$/Al_2O_3 Catalysts for Low-Temperature Methane Steam Reforming. *Energy Fuels* **2014**, *28*, 7109–7121. [CrossRef]
46. Skoufa, Z.; Xantri, G.; Heracleous, E.; Lemonidou, A.A. A study of Ni–Al–O mixed oxides as catalysts for the oxidative conversion of ethane to ethylene. *Appl. Catal. A Gen.* **2014**, *471*, 107–117. [CrossRef]
47. Zecchina, A.; Spoto, G.; Coluccia, S.; Guglielminotti, E. Spectroscopic study of the adsorption of carbon monoxide on solid solutions of nickel oxide and magnesium oxide. Part 1—Standard samples. *J. Chem. Soc. Faraday Trans.* **1984**, *80*, 1875–1889. [CrossRef]
48. Lucrédio, A.F.; Jerkiewickz, G.; Assaf, E.M. Nickel catalysts promoted with cerium and lanthanum to reduce carbon formation in partial oxidation of methane reactions. *Appl. Catal. A Gen.* **2007**, *333*, 90–95. [CrossRef]
49. Pakhare, D.; Spivey, J. A review of dry (CO_2) reforming of methane over noble metal catalysts. *Chem. Soc. Rev.* **2014**, *43*, 7813–7837. [CrossRef] [PubMed]
50. Elsayed, N.H.; Roberts, N.R.M.; Joseph, B.; Kuhn, J.N. Low temperature dry reforming of methane over Pt–Ni–Mg/ceria–zirconia catalysts. *Appl. Catal. B Environ.* **2015**, *179*, 213–219. [CrossRef]
51. Sokolov, S.; Kondratenko, E.V.; Pohl, M.-M.; Barkschat, A.; Rodemerck, U. Stable low-temperature dry reforming of methane over mesoporous La_2O_3-ZrO_2 supported Ni catalyst. *Appl. Catal. B Environ.* **2012**, *113–114*, 19–30. [CrossRef]
52. Lavoie, J.-M. Review on dry reforming of methane, a potentially more environmentally-friendly approach to the increasing natural gas exploitation. *Front. Chem.* **2014**, *2*, 81. [CrossRef] [PubMed]
53. Newson, E. Catalyst Deactivation Due to Pore-Plugging by Reaction Products. *Ind. Eng. Chem. Proc. Des. Dev.* **1975**, *14*, 27–33. [CrossRef]
54. Muraza, O.; Galadima, A. A review on coke management during dry reforming of methane. *Int. J. Energy Res.* **2015**, *39*, 1196–1216. [CrossRef]
55. Alipour, Z.; Rezaei, M.; Meshkani, F. Effect of alkaline earth promoters (MgO, CaO, and BaO) on the activity and coke formation of Ni catalysts supported on nanocrystalline Al_2O_3 in dry reforming of methane. *J. Korean Ind. Eng. Chem.* **2014**, *20*, 2858–2863. [CrossRef]
56. York, A.P.E.; Xiao, T.-C.; Green, M.L.H.; Claridge, J.B. Methane Oxyforming for Synthesis Gas Production. *Catal. Rev.* **2007**, *49*, 511–560. [CrossRef]

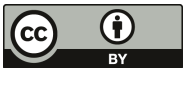

catalysts

MDPI

Article

Methanation of CO_2 on Ni/Al_2O_3 in a Structured Fixed-Bed Reactor—A Scale-Up Study

Daniel Türks, Hesham Mena, Udo Armbruster * and Andreas Martin

Leibniz-Institut für Katalyse e.V., Albert-Einstein-Str. 29a, 18059 Rostock, Germany;
daniel.tuerks@catalysis.de (D.T.); hesham.mena@catalysis.de (H.M.); andreas.martin@catalysis.de (A.M.)
* Correspondence: udo.armbruster@catalysis.de; Tel.: +49-381-1281-257

Academic Editor: Morris D. Argyle
Received: 31 March 2017; Accepted: 4 May 2017; Published: 15 May 2017

Abstract: Due to the ongoing change of energy supply, the availability of a reliable high-capacity storage technology becomes increasingly important. While conventional large-scale facilities are either limited in capacity respective supply time or their extension potential is little (e.g., pumped storage power stations), decentralized units could contribute to energy transition. The concepts of PtX (power-to-X) storage technologies and in particular PtG (power-to-gas) aim at fixation of electric power in chemical compounds. CO_2 hydrogenation (methanation) is the foundation of the PtG idea as H_2 (via electrolysis) and CO_2 are easily accessible. Methane produced in this way, often called substitute natural gas (SNG), is a promising solution since it can be stored in the existing gas grid, tanks or underground cavern storages. Methanation is characterized by a strong exothermic heat of reaction which has to be handled safely. This work aims at getting rid of extreme temperature hot-spots in a tube reactor by configuring the catalyst bed structure. Proof of concept studies began with a small tube reactor (V = 12.5 cm^3) with a commercial 18 wt % Ni/Al_2O_3 catalyst. Later, a double-jacket tube reactor was built (V = 452 cm^3), reaching a production rate of 50 L/h SNG. The proposed approach not only improves the heat management and process safety, but also increases the specific productivity and stability of the catalyst remarkably.

Keywords: methanation; PtG; SNG; Ni/Al_2O_3

1. Introduction

Growing energy consumption and the political target to reduce total CO_2 emissions led to a boom of plant construction for alternative power production. Further, recently in Germany, safety issues played a big a role when the abolishment of nuclear power plants was forced by politics considering past accidents and missing storage options for nuclear waste [1]. In total, 13,147.3 million tons of oil equivalent primary energy was consumed worldwide in 2015, which was mainly covered by fossil energy sources, i.e., oil, natural gas and coal (86.0%). Continental Europe consumed 2834.4 million tons of oil equivalents with a share of 78.8% fossil fuels, wherein Germany used 320.6 million tons of oil equivalents (82.3% fossil fuels). In comparison to 2014, the growth in Germany was +8.7 million tons oil equivalents, mainly covered by renewable energy sources (i.e., wind, geothermal, solar, biomass and waste) [2]. Preferably wind and sun are exploited to get alternatives to energy generation from fossil sources: 26,000 wind power plants generating approximately 45 GW electrical power (GW_{el}) and 1.5 million photovoltaic power plants with a capacity of 40 GW_{el} were installed in Germany by the end of 2015. In 2016, regenerative energy contributed 30% to the total generated electrical power and is planned to reach 40–45% in 2025 [3]. However, this part of the energy sector is subjected to temporal fluctuation due to weather conditions causing shortage or surplus in energy supply. Very often wind turbines have to be switched off not to overstress the power grid. Consequently, the effective storage of electric power is one of the emerging tasks in future energy supply, not only to get rid of a growing

dependency on energy imports, but also to support the change in energy supply [4]. Among other storage opportunities [5], an often discussed option for excess electrical energy from renewable sources is the generation of hydrogen by water electrolysis and its temporal storage in available infrastructures such as the gas grid, underground caverns or high pressure and liquid hydrogen tanks. The problem here is that only low amounts in single-digit percentage range are accepted in gas grid or caverns [6], and expansion of the hydrogen infrastructure needs exorbitant investments. One solution is the chemical conversion of such "green" hydrogen and easily available carbon dioxide into methane (SNG) [7,8].

$$CO + 3\,H_2 \rightleftharpoons CH_4 + H_2O \quad \Delta H_R = -206.3\ \text{kJ/mol} \tag{1}$$

$$CO_2 + 4\,H_2 \rightleftharpoons CH_4 + 2\,H_2O \quad \Delta H_R = -165.1\ \text{kJ/mol} \tag{2}$$

$$CO_2 + H_2 \rightleftharpoons CO + H_2O \quad \Delta H_R = +41.2\ \text{kJ/mol} \tag{3}$$

The long-known methanation Reactions (1) and (2) are used industrially for cleaning of hydrogen from steam reformers in the presence of hydrogenation catalysts to remove CO and CO_2 traces [9,10]. The reactions are highly exothermic and controlled by chemical equilibrium, and due to high activation energy the process is run at 250–400 °C mainly over Ni-containing catalysts. It benefits from increasing pressure and is very selective towards SNG. At higher temperature, other reactions such as reversed water-gas shift Reaction (3) affect the methane yield. There are two mechanisms under discussion: (i) the direct hydrogenation of CO_2 to methane; and (ii) the conversion of CO_2 to CO (reverse water-gas shift reaction) followed by CO methanation. CO forms adsorbed carbon species on the catalyst surface, which are subsequently hydrogenated to methane by surface hydrogen [11,12]. In other words, the methanation mechanism might be characterized by carbon formation and carbon methanation. Additionally, adsorbed CO may react at low temperatures to hydrocarbons via the Fischer–Tropsch reaction (conversion of CO and H_2) [13]. Ethane might also be formed at higher temperatures but it is easily converted to methane in surplus of hydrogen by hydrogenolysis [14].

Biomass, a further brick in the road to energy supply change, can be fermented to biogas which in dependency on the feed contains 40 vol %–75 vol % methane and 25 vol %–55 vol % CO_2; in addition, some impurities such as hydrogen, hydrogen sulfide, nitrogen, ammonia and water vapor are present [15]. World biogas production has rapidly increased in recent years. More than 17,000 biogas plants (>8.3 GW_{el} capacity) existed in Europe by the end of 2014. Germany is Europe's biggest biogas producer and world leader in biogas technology. Roughly 11,000 plants (in 2015) are generating more than 4 GW of power with an annual turnover of 9.2 billion € [16,17]. The downstream methanation of the CO_2 fraction would increase the productivity and earnings of a biogas plant. This would require catalysts that are also robust against named impurities.

Catalytic activities of metals for CO_2 methanation follow the order Ru > Ni > Co > Fe > Mo [18], and noble metal proportions might increase the productivity. An overview on applied catalyst systems is given in [19]. Considering the high costs of Ru, nickel on a suitable support is a cheap and active alternative. Suitable supports have been compared, resulting in the efficiency order CeO_2 > Al_2O_3 > TiO_2 > MgO [20].

Car manufacturer Audi's PTG facility in Werlte (Lower-Saxony, Germany) [21], online since 2013, is fed by a biogas plant; it produces 1.5 million Nm^3/a SNG (6 MW_{el} plant). Clariant has supplied the methanation catalyst [22]. In 2015, the world's largest SNG plant went on-stream (1.4 billion Nm^3/a) in Yining, China with catalysts and process technology from Haldor Topsøe [23]. More descriptions of pilot plants and commercial scale projects can be found in [24].

The high exothermicity of −206.3 kJ/mol is not a problem when only traces of carbon dioxide are converted (for example, gas purification for ammonia production), but in case of selective SNG synthesis at large scale, limited heat transfer causes hot-spots, stressing the construction materials and catalysts, and thermal runaway of the reactor could become the final consequence. Apart from this, the chemical equilibrium shifts away from optimum conditions. Published results from the conversion of a $CO/CO_2/H_2$ stream stemming from biomass gasification showed a hot-spot temperature of 460 °C

and a gas outlet temperature of 270 °C [25]. To get rid of this unwanted effect, reactor concepts such as cascades of fixed bed reactors with limited conversion, wall-cooled fixed bed reactors, fluidized bed reactors or slurry bubble reactors are used or currently investigated [26,27]. These reactor set ups are mainly assisted by internal heat exchange or by diluting the gas inlet with cooled recycle gas and/or water so that combined with high pressure the methane yield can be maximized. An alternative concept with effective removal of the generated heat of reaction uses microchannel reactors, as they offer advantageous surface/volume ratio [28]. Published research results from other groups on structured fixed-bed reactors are not known. The aim of the presented work was to collect data on the heat distribution along various catalyst bed arrangements in a tube reactor at maximum SNG productivity for further scale-up, while also considering catalyst stability.

2. Results and Discussion

2.1. Catalytic Test Runs

Past studies in our group on methanation over monometallic Ni, Ru and bimetallic NiRu catalysts in a bench-scale reactor with low catalyst amount and diluted feed (50 vol % N_2) revealed that the best results with respect to CO_2 conversion and methane selectivity were obtained at 10 bar and 325–350 °C [29,30]. In particular, increased reaction pressure is beneficial to suppress CO and ethane formation. Observed CO_2 conversion always was close to the thermodynamic equilibrium and methane selectivity was above 99.9%. Some ethane formation (<<1%) was detected below 325 °C set point temperature. Table 1 gives an overview on related runs with 5 wt % Ni/ZrO_2 catalyst at 1 and 10 bar gauge pressure.

Table 1. Carbon dioxide conversion and methane selectivity at 300–400 °C at different reaction pressure (1 mL 5 wt % Ni/ZrO_2 + 4 mL quartz diluent, GHSV = 6000 h^{-1}, CO_2:H_2:N_2 = 1:4:5).

Temperature (°C)	X_{eq} (CO_2) (%)	$X_{1\ bar}$ (CO_2) (%)	$X_{10\ bar}$ (CO_2) (%)	$S_{1\ bar}$ (CH_4) (%)	$S_{10\ bar}$ (CH_4) (%)
300	98.5	19.5	96.7	99.0	99.8
325	97.7	38.5	96.8	99.5	99.9
350	96.5	54.3	95.9	99.6	100
375	95.5	66.0	94.6	99.2	99.9
400	94.0	71.1	93.2	98.9	99.9

Later runs with the same bench-scale reactor aiming at increased methane productivity through setting a higher GHSV, lower inert gas dilution and/or larger catalyst volume gave first data on hot-spot formation at the entrance of the catalyst bed [31]. Since knowledge about hot-spot size and position at high catalyst load is needed for upscaling experiments, runs on diluting and stacking various catalyst/quartz beds were made at increased space velocity and decreased inert gas dilution (from 50 vol % to 10 vol % N_2). Therefore, an industrial catalyst containing 18 wt % of Ni supported on Al_2O_3 was selected for upscaling with a larger reactor. This catalyst proved to ignite already around 250 °C (Figure 1).

2.2. Temperature Profiles in the Small Tube Reactor

A scheme of the small bench-scale reactor is depicted in Figure 1. Conventionally, the catalyst bed was fixed in the vertical center of the tube while quartz sand layers were filled at the top and bottom of the reactor with quartz wool as separator. Temperature profile was recorded with a thermocouple which was vertically movable along the reactor through a centered guiding tube. The length scale shown in Figure 1 serves as a reference for the following figures visualizing results obtained with this reactor.

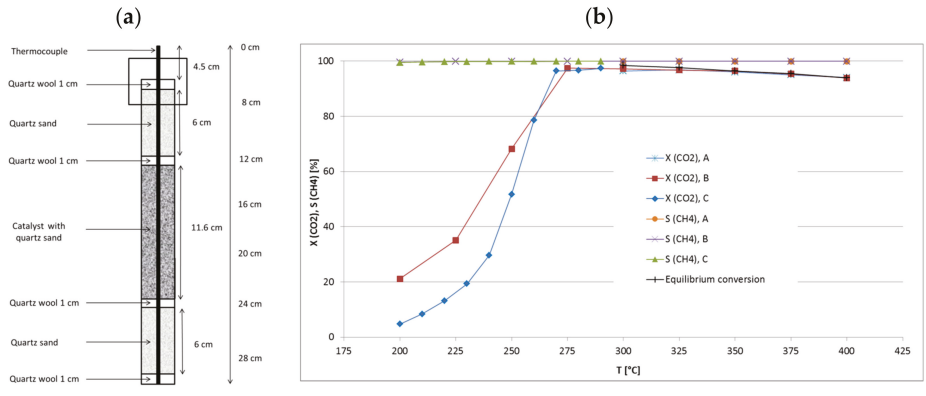

Figure 1. (**a**) Scheme of the bench-scale reactor with catalyst bed (18Ni/Al_2O_3) and quartz fillings. (**b**) CO_2 conversion and CH_4 selectivity in runs with different catalyst loadings (run A: 1 mL of catalyst; run B: 2.5 mL of catalyst; run C: 4 mL of catalyst) in dependence on temperature.

At the beginning, three runs A–C with different catalyst amount were made at a GHSV of approximately 6000 h^{-1} (related to catalyst volume, particle size 500–800 µm) with variation of feed flow rate, aiming at higher CO_2 conversion and methane productivity. The total bed volume (catalyst + quartz) was kept constant at 5 mL while the catalyst/quartz ratio was changed (bed position from 12 to 24 cm). Run A was made with 1 mL of catalyst and 4 mL of quartz, run B with 2.5 mL of catalyst and quartz each, and run C with 4 mL of catalyst and 1 mL of quartz diluent. The feed flow rate was set accordingly: run A 6 L/h, run B 15 L/h and run C 26.4 L/h (GHSV = 6588 h^{-1}) [31]. CO_2 conversion was always near the equilibrium with maxima at the set point temperatures of 325 °C for run A, 300 °C for run B and 290 °C for run C. Because of the increasing catalyst load and methane production from run A to C, the corresponding hot-spot temperatures reached 325 °C, 336 °C and 358 °C, respectively. Decreased CO_2 conversion was observed in runs A and B at higher set point temperatures due to thermodynamic limitation. Data from run C were only collected up to 290 °C because the high absolute methane production raised the hot-spot temperature by >70 K. The selectivity to CH_4 always reached values above 99.9%. Table 2 summarizes these data. It is noteworthy that run C at 290 °C reached higher conversion (97.4%) than run A at 350 °C (96.1%), even though the internal bed temperatures were comparable (358 °C vs. 351 °C). This might be explained by the significantly lower temperature at the bottom of the catalyst bed in run C (Figure 2), which favors methanation over RWGS reaction.

Table 2. Carbon dioxide conversion and methane selectivity during runs with decreasing catalyst dilution (18Ni/Al_2O_3; GHSV ≅ 6000 h^{-1}; CO_2:H_2:N_2 = 1.8:7.2:1; run A: catalyst:quartz = 1:4, feed = 6 L/h; run B: catalyst:quartz = 1:1, feed = 15 L/h; run C: catalyst:quartz = 4:1, feed = 26.4 L/h).

Set Point Temperature	X_{CO2} (%)			S_{CH4} (%)			Hot Spot (K) [1]		
(°C)	A	B	C	A	B	C	A	B	C
270	-	-	96.5	-	-	99.9	-	-	64
280	-	-	96.7	-	-	99.9	-	-	67
290	-	-	97.4	-	-	99.9	-	-	68
300	96.5	97.3	-	99.9	99.9	-	-	36	-
325	96.9	96.8	-	99.9	99.9	-	-	36	-
350	96.1	96.5	-	99.9	99.9	-	1	34	-
375	95.1	95.4	-	99.9	99.9	-	3	31	-

[1] difference between set point and measured reaction temperatures.

By increasing the catalyst amount at constant space velocity, the CH_4 productivity grew from 1.1 L/h (run A) and 2.6 L/h (run B) to 4.6 L/h (run C), and significantly elevated hot-spot temperatures were measured. Since the reaction temperatures were similar in the hot-spot zones, the CO_2 conversions were similar though set point temperatures differed markedly. Then the methane productivity seems to be proportional to the catalyst amount. The recorded temperature profiles (Figure 2) reveal that hot-spot zones are located at the very top of the catalyst bed and very narrow (3 cm). Largest part of the catalyst bed seems not to take part in methanation. With these results in mind, a raised productivity should be expected at more equal temperature distribution over the whole catalyst bed when appropriate catalyst dilution and increased space velocity are combined.

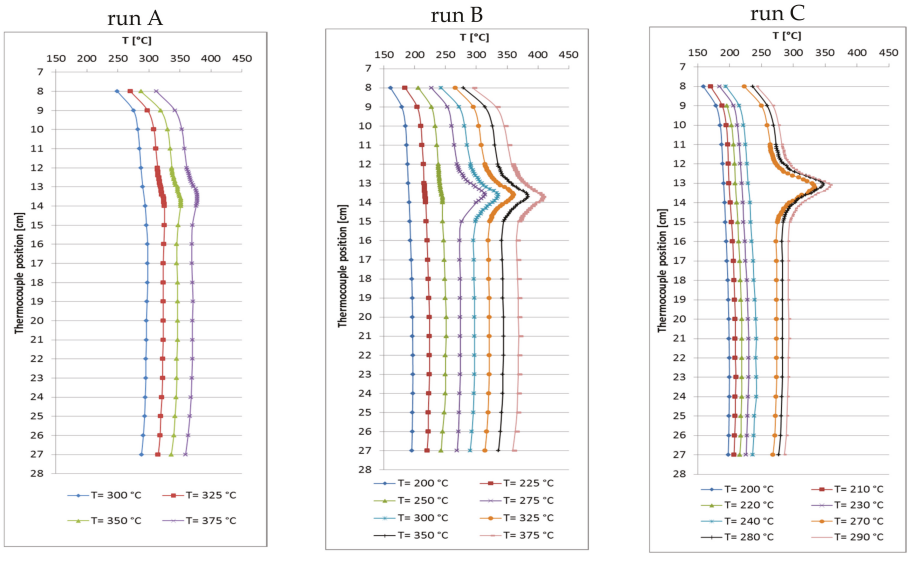

Figure 2. Recorded temperature profiles for methanation on $18Ni/Al_2O_3$. Run A: 1 mL catalyst + 4 mL quartz; run B: 2.5 mL catalyst + 2.5 mL quartz; run C: 4 mL catalyst + 1 mL quartz (GHSV ≅ 6000 h^{-1}; CO_2:H_2:N_2 = 1.8:7.2:1; 10 bar).

Thus, another run D with increased catalyst dilution (catalyst:quartz = 1:9, 0.5 mL catalyst) at an increased GHSV of 12,000 h^{-1} was performed. The carbon dioxide conversion as well as the methane selectivity were almost the same, but reached their maxima at 350 °C (X_{CO2} = 96.6% and S_{CH4} = 99.9%, Table 3) with a methane productivity of almost 1.1 L/h.

The corresponding temperature profile (Figure 3) shows that no notable hot-spot appeared due to high dilution and flow rate. This illustrates the beneficial effect of improved temperature control on the chemical equilibrium.

Based on the results of these preliminary runs, instead of one catalyst bed with constant dilution, three beds of 1.7 mL each (5 mL in total) were used, varying the catalyst:quartz ratio from top to bottom from 1:4 and 1:1 to 4:1 (Figure 4). In total, the catalyst:quartz ratio of 1:1 (as in run B) was kept. Run E was carried out at 6000 h^{-1} and 13.5 L/h feed gas (CO_2:H_2:N_2 = 1.8:7.2:1). CO_2 conversion of 97.5% close to equilibrium was reached at 310 °C set point temperature. The hot spot temperature in the beds reached 325 °C, 327 °C and 317 °C (from top to bottom). The methane productivity reached 2.4 L/h (similar to run B), but the temperature profile changed dramatically and overall reaction temperature decreased significantly, making this configuration most preferable.

Table 3. CO_2 conversion and methane selectivity on $18Ni/Al_2O_3$ in the bench-scale reactor with single bed (run D: catalyst:quartz = 1:9; total 5 mL; GHSV = 12,000 h^{-1}) and triple-bed configuration (run E: catalyst:quartz = 1:4, 1:1, 4:1, total 5 mL; GHSV = 6000 h^{-1}); CO_2:H_2:N_2 = 1.8:7.2:1; 10 bar.

Temperature	X_{CO2} (%)		S_{CH4} (%)		Hot Spot (K) [1]	
(°C)	D	E	D	E	D	E
250	-	72.6	-	99.9	-	16
260	43.6	90.9	99.9	99.9	-	17
270	55.3	93.6	99.9	99.9	-	16
280	68.6	97.2	99.9	99.9	-	20
290	81.9	97.5	99.9	99.9	-	23
300	85.5	97.5	99.9	99.9	-	18
310	-	97.5	-	99.9	-	17
325	96.3	-	99.9	-	-	-
350	96.6	-	99.9	-	-	-
375	95.8	-	99.9	-	-	-
400	94.7	-	99.9	-	-	-

[1] difference between set point and measured reaction temperatures.

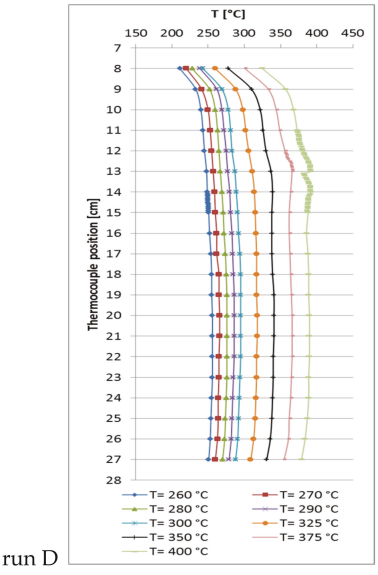

run D

Figure 3. Recorded temperature profiles for methanation on $18Ni/Al_2O_3$ with 0.5 mL catalyst + 4.5 mL quartz (GHSV = 12,000 h^{-1}; CO_2:H_2:N_2 = 1.8:7.2:1; 10 bar).

With these data from the bench-scale reactor [31], first estimations of maximum heat release and heat transfer were made. Additionally, basic kinetic parameters were determined. Afterwards, a larger tube reactor was constructed at an upscale factor of 36. Further optimization aimed at a methane productivity of 50 L/h, being equivalent to an electrical power of 500 W, with minimum catalyst load. It was planned together with industrial partners to integrate such reactors with optimized bed configuration into a tube bundle reactor for upscaling by increasing the number of tubes (modular design) for further increase of productivity.

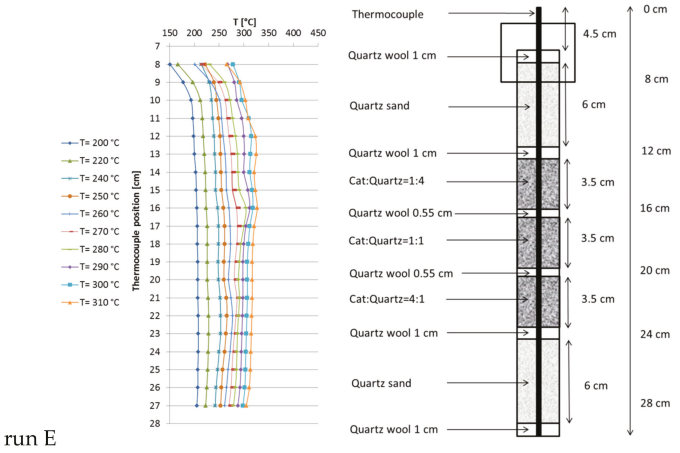

run E

Figure 4. Recorded temperature profiles for methanation on $18Ni/Al_2O_3$ in a triple-bed reactor (catalyst:quartz = 1:4, 1:1, 4:1; 1.7 mL each zone; GHSV = 6000 h^{-1}; CO_2:H_2:N_2 = 1.8:7.2:1; 10 bar).

2.3. Activation Energy

The Arrhenius plot (Figure 5) was calculated from experiments with the bench-scale reactor and a single fixed bed (1 mL of catalyst, catalyst:quartz = 1:4) for an estimation of the activation energy for CO_2 methanation on $18Ni/Al_2O_3$. Measurements were carried out at kinetically controlled conditions at low set point temperatures (250–280 °C) and high space velocities (8000–12,000 h^{-1}). Resulting CO_2 conversion reached 15–70%. Usually (e.g., [32]) very low conversions are preferred (<10%) but the measured conversions are far away from the chemical equilibrium and thus should be valid for a first approximation. The determined apparent activation energy was 120.4 kJ/mol, assuming first order reaction in CO_2. This is slightly higher as compared to results from other groups, possibly as CO_2 conversion was comparatively high. For example Weatherbee and Bartholomew got 80 kJ/mol on Ni/SiO_2 [33], whereas another group reported 60 and 80 kJ/mol on Ru/Al_2O_3 and Ni/Al_2O_3, respectively [10].

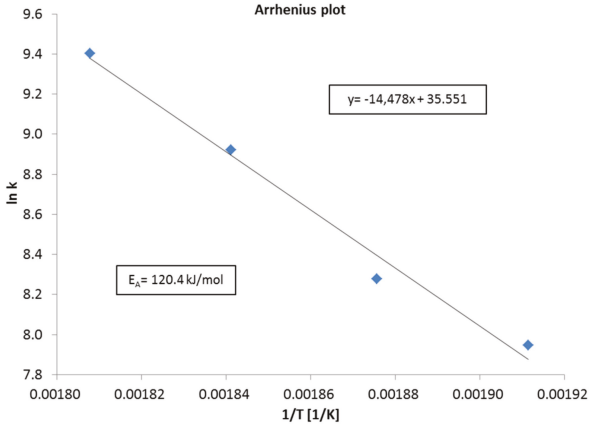

Figure 5. Arrhenius plot for the calculation of the apparent activation energy for CO_2 methanation on $18Ni/Al_2O_3$.

2.4. Temperature Profiles in the Large Tube Reactor

The large reactor was equipped with a double-jacket to circulate liquid heat carrier oil to provide a truly isothermal reactor (without reaction) and to improve heat transfer (dimensions cf. chapter 3). For reference purpose, a single fixed-bed with 1:9 catalyst:quartz dilution (30 mL catalyst, 270 mL quartz) was tested first (run F, Figure 6). At a GHSV of 8000 h^{-1} (total flow = 244.9 L/h; CO_2:H_2:N_2 = 1.8:7.2:1) the CH_4 production at 250 °C set point temperature reached 19 L/h (X_{CO2} = 43.0%) without any detectable hot spot. At 290 °C the methane production increased to 42 L/h (X_{CO2} = 96.1%), accompanied by a significant hot spot 160 K above set point temperature. At 310 °C a total of 46 L/h of methane (X_{CO2} = 96.2%) were formed with almost identical hot spot shape. These more pronounced hot spots are due to the larger reactor diameter and poor radial heat transfer. In view of the fact that, already at a GHSV of 8000 h^{-1}, the hot spot temperature grew that high, no further experiments were done with this single-bed configuration.

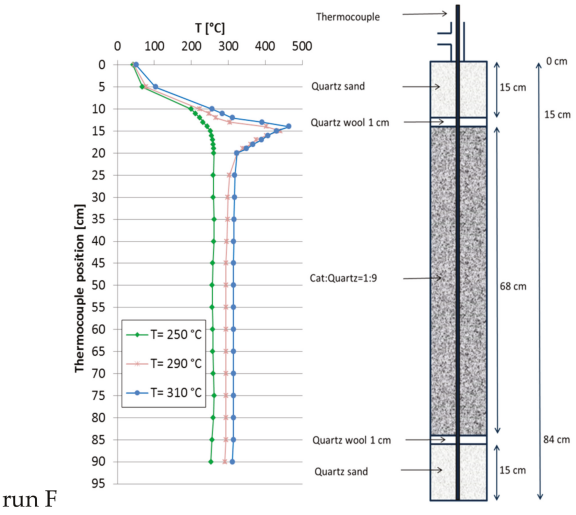

Figure 6. Recorded temperature profiles for methanation on 18Ni/Al_2O_3 in a single fixed-bed used as reference run (catalyst:quartz = 1:9; total bed volume 306 mL; GHSV = 8000 h^{-1}; CO_2:H_2:N_2 = 1.8:7.2:1; 10 bar).

The preferred configuration in the bench-scale reactor consisted of a triple fixed-bed with descending catalyst dilution (run E, Figure 4), because in comparison to run B, the hot spot was only half as high. This scheme was now scaled up with the large reactor. Several catalyst dilutions were tested to modify the heat distribution along the catalyst bed. At the end the compositions given in Figure 7 lead to a satisfactory temperature profile along the tube reactor (run G). The observed height of the hot spot was drastically reduced from 160 K to 62 K compared to the single-bed reactor. This is noteworthy as this remarkable improvement was obtained though the space velocity was elevated to 10,000 h^{-1} (total flow = 301.6 L/h; CO_2:H_2:N_2 = 1.8:7.2:1) and the methane productivity grew up to 50 L/h together with a proportional increase in total heat of reaction. As run G was the one with the highest gas throughput, the specific pressure drop was estimated by means of Ergun equation to be approximately 10.5 mbar/m. This configuration was tested at three set point temperatures: at 310 °C the overall methane productivity was 50.5 L/h (X_{CO2} = 93.1%) and the hot spot was 78 K above set point. At 330 °C, the methane productivity reached 50.3 L/h (X_{CO2} = 92.7%, hot spot + 62 K) and, at 350 °C, the methane flow reached 49.8 L/h (X_{CO2} = 91.7%, hot spot + 68 K). At all temperatures, the selectivity to CH_4 was always above 99.9% (Table 4).

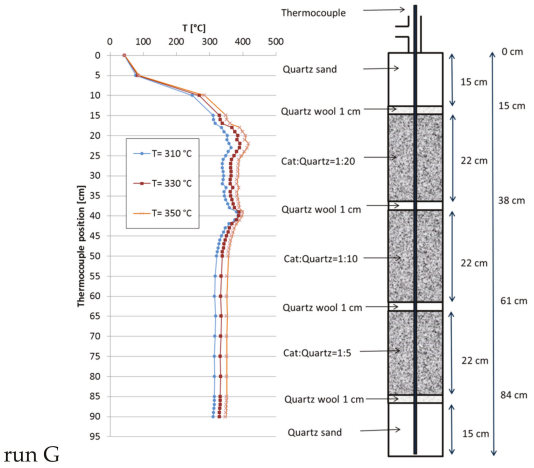

run G

Figure 7. Recorded temperature profiles for methanation on 18Ni/Al_2O_3 in a triple fixed-bed (30 mL of catalyst; catalyst:quartz = 1:20, 1:10, 1:5; 301 mL total; GHSV = 10,000 h^{-1}; CO_2:H_2:N_2 = 1.8:7.2:1; 10 bar).

Regarding the results from run G, obtained with triple-bed configuration, it has to be considered that the increased methane formation compared to reference run F is mostly caused by the higher throughput since at the same time CO_2 conversion dropped slightly (at 310 °C set point temperature from 96.2% to 93.1%). This is also overlapped by the effect of higher linear flow rate, which affects the shape of the temperature profiles by convective heat transfer. However, the most important result at this stage is an improved hot spot control during methanation at high throughput by stacking various fixed-beds with different catalyst dilutions which leads to saver operation conditions for both catalyst and reactor material.

Table 4. CO_2 conversion and methane selectivity on 18Ni/Al_2O_3 in the large reactor with single bed (run F: GHSV = 8000 h^{-1}) and triple fixed-bed with varying catalyst distribution (run G: GHSV = 10,000 h^{-1}; catalyst:quartz = 1:20, 1:10, 1:5). V_{cat} = 30 mL, V_{quartz} = 270 mL; CO_2:H_2:N_2 = 1.8:7.2:1, 10 bar).

Temperature	X_{CO2} (%)		S_{CH4} (%)		Hot Spot (K) [1]	
(°C)	F	G	F	G	F	G
250	43.0	-	99.9	-	-	-
290	96.1	-	99.9	-	160	-
310	96.2	93.1	99.9	99.9	160	78
325	-	92.7	-	99.9	-	62
330	-	91.1	-	99.9	-	68

[1] difference between set point and measured reaction temperatures.

In addition to discussing catalyst efficiency in terms of conversion and selectivity, the specific methane production per catalyst was used as criterion for comparison of the various reactor configurations (Table 5). For each of the configurations, only the temperature set point with the highest productivity was considered. The runs with the bench-scale reactor in single-bed configuration (runs A–C) show direct proportionality between catalyst amount and reactor productivity, coming along with extreme rise of hot-spot temperatures. Run D with half the catalyst load gives the same reactor productivity as run A but without any hot-spot and doubled catalyst productivity, due to efficient catalyst dilution. Comparison of runs B and E confirms that, at similar GHSV, temperature and catalyst load but appropriate bed structure, the hot spot can be reduced from 40 to 20 K at comparable productivity.

Run F with the large reactor can be seen as equivalent to run D with a catalyst dilution of 1:9 in a single-bed as well. By dividing the bed into three parts with descending dilution (run G), the productivity and STY is increased compared to reference run F whereas the hot spot is drastically lowered by approximately 100 K. This indicates that the concept is successfully adapted to the larger scale although the relative gain in productivity is lower than at bench-scale.

Table 5. Comparison of reactor configurations at the temperature set points with highest productivity (CO_2:H_2:N_2 = 1.8:7.2:1, 10 bar).

Run	V_{cat}	V_{dil}	GHSV	T	$X_{CO2,max}$	ΔT_{max}	STY	Productivity
	(mL)	(mL)	(h^{-1})	(°C)	(%)	(K)	(L/(mL_{cat} × h))	(L/h)
A	1	4	6000	300	96.5	5	1.1	1.1
B	2.5	2.5	6000	275	97.4	40	1.1	2.6
C	4	1	6588	270	96.5	65	1.2	4.6
D	0.5	4.5	12,000	350	96.6	-	2.2	1.1
E	2.3	2.3	6000	280	97.2	20	1.1	2.4
F	30	270	8000	310	96.2	160	1.4	42.5
G	30	271	10,000	350	92.5	62	1.7	50

2.5. Catalyst Stability

During extended studies of certain reactor configurations, the catalyst stability was checked routinely by repeating the first set point of the measurement campaign. Since not all configurations were tested on the same elongated time scale, only those configurations with a very long time on stream will be highlighted here. Figure 8 shows such a stability control series for a configuration with four fixed beds (run H, with descending catalyst dilution) together with the corresponding temperature profiles recorded at 290 °C set point temperature. The test campaign included intermediate changes in temperature (including repeated shut down and reactivation from room temperature to 350 °C), space velocity (10,000–20,000 h^{-1}) and pressure (5–15 bar). Thus, the catalyst was also exposed to more severe reaction conditions as described before. Measurement "a" was performed directly after the in situ activation of the catalyst at the campaign start, "b" after 30 h TOS, "c" after 130 h and "d" after 250 h. CO_2 conversion decreased within the first 30 h and was later nearly constant over 220 h. The temperature profiles reveal that the hot spot in the first fixed-bed seems to have wandered slightly downwards, whereas the other three fixed-beds did not change. Maximum temperatures were 338 °C, 356 °C, 324 °C and 349 °C from first to last bed.

Results from TEM imaging after long term testing (run H) showed no deposits on the catalyst (Figure 9) but Ni coated in NiO, which is proven by the measured lattice distances of 0.25 and 0.18 nm. The area of the catalyst surface was investigated with BET method and revealed a minor loss from 125 to 120 m^2/g.

Another, even more complex example, denoted as run I, is given in Figure 10, where two equal stacks of four fixed-beds with descending catalyst dilution similar to run H (Figure 8) were combined. With this configuration (8 beds), the initial CO_2 conversion at a remarkably high GHSV of 20,000 h^{-1} was increased from 84.6% (4 beds) to 95.1%. The set point temperature was 350 °C and the total TOS was more than 310 h. In this case the CO_2 conversion remained nearly constant and the methane selectivity stayed above 99.9%. At the same time, the temperature profiles were almost identical, i.e., no shift of hot spots was observed. The maximum measured temperatures reached values of 456 °C and 389 °C. Similar to run H, the test campaign included changes in temperature (repeated shutdown and reactivation to 350 °C), space velocity (10,000–20,000 h^{-1}) and pressure (5 bar to 15 bar). However, such gain in activity and productivity is only possible with higher complexity of reactor configuration. These two last runs illustrate the potential of appropriate catalyst bed arrangement to improve the reactor performance as well as to reduce the permanent stress and to slow down deactivation.

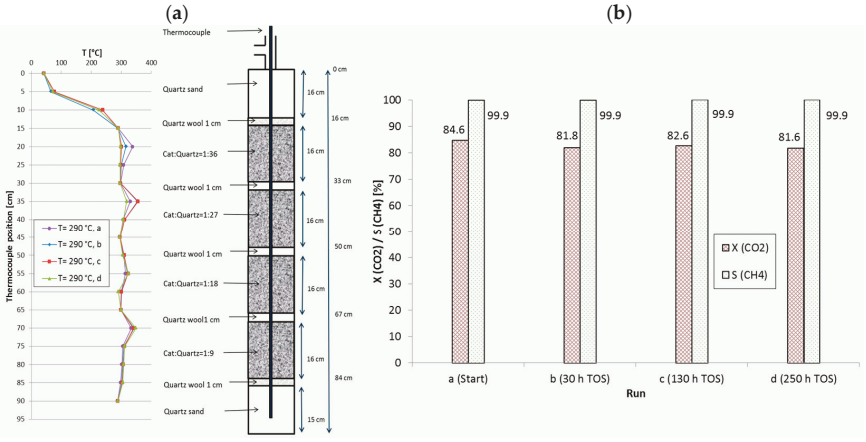

Figure 8. (**a**) Recorded temperature profiles for methanation on $18Ni/Al_2O_3$ in a reactor with four fixed-beds. (**b**) CO_2 conversion and CH_4 selectivity in dependence of TOS. Catalyst:quartz = 1:36, 1:27, 1:18, 1:9; 280 mL total; GHSV = 20,000 h^{-1}; CO_2:H_2:N_2 = 1.8:7.2:1; 10 bar.

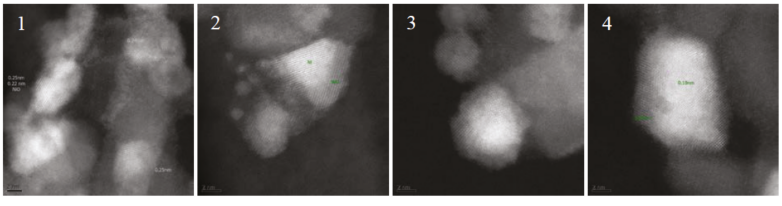

Figure 9. TEM images of fresh and spent catalyst after >250 h TOS in run H. Catalyst before reaction: (**1**) catalyst as delivered, partly reoxidized; and (**2**) after in situ reduction. Catalyst after reaction: (**3**) the top most bed; and (**4**) second catalyst bed.

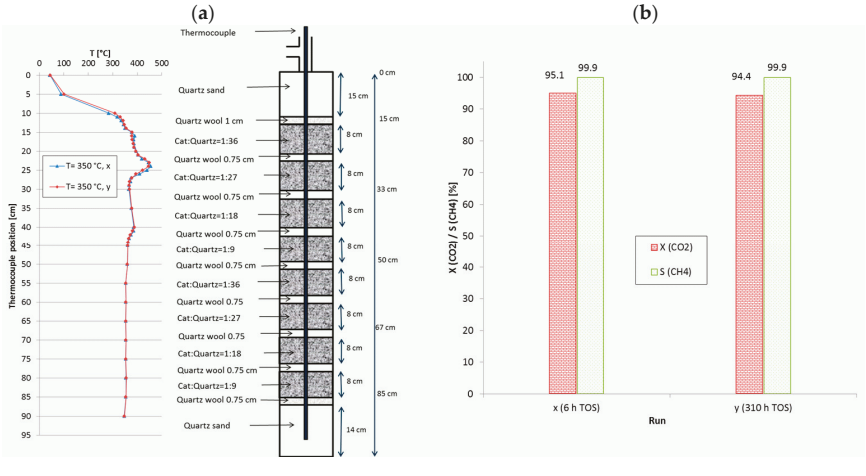

Figure 10. (**a**) Recorded temperature profiles for methanation on $18Ni/Al_2O_3$ in a reactor with 8 fixed-beds. (**b**) CO_2 conversion and CH_4 selectivity in dependence of TOS (catalyst:quartz varied from 1:36 to 1:9; 280 mL total; GHSV = 20,000 h^{-1}; CO_2:H_2:N_2 = 1.8:7.2:1; 10 bar).

3. Materials and Methods

Two stainless steel tubes ((a) L = 276 mm, ID = 7.6 mm, V = 12.5 cm^3 denoted as bench-scale reactor and (b) L = 1000 mm, ID = 24.8 mm, V = 483 cm^3 for upscaling experiments) served as reactors for the catalyst screening. The small tube was heated with an isolated electrical heating cord, the big one with heat carrier oil in the heating jacked. Temperature profiles were recorded in both reactors through stepwise movement of a thermocouple in a guiding tube which was centered in the reactor. The difference between measured and set point temperature is denoted as hot spot in Kelvin. Both reactors can be mounted alternatively into the same test rig which allowed comparison of results with minimum uncertainty. A scheme of the laboratory test rig shows Figure 11.

Ni/Al_2O_3 catalyst (commercial catalyst with 18 wt % Ni on alumina; original size: 2.5 mm × 3–5 mm extruded pellets) was used for all catalytic runs with respect to temperature profile recording. The catalyst particles were crushed and sieved, and a fraction of 500–800 µm was used for the screenings in the bench-scale reactor while the original particle size was kept in the large reactor. For advantageous flow conditions and the prevention of channeling a reactor diameter to particle size ratio of 10 was chosen for both set ups as recommended in [34]. Quartz split of same size was used for catalyst dilution. Before catalytic tests, the catalyst was in-situ activated in flowing hydrogen. Feed gas flow was metered by MFCs and the pressure was controlled with an electrically driven needle valve. All flow rates and GHSV data given in this study are referred to STP conditions (0 °C, 1 bar). The downstream pipes and valves were located in a heated oven box (180 °C) to avoid water condensation. Gas analytics were done with an on line-gas chromatograph (HP5890 II) which contained two lines with argon as carrier gas. Columns: HP Plot Q (30 m × 0.53 mm × 40 µm, for CO_2, CO, CH_4) and HP-Plot molecular sieve (30 m × 0.53 mm × 50 µm, for N_2 and H_2). Detection was done by FID and TCD respectively. Most of the runs reported here were carried out under the following conditions: T = 250–400 °C (set point temperature), p = 10 bar, GHSV = 6000–20,000 h^{-1}, CO_2:H_2 = 1:4. In addition, N_2 (10 vol %) was always present as internal standard to evaluate volume contraction during reaction. Each set point was held for at least two hours and at least 5 chromatograms were recorded at stationary operation conditions.

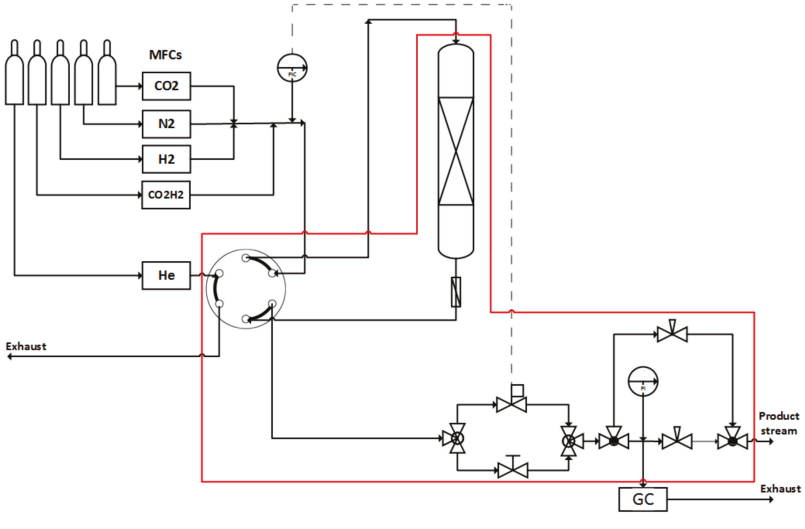

Figure 11. Scheme of the test rig. The set-up is constructed to mount both reactors alternatively. Red line: heated oven box (180 °C).

Carbon dioxide conversion (X_{CO2}) and methane selectivity (S_{CH4}) were determined from mole streams ($\dot{n}$) and stoichiometric coefficients (ν) as follows:

$$X_{CO_2} = \frac{\dot{n}_{CO_2\ (in)} - \dot{n}_{CO_2\ (out)}}{\dot{n}_{CO_2\ (in)}} \times 100\% \quad (4)$$

$$S_{CH_4} = \frac{\dot{n}_{CH_4}}{\dot{n}_{CO_2\ (in)} - \dot{n}_{CO_2\ (out)}} \times \frac{\nu_{CO_2}}{\nu_{CH_4}} \times 100\% \quad (5)$$

4. Conclusions

While exothermicity plays no big role in the conversion of low amounts of CO_2, production of SNG at industrial scale has to face this issue. In this study, we scaled up previously reported tests with a commercial alumina supported nickel catalyst (18 wt % load) from bench-scale to technically relevant reactor diameter, as used, e.g., in tube bundle reactors. Already, the appropriate arrangement of several fixed-beds combined with variable catalyst dilution in each bed allows significant lowering of hot-spot temperatures inside the reactor by nearly 100 K. This comparatively simple measure also shows potential to increase the specific productivity of the catalyst at the same time, as the catalyst can operate at thermodynamically more favored conditions.

Furthermore, some long-term campaigns aiming at stressing the catalyst (higher set point temperature, change of load, pressure variation) evidenced that the initial activity of the catalyst is much better preserved with such a smart catalyst distribution. A minor loss in surface area was observed over 250 h TOS, but catalyst deactivation was negligible. Finally, a production rate of 50 L/h SNG (500 W_{el}) was reached while the temperature hot-spot did not exceed 62 K. At these settings, specific methane productivity of the catalyst could be improved to 1.7 L/(mL_{cat} × h).

The reported results fulfill specified requirements to implement methanation for energy storage purpose in a small decentralized unit and are currently being developed to application by a small enterprise. Apart from the achieved state, further studies will focus on modeling of the up-scaled reactor with regard to optimization of the heat management.

Acknowledgments: The authors thank M.-M. Pohl and C. Kreyenschulte for TEM studies and D. Linke for model calculation. Financial support by LIKAT, Federal state of Mecklenburg-Western Pomerania and European Regional Development Fund (V-630-S-152-2012/141) is gratefully acknowledged.

Author Contributions: D.T., U.A., H.M. and A.M. conceived and designed the experiments; D.T. and H.M. performed the experiments; D.T., H.M. and U.A. analyzed the data; and D.T., U.A. and A.M. wrote the paper.

Conflicts of Interest: The authors declare no conflict of interest.

References

1. German Government on the Change of Energy Supply. Available online: https://www.bundesregierung.de/Content/DE/tatischeSeiten/Breg/Energiekonzept/0-Buehne/ma%C3%9Fnahmen-im-ueberblick.html (accessed on 1 March 2017).
2. BP Statistical Review of World Energy, June 2016. Available online: http://www.bp.com/content/dam/bp/pdf/energy-economics/statistical-review-2016/bp-statistical-review-of-world-energy-2016-full-report.pdf (accessed on 1 March 2017).
3. Bundesministerium für Wirtschaft und Energie (BMWI), Federal Ministry of Economics and Energy, Germany. Dossier Erneuerbare Energien. Available online: https://www.bmwi.de/Redaktion/DE/Dossier/erneuerbare-energien.html (accessed on 1 March 2017).
4. Eurostat Statistics Explained. Available online: http://ec.europa.eu/eurostat/statistics-explained/index.php/Energy_production_and_imports/de (accessed on 1 March 2017).
5. Bajohr, S.; Götz, M.; Graf, F.; Ortloff, F. Speicherung von regenerativ erzeugter elektrischer Energie in der Erdgasinfrastruktur. *Gwf-Gas Erdgas* **2011**, *152*, 200–210.

6. Valentin, F.; von Bredow, H. Power-to-Gas: Rechtlicher Rahmen für Wasserstoff und synthetisches Gas aus erneuerbaren Energien. *Energiewirtschaftliche Tagesfragen* **2011**, *61*, 99–105.
7. Sabatier, P.; Senderens, J.B. Nouvelles syntheses du methane. *C. R. Acad. Sci.* **1902**, *134*, 514–516.
8. Sabatier, P.; Senderens, J.B. Hydrogénation directe des oxydes du carbone en présence de divers métaux divisés. *C. R. Acad. Sci.* **1902**, *134*, 689–691.
9. Nørskov, J.K.; Bligaard, T.; Hvolbæk, B.; Abild-Pedersen, F.; Chorkendorff, I.; Christensen, C.H. The nature of the active site in heterogeneous metal catalysis. *Chem. Soc. Rev.* **2008**, *37*, 2163–2171. [CrossRef] [PubMed]
10. Garbarino, G.; Bellotti, D.; Riani, P.; Magistri, L.; Busca, G. Methanation of carbon dioxide on Ru/Al_2O_3 and Ni/Al_2O_3 catalysts at atmospheric pressure: Catalysts activation, behavior and stability. *Int. J. Hydrog. Energy* **2015**, *40*, 9171–9182. [CrossRef]
11. Peebles, D.E.; Goodman, D.W.; White, J.M. Methanation of carbon dioxide on nickel(100) and the effects of surface modifiers. *J. Phys. Chem.* **1983**, *27*, 4378–4387. [CrossRef]
12. Wang, W.; Gong, J. Methanation of carbon dioxide: an overview. *Front. Chem. Sci. Eng.* **2011**, *5*, 2–10.
13. Van der Laan, G.P.; Beenackers, A.A.C.M. Kinetics and Selectivity of the Fischer-Tropsch Synthesis: A Literature Review. *Catal. Rev. Sci. Eng.* **1999**, *41*, 255–318. [CrossRef]
14. Yang, J.; Ma, W.; Chen, D.; Holmen, A.; Davis, B.H. Fischer-Tropsch synthesis: A review of the effect of CO conversion on methane selectivity. *Appl. Catal. A Gen.* **2014**, *470*, 250–260. [CrossRef]
15. Renewable Energy Concepts. Available online: http://www.renewable-energy-concepts.com/german/bioenergie/biogas-basiswissen/biogaszusammensetzung.html (accessed on 1 March 2017).
16. European Biogas Association. EBA Biomethane & Biogas Report 2015. Available online: http://european-biogas.eu/2015/12/16/biogasreport2015/ (accessed on 2 March 2017).
17. Fachverband Biogas e.V. Available online: http://www.biogas.org/edcom/webfvb.nsf/id/DE-Zahlen-und-Fakten (accessed on 2 March 2016).
18. Mills, G.A.; Steffgen, F.W. Catalytic methanation. *Catal. Rev. Sci. Eng.* **1974**, *8*, 159–210. [CrossRef]
19. Garbarino, G.; Riani, P.; Magistri, L.; Busca, G. A study of the methanation of carbon dioxide on Ni/Al_2O_3 catalysts at atmospheric pressure. *Int. J. Hydrog. Energy* **2014**, *39*, 11557–11565. [CrossRef]
20. Aziz, M.A.A.; Jalil, A.A.; Triwahyono, S.; Ahmad, A. CO_2 methanation over heterogeneous catalysts: recent progress and future prospects. *Green Chem.* **2015**, *17*, 2647–2663. [CrossRef]
21. Car Manufacturer Audi: Audi E-Gas Project. Available online: http://www.audi-cr2014.de/uploads/files/901411328702714676-umweltbilanz-e-gas-project.pdf (accessed on 2 March 2017).
22. Clariant Supplies Catalyst for Audi's German Methanation Plant. Available online: http://www.chemicals-technology.com/news/news-clariant-catalyst-audi-german-methanation-plant (accessed on 2 March 2017).
23. World's Largest SNG Plant Goes On-Stream in China with Catalysts and Process Technology from Haldor Topsoe A/S. Available online: http://www.topsoe.com/content/world%E2%80%99s-largest-sng-plant-goes-stream-china-catalysts-and-process-technology-haldor-tops%C3%B8e (accessed on 2 March 2017).
24. Younas, M.; Kong, L.L.; Bashir, M.J.K.; Nadeem, H.; Shehzad, A.; Sethupathi, S. Recent Advancements, Fundamental Challenges, and Opportunities in Catalytic Methanation of CO_2. *Energy Fuels* **2016**, *30*, 8815–8831. [CrossRef]
25. Kienberger, T.; Karl, J. Substitute natural gas (SNG)—Stand der Technik, theoretische Grundlagen, Forschung am Institut für Wärmetechnik. In Proceedings of the 11th Symposium Energieinnovation, Graz, Austria, 10–12 February 2010.
26. Sudiro, M.; Bertucco, A. *Natural Gas*; Sciyo: Rijeka, Croatia, 2010; pp. 105–126.
27. Hydrogen Energy. Available online: http://www.netl.doe.gov/research/coal/energy-systems/gasification/gasifipedia/coal-to-sng (accessed on 2 March 2017).
28. Brooks, K.P.; Hu, J.; Zhu, H.; Kee, R.J. Methanation of carbon dioxide by hydrogen reduction using the Sabatier process in microchannel reactors. *Chem. Eng. Sci.* **2007**, *62*, 1161–1170. [CrossRef]
29. Schoder, M.; Armbruster, U.; Martin, A. Heterogen-katalysierte Hydrierung von CO_2 zu Methan unter erhöhten Drücken. *Chem. Ing. Tech.* **2013**, *82*, 344–352. [CrossRef]
30. Lange, F.; Armbruster, U.; Martin, A. Heterogeneously-catalyzed hydrogenation of carbon dioxide to methane over RuNi-bimetallic catalysts. *Energy Technol.* **2015**, *3*, 55–62. [CrossRef]
31. Martin, A.; Türks, D.; Mena, H.; Armbruster, U. Hydrogenation of Carbon Dioxide to Synthetic Natural Gas: Impact of Catalyst Bed Arrangement. *JECM* **2016**, *3*, 25–30.
32. Reschetilowski, W. *Einführung in Die Heterogene Katalyse*; Springer: Berlin/Heidelberg, Germany, 2015.

33. Weatherbee, G.D.; Bartholomew, C.D. Hydrogenation of CO_2 on group VIII metals. *J. Catal.* **1981**, *68*, 67–76. [CrossRef]
34. Dautzenberg, F.M. Ten Guidelines for Catalyst Testing. In *Characterization and Catalyst Development*; ACS Symposium Series; American Chemical Society: Washington, DC, USA, 1989; Volume 411, pp. 99–119.

catalysts

MDPI

Article

Methanol Steam Reforming: Na Doping of Pt/YSZ Provides Fine Tuning of Selectivity

Michela Martinelli, Gary Jacobs, Uschi M. Graham and Burtron H. Davis *

Center for Applied Energy Research, University of Kentucky, 2540 Research Park Dr., Lexington, KY 40511, USA; michela.martinelli@uky.edu (M.M.); gary.jacobs@uky.edu (G.J.); uschi.graham@uky.edu (U.M.G.)
* Correspondence: burtron.davis@uky.edu; Tel.: +1-859-257-0251; Fax: +1-859-257-0302

Academic Editor: Morris D. Argyle
Received: 14 March 2017; Accepted: 3 May 2017; Published: 10 May 2017

Abstract: In this work, we found that sodium doping can be used to improve CO_2 selectivity for supported Pt catalyst during methanol steam reforming. These materials are usually very active in the low temperature range; however, they are characterized by high selectivity of CO, which is a poison in downstream polymer electrolyte membrane fuel cells (PEM-FC) application. With Na doping, we found that CO_2 selectivity was higher than 90% when 2.5 wt.% of sodium was added to Pt/YSZ. We have speculated that the different product distribution is due to a different reaction pathway being opened for CH_3OH decomposition. Methanol decarbonylation was favored when Na was absent or low, while a formate decarboxylation pathway was favored when Na content reached 2.5 wt.%. The proposal is rooted in the observed weakening of the C-H bond of formate, as demonstrated in in situ diffuse reflectance infrared Fourier transform spectroscopy (DRIFTS) and kinetic isotope effect (KIE) experiments for the water-gas shift reaction conducted at low temperature. When adsorbed methoxy, produced when methanol is dissociatively adsorbed, was converted in the presence of H_2O in DRIFTS spectroscopy, formate species were prevalent for a 2% Pt–2.5% Na/YSZ catalyst, while only a minor contribution was observed for 2% Pt/YSZ. Moreover, the formate produced on Na-doped Pt/YSZ exhibited ν(CH) stretching bands at low wavenumber, consistent with C–H bond weakening, thus favoring dehydrogenation (and decarboxylation). It is proposed that when Na is present, formate is likely an intermediate, and because its dehydrogenation is favored, selectivity can be fine-tuned between decarbonylation and decarboxylation based on Na dopant level.

Keywords: methanol steam reforming (MSR); yttrium stabilized zirconia (YSZ); Na doping; DRIFTS; methoxy; formate

1. Introduction

Fuel cells are a promising and relatively environmentally benign technology for producing electrical power. Polymer electrolyte membrane fuel cells (PEM-FC) may become convenient devices for portable power generation and transportation. However, they require H_2 as fuel, and hydrogen storage remains a significant challenge [1]. Methanol has several advantages as a liquid chemical carrier of hydrogen for PEM-FC applications [2]. In fact, methanol has a H/C ratio (4:1) that is the same as methane; it is liquid at 1 atm and ambient temperature with a low boiling point (65 °C) and a low melting point (−144 °C); also, it is biodegradable. Methanol can be produced by renewable and fossil resources, and can be synthesized from CO or CO_2 [2,3]. Moreover, the steam reforming reaction occurs at a low temperature (200–300 °C) compared to other fuels (>500 °C) because no strong C–C bonds need to be broken. Methanol steam reforming (MSR) can be described by Equations (1) and (2), while water-gas shift (WGS) is given in Equation (3):

$$CH_3OH + H_2O \leftrightarrow CO_2 + 3H_2 \quad \Delta H = 49.6\,kJ/mol \tag{1}$$

$$CH_3OH \leftrightarrow CO + 2H_2 \quad \Delta H = 90.8\,kJ/mol \tag{2}$$

$$CO + H_2O \leftrightarrow CO_2 + H_2 \quad \Delta H = -41.2\,kJ/mol \tag{3}$$

Copper-based catalysts are the most commonly used for MSR due to their high activity and selectivity [4–9]. However, these catalysts have a number of drawbacks, including deactivation in excess steam, pyrophoricity, as well as complicated preconditioning steps that impact start-up/shutdown cycles [10,11]. Group VIII metals (e.g., Pd, Pt and Ni) were studied as possible alternatives to copper-based catalysts [12–17]. These materials are very attractive because of their thermal stability at higher temperature; however, a high fraction of CO is usually produced by the decomposition of methanol (Equation (2)). This can preclude their use when hydrogen production is desired. Iwasa et al. [15,18,19] reported that Pd/ZnO has high CO_2 selectivity. The formation of PdZn alloy phase, pre-reduced at high temperatures, has been implicated as the cause for the high selectivity to CO_2. The preparation of bimetallic PdZn is highly sensitive to the preparation procedure and the formation of metallic Pd compromises the catalyst performance by increasing the CO selectivity. MSR on Pt catalysts have also been reported in literature [20–24]. Liu et al. [20] found that when Al_2O_3 is doped with In_2O_3 a strong interaction between Pt and In_2O_3 is observed. Consequently, CO selectivity is minimized and catalyst stability is enhanced. Recently, Martinelli et al. [23] have found that sodium doping of Pt promoted yttrium stabilized zirconia (YSZ) improves CO_2 selectivity during both MSR and steam assisted formic acid decomposition (SAFAD). CO-free hydrogen production during SAFAD has been also reported by Bulushev et al. [25] on Au/Al_2O_3 catalyst doped with potassium.

The development of alkali-doped Pt/ZrO_2 catalysts has its roots in WGS catalysis. Iwasawa [26] proposed that the rate-limiting step of WGS for a number of partially reducible oxides with or without supported metal particles was C-H bond breaking of formate. After joint research between Honda Research USA, Inc. and Symyx using a combinatorial catalysis approach [27] discovered that addition of light alkali to metal/zirconia catalysts resulted in a significant increase in the low temperature water gas shift rate. Joint research between Honda Research USA, Inc. and UK-CAER [28,29] demonstrated that surface formates were significantly more reactive through: (1) forward formate decomposition experiments in H_2O; (2) formate H/D exchange experiments; (3) the observed weakening of the formate ν(CH) bond as observed in infrared spectroscopy; and (4) ^{13}CO isotopic switching experiments. More recently, the catalyst was improved by doping 10% (molar) Y to Zr [30]. Doping of the larger Y^{3+} cation to the lattice was confirmed by a shift in 2θ in XRD to lower values. Adding Y^{3+} generated additional vacancy sites for dissociation of H_2O, as confirmed by the more significant bridging OH band intensity (a negative band) during CO adsorption and the significant increase in the formate/Pt-CO ratio (25% higher) for the 0.5% Pt/YSZ catalyst as compared to the 0.5% Pt/ZrO_2 catalyst. Increased surface *O*-mobility due to lattice strain was also suggested as the formates, bound by their O atoms to the surface of the catalyst, were transported to the metal-support interface and decomposed more rapidly. These aspects were proposed to contribute to the higher WGS activity (e.g., 67% increase in CO conversion at 300 °C) of the 0.5% Pt/YSZ catalyst compared to the 0.5% Pt/ZrO_2 catalyst.

More recently [31], addition of 2.5% Na to 2% Pt/ZrO_2 or 2% Pt/YSZ catalyst was found to shift the light-off curve for low temperature shift to lower temperature by Δ 40 °C. The best catalyst was one containing both Na and Y. Diffuse reflectance infrared Fourier transform spectroscopy (DRIFTS) of adsorbed CO were used to probe the defect-associated bridging OH groups following activation/steaming, and the formate ν(CH) band was shifted from 2880 cm^{-1} to 2802 cm^{-1} by adding Na. Switching from H_2O + CO to D_2O + CO led to a normal kinetic isotope effect of 1.4 for the 2% Pt/YSZ catalyst and 1.2 for the 2% Pt–2.5% Na/YSZ catalyst. The electronic weakening of the formate C-H bond, as reflected in the lower wavenumber formate ν(CH) band and small kinetic isotope effect, is consistent with the proposal of Iwasawa that formate C–H bond breaking may be the rate limiting step of water gas shift. A related reaction of SAFAD was also examined, such that replacing CO (i.e., WGS) with HCOOH (i.e., SAFAD) led to higher activity [23]. Not only did Na significantly improve the rate of the reaction, but switching from H_2O + HCOOH to H_2O + DCOOH resulted in

an identical kinetic isotope effect of 1.4 for 2% Pt/YSZ and 1.2 for 2.5% Na–2% Pt/YSZ, providing further evidence of the involvement of formate in both reactions.

In MSR, there was also an effect of the Na dopant. While conversion slightly decreased, the selectivity to CO_2 increased significantly (from just 22% for 2% Pt/YSZ to >90% for 2% Pt–2.5%Na/YSZ at 300 °C). Na did not impact the normal kinetic isotope effect, suggesting that formate was probably not the rate limiting step. Nevertheless, the involvement of formate was suggested by the remarkable difference in CO_2 selectivity.

The aim of this work is to probe the characteristic that defines the active site for YSZ supported Pt catalyst and understand the key factor the governs the product selectivity during MSR. In order to achieve this goal, a series of Pt/YSZ catalysts with different sodium loadings were prepared, characterized and tested. DRIFTS experiments were also carried out in order to investigate intermediate species during the reaction and determine if they can be influenced by a chemical effect of Na.

2. Results and Discussion

Adding 2 wt.% Pt to YSZ slightly decreased the BET surface area (Table 1). Assuming that YSZ contributed to the surface area, adding Pt did not result in significant pore blocking. The effect of sodium loading is reported in Table 1. The surface area passed through a maximum sodium loading increased from 0 to 2.5 wt.%, indicating Na may cause a change in the morphology of the catalyst (e.g., a narrowing of the pores). At a high Na doping level of 2.5 wt.%, some pore blocking was likely, as surface area decreased by $\Delta 50$ m^2/g.

Table 1. Brunauer-Emmett-Teller (BET) surface area and porosity data from physisorption measurements of nitrogen at 77 K.

Sample Description	Catalyst Composition	BET SA (m^2/g)	Single Point Average Pore Volume (cm^3/g)	Single Point Average Pore Diameter (nm)
YSZ	$Zr_{0.9}Y_{0.1}O_{1.95}$	149.2	0.19	3.6
2% Pt/YSZ	2% Pt/$Zr_{0.9}Y_{0.1}O_{1.95}$	143.6	0.18	3.6
2% Pt–0.25% Na/YSZ	2% Pt–0.25% Na/$Zr_{0.9}Y_{0.1}O_{1.95}$	163.6	0.16	4.0
2% Pt–0.5% Na /YSZ	2% Pt–0.5% Na/$Zr_{0.9}Y_{0.1}O_{1.95}$	150.5	0.15	4.0
2% Pt–1% Na/YSZ	2% Pt–1% Na/$Zr_{0.9}Y_{0.1}O_{1.95}$	145.4	0.14	4.0
2% Pt–2.5% Na /YSZ	2% Pt–2.5% Na/$Zr_{0.9}Y_{0.1}O_{1.95}$	94.9	0.13	3.4

Temperature programmed reduction results are reported in Figure 1. Effects of Pt and Y-doping on TPR were presented in our previous work [30]. Pt accelerates the decomposition of surface carbonate species, as well as promotes O-vacancy and bridging OH group formation. A TPR-XANES investigation in that work demonstrated that the first peak involved platinum oxide reduction to Pt. With the addition of Na to the Pt/YSZ catalyst, the first peak increases primarily due to Pt facilitating carbonate decomposition once Pt oxide is reduced. Na, due to its basicity, systematically increases the amount of surface carbonate on the catalyst, as confirmed by DRIFTS experiments (not shown for the sake of brevity). The peak position reflected metal-support interactions and correlated with the surface area such that the lower surface area materials (2% Pt/YSZ, 2% Pt–2.5% Na/YSZ) had the first peak forming at a lower temperature. Thus, the maximum in the position of the first peak occurred when the Na loading was between 0.25 wt.% and 1 wt.% Na.

Figure 2a,b illustrate TEM and HRTEM results for Pt dispersion and particle size on catalyst support without Na. Figure 2c,d illustrate TEM and HRTEM results for Pt dispersion and particle size on catalyst support with Na. The Pt particle size range for both catalysts was similar and less than 2.5 nm.

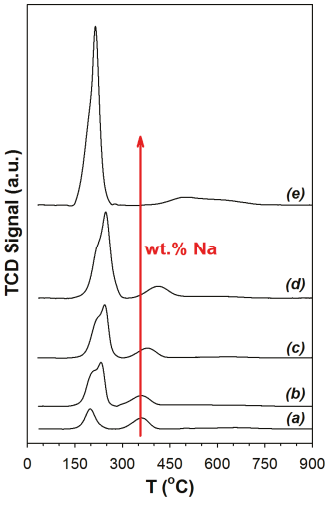

Figure 1. Results of temperature programmed reduction (**a**) 2% Pt/YSZ (**b**) 2% Pt–0.25 Na/YSZ (**c**) 2% Pt–0.5% Na/YSZ (**d**) 2% Pt–1% Na/YSZ (**e**) 2% Pt–2.5% Na/YSZ (heating from room temperature to 950 °C at 10 °C/min, 30 cm^3/min, H_2/He 10/90 v/v).

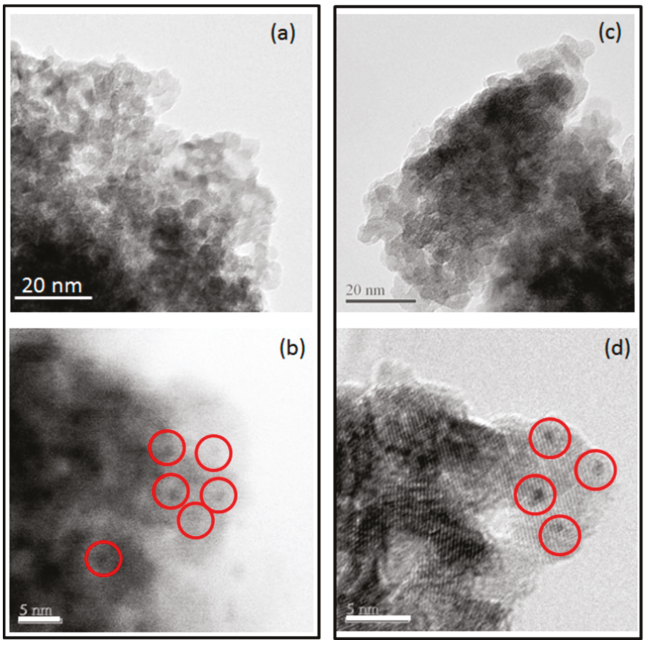

Figure 2. Transmission electron microscopy (TEM) (**a**) and high-resolution transmission electron microscopy (HRTEM) (**b**) images of yttrium stabilized zirconia support with Pt nanoparticle dispersion. TEM (**c**) and HRTEM (**d**) images of Na-yttrium stabilized zirconia support with Pt nanoparticle dispersion.

Figure 3a HR-STEM image of Pt particles on catalyst support. Individual bright spots in the image represent Pt nanoparticles. The energy dispersive X-ray spectroscopy (EDS) spectrum corresponds to

the area marked with the yellow square and was selected to show the Na concentration of the support without presence of Pt particles.

Figure 3b HR-STEM image of Pt particles on catalyst support. Individual bright spots in the image represent Pt nanoparticles. The EDS spectrum corresponds to the area marked with the yellow circle and was selected to show the Na concentration where Pt particles occur on the support. Na was observed in EDS spectra to occur in both locations, with and without the presence of Pt particles.

CO is an important probe molecule for bridging OH groups on active oxides, producing surface formates [32]. In Figure 4 (left) DRIFTS of adsorbed CO reveals, in addition of Pt carbonyl bands, ν(CH) and ν(OCO) asymmetric and symmetric stretching bands of formate. The ν(CH) band of the Na-doped catalyst were at lower wavenumbers, consistent with our earlier findings [28,29]. Therefore, DRIFTS—in agreement with EDS results—provides evidence that Na is located on the support. Figure 4 (right) demonstrates that adding Na affects the Pt-carbonyl bands, systematically shifting them to lower temperature. This may be due to a geometric or electronic effect, such as Na causing increased back-donation of electron density from Pt to the $2\pi^*$ antibonding molecular orbitals of CO. This, in addition to EDS results, indicates that Na is interacting with Pt. The area intensity of the Pt carbonyl bands of the unpromoted and Na-doped 2% Pt/YSZ catalysts were virtually identical and double that of a 1% Pt/Al_2O_3 catalyst (completely dispersed), except for the 2.5% Na-doped case, which was 87% of the area of the other Pt/YSZ catalysts.

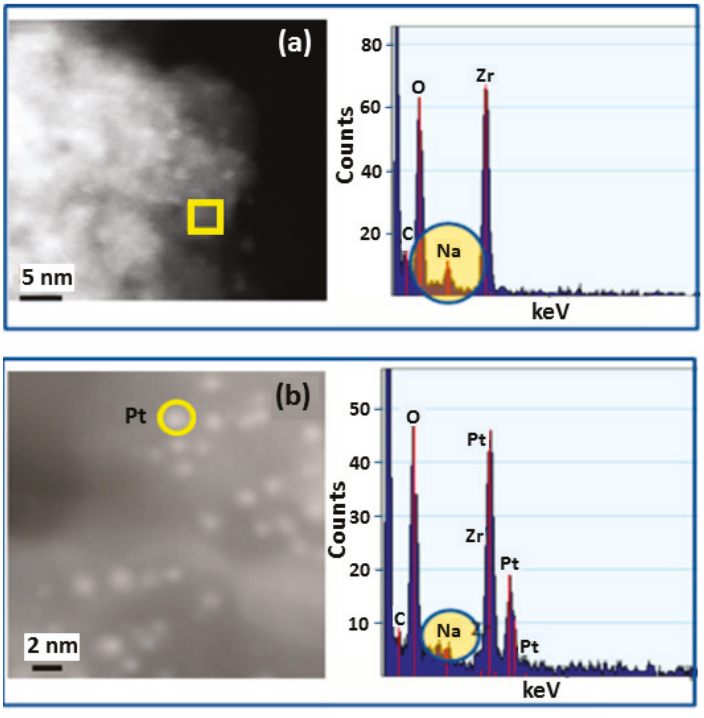

Figure 3. High resolution scanning transmission electron microscopy (STEM) and energy dispersive X-ray spectroscopy (EDS) analysis: (**a**) analysis in area without Pt nanoparticle on Na-Yttrium stabilized zirconia support; (**b**) analysis over area with 2.5 nm Pt nanoparticle.

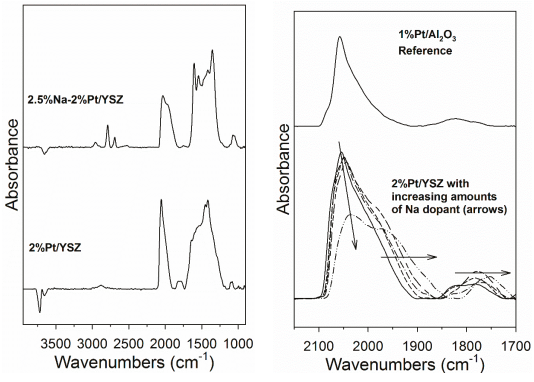

Figure 4. (**left**) Diffusive reflectance infrared Fourier transform spectroscopy (DRIFTS) of adsorbed CO shows **ν**(CH) and **ν**(OCO) asymmetric and symmetric stretching bands of formate; (**right**) Adding Na shifts the Pt-carbonyl bands systematically to lower T. Following the arrow, this includes undoped and Na-doped Pt/YSZ with 0.25, 0.5, 1, and 2.5 wt.% Na.

Carbon dioxide is acidic and thus is an excellent probe molecule for metal oxides. DRIFTS results shown in Figure 5 indicate that CO_2 readily adsorbed on the activated catalyst, forming asymmetric (higher wavenumber) and symmetric (lower wavenumber) ν(OCO) stretching bands in the region between 1700 and 1200 cm^{-1} [32]. Figure 5 shows that there was more carbonate adsorbed on the catalysts with higher Na doping levels, indicating that Na increased the support basicity. Moreover, Figure 4 and Table 2 show that carbonate was more strongly held on the catalysts with greater Na content. For example, Table 2 shows that by 350 °C, almost 60% of the carbonate had decomposed on the catalyst without Na doping, while just 38% and 24% had decomposed on the 1% and 2.5% Na doped catalysts, respectively, at 350 °C.

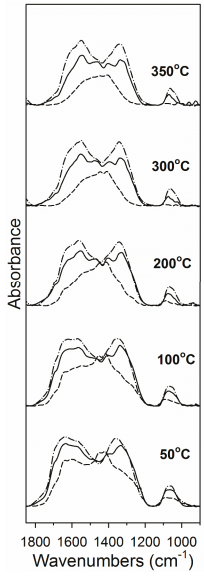

Figure 5. DRIFTS spectra during CO_2 temperature programmed desorption (TPD) for 2% Pt/YSZ (dashed line), 2% Pt–1% Na/YSZ (solid line) and 2% Pt–2.5% Na/YSZ (dashed-dotted line) catalyst following reduction in 25% H_2 at 350 °C.

Table 2. DRIFTS analysis of CO_2 TPD on undoped and Na-doped 2% Pt/YSZ catalysts.

TPD T (°C)	2% Pt/YSZ (% of Band at 50 °C)	2% Pt–1%Na/YSZ (% of Band at 50 °C)	2% Pt–2.5% Na/YSZ (% of Band at 50 °C)
50	100	100	100
100	85	93	95
200	58	80	84
300	41	68	80
350	37	62	76

Adsorption of methanol to the surface of H_2-activated 2% Pt/YSZ diminished ν(OH) bands associated with bridging OH groups located at 3800–3600 cm^{-1} (Figure 6, bottom left) and produced bands characteristic of methoxy species (Figure 6, bottom right), including ν(OC) bands within 1175–1000 cm^{-1} and ν(CH) bands at 3100–2700 cm^{-1}. The ν(OH) band intensity was lower in the case of the Na-doped catalyst (Figure 6, bottom left, spectrum b), indicating that the decrease in bridging OH groups for Na-doped catalyst was lower; this in turn suggests that Na doping may decrease the bridging OH group population on the catalyst surface. Moreover, unlike those on the Na-doped catalyst, the bridging OH groups that reacted for undoped 2% Pt/YSZ (Figure 6, bottom left, spectrum a) contained a higher fraction of Type I (3725, 3750 cm^{-1}) rather than Type II (3650, 3690 cm^{-1}) species. Likewise, a higher fraction of the higher wavenumber Type I [33] methoxy ν(OC) bands was observed for the undoped catalyst (Figure 6, bottom right, spectrum a), indicating that Na altered the ratio of adsorption sites to favor a higher fraction of sites with greater coordinative unsaturation.

DRIFTS results for the reaction of methoxy species with water are presented in Figure 6. At the start of steaming, the primary chemical species in the 3100–2700 cm^{-1} range during decomposition were methoxy species. With the undoped Pt/YSZ catalyst, a weak new band formed at 2866 cm^{-1} after 50% decomposition of the ν(CH) bands. This band became more pronounced at 67% and especially 88% decomposition of ν(CH) bands, and the position increased to 2868 cm^{-1}. The band position was in good agreement with surface formate by comparison with a formate reference spectrum (pink spectrum) produced from the reaction of bridging OH groups with CO. With the Na-doped Pt/YSZ catalyst, a shift in band position to higher wavenumber from 2795 to 2801 and 2802 cm^{-1} in moving from methanol adsorption to 50% and 67% decomposition indicates the formation of a n species with a new chemical identity. As in the case of the undoped catalyst, a comparison with a formate reference spectrum formed by reacting CO with bridging OH groups also showed good agreement with the new chemical species. In summary, methoxy decomposition produces formate species that are similar to those observed previously in low temperature WGS studies. However, the fraction of formates on the catalyst surface was lower for the un-doped Pt/SZ than for Na-doped Pt/YSZ at similar extents of methanol decomposition. The weakening of the C-H bond of formate by Na was also observed in the case of MSR as the wavenumbers of the main ν(CH) shifts significantly, from 2869 cm^{-1} to 2800 cm^{-1}.

The effect of the time on-stream (TOS.) on the conversion and product selectivity is reported in Figure 7 (left) for the undoped catalyst. The conversion is stable at each tested condition, while an evolution of the product selectivity was detected in the first few hours at 350 °C. In fact, in this condition, CO selectivity decreases from 68% to 44%, while CO_2 selectivity increases from 31% to 54%. In contrast, CH_4 selectivity was stable at a value of 1.2%. Liu et al. [20] have also observed that the CO selectivity decreases, while the CH_3OH conversion and CO_2 selectivity increases on $1Pt/30ZnO/Al_2O_3$. The authors explained this phenomenon as an activation of the catalyst surface. At temperatures lower than 350 °C, both conversion and selectivities were stable with TOS. No deactivation phenomena were observed.

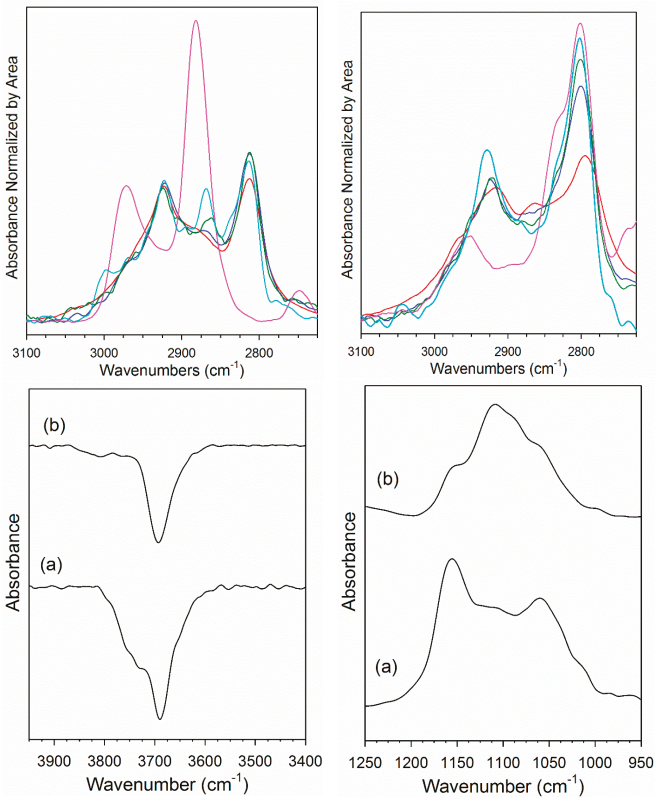

Figure 6. (**Top**) DRIFTS spectra in the ν(CH) region after (red) adsorption of MeOH; (pink) formation of formate from reacting CO with bridging OH species; catalyst after (blue) 50%, (green) 67%, or (cyan) 88% of ν(CH) region bands decomposed in H_2O, including (**top left**) 2% Pt/YSZ and (**top right**) 2% Pt–2.5% Na/YSZ. Bands were normalized by area in the range 2725–3100 cm^{-1} for the purpose of comparison. (**Bottom left**) Decrease in ν(OH) bands and (**bottom right**) formation of methoxy ν(OC) bands during adsorption of MeOH for (**a**) 2% Pt/YSZ and (**b**) 2% Pt–2.5% Na/YSZ.

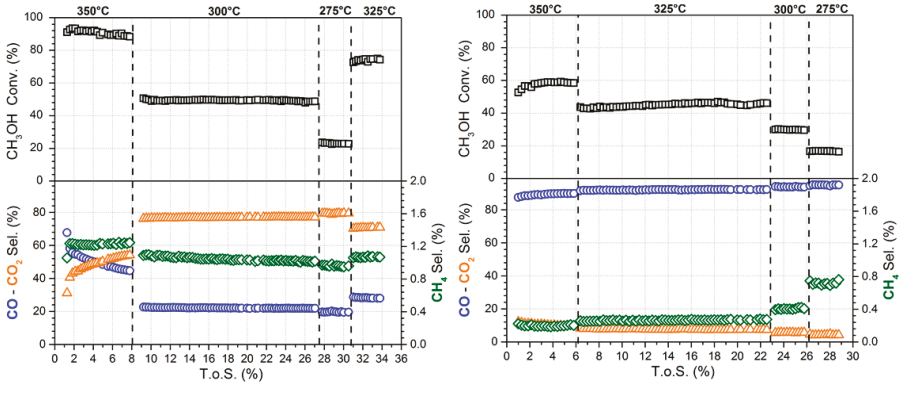

Figure 7. Evolution with time on-stream (TOS) of CH_3OH conversion and product selectivity for 2% Pt/YSZ (**left**) and 2% Pt–2.5% Na/YSZ (**right**).

The effect of TOS on conversion and product selectivity is reported in Figure 7 (right) for the 2% Pt–2.5% Na/YSZ. In the first 2 h CH_3OH conversion increases from 53% until the steady state value (58%), while CO and CO_2 selectivities are stable at 10.1% and 89.7%, respectively. Steady state conversion and selectivities were reached faster when alkali was added.

CH_3OH conversion systematically decreased by increasing sodium dopant from 0 to 2.5 wt.% (Table 3). This inhibition on the rate during MSR with Na doping was in sharp contrast to low temperature WGS and SAFAD results where an improvement was observed on both Pt/YSZ [23] or Pt/CeO_2 [28,34]. However, the sodium addition had a beneficial effect on CO_2 selectivity which was higher than 90% for 2% Pt–2.5% Na/YSZ sample in the temperature range of 275–350 °C. In contrast, only 19.7% of CO_2 was detected at 275 °C for the undoped catalyst one and CO_2 selectivity reached a value of 45.6% only at 350 °C. Even up to 350 °C, the CH_4 selectivity remained quite low (<3% for all catalysts and <1% for the 2.5% Na doped case). Qi et al. [8] reported an enhancing of the CO_2 production when Na or K is added. Contrary to our data, the authors also observed an improvement of the methanol conversion, however they used a K or Na promoted Ni/Al layered double hydroxide catalyst.

Table 3. Conversion and selectivities during MSR. Process conditions: P = 1 atm; GHSV = 381,000 h^{-1}; 2.9% CH_3OH: 4.3% N_2: 29.9% H_2: 26.1% H_2O:36.8% He.

Catalyst	T (°C)	% CH_3OH Conv.	% CO Select.	% CO_2 Select.	% CH_4 Select.
2% Pt/YSZ	275	21.6 ± 0.1	79.3 ± 0.1	19.7 ± 0.1	1.0 ± 0.005
	300	49.4 ± 0.1	76.8 ± 0.05	22.1 ± 0.05	1.1 ± 0.005
	325	74.1 ± 0.3	70.5 ± 0.1	28.5 ± 0.1	1.1 ± 0.003
	350	89.1 ± 0.5	53.2 ± 0.6	45.6 ± 0.5	1.2 ± 0.02
2% Pt–0.25% Na/YSZ	275	21.5 ± 0.1	76.2 ± 0.1	23.1 ± 0.1	0.8 ± 0.02
	300	44.2 ± 0.2	74.3 ± 0.1	24.9 ± 0.1	0.8 ± 0.01
	325	68.7 ± 0.6	68.2 ± 0.1	30.9 ± 0.1	0.9 ± 0.02
	350	87.8 ± 0.3	55.9 ± 0.9	43.2 ± 0.9	1.0 ± 0.01
2% Pt–0.5% Na /YSZ	275	20.6 ± 0.1	71.0 ± 0.1	28.2 ± 0.1	0.7 ± 0.01
	300	41.1 ± 0.1	67.9 ± 0.05	31.2 ± 0.05	0.8 ± 0.01
	325	63.3 ± 0.5	59.2 ± 0.05	40.0 ± 0.05	0.9 ± 0.01
	350	79.9 ± 0.6	38.9 ± 0.4	60.2 ± 0.4	2.8 ± 0.02
2% Pt–1% Na/YSZ	275	14.4 ± 0.1	60.0 ± 0.2	38.0 ± 0.1	0.5 ± 0.06
	300	31.9 ± 0.10	59.7 ± 0.1	39.3 ± 0.1	0.6 ± 0.01
	325	53.6 ± 0.4	55.6 ± 0.05	43.3 ± 0.06	0.7 ± 0.02
	350	80.9 ± 0.3	43.2 ± 0.5	60.6 ± 0.5	0.8 ± 0.02
2% Pt–2.5% Na /YSZ	275	16.7 ± 0.1	4.3 ± 0.1	95.0 ± 0.1	0.7 ± 0.01
	300	29.9 ± 0.1	5.7 ± 0.1	94.0 ± 0.1	0.4 ± 0.004
	325	45.2 ± 0.2	7.6 ± 0.1	92.2 ± 0.1	0.3 ± 0.002

DRIFTS and catalytic activity results allow the proposal of a tentative reaction mechanism (Figure 8) involving defect sites on the oxide adjacent to metal particles. The proposed mechanism has the following steps: (1) dissociation of methanol on the defect sites of YSZ to produce adsorbed methoxy species and a bridging OH group; (2) decomposition of methoxy species to produce adsorbed CO and H_2 (k_1). Depending on the catalyst surface properties, adsorbed CO can desorb (k_2) or can react with adsorbed H_2O to produce formate species (k_3). When water was present, formate species rapidly decomposed in the forward direction (k_4) to produce H_2 and monodentate carbonate, which then decomposes further to CO_2. The different selectivity between the undoped and Na-doped catalyst may be explained by the values of the kinetic rate constants (k_2, k_3 or k_4). In this proposal, $k_{3,4} > k_2$ for the Na-doped catalyst, where CO_2 is the main product detected during the activity test. Moreover, DRIFTS results suggested that a significant fraction of the methoxy species decomposed to formate. Since the C–H bond is weakened (i.e., the ν(CH) band of the formate is shifted at lower

wavenumber), this increased the formate decomposition rate, promoting dehydrogenation and yielding CO_2. The promoting impact of alkali on the formate decomposition rate is already well known for both WGS and SAFAD reactions [23,28,34].

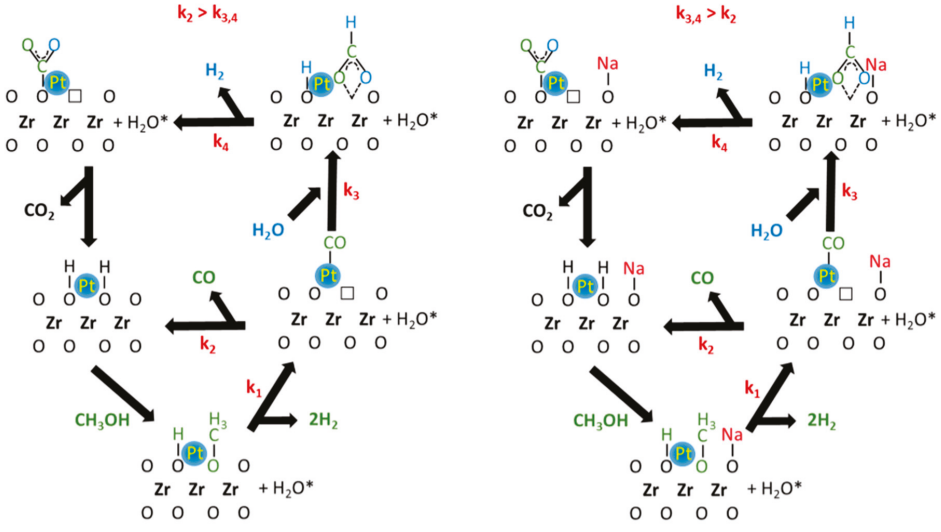

Figure 8. Proposed methanol steam reforming (MSR) pathways on (**right**) undoped Pt/YSZ and (**left**) Na-doped Pt/YSZ.

The different selectivity observed for the undoped catalyst suggests that the main pathway is not the formate decomposition to CO_2, but rather methanol decarbonylation (i.e., $k_2 > k_{3,4}$). The higher CO selectivity during MSR on group VIII has been previously reported by Iwasa and Tabezawa on Pd/Pt supported catalysts [17]. The authors explained that intermediate HCHO species rapidly decomposed due to strong back-donation of electron density from the metal to the π_{co}* antibonding orbitals of this intermediate species. Thus, CO and H_2 are primarily produced during MSR. Then, CO is then partially transformed to CO_2 through the secondary WGS reaction [2]. The authors reported CO selectivity very close to 100%, but their supports that are not active for WGS. However, the YSZ support has an important role to play in the WGS mechanism, which may explain the lower CO selectivities obtained on our undoped catalyst. In contrast to Ranganathan et al. [12], we found that the more basic support was characterized by higher selectivity to CO_2, but it is well known that the sodium improves the WGS rate, as well the rate and CO_2 selectivity during the steam-assisted formic acid decomposition [23].

Na addition does not improve the methanol conversion rate. This is in contrast to WGS and SAFAD, where increases in the carbon-containing reactant (i.e., CO and HCOOH respectively) were observed. In those cases, formate was the primary intermediate and postulated to be involved in the rate-determining step. With MSR [23], an identical normal kinetic isotopic effect (NKIE) value was obtained for the Na-doped and the undoped catalyst during NKIE experiments, suggesting that the rate determining step, contrary to WGS and SAFAD, is not the formate decomposition, but more likely the methoxy dehydrogenation step (k_1). However, Na-doping plays a critical role in selectivity control.

3. Materials and Methods

3.1. Catalyst Preparation

Yttria stabilized zirconia (YSZ), having a Y/Zr molar ratio of 0.11, was prepared by homogeneous precipitation. Zirconyl (Sigma Aldrich, 99%, St. Louis, MO, USA) and yttrium nitrates (Alfa Aesar,

99.9%, Haverhill, MA, USA) served as precursors and were precipitated with 1 M sodium hydroxide (Fisher Chemical, >97%, Hampton, NH, USA) following the procedure reported in [30]. The precipitate was filtered, washed, dried at 110 °C overnight, and then calcined at 400 °C (4 h). To this support, 2% by weight Pt was added by incipient wetness impregnation (IWI), and the catalyst dried (110 °C, overnight) and calcined (350 °C, 4 h). The prepared material was promoted with different sodium loadings (0.25, 0.5, 1 and 2.5 wt.%) by IWI of $Na(NO_3)$ solution (Alfa Aesar, 99.99%, Haverhill, MA, USA). Finally, the catalysts were dried at 110 °C (overnight) and re-calcined (300 °C, 3 h). The samples were sieved to 63 μm < φ < 106 μm for catalyst testing.

3.2. Catalyst Characterization

3.2.1. BET Analysis

BET surface area was measured using Micromeritics TRISTAR 3000 instrument (Micromeritics, Norcross, GA, USA). Approximately 300 mg of material was used. N_2 (Scott-Gross Co., UHP, Lexington, KY, USA) served as the adsorption gas and analysis was conducted at the boiling point of liquid N_2. Samples were outgased in vacuum for 12 h at 160 °C before conducting the physisorption measurements. Specific surface areas were assessed using the Brunauer-Emmett-Teller (BET) approach.

3.2.2. Temperature Programmed Reduction

Temperature programmed reduction (TPR) was performed on a Zeton-Altamira AMI-200 instrument (Altamira Instruments, Pittsburgh, PA, USA). Argon served as the reference gas, and 10% H_2 in Ar (Scott-Gross Co., UHP, Lexington, KY, USA) was flowed at 30 cm^3/min while temperature was ramped from 50 to 950 °C at 10 °C/min. The thermocouple was positioned within the catalyst bed; 100 mg of sample was used.

3.2.3. Scanning Transmission Electron Microscopy (STEM)

Catalyst powders were collected on copper grids for scanning transmission electron microscopy (STEM) analysis (200-mesh, Ted Pella, Inc., Redding, CA, USA). Transmission electron microscopy (TEM) imaging was performed using a JEOL 2010F (JEOL USA, Inc., Peabody, MA, USA) field-emission gun transmission electron microscope (accelerating voltage of 200 keV and magnification ranging from 50 K to 1000 K). A symmetrical multi-beam illumination was used for high-resolution imaging (HRTEM) with a beam resolution of 0.5 nm. Images were recorded with a Gatan Ultrascan 4 k × 4 k CCD camera (Gatan, Pleasanton, CA, USA). All data processing and analysis was performed using Gatan Digital Micrograph software (Gatan, Pleasanton, CA, USA). STEM imaging was performed with a high angle annular dark field (HAADF) detector and Gatan imaging filter (GIF, Gatan, Pleasanton, CA, USA).

3.2.4. Diffuse Reflectance Fourier Transform Infrared Spectroscopy

A Nicolet Nexus 870 IR spectrometer (ThermoFischer, Waltham, MA, USA) with a DTGS-TEC detector was utilized. A reaction cell with ZnSe windows served as the reactor for in situ measurements. Experimental procedures are detailed in reference [35].

H_2 or CO chemisorption are not recommended for these systems due to the possibility of adsorption of both gases on ceria or zirconia [36,37]. In order to measure the Pt dispersion, CO adsorption experiments have been carried out for the prepared samples, and the intensity of the Pt carbonyl bands have been compared to those obtained for a Pt/Al_2O_3 reference sample. Firstly, the dispersion of Pt/Al_2O_3 was determined by H_2 chemisorption. The catalyst was reduced in 100 cm^3/min of 25% H_2 (balance He Scott-Gross Co., UHP, Lexington, KY, USA) at 350 °C and then cooled in 100 cm^3/min of helium (Scott-Gross Co., UHP, Lexington, KY, USA) to 50 °C. 100 cm^3/min of 1% CO in helium (Scott-Gross Co., UHP, Lexington, KY, USA) was adsorbed for 20 min and then a purge in flowing helium (100 cm^3/min) was carried out for 20 min at the same temperature.

For CO_2 adsorption experiments, the catalyst was reduced in 100 cm^3/min of 25% H_2 (balance He, Scott-Gross Co., UHP, Lexington, KY, USA) at 350 °C and then cooled in 100 cm^3/min of helium to 50 °C. 100 cm^3/min of 5% CO_2 in helium (Scott-Gross Co., UHP, Lexington, KY, USA) was adsorbed for 30 min and then a temperature programmed reduction (TPD) in flowing helium (100 cm^3/min) was carried out, with scans performed at 50 °C, 100 °C, 200 °C, 300 °C, and 350 °C.

In the transient methanol decomposition test, the catalyst was activated in H_2 (100 cm^3/min, Scott-Gross Co., UHP, Lexington, KY, USA) at 350 °C for 1 h and cooled to 160 °C in flowing He (100 cm^3/min). Methanol (Alfa Aesar, 99%, Haverhill, MA, USA) was adsorbed by flowing 82 cm^3/min of helium through a bubbler to saturate the surface of the reduced catalyst with methoxy species at 160 °C. Decomposition of adsorbed methanol was performed by flowing 90 cm^3/min of helium through a saturator filled with distilled water.

3.3. Reaction Testing

Catalytic tests were performed in a stainless steel tubular reactor (0.444 in. i.d.) with a fixed bed at steady state. The experimental setup, which was used for the reaction test, is sketched in Figure 9; additional details can be found elsewhere [23]. In a typical run, 40 mg of catalyst sample (63–106 μm) diluted with 500 mg of SiO_2 beads (60–80 μm) were activated in hydrogen (100 cm^3/min) at 350 °C for 1 h (ramp rate = 4 °C/min). Then, the gas was switched to a mixture containing 2.9% CH_3OH (Alfa Aesar, 99%, Haverhill, MA, USA), 26.1% H_2O, 29.9% H_2, 4.3% N_2 (balance He) at P = 1 atm, GHSV = 381,000 h^{-1}, and T = 275–350 °C. Products passed through a cold trap (cooled to 0 °C) to collect condensable compounds and the gas phase was analyzed by on-line GC. The SRI 8610 GC has two columns (i.e., a 3.658 m silica gel packed column and a 1.829 m molecular sieve packed column) as well as two detectors (i.e., FID and TCD). To improve the sensitivity of the CO and CO_2 signals, the SRI GC includes a methanizer (SRI, Torrance, CA, USA), so that analysis can be made by FID.

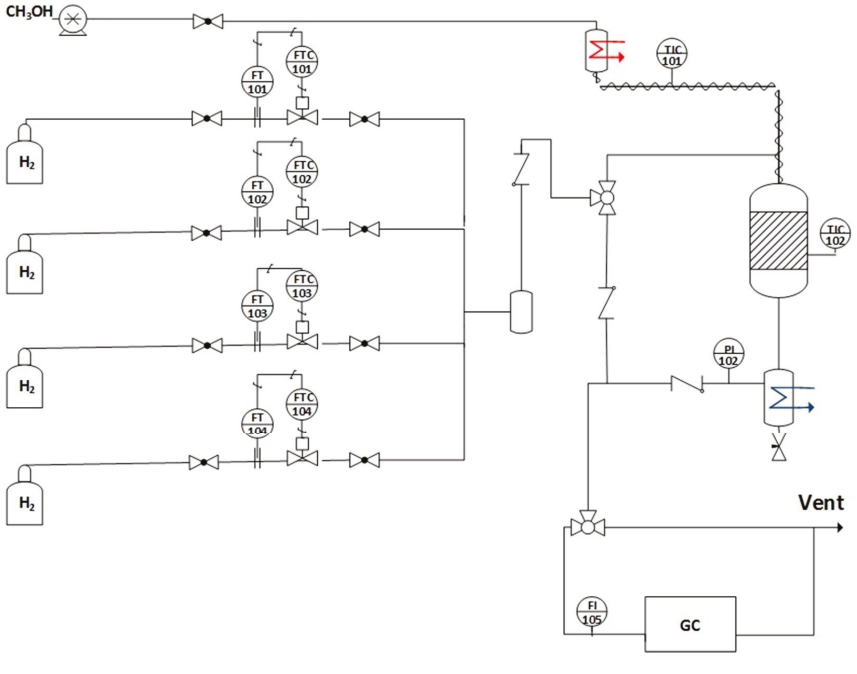

Figure 9. Experimental setup for the methanol steam reforming.

4. Conclusions

Na doping of Pt/YSZ was found to change the morphological properties as well as the reducibility profile. The reaction testing results demonstrate that CO_2 selectivity can be boosted remarkably by simply increasing the sodium loading. Indeed, CO_2 selectivity higher than 90% can be reached when the Na loading is 2.5 wt.% DRIFTS experiments have shown that adsorbed formates likely participate in the reaction pathway of Na-promoted Pt/YSZ catalysts. Furthermore, the formate produced on Na-doped Pt/YSZ exhibited ν(CH) stretching bands at low wavenumber, consistent with C-H bond weakening, favoring the formation of hydrogen and CO_2. Consequently, the reaction of adsorbed CO with water to produce formate species, which subsequently decomposes to CO_2, is favored over CO desorption (i.e., which occurs predominantly on the undoped catalyst). DRIFTS of adsorbed CO_2 showed that the basicity of the catalyst is increased, while DRIFTS of adsorbed CO and STEM/EDS data indicated that Na was located on the support and in interaction with Pt nanoparticles (<2.5 nm).

Acknowledgments: This work was funded by the Commonwealth of Kentucky.

Author Contributions: All authors conceived and designed the experiments; M.M., G.J. and U.M.G. performed the experiments and analyzed the data; B.H.D. contributed reagents/materials/analysis tools; all authors wrote the paper.

Conflicts of Interest: The authors declare no conflict of interest.

References

1. Ramirez, D.; Beites, L.F.; Blazquez, F.; Ballesteros, J.C. Distributed generation system with PEM fuel cell for electrical power quality improvement. *Int. J. Hydrog. Energy* **2008**, *33*, 4433–4443. [CrossRef]
2. Palo, D.R.; Dagle, R.A.; Holladay, J.D. Methanol steam reforming for hydrogen production. *Chem. Rev.* **2007**, *107*, 3992–4021. [CrossRef] [PubMed]
3. Olah, G.A. After oil and gas: Methanol economy. *Catal. Lett.* **2004**, *93*, 1–2. [CrossRef]
4. Lindström, B.; Pettersson, L.J. Hydrogen generation by steam reforming of methanol over copper-based catalysts for fuel cell applications. *Int. J. Hydrog. Energy* **2001**, *26*, 923–933. [CrossRef]
5. Papavasiliou, J.; Avgouropoulos, G.; Ioannides, T. Steady-state isotopic transient kinetic analysis of steam reforming of methanol over Cu-based catalysts. *Appl. Catal. B Environ.* **2009**, *88*, 490–496. [CrossRef]
6. Peppley, B.A.; Amphlett, J.C.; Kearns, L.M.; Mann, R.F. Methanol–steam reforming on $Cu/ZnO/Al_2O_3$. Part 1: The reaction network. *Appl. Catal. A Gen.* **1999**, *179*, 21–29. [CrossRef]
7. Peppley, B.A.; Amphlett, J.C.; Kearns, L.M.; Mann, R.F. Methanol–steam reforming on $Cu/ZnO/Al_2O_3$ catalysts. Part 2. A comprehensive kinetic model. *Appl. Catal. A Gen.* **1999**, *179*, 31–49. [CrossRef]
8. Qi, C.; Amphlett, J.C.; Peppley, B.A. K (Na)-promoted Ni, Al layered double hydroxide catalysts for the steam reforming of methanol. *J. Power Source* **2007**, *171*, 842–849. [CrossRef]
9. Jiang, C.J.; Trimm, D.L.; Wainwright, M.S.; Cant, N.W. Kinetic study of steam reforming of methanol over copper-based catalysts. *Appl. Catal. A Gen.* **1993**, *93*, 245–255. [CrossRef]
10. Yao, C.; Wang, L.; Liu, Y.; Wu, G.; Cao, Y.; Dai, W.; He, H.; Fan, K. Effect of preparation method on the hydrogen production from methanol steam reforming over binary Cu/ZrO_2 catalysts. *Appl. Catal. A Gen.* **2006**, *297*, 151–158. [CrossRef]
11. Karim, A.M.; Conant, T.; Datye, A.K. Controlling ZnO morphology for improved methanol steam reforming reactivity. *Phys. Chem. Chem. Phys.* **2008**, *10*, 5584–5590. [CrossRef] [PubMed]
12. Ranganathan, E.S.; Bej, S.K.; Thompson, L.T. Methanol steam reforming over Pd/ZnO and Pd/CeO_2 catalysts. *Appl. Catal. A Gen.* **2005**, *289*, 153–162. [CrossRef]
13. Conant, T.; Karim, A.M.; Lebarbier, V.; Wang, Y.; Girgsdies, F.; Schlögl, R.; Datye, A. Stability of bimetallic Pd–Zn catalysts for the steam reforming of methanol. *J. Catal.* **2008**, *257*, 64–70. [CrossRef]
14. Suwa, Y.; Ito, S.-I.; Kameoka, S.; Tomishige, K.; Kunimori, K. Comparative study between Zn–Pd/C and Pd/ZnO catalysts for steam reforming of methanol. *Appl. Catal. A Gen.* **2004**, *267*, 9–16. [CrossRef]
15. Iwasa, N.; Masuda, S.; Ogawa, N.; Takezawa, N. Steam reforming of methanol over Pd/ZnO: Effect of the formation of PdZn alloys upon the reaction. *Appl. Catal. A Gen.* **1995**, *125*, 145–157. [CrossRef]
16. Jacobs, G.; Davis, B.H. In situ DRIFTS investigation of the steam reforming of methanol over Pt/ceria. *Appl. Catal. A Gen.* **2005**, *285*, 43–49. [CrossRef]

17. Takezawa, N.; Iwasa, N. Steam reforming and dehydrogenation of methanol: Difference in the catalytic functions of copper and group VIII metals. *Catal. Today* **1997**, *36*, 45–56. [CrossRef]
18. Iwasa, N.; Mayanagi, T.; Nomura, W.; Arai, M.; Takezawa, N. Effect of Zn addition to supported Pd catalysts in the steam reforming of methanol. *Appl. Catal. A Gen.* **2003**, *248*, 153–160. [CrossRef]
19. Iwasa, N.; Yoshikawa, M.; Nomura, W.; Arai, M. Transformation of methanol in the presence of steam and oxygen over ZnO-supported transition metal catalysts under stream reforming conditions. *Appl. Catal. A Gen.* **2005**, *292*, 215–222. [CrossRef]
20. Liu, D.; Men, Y.; Wang, J.; Kolb, G.; Liu, X.; Wang, Y.; Sun, Q. Highly active and durable $Pt/In_2O_3/Al_2O_3$ catalysts in methanol steam reforming. *Int. J. Hydrog. Energy* **2016**, *41*, 21990–21999. [CrossRef]
21. Kaftan, A.; Kusche, M.; Laurin, M.; Wasserscheid, P.; Libuda, J. KOH-promoted Pt/Al_2O_3 catalysts for water gas shift and methanol steam reforming: An operando DRIFTS-MS study. *Appl. Catal. B Environ.* **2017**, *201*, 169–181. [CrossRef]
22. Wichert, M.; Zapf, R.; Ziogas, A.; Kolb, G.; Klemm, E. Kinetic investigations of the steam reforming of methanol over a $Pt/In_2O_3/Al_2O_3$ catalyst in microchannels. *Chem. Eng. Sci.* **2016**, *155*, 201–209. [CrossRef]
23. Martinelli, M.; Jacobs, G.; Shafer, W.D.; Davis, B.H. Effect of alkali on CH bond scission over Pt/YSZ catalyst during water-gas-shift, steam-assisted formic acid decomposition and methanol steam reforming. *Catal. Today* **2016**. [CrossRef]
24. Iwasa, N.; Mayanagi, T.; Ogawa, N.; Sakata, K.; Takezawa, N. New catalytic functions of Pd–Zn, Pd–Ga, Pd–In, Pt–Zn, Pt–Ga and Pt–In alloys in the conversions of methanol. *Catal. Lett.* **1998**, *54*, 119–123. [CrossRef]
25. Bulushev, D.A.; Zacharska, M.; Guo, Y.; Beloshapkin, S.; Simakov, A. CO-free hydrogen production from decomposition of formic acid over Au/Al_2O_3 catalysts doped with potassium ions. *Catal. Commun.* **2017**, *92*, 86–89. [CrossRef]
26. Iwasawa, Y. Surface catalytic reactions assisted by gas phase molecules. *Acc. Chem. Res.* **1997**, *30*, 103–109. [CrossRef]
27. Brooks, A.H.C.J.; Yaccato, K.; Carhart, R.; Herrman, M.; Lesik, A.; Strasser, P.; Volpe, A.; Turner, H.; Weinberg, H. Combinatorial methods for the discovery of novel catalysts for the WGS reaction. In Proceedings of the 19th Meeting of the North American Catalysis Society, Philadelphia, PA, USA, 22–27 May 2005.
28. Pigos, J.M.; Brooks, C.J.; Jacobs, G.; Davis, B.H. Low temperature water-gas shift: Characterization of Pt-based ZrO2 catalyst promoted with Na discovered by combinatorial methods. *Appl. Catal. A Gen.* **2007**, *319*, 47–57. [CrossRef]
29. Davis, B.H.; Occelli, M.L. *Advances in Fischer-Tropsch Synthesis, Catalysts, and Catalysis*; CRC Press: Boca Raton, FL, USA, 2010; pp. 365–394.
30. Martinelli, M.; Jacobs, G.; Graham, U.M.; Shafer, W.D.; Cronauer, D.C.; Kropf, A.J.; Marshall, C.L.; Khalid, S.; Visconti, C.G.; Lietti, L.; et al. Water-gas shift: Characterization and testing of nanoscale YSZ supported Pt catalysts. *Appl. Catal. A Gen.* **2015**, *497*, 184–197. [CrossRef]
31. Davis, B.H.; Occelli, M.L. *Fischer-Tropsch Synthesis, Catalysts and Catalysis: Advances and Applications*; CRC Press: Boca Raton, FL, USA, 2016; pp. 309–326.
32. Lavalley, J.C. Infrared spectrometric studies of the surface basicity of metal oxides and zeolites using adsorbed probe molecules. *Catal. Today* **1996**, *27*, 377–401. [CrossRef]
33. Binet, C.; Daturi, M.; Lavalley, J.-C. IR study of polycrystalline ceria properties in oxidised and reduced states. *Catal. Today* **1999**, *50*, 207–225. [CrossRef]
34. Pigos, J.M.; Brooks, C.J.; Jacobs, G.; Davis, B.H. Low temperature water–Gas shift: The effect of alkali doping on the CH bond of formate over Pt/ZrO_2 catalysts. *Appl. Catal. A Gen.* **2007**, *328*, 14–26. [CrossRef]
35. Jacobs, G.; Williams, L.; Graham, U.; Thomas, G.A.; Sparks, D.E.; Davis, B.H. Low temperature water–Gas shift: In situ DRIFTS-reaction study of ceria surface area on the evolution of formates on Pt/CeO_2 fuel processing catalysts for fuel cell applications. *Appl. Catal. A Gen.* **2003**, *252*, 107–118. [CrossRef]
36. Rogemond, E.; Essayem, N.; Frety, R.; Perrichon, V.; Primet, M.; Mathis, F. Characterization of model three-way catalysts. *J. Catal.* **1997**, *166*, 229–235. [CrossRef]
37. Pantu, P.; Gavalas, G.R. Methane partial oxidation on Pt/CeO_2 and Pt/Al_2O_3 catalysts. *Appl. Catal. A Gen.* **2002**, *223*, 253–260. [CrossRef]

catalysts

MDPI

Article

Catalysts Promoted with Niobium Oxide for Air Pollution Abatement

Wendi Xiang [2], Xiaochen Han [1], Jennifer Astorsdotter [3] and Robert Farrauto [1,*]

[1] Earth and Environmental Engineering Department, Columbia University, New York, NY 10027, USA; xh2271@columbia.edu
[2] Chemical Engineering Department, Columbia University, New York, NY 10027, USA; xiang.wendi@columbia.edu
[3] Chemical Engineering for Energy and the Environment Department, KTH Royal Institute of Technology, 10044 Stockholm, Sweden; jennifer.astorsdotter@gmail.com
* Correspondence: rf2182@columbia.edu; Tel.: +1-212-854-6390

Academic Editor: Morris D. Argyle
Received: 31 March 2017; Accepted: 4 May 2017; Published: 8 May 2017

Abstract: Pt-containing catalysts are currently used commercially to catalyze the conversion of carbon monoxide (CO) and hydrocarbon (HC) pollutants from stationary chemical and petroleum plants. It is well known that Pt-containing catalysts are expensive and have limited availability. The goal of this research is to find alternative and less expensive catalysts to replace Pt for these applications. This study found that niobium oxide (Nb_2O_5), as a carrier or support for certain transition metal oxides, promotes oxidation activity while maintaining stability, making them candidates as alternatives to Pt. The present work reports that the orthorhombic structure of niobium oxide (formed at 800 °C in air) promotes Co_3O_4 toward the oxidation of both CO and propane, which are common pollutants in volatile organic compound (VOC) applications. This was a surprising result since this structure of Nb_2O_5 has a very low surface area (about 2 m^2/g) relative to the more traditional Al_2O_3 support, with a surface area of 150 m^2/g. The results reported demonstrate that 1% Co_3O_4/Nb_2O_5 has comparable fresh and aged catalytic activity to 1% Pt/γ-Al_2O_3 and 1% Pt/Nb_2O_5. Furthermore, 6% Co_3O_4/Nb_2O_5 outperforms 1% Pt/Al_2O_3 in both catalytic activity and thermal stability. These results suggest a strong interaction between niobium oxide and the active component—cobalt oxide—likely by inducing an oxygen defect structure with oxygen vacancies leading to enhanced activity toward the oxidation of CO and propane.

Keywords: cobalt on Nb_2O_5 catalyst; CO and propane oxidation; promoting effects of Nb_2O_5

1. Introduction

Carbon monoxide (CO) is produced by incomplete combustion of carbon-containing fuels. When this deadly toxic gas combines with hemoglobin in blood, oxygen (O_2) cannot be delivered to vital organs essential for life. Propane (C_3H_8) is produced during the process of combusting liquefied petroleum gas, but can also be considered a model of volatile organic compounds (VOCs). An active low-temperature oxidation catalyst has attracted immense attention to meet ever-changing stringent environmental regulations for oxidation of volatile organic compounds in chemical plants, petroleum refineries, pharmaceutical plants, automobile manufacturing, etc. [1,2].

Volatile organic compounds are toxic and mainly contribute to the formation of photochemical smog with a with a negative impact on air quality [3]. Catalytic oxidation is a main technology used

commercially in their reduction [4,5]. The basic catalytic oxidation reactions of CO (1) and hydrocarbon (C_xH_y) (2) are shown as follows [2]:

$$CO + 1/2O_2 \overset{Catalyst}{\rightarrow} CO_2 \quad (1)$$

$$C_xH_y + (x + y/4)(O_2) \overset{Catalyst}{\rightarrow} xCO_2 + y/2H_2O \quad (2)$$

Many environmental abatement catalysts are precious metals, such as Pt and Pd, due to their excellent performance and superior life in abating real exhausts. However, their high price is a disadvantage, and therefore alternative materials are always being sought. However, this is very challenging. For low temperature applications, such as VOCs removal in indoor air, transition metal oxides have been proposed as replacements for precious metals [6]. Among transition metal oxides, cobalt oxide (Co_3O_4) shows very high CO oxidation activity in CO/O_2 mixtures even at ambient temperature [7]. Co_3O_4 is also highly effective for the total oxidation of propane under conditions relevant for VOC emission control [8]. Moreover, the evasive "holy grail" for catalytic applications is a precious metal–free catalyst for three-way automobile gasoline exhaust catalysts [9].

It is an essential to disperse the catalytic components on a carrier with a high surface area, such as Al_2O_3, TiO_2, SiO_2, ZrO_2, or SiO_2-Al_2O_3, in order to maximize active sites available for reactants. Furthermore, supported catalysts are deposited (as washcoats) on high cell density monoliths (ceramic and metal) to minimize pressure drop and volume relative to packed beds [2]. Niobium pentoxide (Nb_2O_5) has been reported to show strong metal support interaction (SMSI) with certain metals [1,10,11]. However, no commercial VOC applications that include Nb_2O_5 are known.

The goal of this study was to investigate Nb_2O_5's promoting effects on base metal catalysts for CO and propane oxidation. Nb_2O_5 has the ability to form defect structures with oxygen vacancies when combined with base metal oxide materials to enhance catalytic activity [12,13]. The active oxidation state for cobalt is +3 in Co_3O_4 and has been reported to be a prime candidate for precious metal replacement in VOC applications due to its high catalytic activity [14,15]. Retaining Co in the active +3 state will enhance its thermal stability. The current study was designed to further explore the performance of Co supported on Nb_2O_5 and to investigate whether other transition metal oxides combined with Nb_2O_5 could also have a beneficial effect for VOC applications. This feasibility study compared the oxidation performance of Co_3O_4/Nb_2O_5 with traditional Co_3O_4/Al_2O_3. Furthermore, the study expanded to evaluate other base metal oxides such as iron oxide (Fe_2O_3), copper oxide (CuO), and nickel oxide (NiO), all of which were deposited on Nb_2O_5 relative to Al_2O_3 with the aim to broaden the understanding of the promoting effects of Nb_2O_5 in VOC applications. Finally, the catalytic performance of Co_3O_4/Nb_2O_5 was compared to that of Pt/γ-Al_2O_3.

The catalytic protocols used in establishing performance characteristics were fresh and aging activity tests. Thermal gravimetric analysis (TGA) was used to establish minimum time and temperature necessary for complete decomposition of precursor to the respective oxides.

2. Result and Discussion

2.1. TGA Results for Precursor of Cobalt (Co)

Thermal gravimetric analysis (TGA) measures the weight change of a material upon heating in various gaseous environments. Figure 1 shows the TGA results of three samples: the precursor $Co(NO_3)_2 \cdot 6H_2O$, the impregnated precursor on carriers, 6% $Co(NO_3)_2/Nb$@800 (the term Nb@800 = pre calcination temperature of Nb_2O_5 at 800 °C in air for 2 h), 6% $Co(NO_3)_2/Al$@800 (pre calcination of Al_2O_3 in air for 2 h). The precursor $Co(NO_3)_2 \cdot 6H_2O$ decomposes completely to Co_3O_4 at about 300 °C where no additional weight loss occurs [16] upon continued heating as shown in Figure 1. The impregnated catalysts also achieve constant weight at 300 °C. Thus, all impregnated catalysts were calcined at 300 °C. The cobalt oxide content was 6% by weight on supported carriers.

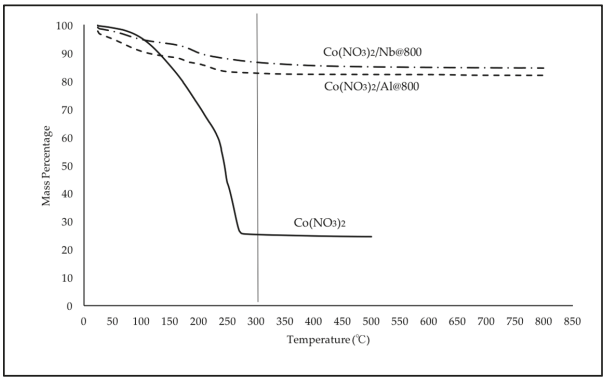

Figure 1. Thermal gravimetric analysis (TGA) tests for the decomposition of the $Co(NO_3)_2{\cdot}6H_2O$ and impregnated catalysts $Co(NO_3)_2/Nb@800$ and $Co(NO_3)_2/Al@800$. Both Nb_2O_5 and Al_2O_3 were pre-calcined at 800 °C for 2 h in air. The supported catalysts were prepared to give 6% cobalt oxide.

2.2. Preparative Details of Co/Nb and Co/Al

2.2.1. Pre-Calcination Temperature of Carriers Nb_2O_5 and Al_2O_3

Nb_2O_5 has different crystal phases at different temperature [17]. The pre-calcination temperature affects the crystal phase of Nb_2O_5, which in turn affects the chemical and physical properties of Nb_2O_5. The structure of Al_2O_3 is similarly affected. The monohydrate and tri-hydrate alumina structures change as a function of the temperature (°C) in air [18]. The impact of pre-calcination temperature on carriers and final catalysts were therefore explored.

All carriers were pre-calcined at specified temperatures for 2 h in air. After pre-calcination of the carriers, $Co(NO_3)_2{\cdot}6H_2O$ was deposited on each carrier and calcined at 300 °C in air for 2 h to give 6% Co@300/Nb and 6% Co@300/Al. This nomenclature indicates 6% cobalt oxide calcined at 300 °C after deposited on Nb_2O_5 or Al_2O_3.

Table 1 demonstrates catalytic performances of fresh catalysts of 6% Co/Nb with different pre-calcination temperatures of Nb_2O_5. In Table 1, all carriers were Nb_2O_5 pre-calcined from 500 °C to 900 °C. T_{20}, T_{50} and T_{90} values (temperature for 20%, 50% and 90% conversion) are compared. T_{20} and T_{50} are indicative of chemical kinetic control, while T_{90} often reflects some pore diffusion control. It is clear that Co on Nb@700 and Nb@800 show better catalytic performance of CO oxidation with the Nb@800 showing the best performance.

Table 1. Six percent Co@300/Nb with the number following @ = pre-calcination temperatures of the carrier for CO oxidation.

Catalyst	T_{20} (°C)	T_{50} (°C)	T_{90} (°C)
6% Co@300/Nb@500	190	200	220
6% Co@300/Nb@700	150	155	160
6% Co@300/Nb@800	130	145	160
6% Co@300/Nb@900	130	155	185

Table 2 provides catalytic results of fresh 6% Co/Al with different pre-calcination temperatures of Al_2O_3. The T_{20}, T_{50} and T_{90} indicate that Al@800, pre-calcined at 800 °C, yielded the best results.

Table 2. Six percent Co/Al with @ = pre-calcination temperatures of the carrier for CO oxidation.

Catalyst	T_{20} (°C)	T_{50} (°C)	T_{90} (°C)
6% Co@300/Al@500	205	225	245
6% Co@300/Al@700	200	215	-
6% Co@300/Al@800	185	205	240
6% Co@300/Al@900	215	240	270

One can conclude that the optimal pre-calcination temperature for both Nb_2O_5 and Al_2O_3 was 800 °C. Therefore, both Nb_2O_5 and Al_2O_3 were pre-calcined at 800 °C for all experiments conducted henceforth.

Further, Figure 2 compares the activity of cobalt catalysts as a function of the pre-calcination temperature of the two carriers. Clearly, 6% Co@300/Nb@800 yielded the best performance of all for CO oxidation.

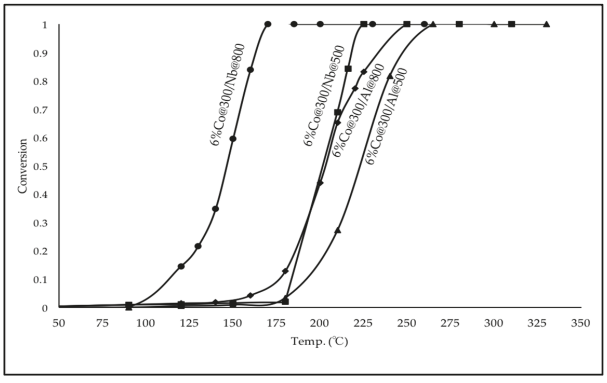

Figure 2. Six percent Co@300/Nb@800, 6% Co@300/Nb@500, 6% Co@300/Al@800 and 6% Co@300/Al@500 for CO oxidation. Both Nb@800 and Al@800 were pre-calcined at 800 °C for 2 h in air, and both Nb@500 and Al@500 were pre-calcined at 500 °C for 2 h in air. All four impregnated catalysts were calcined at 300 °C for 2 h in air. Gas composition: CO 1.5 vol %; O_2 14.5 vol %, N_2 84 vol %. Catalysis volume: 0.1 mL; GHSV: 64,800 (h^{-1}).

To further quantify the advantages offered by fresh 6% Co@300/Nb@800 relative to fresh 6% Co@300/Al@800 turn over frequencies (TOF) are presented in Table 3 for different temperatures.

$$T = \frac{\left(\frac{gram}{hr}\ of\ CO\right) \bullet (fractional\ conversion\ of\ CO)}{gram\ of\ Co_3O_4}$$

Table 3. Turnover Frequencies (TOF) for CO oxidation for fresh 6% Co@300/Nb@800 relative to fresh 6% Co@300/Al@800.

Catalyst	TOF@150 °C ($h^{-1} \times 10^5$)	TOF@170 °C ($h^{-1} \times 10^5$)	TOF@190 °C ($h^{-1} \times 10^5$)	TOF@210 °C ($h^{-1} \times 10^5$)
6% Co@300/Nb@800	897.8	1508	1508	1508
6% Co@300/Al@800	53.48	129.9	496.6	1241

2.2.2. Catalytic Performance of Fresh and Aged Co Catalysts for CO Oxidation

Based on the data in Tables 1–3, the pre-calcination temperature of carriers was set at 800 °C with the precursor decomposition at 300 °C for 2 h in air.

Figure 3 shows that fresh 6% Co@300/Nb@800 outperforms fresh 6% Co@300/Al@800 for CO oxidation over the entire conversion-temperature profile including the kinetic control regime up to fractional conversion approaching of 1.0 (100% conversion). Catalytic performance of each catalysts aged at 400 °C for 12 h in reaction gases is also shown in this figure. This temperature is approximately the maximum experienced in abating VOC from some stationary chemical plants. Clearly, 6% Co@300/Nb@800 outperformed its counterpart however, both catalysts suffered some deactivation after aging. Six percent Co@300/Nb@800 seemed to experience some reaction rate limited by pore diffusion (slightly lower slope at T_{50} region), while the chemical kinetic control region (T_{20}) was not affected. For 6% Co@300/Al@800 both kinetic control (T_{20} region) and pore diffusion control (T_{50} region) were negatively affected as evidenced by the large shift to higher temperature and the decrease in their respective slopes. One can speculate that the shift to higher temperature and a slightly lower slope reflects a loss of accessibility to the Co active sites due to its reaction rate limited by pore diffusion.

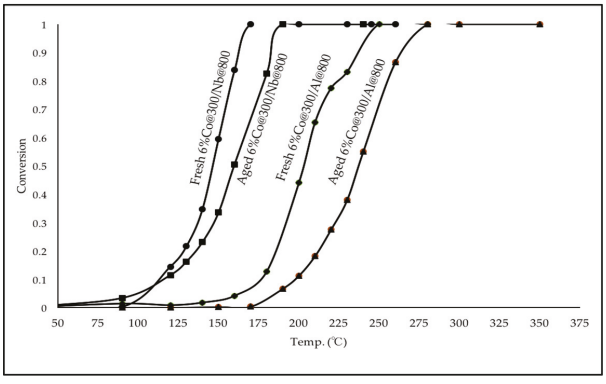

Figure 3. Fresh 6% Co@300/Nb@800, aged 6% Co@300/Nb@800, fresh 6% Co@300/Al@800 and aged 6% Co@300/Al@800 for CO oxidation. Aging was conducted at 400 °C for 12 h with reaction gases flowing. Gas composition: CO 1.5 vol %; O_2 14.5 vol %, N_2 84 vol %. Catalysis volume: 0.1 mL; GHSV: 64,800 (h^{-1}).

2.3. Various Loadings of Co_3O_4 Supported on Nb_2O_5

2.3.1. Catalysts with Various Co_3O_4 Loadings: Propane Oxidation

Various Co_3O_4 loadings were studied to optimize Co_3O_4 content. The oxidation of propane was used as the metric because it is more difficult to oxidize than CO. In Figure 4 (left), three fresh catalysts with cobalt contents, 1%, 3%, and 6% are compared. All three completed propane oxidation up to 400 °C. Not surprisingly 6% Co@300/Nb@800 shows the best catalytic performance. The sensitivity of performance to cobalt loading confirms that the activity is in the kinetic regime suitable for activity comparison.

In Figure 4 (right), all cobalt oxides on niobium oxide were aged at 400 °C for 12 h in reaction propane gas.

Detailed information of these Co@300/Nb@800 are provided in Table 4. It is clear that 6% Co@300/Nb@800 presents the lowest T_{20}, T_{50}, and T_{90} over the entire conversion profile.

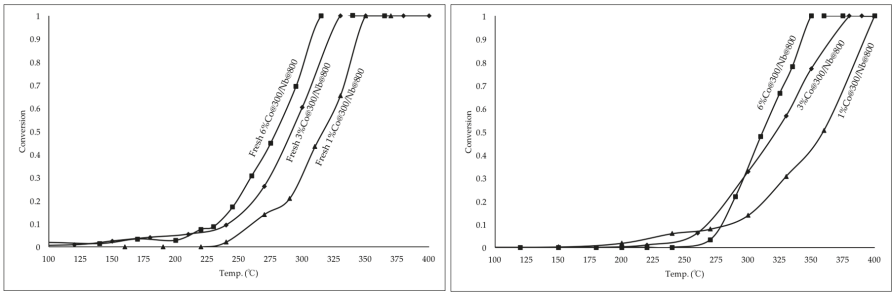

Figure 4. Fresh Co@300/Nb@800 with loadings of 1%, 3%, and 6%, for propane oxidation (**left**); aged Co@300/Nb@800 for propane oxidation (**right**). Aging was conducted at 400 °C with reaction gases for 12 h. Gas composition: C_3H_8 0.1 vol %, O_2 18.9 vol %, N_2 81 vol %. Catalysis volume: 0.1 mL, GHSV: 64,800 (h^{-1}).

Table 4. Co@300/Nb@800 with various cobalt loadings for propane oxidation: fresh and aged.

Catalyst	T_{20} (°C)	T_{50} (°C)	T_{90} (°C)
Fresh 6% Co@300/Nb@800	250	280	305
Aged 6% Co@300/Nb@800	290	310	340
Fresh 3% Co@300/Nb@800	260	270	310
Aged 3% Co@300/Nb@800	285	320	360
Fresh 1% Co@300/Nb@800	290	315	345
Aged 1% Co@300/Nb@800	315	355	390

2.3.2. Propane Oxidation with and without Moisture

Results for both fresh 6% Co@300/Nb@800 and 6% Co@300/Al@800, are presented in Figure 5. Once again, the superiority of fresh 6% Co@300/Nb@800 relative to the baseline 6% Co@300/Al@800 is demonstrated.

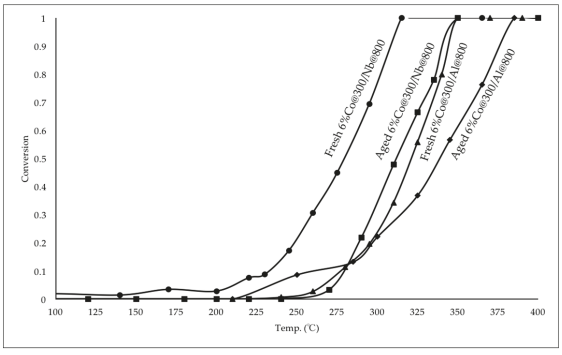

Figure 5. Fresh and aged 6% Co@300/Nb@800 and 6% Co@300/Al@800 for propane oxidation. Aging was conducted at 400 °C with reaction gases for 12 h. Gas composition: C_3H_8 0.1 vol %, O_2 18.9 vol %, N_2 81 vol %. Catalysis volume: 0.1 mL, GHSV: 64,800 (h^{-1}).

Moisture (from upstream combustion) is always present and typically has a poisoning or inhibiting effect on the performance of the catalyst. Tests were conducted with a feed containing 5% H_2O (steam) for both 6% Co@300/Nb@800 and 6% Co@300/Al@800. In Figure 6, fresh and aged 6% Co@300/Nb@800 and 6% Co@300/Al@800 are compared for propane oxidation with 5% H_2O

present. 6% Co@300/Nb@800 retains much of its activity, and is far more resistant to deactivation than 6% Co@300/Al@800. However, moisture does inhibit 6% Co@300/Nb@800, but far less than for the 6% Co@300/Al@800.

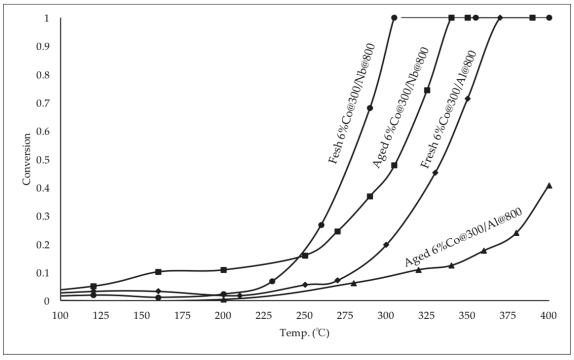

Figure 6. Fresh and aged 6% Co@300/Nb@800 and 6% Co@300/Al@800 for propane oxidation with moisture. Aging test was conducted at 400 °C with reaction gases for 12 h. Gas composition with H_2O 5 vol %, C_3H_8 0.1 vol %, O_2 17.85 vol %, N_2 77.05 vol %. Catalysis volume: 0.1 mL, GHSV: 64,800 (h^{-1}).

This figure also demonstrates the obvious advantage of 6% Co@300/Nb@800 over 6% Co@300/Al@800 when both catalysts were aged for 12 h in feed gas containing H_2O at 5 vol %. The aged 6% Co@300/Al@800 lost the majority of its active sites achieving only about 40% (0.4) conversion at 400 °C. Aged 6% Co@300/Nb@800 showed significant catalytic activity even after being aged in steam containing reaction gas at 400 °C for 12 h.

2.4. Comparison of Co_3O_4 and Pt for Propane Oxidation

The state of the art catalyst used in VOC abatement is typically 1% Pt/Al_2O_3. For the purpose of a practical application, the behavior of 1% Co@300/Nb@800 and 6% Co@300/Nb@800 was compared with 1% Pt/Nb@800 and 1% Pt/Al@800 for propane oxidation. The result shown in Figure 7 (left) indicates that 6% Co@300/Nb@800 shows a performance advantage over 1% Pt@500/Nb@800 and 1% Pt@500/Al@800. Some advantage for 1% Co@300/Nb@800 is noted at both low and higher conversions however, diffusional effects may be operative. 1% Pt@500/Nb@800 shows no advantage over 1% Pt@500/Al@800. Figure 7 (right) shows results of 1% Co@300/Nb@800, 6% Co@300/Nb@800 and 1% Pt@500/Nb@800 subjected to aging test at 400 °C for 12 h in air. The 6% cobalt system suffers slightly, relative to the Pt system, at light off but recovers its performance advantage as 100% conversion is approached. From these encouraging results, monolith-supported catalysts will be prepared in the future and comparison extended closer to an actual system.

Tables 5 and 6 exhibit T_{20}, T_{50}, and T_{90} of Co catalysts and Pt catalysts showed in Figure 7. The advantages 6% Co@300/Nb@800 over 1% Pt@500/Nb@800 are clear to see.

Table 5. T_{20}, T_{50}, and T_{90} of fresh Co catalysts and Pt catalysts for propane oxidation.

Catalysts	T_{20} (°C)	T_{50} (°C)	T_{90} (°C)
6% Co@300/Nb@800	250	280	305
1% Co@300/Nb@800	290	315	345
1% Pt@500/Nb@800	275	325	370
1% Pt@500/Al@800	275	340	370

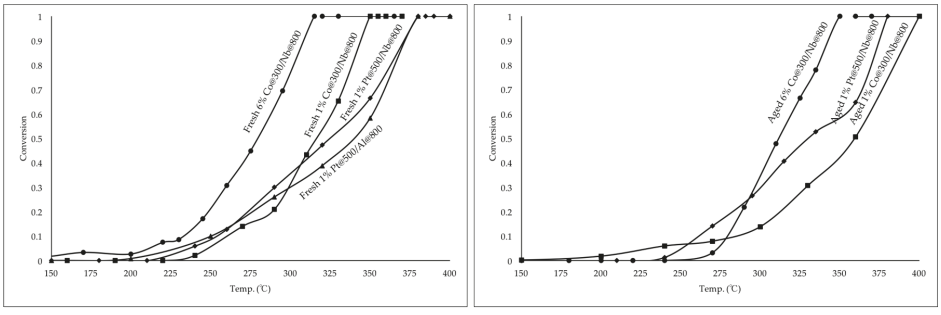

Figure 7. Fresh cobalt oxide catalyst and fresh platinum catalyst for propane oxidation (**left**); aged cobalt oxide and aged platinum on niobium oxide for propane oxidation (**right**). Impregnated platinum catalysts were calcined at 500 °C. Aging was conducted at 400 °C with reaction gases for 12 h. C_3H_8 0.1 vol %, O_2 18.9 vol %, N_2 81 vol %. Catalysis volume: 0.1 mL; GHSV: 64,800 (h^{-1}).

Table 6. T_{20}, T_{50}, and T_{90} of aged Co catalysts and Pt catalysts for propane oxidation.

Catalysts	T_{20} (°C)	T_{50} (°C)	T_{90} (°C)
6% Co@300/Nb@800	290	310	340
1% Co@300/Nb@800	315	355	390
1% Pt@500/Nb@800	290	335	375

2.5. Other Base Metal Oxides for Propane Oxidation

Based on the encouraging results with 6% Co@300/Nb@800 for both CO and C_3H_8 the study was expanded to include nickel (Ni), copper (Cu) and iron (Fe) each deposited on Nb@800 and Al@800. A comparison is shown in Figure 8 (left) for propane oxidation. All four base metal oxides were prepared with a loading of 6% on Nb@800. It is clear that Co_3O_4 on Nb_2O_5 has lowest light-off and full oxidation performance. Aging for 12 h at 400 °C in reacting gases also showed the superiority of the cobalt system. Figure 8 (right) shows results that Nb_2O_5 has a much greater promoting effects on Co_3O_4 than on NiO.

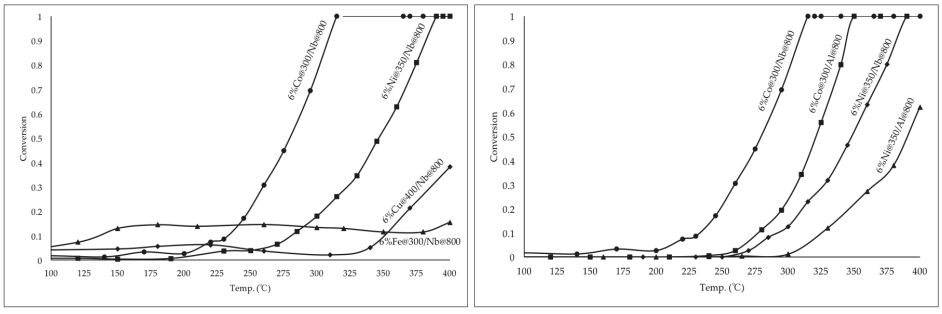

Figure 8. Different metal oxides (6%) on Nb@800 for propane oxidation (**left**); 6% Co_3O_4 and 6% NiO on different carriers for propane oxidation (**right**). The iron catalysts were calcined at 300 °C, impregnated nickel catalysts were calcined at 350 °C, and impregnated copper catalysts were calcined at 400 °C. C_3H_8 0.1 vol %, O_2 18.9 vol %, N_2 81 vol %. Catalyst volume: 0.1 mL; GHSV: 64,800 (h^{-1}).

2.6. Cobalt Oxide Catalyst Characterization

BET Tests for Catalysts and Carriers

Surface area of the carrier is among the most fundamentally important properties in catalysis because the active sites are present or dispersed throughout the internal surface through which reactants and products are transported [2]. Quantachrome ChemBET Pulsar TPR/TPD is used to measure surface area of Al_2O_3 and Nb_2O_5.

A 50 mg sample is used for Al_2O_3 and 6% Co_3O_4/Al_2O_3; 200 mg sample is used for Nb_2O_5 and 6% Co_3O_4/Nb_2O_5. Figure 9 shows that Nb_2O_5 pre-calcined at 500 °C has a surface area of 53 m^2/g. When pre-calcined at 700 °C, Nb_2O_5 has a surface area decrease to 5 m^2/g, while at 800 °C it, decreased to 2 m^2/g. Meanwhile, Al_2O_3 has a 100 times larger surface area than Nb_2O_5. After pre-calcined at 800 °C Al_2O_3 still has a surface area of about 120 m^2/g. Nb_2O_5 has no surface area stability advantages over Al_2O_3, indicating some other interaction of Nb_2O_5 and Co_3O_4 gives rise to the enhancement of activity. In Figure 10 (left), when 6% Co_3O_4 is impregnated onto Nb_2O_5, the total surface area increases. But the final surface area is still very small compared to the surface area of Al_2O_3. Figure 10 (right) shows no change in surface area after Co impregnation.

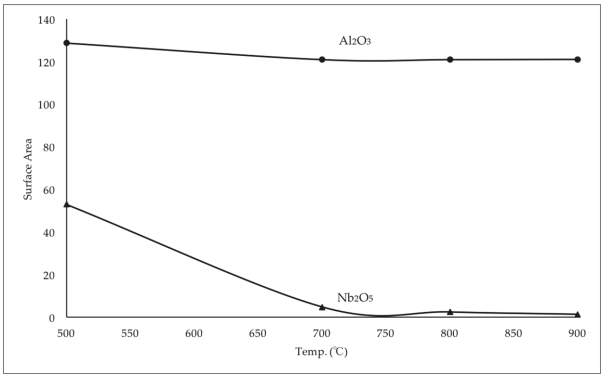

Figure 9. Surface area of Al_2O_3 and Nb_2O_5 pre-calcined at different temperatures. BET test was conducted on Quantachrome ChemBET Pulsar TPR/TPD carrier gas is 30% N_2/He.

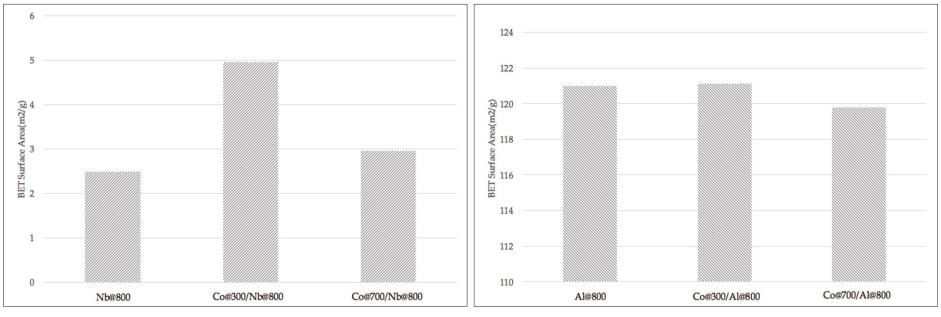

Figure 10. Comparison between Co_3O_4/Nb_2O_5 and Nb_2O_5 (**left**); comparison between Co_3O_4/Al_2O_3 and Al_2O_3 (**right**). BET test was conducted on Quantachrome ChemBET Pulsar TPR/TPD, carrier gas is 30% N_2/He.

3. Materials and Methods

3.1. Carrier Preparation

Niobium Oxide Hydrate ($Nb_2O_5 \cdot 5H_2O$) was received from CBMM Brazil (Sao Paolo, Brazil). Alumina (gamma-Al_2O_3) was provided by BASF (Iselin, NJ, USA). Both Nb_2O_5 and Al_2O_3 were pre-calcined at various temperatures prior to deposition of cobalt nitrate hydrate ($Co(NO_3)_2 \cdot 6H_2O$).

3.2. Catalyst Preparation

Incipient wetness was used for metal impregnations. In order to determine the required volume to fill the pores, water was slowly added to the calcined carrier until saturation was achieved. The precursor salt was dissolved in this precise amount of water, which was then added to the carrier. It was dried in air at 130 °C for one hour and then calcined in air to various temperatures as shown in the Results and Discussion section.

3.2.1. Co-Containing Catalyst Preparation

The cobalt nitrate impregnated catalyst was dried at 130 °C for 1 h in air to remove all the water and then calcined at 300 °C in air to completely decompose the precursor salt for 2 h. The heating rate was 10 °C/min. Cobalt catalysts were prepared with loadings from 1%, 3% to 6% on both carriers. Percentages are based on the metal oxide component.

3.2.2. Pt-Containing Catalysts Preparation

A water soluble platinum amine salt, which is alkali and halide free, provided by BASF (Iselin, NJ, USA), was used for preparation of the Pt catalyst using incipient wetness. 1% Pt/Nb_2O_5 and 1% Pt/Al_2O_3 were prepared with the 800 °C pre-calcined carriers. Drying was accomplished 130 °C in air and the final calcination at 500 °C for 2 h in air at a heating rate of 10 °C/min.

3.3. Reactor Test

3.3.1. Reactor Preparation

The 0.1 mL (about 0.08–0.09 g) of finished catalyst was uniformly mixed with about 0.75 g of diluent quartz to maintain the bed temperature approximately constant. Air and propane (1% C_3H_8 in N_2 were introduced into the reactor. The reactor quartz tubing was 10.5 mm (ID) × 12.75 mm (OD) with a length of 50 cm with XC-course quartz frit provided by Quartz Scientific, Inc. Harbor, OH, USA to support the catalyst.

3.3.2. Reactor Gas Flow Rate

The volume of catalyst used for all experiments was 0.1 mL and the total volumetric flow rate was 108 mL/min. Thus the GHSV was set at 64,800 h^{-1}.

$$GHSV = \frac{Flow\ Rate\ (STP)}{Catalyst\ Volume} = \frac{108\ \text{mL/min}}{0.1\ \text{mL}} = 1080\ \text{min}^{-1} = 64,800\ \text{h}^{-1}$$

Reactor Gas Flow without Steam for CO Oxidation

21% O_2/N_2 with flow rate 75 mL/min and 4.94% CO/N_2 with flow rate 33 mL/min was used as reactant gases. Flow rates are measured at room temperature of 25 °C and pressure of 1 atm. The GHSV here is: 64,800 h^{-1}. Rotameters were calibrated with a soap film bubble meter and used to control flow rates.

Reactor Gas Flow without Steam for Propane Oxidation

21% O_2/N_2 at flow rate of 97.2 mL/min and 1% C_3H_8/N_2 at a flow rate of 10.8 mL/min was used as reactant gases giving C_3H_8 = 0.1% C_3H_8 or 1000 ppm. All flow rates were measured at room temperature of 25 and pressure of 1 atm. The GHSV here was: 64,800 h^{-1}. Rotameters were calibrated with a soap film bubble meter and used to control flow rates.

Reactor Gas Flow with Steam for Propane Oxidation

Twenty-one percent O_2/N_2 at a flow rate of 91.8 mL/min, 1% C_3H_8/N_2 at a flow rate of 10.8 mL/min and H_2O (steam) was introduced giving a flow rate of 5.4 mL/min. This gives 0.1% C_3H_8 with 5% steam and balance air. Liquid water was injected into the reactor connected into a heated transfer line. The heating tape was set at 150 °C; sufficiently high to generate a homogenous gaseous mixture. The GHSV here is 64,800 h^{-1}. Rotameters were calibrated with a soap film bubble meter and used to control flow rate.

3.4. Data Management

3.4.1. Data Acquisition

Catalytic oxidations were carried out in a fixed-bed quartz flow reactor at atmospheric pressure. A cold trap was placed at the outlet to condense water produced during the reaction prior to entering the gas chromatography (GC). Effluent gases of O_2, CO, CO_2, C_3H_8 and N_2 were analyzed by the micro GC. The temperature of the catalyst bed was measured by a K-type thermocouple and controlled by Omega CN7800 series temperature controller. An INFICON 3000 Micro GC, East Syracuse, NY, USA was used to analyze gas composition. Five single runs were conducted at each temperature. The GC was calibrated using 4 different certified standard gases before measurement.

3.4.2. Data Processing

Raw data from the GC was managed and analyzed in Excel to obtain plots of conversion as a function of temperature. The inlet catalyst temperature was increased and held until steady conversion was achieved. The temperature was controlled by a thermocouple located inside the reactor immediately above the catalyst inlet and connected to the MELLEN TEMPERATURE CONTROLLER. The temperature was increased in increments of 10 °C and the conversion measured.

Conversion of CO and C_3H_8 oxidation at each temperature point is as follows:

$$CO(Conversion)\% = \frac{CO_{(initial)} - CO_{(exit)}}{CO_{(inital)}} \times 100\% \quad (3)$$

$$C_3H_8(Conversion)\% = \frac{C_3H_{8(initial)} - C_3H_{8(exit)}}{C_3H_{8(initial)}} \times 100\% \quad (4)$$

The oxidation reaction of CO and C_3H_8 to CO_2 is as follows:

$$CO + \frac{1}{2}O_2 \rightarrow CO_2 \quad (1)$$

$$C_3H_8 + 5O_2 \rightarrow 3CO_2 + 4H_2O \quad (2)$$

3.5. Aging Test

The aging temperature was maintained at 400 °C for 12 h in the reactant gases, followed by the generation of a conversion vs. temperature profile.

4. Conclusions

The pre-calcination temperature of the Nb_2O_5 carrier of 800 °C with cobalt calcined at 300 °C gives the best fresh and aged performance for both CO and propane oxidation. Nb_2O_5 shows a significant advantage over Al_2O_3 as the carrier. Six percent Co@300/Nb@800 has better fresh catalytic performance, higher thermal stability and greater resistance to steam than its counterpart, 6% Co@300/Al@800. Co_3O_4/Nb_2O_5 demonstrates increasing catalytic performance with Co_3O_4 loading from 1% to 6%. 6% Co@300/Nb@800 outperforms 1% Pt@500/Nb@800 for both fresh and aged states. Nb_2O_5 promotes Co_3O_4 and fresh NiO. However there is no advantage for CuO and Fe_2O_3 compared to the traditional Al_2O_3 carrier. Additionally, 6% Ni@350/Nb@800 has poor thermal stability relative to 6% Co@300/Nb@800. Therefore, 6% Co@300/Nb@800 is a viable candidate for replacing 1% Pt@500/Al@800 even though some small decrease in GHSV may be necessary to insure equal performance. However, this will not negatively affect the cost advantage of Co_3O_4 compared to Pt-containing catalysts. Naturally, candidate catalysts must be deposited on monolith and subjected to real VOC feed streams before a definitive recommendation can be made regarding replacement for Pt.

Acknowledgments: The authors are indebted to CBMM, San Paolo, Brazil, for their financial support. The authors especially want to thank Rogerio Ribas of CBMM and Robson Monteiro of Catalysis Consultoria Ltda for valuable contributions throughout these studies.

Author Contributions: Wendi Xiang designed the experiments under instruction of Robert J. Farrauto. Xiaochen Han conducted most of the propane experiments, and Jennifer Astorsdotter conducted most of the CO experiments. Both Wendi Xiang and Xiaochen Han analyzed the data and prepared this paper. Robert J. Farrauto is the only advisor for this research and contributed substantially to the editing of this paper.

Conflicts of Interest: The authors declare no conflict of interest.

References

1. Leung, E.; Shimizu, A.; Barmak, K.; Farrauto, R. Copper oxide catalyst supported on niobium oxide for CO oxidation at low temperatures. *Catal. Commun.* **2017**. [CrossRef]
2. Heck, R.M.; Farrauto, R.J.; Gulati, S.T. *Catalytic Air Pollution Control: Commercial Technology*, 3rd ed.; John Wiley and Sons: Hoboken, NJ, USA, 2012.
3. Liotta, L.F. Catalytic oxidation of volatile organic compounds on supported noble metals. *Appl. Catal. B Environ.* **2010**, *100*, 403–412. [CrossRef]
4. Spivey, J.J. Complete catalytic oxidation of volatile organics. *Ind. Eng. Chem. Res.* **1987**, *26*, 2165–2180. [CrossRef]
5. Duprez, D.; Cavani, F. *Handbook of Advanced Methods and Processes in Oxidation Catalysis "from Laboratory to Industry"*; Imperial College Press: London, UK, 2014; Chapters 1–8.
6. Busca, G.; Daturi, M.; Finocchio, E.; Lorenzelli, V.; Ramis, G.; Willey, R.J. Transition metal mixed oxides as combustion catalysts: Preparation, characterization and activity mechanisms. *Catal. Today* **1997**, *33*, 239–249. [CrossRef]
7. Thormahlen, P.; Thormählen, P.; Skoglundh, M.; Fridell, E.; Andersson, B. Low-Temperature CO Oxidation over Platinum and Cobalt Oxide Catalysts. *J. Catal.* **1999**, *188*, 300–310. [CrossRef]
8. Solsona, B.; Vázquez, I.; Garcia, T.; Davies, T.E.; Taylor, S.H. Complete oxidation of short chain alkanes using a nanocrystalline cobalt oxide catalyst. *Catal. Lett.* **2007**, *116*, 116–121. [CrossRef]
9. Glisenti, A.; Pacella, M.; Guiotto, M.; Natile, M.M.; Canu, P. Largely Cu-doped $LaCo_{1-x}Cu_xO_3$ perovskites for TWC: Toward new PGM-free catalysts. *Appl. Catal. B Environ.* **2016**, *180*, 94–105. [CrossRef]
10. Tauster, S.J.; Fung, S.C.; Baker, R.T.; Horsley, J.A. Strong interactions in supported-metal catalysts. *Science* **1981**, *211*, 1121–1125. [CrossRef] [PubMed]
11. Hu, Z.; Nakamura, H.; Kunimori, K.; Asano, H.; Uchijima, T. Ethane hydrogenolysis and hydrogen chemisorption over niobia-promoted rhodium catalysts: A new phase by a strong rhodium-niobia interaction. *J. Catal.* **1988**, *112*, 478–488. [CrossRef]
12. Leung, E.; Lin, Q.; Farrauto, R.J.; Barmak, K. Oxygen storage and redox properties of Nb-doped ZrO_2-CeO_2-Y_2O_3 solid solutions for three-way automobile exhaust catalytic converters. *Catal. Today* **2016**, *277*, 227–233. [CrossRef]

13. Sasaki, K.; Zhang, L.; Adzic, R.R. Niobium oxide-supported platinum ultra-low amount electrocatalysts for oxygen reduction. *Phys. Chem. Chem. Phys. PCCP* **2008**, *10*, 159–167. [CrossRef] [PubMed]
14. Sun, Y.; Lv, P.; Yang, J.Y.; He, L.; Nie, J.C.; Liu, X.; Li, Y. Ultrathin Co_3O_4 nanowires with high catalytic oxidation of CO. *Chem. Commun.* **2011**, *47*, 11279–11281. [CrossRef] [PubMed]
15. Xie, X.; Li, Y.; Liu, Z.-Q.; Haruta, M.; Shen, W. Low-temperature oxidation of CO catalysed by Co_3O_4 nanorods. *Nature* **2009**, *458*, 746–749. [CrossRef] [PubMed]
16. Ehrhardt, C.; Gjikaj, M.; Brockner, W. Thermal decomposition of cobalt nitrato compounds: Preparation of anhydrous cobalt (II) nitrate and its characterisation by Infrared and Raman spectra. *Thermochim. Acta* **2005**, *432*, 36–40. [CrossRef]
17. Yan, L.; Rui, X.; Chen, G.; Xu, W.; Zou, G.; Luo, H. Recent advances in nanostructured Nb-based oxides for electrochemical energy storage. *Nanoscale* **2016**, *8*, 8443–8465. [CrossRef] [PubMed]
18. Wefers, K.; Misra, C. *Oxides and Hydroxides of Aluminum*; Alcoa Laboratories: East Saint Louis, IL, USA, 1987.

catalysts

MDPI

Article

Carbon-Modified Mesoporous Anatase/TiO_2(B) Whisker for Enhanced Activity in Direct Synthesis of Hydrogen Peroxide by Palladium

Rui Tu [1], Licheng Li [2], Suoying Zhang [1], Shuying Chen [1], Jun Li [1,*] and Xiaohua Lu [1,*]

[1] State Key Laboratory of Materials-Oriented Chemical Engineering, College of Chemical Engineering, Nanjing Tech University, Nanjing 210009, China; ruitu@njtech.edu.cn (R.T.); iamsyzhang@njtech.edu.cn (S.Z.); csy1002@njtech.edu.cn (S.C.)

[2] College of Chemical Engineering, Nanjing Forestry University, Nanjing 210037, China; llc0024@yahoo.com

* Correspondence: lijun@njtech.edu.cn (J.L.); xhlu@njtech.edu.cn (X.L.); Tel.: +86-25-8358-8063 (X.L.)

Academic Editor: Morris D. Argyle
Received: 16 March 2017; Accepted: 22 May 2017; Published: 2 June 2017

Abstract: The regulation of the interaction between H_2O_2 and its catalysts is a promising route to achieve high productivity and selectivity towards H_2O_2. Herein, mesoporous anatase/TiO_2(B) whisker (mb-TiO_2) modified with heterogeneous carbon was prepared as the support of Pd-based catalysts for the direct synthesis of H_2O_2. The morphology and structure of the catalyst were investigated by transmission electron microscopy, X-ray diffraction, Raman spectroscopy, Brunner-Emmet-Teller measurements, and X-ray photoelectron spectroscopy. The interaction between H_2O_2 and the support was studied by isothermal calorimeter. The carbon heterogeneous modification can weaken the interaction between H_2O_2 and the support, then accelerate the desorption of H_2O_2 and reduce the re-adsorption of H_2O_2 in the reaction medium. Meanwhile, the synergistic effects between TiO_2 and Pd nanoparticles are not influenced by the heterogeneous carbon distribution. The catalyst exhibits better performance for the synthesis of H_2O_2 compared with the corresponding unmodified catalyst; the productivity of H_2O_2 increases more than 40%, which can be ascribed to the decrease of further H_2O_2 conversion under the weakened interaction.

Keywords: direct synthesis of H_2O_2; mesoporous anatase/TiO_2(B) whisker; carbon modification; palladium; H_2O_2 desorption; isothermal microcalorimetry

1. Introduction

As a green and excellent oxidant, hydrogen peroxide (H_2O_2) has been widely applied in the pulp/paper industry, water purification, and chemical synthesis [1]. With the increasing demand for H_2O_2 in the international market, the direct synthesis of H_2O_2 from hydrogen and oxygen is believed to be a promising route because of its remarkable advantages [2–7], such as its lower levels of environmental pollution and lower cost. However, three inevitable side reactions in the direct synthesis process, including the combustion of H_2 and the hydrogenation/decomposition of H_2O_2, reduce the productivity and selectivity towards H_2O_2, which is the major drawback of this process [2,4,8].

The surface property of the support has been proved to have an important effect on the performance of H_2O_2 synthesis. For example, the hydrophilic/hydrophobic moderation of the support is an efficient approach to improve the catalytic activity. As early as the 1970s, Pd catalysts supported on more hydrophobic materials were prepared to improve the productivity of H_2O_2 [9]. Hu et al. came to similar conclusions; they speculated further that more hydrophilic support might increase the re-adsorption of H_2O_2, resulting in the further conversion of H_2O_2 and the lower selectivity of H_2O_2 synthesis [8]. In addition, the crystal phase of the support surface can also lead to the enhancement of

catalytic performance by the suppression of side reactions. TiO_2 is a promising candidate support for H_2O_2 synthesis and has been widely studied [10–12]. According to our previous work with assistance from molecular dynamic simulations [13], it has been indicated that introducing the proper amount of TiO_2(B) phase in the catalyst surface can accelerate the desorption of H_2O_2 from the catalyst due to the weak interaction between H_2O_2 and TiO_2(B), and consequently improve the productivity of H_2O_2 over Pd-TiO_2(B)/anatase catalyst.

In fact, the interaction between H_2O_2 and the support is the origin of the support effect according to the analysis mentioned above, and the selectivity and productivity of H_2O_2 is thus influenced by the moderation of the interaction between H_2O_2 and the support. Carbon-modified TiO_2 has been proved to weaken the adsorption of polar molecules and accelerate their transfer [14]. Meanwhile, the carbon modification method is facile, inexpensive, and minimally changes the structure of supports. Herein, we fabricated a heterogeneous carbon-modified catalyst for the direct synthesis of H_2O_2 on the basis of mesoporous anatase/TiO_2(B) whisker (mb-TiO_2). mb-TiO_2 whisker with excellent performance in various catalytic systems has been successfully prepared in our previous work [15–18]. Carbon heterogeneous surface modification can regulate the adsorption of H_2O_2 on the catalyst surface without changing the strong synergy between active sites and TiO_2. The experimental results showed that the Pd-supported, carbon-modified mb-TiO_2 (C-mb-TiO_2) catalyst exhibited higher productivity and selectivity towards H_2O_2 compared with the unmodified Pd/mb-TiO_2 catalyst. X-ray diffraction (XRD), Raman spectra, transmission electron microscopy (TEM), X-ray photoelectron spectroscopy (XPS), and isothermal microcalorimeter (IMC) characterization techniques were applied to analyze the structure–performance relationship.

2. Results and Discussion

2.1. Structural Characterization of the Catalysts

Figure 1 shows the XRD and Raman patterns of mb-TiO_2, C-mb-TiO_2, and the corresponding Pd-supported catalysts. Five distinct diffraction peaks are assigned to anatase phase of TiO_2 (JCPDF 21-1272) [19]. Meanwhile, the weak observed peaks at 2θ of 14.3°, 28.7° and 43.6° correspond to (001), (002) and (003) of TiO_2(B) phase (JCPDF 35-0088) [20]. Evidently, no extra diffraction peaks of carbon can be found in C-mb-TiO_2, which implies that either the amount of carbon is too little or the generated carbon is amorphous [21]. In addition, the diffraction peaks for Pd are indistinguishable, which may be caused by the low content or good dispersion, as previously reported [22]. The bicrystalline structure was also confirmed by Raman spectra. Peaks at 234 cm^{-1}, 431 cm^{-1} and 469 cm^{-1} are all indexed to the TiO_2(B) phase [13]. The specific crystal structure has been explored in our previous work [15]. As shown in Figure 1b, two Raman bands located at 1300–1450 cm^{-1} (D-band) and 1500–1650 cm^{-1} (G-band) are only observed in C-mb-TiO_2 rather than mb-TiO_2, which verifies the existence of carbon species on the surface of C-mb-TiO_2 [8]. The TG analysis shows that the content of carbon species of C-mb-TiO_2 is less than 1 wt % (seen in Figure S2), and only about one third of mb-TiO_2 surface is covered by the introduced carbon species according to our previous calculation [14].

N_2 adsorption-desorption isotherms were measured at 77 K to characterize the physical and chemical properties of supports and corresponding catalysts, as shown in Figure 2. The typical type IV isotherms according to IUPAC classification are observed for all samples, indicating the presence of a mesoporous structure [17]. The corresponding pore size distribution curves (seen in Figure 2) show a narrow distribution ranging from 5 to 9 nm with a maximum around 7 nm for all samples. Details about the BET surface area and average pore volume/size are summarized in Table 1. It can be seen that the surface area and pore volume of C-mb-TiO_2 are nearly identical to that of mb-TiO_2, indicating that almost nothing has changed in the initial structure of mb-TiO_2 after the carbon modification. Both the average pore size and the pore volume decrease after loading with Pd, which can be ascribed to the adhesion of metallic Pd nanoparticles inside the pores.

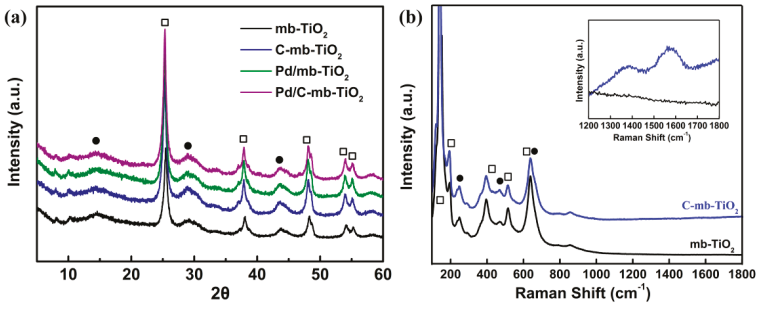

Figure 1. (**a**) XRD pattern and (**b**) Raman spectra of the samples. (□ anatase, ● TiO_2(B)).

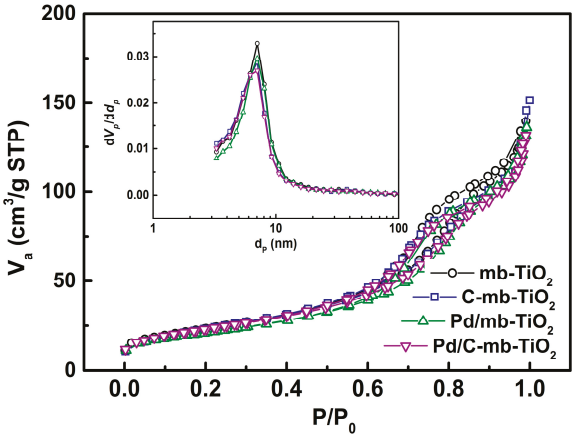

Figure 2. N_2 adsorption-desorption isotherms and the pore-size distribution of the samples.

Table 1. Structural properties of the supports and catalysts.

Sample	Surface Area ($m^2 \cdot g^{-1}$)	Pore Volume ($cm^3 \cdot g^{-1}$)	Average Pore Size (nm)
mb-TiO_2	82.2	0.22	10.5
C-mb-TiO_2	81.8	0.22	10.4
Pd/mb-TiO_2	78	0.20	10.2
Pd/C-mb-TiO_2	79	0.19	10.1

To obtain more information about the surface morphology, the samples were characterized by SEM and HRTEM. Figure S1 shows the SEM images of C-mb-TiO_2, which is fibrous whisker with a uniform width of 300–400 nm, and the morphology shows little change from the mb-TiO_2. The structure of Pd-supported C-mb-TiO_2 was further studied by HRTEM and ED mapping. Well-crystallized TiO_2(B) can be observed in Figure 3a; the nanocrystal with lattice fringes of 0.38 nm is assigned to d_{003} of TiO_2(B) facet, and the lattice fringe spacing of 0.35 nm corresponds to d_{101} of anatase [15], with the majority being the anatase phase. Furthermore, we find that the evident anatase phase is covered by a thin area without crystal lattice fringes (see the two yellow dot lines in Figure 3b), which can be ascribed to the generated amorphous carbon species [21], and is consistent with the results of the Raman analysis. Figure 3c shows that the Pd particles are closed to the carbon and anatase phases, but it is difficult to obtain the accurate positioning of Pd from HRTEM images. The loading of Pd is confirmed by elemental mapping, as shown in Figure 3d. The blue regions represent the presence of

Pd on the surface of TiO_2 in the TEM maps. The relatively low levels of carbon cannot be distinguished due to the external introduction of the carbon source during the testing process. The average particle size of Pd on C-mb-TiO_2 (11.2 nm) is very close to that on mb-TiO_2 (10.5 nm), indicating that the size effect of the Pd particles can be ignored.

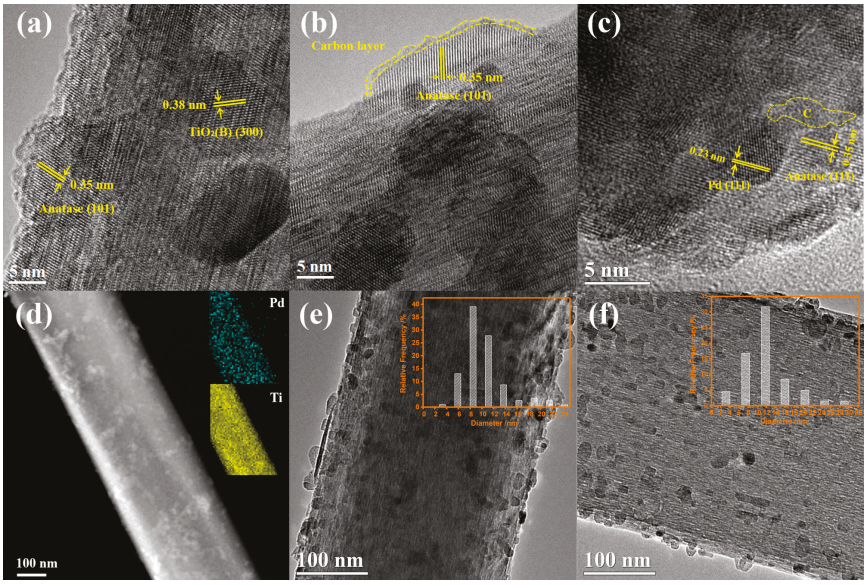

Figure 3. TEM images of the samples: (**a**–**e**) Pd/C-mb-TiO_2 and (**f**) Pd/mb-TiO_2; (**d**) Elemental Pd and Ti maps of Pd/C-mb-TiO_2.

Figure 4 shows the Pd3d core-level spectra of the fresh catalysts. The binding energies at 336.6 and 341.9 eV are ascribed to $Pd^{2+}3d_{5/2}$ and $Pd^{2+}3d_{3/2}$, respectively [23]. The binding energy position of Pd^0 and Pd^{2+} is unchanged between the two catalysts. The presence of Pd^{2+} in the fresh reduced sample is caused by TiO_2-assisted partial oxidation of Pd^0 when exposed to air. As shown in Table S1, the ratio of Pd^{2+}/Pd^0 of the two catalysts is very similar, indicating that the property of active sites is not affected by the carbon heterogeneous modification [11,13]. According to the literature focusing on carbon riveted supported catalysts, the electronic structure of the supported metal would be altered obviously when the generated carbon species are in intimate contact with metallic particles [24,25]. Therefore, it can be deduced that most of the Pd particles deposit onto the TiO_2 phase.

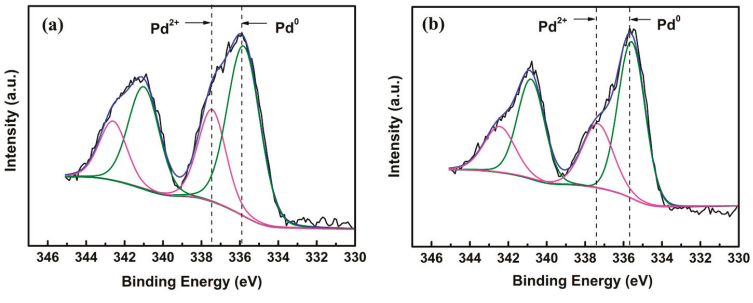

Figure 4. XPS Pd3d spectroscopy of (**a**) Pd/mb-TiO_2 and (**b**) Pd/C-mb-TiO_2.

2.2. The Adsorption Properties of H_2O_2 on the Supports

Isothermal calorimeter was used to investigate the adsorption properties of H_2O_2 on the supports. The adsorption thermodynamic data was calculated from the calorimetric profile recorded through in situ monitoring; the actual amount of adsorbed H_2O_2 was confirmed by the colorimetric method. Finally, their ratio (the adsorption energy of H_2O_2) can be used to represent the interaction strength between H_2O_2 and the support. The detailed process is described in Electronic Supplementary Information (ESI). Figure 5 shows the data of the adsorption properties of H_2O_2 on the support. It can be seen that the adsorption heat of H_2O_2 on C-mb-TiO_2 is obviously lower than that on mb-TiO_2, meaning that the adsorption of H_2O_2 on C-mb-TiO_2 is weaker. The value of adsorption heat of H_2O_2 indicates a reversible physical adsorption. In other words, the generated H_2O_2 is more easily desorbed from the C-mb-TiO_2 surface and H_2O_2 in the reaction medium is more difficult to re-adsorb on the support.

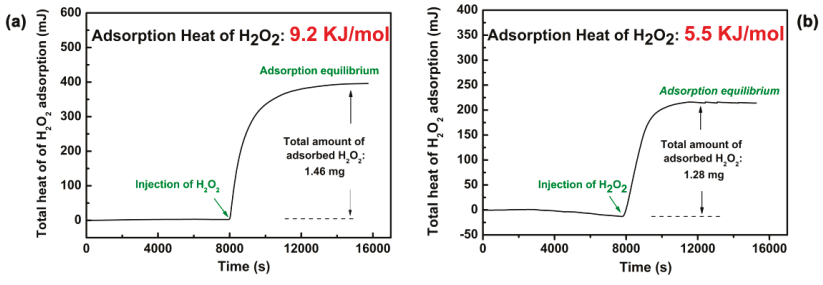

Figure 5. Adsorption heat of H_2O_2 in the studied TiO_2 samples: (**a**) mb-TiO_2 and (**b**) C-mb-TiO_2.

2.3. The Catalytic Activity of the Catalysts

The direct synthesis of H_2O_2 from H_2 and O_2 over Pd/mb-TiO_2 and Pd/C-mb-TiO_2 catalysts were investigated at 283 K and ambient pressure. As shown in Figure 6a, the conversion of H_2 shows little variation over time, while the selectivity and productivity of H_2O_2 decrease along with the time for both catalysts. The Pd/C-mb-TiO_2 catalyst exhibits better activity for H_2O_2 synthesis. The conversion of H_2 over Pd/C-mb-TiO_2 is approximately 35% higher than that over Pd/mb-TiO_2. The Pd/mb-TiO_2 catalyst shows H_2O_2 productivity of 1933 and 1717 mmol/g_{Pd}/h after 0.5 h and 1h, respectively, while the corresponding productivity on Pd/C-mb-TiO_2 is 2848 and 2411 mmol/g_{Pd}/h with an improvement of more than 40%. Meanwhile, the H_2O_2 selectivity over Pd/C-mb-TiO_2 is also promoted by 9% when compared with that over Pd/mb-TiO_2. The analysis above indicates that the catalyst performance is significantly improved due to the carbon modification. Notably, the catalytic performance of both the Pd/mb-TiO_2 and Pd/C-mb-TiO_2 are superior to the Pd/P25 catalyst [4,8,11], which is widely investigated for the direct synthesis of H_2O_2.

To further unveil the effect of the support, we also performed the decomposition and hydrogenation of H_2O_2 under N_2 and N_2/H_2 atmospheres, respectively, which are the two main side reactions in the direct synthesis of H_2O_2. As illustrated in Figure 6b, neither of the catalysts showed activity for the decomposition of H_2O_2 in pure N_2 flow. When the H_2/N_2 mixture was fed into the reactor, the H_2O_2 was catalytically hydrogenated to form H_2O, demonstrating that the hydrogenation of H_2O_2 is mainly responsible for the productivity and selectivity in this system. Similar results have also been observed for Pd/P25 [26]. Furthermore, it is observed that Pd/C-mb-TiO_2 exhibits much lower hydrogenation rate than Pd/mb-TiO_2. Willock et al. suggested that the production of H_2O_2 takes place at the interface between the particle and TiO_2 [27]. Therefore, it is reasonable for us to assume that the properties of both active sites and supports have great impact on the catalytic synthesis of H_2O_2. Additionally, in our previous work, we confirmed that the accelerated desorption of

H_2O_2 from the support can decrease the hydrogenation rate of H_2O_2 and then improve the selectivity towards H_2O_2 over the corresponding catalyst [13]. As mentioned above, the presence of carbon species can significantly weaken the interaction between H_2O_2 and the catalyst under the premise of similar property of active sites. Therefore, it can be concluded that the weaker interaction can reduce the concentration of H_2O_2 on the surface of the catalyst and then decrease the hydrogenation rate of H_2O_2. In addition, the improvement of H_2O_2 desorption can provide more reactive sites for H_2O_2 formation. As a result, the enhanced selectivity of H_2O_2 and the conversion of H_2 improve the productivity of H_2O_2.

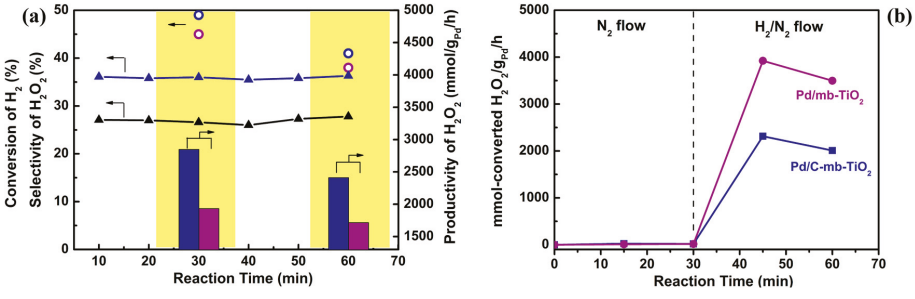

Figure 6. (**a**) H_2 conversion, H_2O_2 selectivity and productivity, and (**b**) decomposition and hydrogenation of H_2O_2 over Pd/mb-TiO_2 and Pd/C-mb-TiO_2. (Blue color indicates Pd/C-mb-TiO_2, purple color indicates Pd/mb-TiO_2. Filled triangles: H_2 conversion. Open circles: H_2O_2 selectivity. Histogram: H_2O_2 productivity).

3. Materials and Methods

3.1. Synthesis of Carbon-Modified TiO_2 Whisker

First, the mesoporous and bicrystalline TiO_2 whisker was prepared according to our previous report [15]. Briefly, $K_2Ti_2O_5$ was suspended in 0.1 M H_2SO_4 solution with vigorous stirring to form $H_2Ti_2O_5$. The suspension was filtered and washed, following which it was dried at 353 K under vacuum and then calcinated at 723 K for 2 h in muffle to obtain mesoporous and bicrystalline TiO_2 whisker. The final catalyst was denoted as mb-TiO_2.

The carbon-modified mb-TiO_2 was prepared as follows [14]. 1 g of mb-TiO_2 was dispersed in 20 mL of dichloromethane containing 0.377 g of benzenephosphonous acid. After stirring for 24 h, the precipitation was filtered and washed with water/acetone (50/50 by volume) solution, and then dried in an oven at 373 K. The dried sample was treated at 673 K in Ar gas flow for 4 h and denoted as C-mb-TiO_2.

3 wt % Pd-supported catalysts were prepared by incipient wetness impregnation. A certain amount of $PdCl_4^{2-}$ solution was slowly dropped into the support under stirring. The paste was left in natural environment for 4 h, following which it was dried at 383 K overnight. Prior to the reaction, all the catalysts were reduced at 573 K in H_2 (40 mL·min^{-1}) for 1 h. For comparison, commercial titania (P25, Degussa Co., Frankfurt am Main, Germany) was loaded with Pd using the same method.

3.2. Catalyst Characterization

X-ray diffraction (XRD) Spectrogram was collected on a D8 Advance X-ray diffractometer operating at a 40 kV with a current of 100 mA with Cu-Kα radiation. The data was collected in the 2θ range from 5° to 60° at a rate of 0.2 s step^{-1}. Raman spectroscopy (Horiba HR 800) with a multichannel air-cooled CCD camera detector was employed to determine the surface crystal phases of supports using a 514.5 nm He-Cd laser beam. Nitrogen adsorption/desorption at −196 °C were achieved by using the TriStarII 3020M machine (Micromeritics Instrument Co., Atlanta, GA, USA). Surface area was

calculated by the BET method; pore volume was determined by N_2 adsorption at a relative pressure of 0.99. The Pd content of the catalysts was confirmed by ICP-AES (PerkinElmer Co., Waltham, MA, USA). SEM for the morphology of catalyst samples was taken by an America Quanta200 environmental scanning electron microscope. The information of dispersion and size of Pd nanoparticles were obtained by high-resolution transmission electron microscopy (HRTEM) performed on a Japan JEM-2100 at 200 kV. XPS was recorded by an AXIS UltraDLD spectrometer with the monochromatic Al Ka X-ray source. The interaction between H_2O_2 and the support was characterized on a TAM air Calorimeter from TA Instruments.

3.3. Catalytic Reaction

The direct synthesis of H_2O_2 was performed under atmosphere pressure in a glass tri-phase reactor. The reagent gases ($H_2/O_2/N_2$ = 9:36:15) with a total flow rate of 60 mL/min were premixed in a steel mixer, and then introduced into the reactor via a frit fixed at the bottom. The temperature of 60 mL slurry containing 50 mg catalyst and 0.38 mL H_2SO_4 was controlled at 10 °C through the water circulated jacket. Vigorous stirring (950 rpm) was adopted to minimize mass transfer resistance. The outlet of the reactor was linked to a gas chromatography equipped with a 5A molecular sieve packed column and a thermal conductivity detector (SP-6890, Rainbow Chemical Instrument Co., Jinan, China), which helped to continuously analyze the conversion of H_2. The concentration of H_2O_2 in the medium was determined by the colorimetric method after the complexation with a $TiOSO_4/H_2SO_4$ reagent using a UV-vis spectrophotometer (UV-2802S, Unico (Shanghai) Instrument Co., Shanghai, China) at a wavelength of 400 nm. The selectivity of H_2O_2 ($S_{H_2O_2}$) was calculated from the following formula:

$$S_{H_2O_2} = \frac{\text{rate of } H_2O_2 \text{ formation (mol/min)}}{\text{rate of } H_2 \text{ conversion (mol/min)}} \times 100\% \quad (1)$$

The reaction of H_2O_2 hydrogenation and decomposition was also implemented. The process was similar to that described above except for the initial composition of reaction medium. H_2O_2 was added to ethanol solution with the concentration of 0.25 wt %, then the decomposition and hydrogenation of H_2O_2 were tested under a flow of pure N_2 (60 mL/min) and a flow of H_2/N_2 (9:51 mL/min), respectively. The same tests using bare supports or the absence of catalysts were also performed under the conditions mentioned above.

4. Conclusions

In this work, a simple heterogeneous carbon modification was applied to introduce carbon species on the surface of mb-TiO_2. Pristine mb-TiO_2 and carbon-modified mb-TiO_2 were used as the supports of Pd-based catalysts for the direct synthesis of H_2O_2. The interaction between H_2O_2 and the supports was characterized by isothermal microcalorimetry. It was demonstrated that the carbon-decorated TiO_2 exhibited weaker interaction with H_2O_2 than that achieved with the pristine TiO_2. Therefore, the carbon-modified catalyst can effectively accelerate the desorption of H_2O_2 from the catalyst surface and reduce the re-adsorption of H_2O_2 in the reaction medium, which benefits the decrease of side reaction and the improvement of H_2O_2 productivity. Meanwhile, the properties of metallic active sites are not influenced by the carbon modification. As a result, the Pd/C-mb-TiO_2 shows better performance for the direct synthesis of H_2O_2 compared with Pd/mb-TiO_2. More than 40% increase in the productivity of H_2O_2 was achieved, and the selectivity of H_2O_2 improved by 9%. In addition, the catalytic performance of both Pd/mb-TiO_2 and Pd/C-mb-TiO_2 are superior to Pd/P25, which is widely investigated for the direct synthesis of H_2O_2. Hence, heterogeneous carbon modification represents a promising approach to tune the properties of the catalysts, as demonstrated here with TiO_2-supported Pd catalyst for H_2O_2 synthesis.

Supplementary Materials: The following are available online at www.mdpi.com/2073-4344/7/6/175/s1, Figure S1: SEM images of (a,b) mb-TiO_2 and (c,d) C-mb-TiO_2, Figure S2: TG and DSC curves of C-mb-TiO_2,

Figure S3: The scheme of reaction process, Table S1: Quantified XPS data for the surface Pd atoms, Table S2: Calorimetric measurement of H_2O_2 adsorption, Table S3: The performance of Pd catalysts for H_2O_2 synthesis, decomposition and hydrogenation.

Acknowledgments: This work was supported by the National Key Basic Research Program of China (2013CB733505, 2013CB733501), the National Natural Science Foundation of China (Nos. 91334202, 21406118), the Natural Science Foundation of Jiangsu Province of China (BK2012421, BK20160993), the Postdoctoral Science Foundation of China (2016M591837), the Research Fund for the Doctoral Program of Higher Education of China (20123221120015), and the Project for Priority Academic Program Development of Jiangsu Higher Education Institutions (PAPD).

Author Contributions: Rui Tu, Jun Li and Xiaohua Lu designed the framework of experiments; Rui Tu and Shuying Chen performed all the experimental work; Rui Tu analyzed the experimental data and wrote the paper; Licheng Li, Suoying Zhang and Jun Li participated in the modification of the article.

Conflicts of Interest: The authors declare no conflict of interest.

References

1. Campos-Martin, J.M.; Blanco-Brieva, G.; Fierro, J.L. Hydrogen peroxide synthesis: An outlook beyond the anthraquinone process. *Angew. Chem. Int. Ed.* **2006**, *45*, 6962–6984. [CrossRef] [PubMed]
2. Landon, P.; Collier, P.J.; Papworth, A.J.; Kiely, C.J.; Hutchings, G.J. Direct formation of hydrogen peroxide from H_2/O_2 using a gold catalyst. *Chem. Commun.* **2002**, *18*, 2058–2059. [CrossRef]
3. Samanta, C. Direct synthesis of hydrogen peroxide from hydrogen and oxygen: An overview of recent developments in the process. *Appl. Catal. A Gen.* **2008**, *350*, 133–149. [CrossRef]
4. Edwards, J.K.; Hutchings, G.J. Palladium and gold-palladium catalysts for the direct synthesis of hydrogen peroxide. *Angew. Chem. Int. Ed.* **2008**, *47*, 9192–9198. [CrossRef] [PubMed]
5. Garcia, T.; Murillo, R.; Agouram, S.; Dejoz, A.; Lazaro, M.J.; Torrente-Murciano, L.; Solsona, B. Highly dispersed encapsulated Au-Pd nanoparticles on ordered mesoporous carbons for the direct synthesis of H_2O_2 from molecular oxygen and hydrogen. *Chem. Commun.* **2012**, *48*, 5316–5318. [CrossRef] [PubMed]
6. Edwards, J.K.; Solsona, B.; Ntainjua, N.E.; Carley, A.F.; Herzing, A.A.; Kiely, C.J.; Hutchings, G.J. Switching off hydrogen peroxide hydrogenation in the direct synthesis process. *Science* **2009**, *323*, 1037–1041. [CrossRef] [PubMed]
7. Yi, Y.; Wang, L.; Li, G.; Guo, H. A review on research progress in the direct synthesis of hydrogen peroxide from hydrogen and oxygen: Noble-metal catalytic method, fuel-cell method and plasma method. *Catal. Sci. Technol.* **2016**, *6*, 1593–1610. [CrossRef]
8. Hu, B.; Deng, W.; Li, R.; Zhang, Q.; Wang, Y.; Delplanque-Janssens, F.; Paul, D.; Desmedt, F.; Miquel, P. Carbon-supported palladium catalysts for the direct synthesis of hydrogen peroxide from hydrogen and oxygen. *J. Catal.* **2014**, *319*, 15–26. [CrossRef]
9. Fu, L.; Chuang, K.T.; Fiedorow, R. Selective oxidation of hydrogen to hydrogen peroxide. *Stud. Surf. Sci. Catal.* **1992**, *72*, 33–41.
10. Ouyang, L.; Da, G.; Tian, P.; Chen, T.; Liang, G.; Xu, J.; Han, Y. Insight into active sites of Pd–Au/TiO_2 catalysts in hydrogen peroxide synthesis directly from H_2 and O_2. *J. Catal.* **2014**, *311*, 129–136. [CrossRef]
11. Ouyang, L.; Tian, P.; Da, G.; Xu, X.; Ao, C.; Chen, T.; Si, R.; Xu, J.; Han, Y. The origin of active sites for direct synthesis of H_2O_2 on Pd/TiO_2 catalysts: Interfaces of Pd and PdO domains. *J. Catal.* **2015**, *321*, 70–80. [CrossRef]
12. Edwards, J.K.; Ntainjua, E.; Carley, A.F.; Herzing, A.A.; Kiely, C.J.; Hutchings, G.J. Direct synthesis of H_2O_2 from H_2 and O_2 over gold, palladium, and gold-palladium catalysts supported on acid-pretreated TiO_2. *Angew. Chem. Int. Ed.* **2009**, *48*, 8512–8515. [CrossRef] [PubMed]
13. Tu, R.; Chen, S.; Cao, W.; Zhang, S.; Li, L.; Ji, T.; Zhu, J.; Li, J.; Lu, X. The effect of H_2O_2 desorption on achieving improved selectivity for direct synthesis of H_2O_2 over TiO_2(B)/anatase supported Pd catalyst. *Catal. Commun.* **2017**, *89*, 69–72. [CrossRef]
14. Li, L.; Zhu, Y.; Lu, X.; Wei, M.; Zhuang, W.; Yang, Z.; Feng, X. Carbon heterogeneous surface modification on a mesoporous TiO_2-supported catalyst and its enhanced hydrodesulfurization performance. *Chem. Commun.* **2012**, *48*, 11525–11527. [CrossRef] [PubMed]
15. Li, W.; Liu, C.; Zhou, Y.; Bai, Y.; Feng, X.; Yang, Z.; Lu, L.; Lu, X.; Chan, K. Enhanced photocatalytic activity in anatase/TiO_2(B) core-shell nanofiber. *J. Phys. Chem. C* **2008**, *112*, 20539–20545. [CrossRef]

16. Li, W.; Bai, Y.; Liu, C.; Yang, Z.; Feng, X.; Lu, X.; van der Laak, N.K.; Chan, K. Highly thermal stable and highly crystalline anatase TiO_2 for photocatalysis. *Environ. Sci. Technol.* **2009**, *43*, 5423–5428. [CrossRef] [PubMed]
17. Bai, Y.; Li, W.; Liu, C.; Yang, Z.; Feng, X.; Lu, X.; Chan, K. Stability of Pt nanoparticles and enhanced photocatalytic performance in mesoporous Pt-(anatase/TiO_2(B)) nanoarchitecture. *J. Mater. Chem.* **2009**, *19*, 7055–7061. [CrossRef]
18. Li, L.; Shi, K.; Tu, R.; Qian, Q.; Li, D.; Yang, Z.; Lu, X. Black TiO_2(B)/anatase bicrystalline TiO_{2-x} nanofibers with enhanced photocatalytic performance. *Chin. J. Catal.* **2015**, *36*, 1943–1948. [CrossRef]
19. Ji, T.; Li, L.; Wang, M.; Yang, Z.; Lu, X. Carbon-protected Au nanoparticles supported on mesoporous TiO_2 for catalytic reduction of p-nitrophenol. *RSC Adv.* **2014**, *4*, 29591–29594. [CrossRef]
20. Huang, J.; Yuan, D.; Zhang, H.; Cao, Y.; Li, G.; Yang, H.; Gao, X. Electrochemical sodium storage of TiO_2(B) nanotubes for sodium ion batteries. *RSC Adv.* **2013**, *3*, 12593–12597. [CrossRef]
21. Chao, K.; Cheng, W.; Yu, T.; Lu, S. Large enhancements in hydrogen production of TiO_2 through a simple carbon decoration. *Carbon* **2013**, *62*, 69–75. [CrossRef]
22. He, Y.; Feng, J.; Du, Y.; Li, D. Controllable synthesis and acetylene hydrogenation performance of supported Pd nanowire and cuboctahedron catalysts. *ACS Catal.* **2012**, *2*, 1703–1710. [CrossRef]
23. Datye, A.K.; Bravo, J.; Nelson, T.R.; Atanasova, P.; Lyubovsky, M.; Pfefferle, L. Catalyst microstructure and methane oxidation reactivity during the Pd↔PdO transformation on alumina supports. *Appl. Catal. A Gen.* **2000**, *198*, 179–196. [CrossRef]
24. Jiang, Z.; Wang, Z.; Chu, Y.; Gu, D.; Yin, G. Ultrahigh stable carbon riveted Pt/TiO_2-C catalyst prepared by in situ carbonized glucose for proton exchange membrane fuel cell. *Energy Environ. Sci.* **2011**, *4*, 728–735. [CrossRef]
25. Song, W.; Chen, Z.; Yang, C.; Yang, Z.; Tai, J.; Nan, Y.; Lu, H. Carbon-coated, methanol-tolerant platinum/graphene catalysts for oxygen reduction reaction with excellent long-term performance. *J. Mater. Chem. A* **2015**, *3*, 1049–1057. [CrossRef]
26. Ao, C.; Tian, P.; Ouyang, L.; Da, G.; Xu, X.; Xu, J.; Han, Y. Dispersing Pd nanoparticles on N-doped TiO_2: A highly selective catalyst for H_2O_2 synthesis. *Catal. Sci. Technol.* **2016**, *6*, 5060–5068. [CrossRef]
27. Thetford, A.; Hutchings, G.J.; Taylor, S.H.; Willock, D.J. The decomposition of H_2O_2 over the components of Au/TiO_2 catalysts. *Proc. R. Soc. A* **2011**, *467*, 1885–1899. [CrossRef]

catalysts

MDPI

Article

Structural Changes of Highly Active Pd/MeO$_x$ (Me = Fe, Co, Ni) during Catalytic Methane Combustion

Dominik Seeburg [1], Dongjing Liu [1,2], Joerg Radnik [1,3], Hanan Atia [1], Marga-Martina Pohl [1], Matthias Schneider [1], Andreas Martin [1] and Sebastian Wohlrab [1,*]

[1] Leibniz Institute for Catalysis at the University of Rostock, Albert-Einstein-Str. 29a, D-18059 Rostock, Germany; dominik.seeburg@catalysis.de (D.S.); liudongjing19@163.com (D.L.); joerg.radnik@bam.de (J.R.); hanan.atia@catalysis.de (H.A.); marga-martina.pohl@catalysis.de (M.-M.P.); m.schneider51@gmx.de (M.S.); a.martin.1955@gmx.de (A.M.)

[2] School of Energy and Power Engineering, Jiangsu University, Xuefu Str. 301, Zhenjiang 212013, China

[3] Federal Institute of Materials Testing and Research (BAM), Unter den Eichen 44-46, D-12203 Berlin, Germany

* Correspondence: sebastian.wohlrab@catalysis.de; Tel.: +49-381-1281-328

Received: 15 December 2017; Accepted: 19 January 2018; Published: 23 January 2018

Abstract: Fe_2O_3, Co_3O_4 and NiO nanoparticles were prepared via a citrate method and further functionalized with Pd by impregnation. The pure oxides as well as Pd/Fe_2O_3, Pd/Co_3O_4, and Pd/NiO (1, 5 and 10 wt % Pd) were employed for catalytic methane combustion under methane lean (1 vol %)/oxygen rich (18 vol %, balanced with nitrogen) conditions. Already, the pure metal oxides showed a high catalytic activity leading to complete conversion temperature of $T_{100} \leq 500$ °C. H_2-TPR (Temperature-programmed reduction) experiments revealed that Pd-functionalized metal oxides exhibited enhanced redox activity compared to the pure oxides leading to improved catalytic combustion activity at lower temperatures. At a loading of 1 wt % Pd, 1Pd/Co_3O_4 (T_{100} = 360 °C) outperforms 1Pd/Fe_2O_3 (T_{100} = 410 °C) as well as 1Pd/NiO (T_{100} = 380 °C). At a loading of 10 wt % Pd, T_{100} could only be slightly reduced in all cases. 1Pd/Co_3O_4 and 1Pd/NiO show reasonable stability over 70 h on stream at T_{100}. XPS (X-ray photoelectron spectroscopy) and STEM (Scanning transmission electron microscopy) investigations revealed strong interactions between Pd and NiO as well as Co_3O_4, respectively, leading to dynamic transformations and reoxidation of Pd due to solid state reactions, which leads to the high long-term stability.

Keywords: methane total oxidation; methane slip; methane removal; carbon dioxide; combustion

1. Introduction

Nowadays, methane is being considered as a renewable energy carrier [1]. However, it is a questionable development since methane possesses a 25 times higher greenhouse gas potential [2], and low temperature exhaust gas streams from combustion engines contain up to 5000 ppm of unburned methane [3]. Hence, the reduction of methane emissions is addressed to novel catalysts, which are highly active at low temperature over time on stream. However, such catalysts are still not yet available.

Pure oxide catalysts, like perovskites [4], are ineligible due to their high temperature demand. It is well known that palladium or platinum are the most efficient active components for the complete oxidation of methane at lower temperature [5]. Particularly, redox active metal oxides can enhance the catalytic performance of Pd active sites via a Mars–van-Krevelen mechanism [6,7]. Redox active supports increase the activity of Pd and provide an enhanced stability on stream [8–11]. Moreover, nanoscale catalysts offer a higher interface and more efficiency for the exhaust gas catalysis [12].

The catalytic activity of Pd is size dependent and increases with increasing particle size due to weakening of the Pd-O bonding [13]. Hoffmann et al. found that a retained redox activity of surface CeO_2 can further enhance the catalytic activity and stability [14]; however, at T_{100}, slight activity loss over the first hours on stream was observed.

Huge differences in methane activation abilities have been observed for Pd functionalized Fe, Co and Ni oxides. The reported temperatures of complete combustion differ tremendously by several hundred degrees centigrade, e.g., T_{100} = 365 °C for (1 wt %) Pd/Co_3O_4 [15], T_{100} = 540 °C for (1 wt %) Pd/NiO [16] and T_{100} = 700 °C for (1 wt %) Pd/Fe_2O_3 [16]. Out of the iron group elements, only Co based oxide catalysts were described in literature efficient enough for low temperature methane combustion [17–25]. Moreover, Pd/Co_3O_4 coatings on open cell foams already demonstrated a realistic application potential [26].

In this work, we show that a citrate based synthesis method for Fe_2O_3, Co_3O_4 and NiO nanoparticles as well as a targeted Pd deposition onto these oxides leads to convergence of the methane dry combustion performance for all these catalysts. Moreover, strong interactions between Pd and NiO as well as Pd and Co_3O_4 were recorded over time, leading to a change of the nature of the active sites, which is discussed according to XPS (X-ray photoelectron spectroscopy) and TEM (Transmission electron microscopy) data.

2. Results and Discussion

2.1. Catalytic Performance in Methane Combustion

The three oxides, Fe_2O_3, Co_3O_4 and NiO, were prepared from their nitrate precursors under comparable conditions using a citrate method followed by impregnation with a $Pd(NO_3)_2{\cdot}2H_2O$ aqueous solution to obtain 1, 5 and 10 wt % Pd loading. Figure 1 shows the catalytic combustion of 1 vol % methane in mixture with 18 vol % O_2 and 81 vol % N_2 over the pure oxides as well as over the $1Pd/MeO_x$ (1 wt % Pd) catalysts. In all tests, carbon dioxide was the only carbonaceous product.

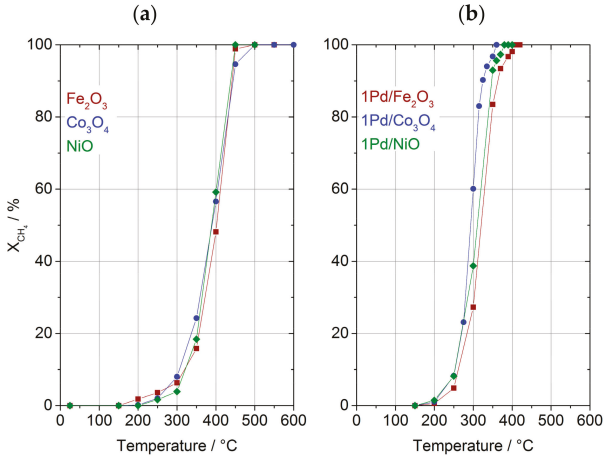

Figure 1. Catalytic activity tests for methane combustion, feed gas consisting of CH_4:O_2:N_2 = 1:18:81, GHSV (Gas hourly space velocity) = 22,500 $L{\cdot}kg^{-1}{\cdot}h^{-1}$: (**a**) Fe_2O_3, Co_3O_4, NiO (**b**) $1Pd/Fe_2O_3$, $1Pd/Co_3O_4$, 1Pd/NiO.

The light off curves obtained from the reaction over the three pure metal oxide catalysts show nearly the same activity in methane oxidation and reach full conversion at 450 °C in case of NiO and 500 °C in case of Fe_2O_3, and Co_3O_4, respectively. The combustion temperature decreases of

about 100–150 °C by functionalization of the metal oxides with 1 wt % Pd and full conversion over $1Pd/Co_3O_4$, 1Pd/NiO, and $1Pd/Fe_2O_3$ is achieved at 360 °C, 380 °C, and 410 °C, respectively (GHSV (Gas hourly space velocity): 22,500 $L \cdot kg^{-1} \cdot h^{-1}$, for GHSV variations: see Figure S1). In comparison, Pd supported on Al_2O_3 performs less efficient due to the inert nature of this kind of support [27–30].

A further decrease in T_{100} is possible by functionalization with a higher Pd-content (5 wt % and 10 wt %) as shown in Figure S2. In the case of $5Pd/MeO_x$ catalysts, $5Pd/Co_3O_4$ shows the lowest T_{100} of 325 °C, $5Pd/Fe_2O_3$ and 5Pd/NiO present a very similar performance with T_{100} of about 340 °C. $10Pd/Co_3O_4$ and 10Pd/NiO have nearly the same performance and reach T_{100} at 315 °C. In comparison to $5Pd/Fe_2O_3$, $10Pd/Fe_2O_3$ surprisingly possesses a reduced activity so that a higher T_{100} of 365 °C for full CH_4 conversion was reached. However, the slightly increased activity does not justify the higher noble metal contents. Hence, we concentrated our further research to the $1Pd/MeO_x$ catalysts.

Figure 2a,b depict long-term tests on stream at ~T_{20} and T_{100} for the three pure metal oxides (over 50 h) and corresponding $1Pd/MeO_x$ catalysts (over 70 h), respectively.

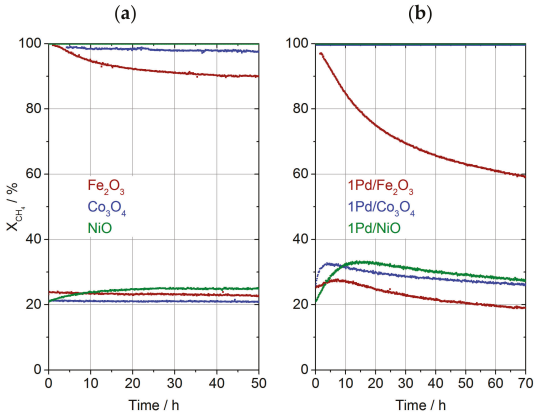

Figure 2. Long-term tests at T_{20} and T_{100}, feed gas consisting of CH_4:O_2:N_2 = 1:18:81, GHSV = 22,500 $L \cdot kg^{-1} \cdot h^{-1}$: (**a**) Fe_2O_3, Co_3O_4, NiO (**b**) $1Pd/Fe_2O_3$, $1Pd/Co_3O_4$, 1Pd/NiO.

The activities of the three pure metal oxides at ~T_{20} show reasonable consistency. Fe_2O_3 and Co_3O_4 show slight deactivation reflected in methane conversion loss from 23.0 to 22.5% and from 21.0 to 20.8%, respectively. Interestingly, NiO undergoes an activation period seen in an increase in methane conversion from 21.0 to 24.5%. At T_{100}, only NiO performs constantly high, whereas Co_3O_4 and Fe_2O_3 deactivate to a certain extent. In the case of Co_3O_4, a minor loss in methane conversion from 100 to 97% is observed, whereas deactivation is more pronounced for Fe_2O_3 indicated in a loss in methane conversion from 100 to 91%. All of the corresponding $1Pd/MeO_x$ catalysts exhibited an initial activation period at ~T_{20} followed by slow deactivation, whereas $1Pd/Fe_2O_3$ is the worst performer. $1Pd/Fe_2O_3$ shows an increase in methane conversion from the start of the experiment from 25.3 to 27.7% after 7.5 h on stream. After reaching a maximum in methane conversion, a slow deactivation takes place and conversion drops down to 19% after 70 h on stream. A better performance was observed using the $1Pd/Co_3O_4$ catalyst. Here, the methane conversion increases from 25.7 to 32.7% after 5 h on stream. Afterwards, the conversion decreases to 26.9% after 70 h on stream. Interestingly, over the 1Pd/NiO catalyst, within 14 h on stream, an increase in conversion from 20.9 to 33.3% is observed, as well as a slow deactivation also occurs after reaching the maximum in methane conversion. Deactivation after 70 h on stream at T_{100} was only observed for $1Pd/Fe_2O_3$, which is reflected in a decrease in methane conversion from 100 to 58%. Importantly, $1Pd/Co_3O_4$ but also 1Pd/NiO perform stable over time at T_{100}.

The applicability of these catalysts under exhaust gas conditions, i.e., in the off-gas of a natural gas combustion engine, was simulated and tested. The catalytic activity tests (exhaust gas test—EGT) were performed in a temperature range from 150 to 500 °C with a feed consisting of 0.1 vol % CH_4, 5.5 vol % CO_2, 9.0 vol % O_2, 10.5 vol % H_2O balanced with N_2 at a modified GHSV of 90,000 $L \cdot kg^{-1}\ h^{-1}$ (Figure 3).

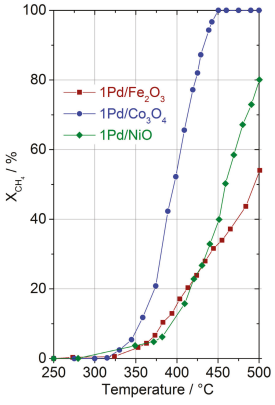

Figure 3. Catalytic activity tests under near exhaust gas condition (EGT) with a feed consisting of 0.1 vol % CH_4, 5.5 vol % CO_2, 9.0 vol % O_2, 10.5 vol % H_2O balanced with N_2 at 90,000 $L \cdot kg^{-1} \cdot h^{-1}$ for 1Pd/Fe_2O_3, 1Pd/Co_3O_4, 1Pd/NiO.

Under these conditions the performance of all 1Pd/MeO_x catalysts is reduced. Accordingly, full conversion was not reached up to 500 °C for Pd/NiO (X_{CH4} = 80%) and Pd/Fe_2O_3 (X_{CH4} = 54%). Only in case of Pd/Co_3O_4 complete conversion was recorded at 450 °C (T_{100}) and above, which is a quite remarkable result considering occurring water caused deactivation processes at this low temperature in general [31].

2.2. Structural Properties and Reducibility of the Catalytic Materials

The obtained specific surface areas of the pure oxides are shown in Table 1. Interestingly, the surface areas of the oxides differ more from each other than their domain sizes. Especially in the case of Co_3O_4, the low surface area can be attributed to more intergrown particles compared to Fe_2O_3, which reduces the effective surface area. From XRD (X-ray diffraction) investigations, the initial oxide phases were identified as Fe_2O_3-hematite (ICSD 088418, [32]), Co_3O_4 in spinel structure (ICSD 027497, [33]), and NiO in a sodium chloride-like structure (ICSD 043740, [34]) (Figure S3a–c).

Table 1. Specific surface areas, Pd-content and MeO_x crystallite sizes.

Material	S_{BET} [1] / $m^2\ g^{-1}$	Pd [2] / wt %	Crystallite Size [3] / nm
Fe_2O_3	18.7		49 (60)
1Pd/Fe_2O_3		1.07	52 (61)
Co_3O_4	2.22		63 (63)
1Pd/Co_3O_4		0.85	55 (63)
NiO	5.25		40 (52)
1Pd/NiO		0.98	38 (48)

[1] derived from Krypton sorption measurements using the BET (Brunauer–Emmett–Teller) method; [2] from ICP-OES (Inductively Coupled Plasma—Optical Emission Spectrometry) data; [3] calculated from the Scherrer equation at representative Fe_2O_3 (012), Co_3O_4 (220) and NiO (111) reflections calculating with the full width half maximum, numbers in brackets are calculated from the reflection area.

Pd crystalline phases were not detectable in $1Pd/MeO_x$ catalysts because of the minor metal content and signal broadening of present Pd nanocrystals (see below). The crystallite domain sizes were estimated based on the Scherrer Equation [35] at the (012) reflection of Fe_2O_3, the (220) reflection of Co_3O_4 and the (111) reflection of NiO and are given in Table 1. No significant change of the metal oxide domain size was observed after impregnation with the Pd precursor and subsequent calcination. The determined Pd loading was in the range of the targeted values (~1 wt %) for all Pd-functionalized metal oxides.

H_2-reduction of the pure MeO_x as well as the $1Pd/MeO_x$ was performed and the specific consumption of hydrogen over temperature is shown in Figure 4. The formation of intermediate phases and their transformation was detected with in situ XRD measurements (Figures S4–S6) showing that the reduction of the pure metal oxides starts at ca. 300 °C in all cases.

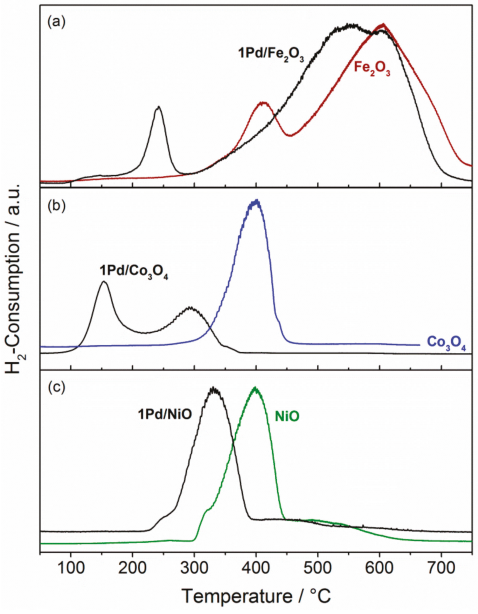

Figure 4. H_2-TPR (Temperature-programmed reduction) profiles of (**a**) Fe_2O_3 and $1Pd/Fe_2O_3$ (**b**) Co_3O_4 and $1Pd/Co_3O_4$, (**c**) NiO and 1Pd/NiO.

The reduction of Co_3O_4 completed at ca. 450 °C and Co metal was detected. For NiO and Fe_2O_3, the required temperatures are remarkably higher at 600 °C and 750 °C, respectively. Only in the case of the iron oxide does an intermediate phase appear and Fe_3O_4 is obtained at ca. 400 °C, which is further reduced to metallic Fe with increasing temperature. In all cases, Pd functionalization decreases the reduction temperature in comparison to the pure metal oxides, presumably, by hydrogen spillover from the Pd to the supports and subsequent reduction of the metal oxides [36]. Additional intermediates appear only in the case of Pd/Co_3O_4 reduction as CoO at around 300 °C, which is subsequently reduced to Co. Generally, the reducibility with H_2 is a good measure to roughly evaluate the redox activity, which can be classified in the following order: $1Pd/Co_3O_4$ >> $1Pd/Fe_2O_3$ > 1Pd/NiO (with onset temperatures of 100 °C, 200 °C, 220 °C, respectively). Since all $1Pd/MeO_x$ catalysts do not differ much under dry oxidation conditions, these differences could help to explain the different activities in the exhaust gas tests. Ciuparu and co-workers found that high oxygen mobility in oxides leads to stronger resistance against water caused deactivation [37]. From the H_2-TPR results, we can assume that surface oxygen activation on $1Pd/Co_3O_4$ occurs at much lower temperature than on the other

catalysts. This behaviour could be reflected in the catalytic methane oxidation under simulated exhaust gas conditions (Figure 3).

HAADF-STEM (High-angle annular dark-field scanning transmission electron microscopy) images of fresh 1Pd/MeO_x (Figure 5) show that Pd (PdO) particles (bright particles) of ca. 2–8 nm are randomly distributed over all the metal oxides. The Pd particles have irregular morphologies with compact height. Particle sizes of MeO_x (Me = Fe, Co, Ni) detected via STEM are in accordance to crystallite domain sizes determined from XRD (Scherrer method).

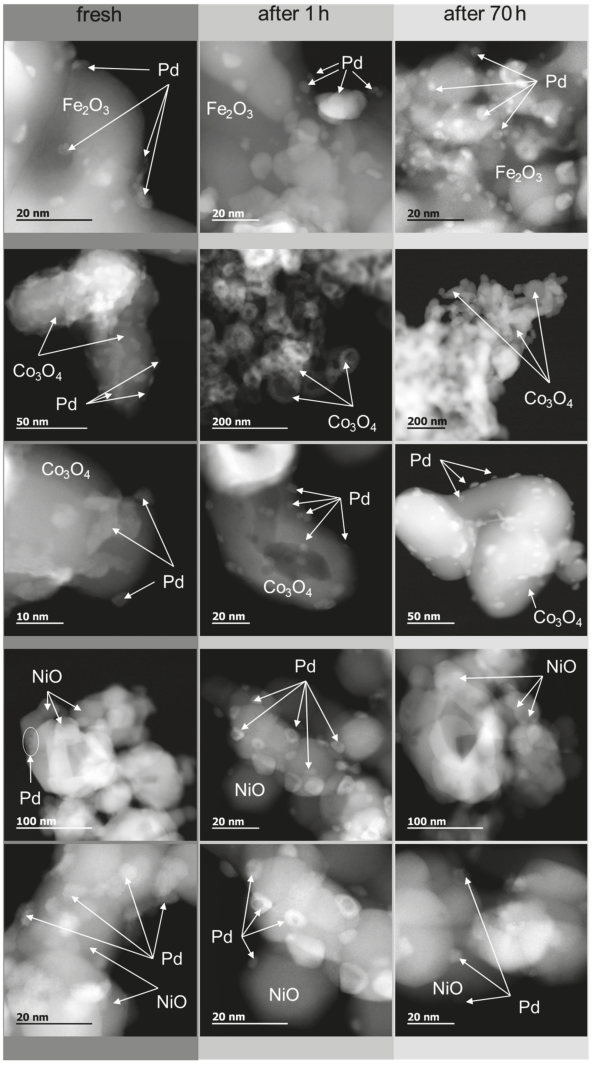

Figure 5. HAADF-STEM (High-angle annular dark-field scanning transmission electron microscopy) images of fresh and spent samples after long-term tests (at T_{100}, feed gas consisting of CH_4:O_2:N_2 = 1:18:81, at 22,500 L·kg^{-1}·h^{-1}): 1Pd/Fe_2O_3, 1Pd/Co_3O_4 and 1Pd/NiO.

2.3. Catalyst Transformation during Time on Stream

Spent 1Pd/MeO_x catalysts were examined via transmission electron microscopy (Figure 5 and Figures S7, S13 and S16). In addition, 1Pd/Co_3O_4 and 1Pd/NiO showed a changed morphology after being used on stream. In the case of 1Pd/Co_3O_4, a sponge-like structure gets visible after 1 h on stream (Figure S12), whereas, after 70 h, the catalyst seems to be restructured. In the case of 1Pd/NiO, holes in the Pd particles are formed and a flat surface coverage of Pd on the NiO surface can be detected after 70 h on stream. Since the Pd phase is located at an oxidic support, EDX (Energy-dispersive X-ray spectroscopy) does not help to reveal the oxidation state of the Pd. When analysing the oxidation states of the Pd particles via FFT (fast Fourier transform), we found mostly PdO in the fresh catalysts, Pd or Pd suboxides in the catalysts after 1 h on stream, and reoxidation to PdO in the catalysts after 1 h on stream (FFT of the high resolution images (see Figures S8–S11, S14, S15, S17 and S18)). However, these investigations are single shots on some particles. Although they show that Pd is present in different oxidation states, a method describing the whole sample was required.

In order to understand the dynamic processes to their full extent, XPS spectra of fresh and spent (after 1 h and 70 h on stream and after tests with simulated exhaust gas) 1Pd/MeO_x were recorded and presented in Figure 6. For all three 1Pd/MeO_x catalysts at the different reaction stages, no significant change in Fe, Co and Ni spectra was observed, which indicates no change in metal oxide phase (Figures S19–S21).

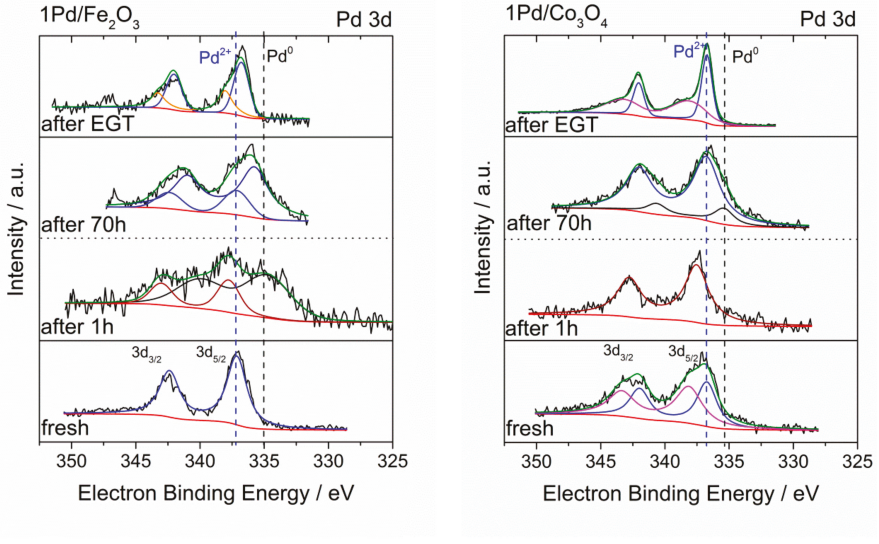

Figure 6. *Cont.*

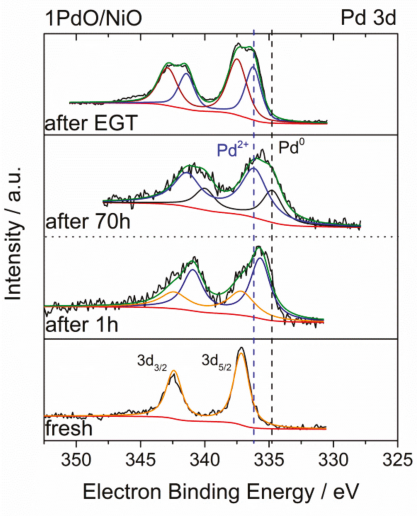

(**c**)

Figure 6. XPS (X-ray photoelectron spectroscopy) spectra of Pd 3d electrons of fresh and spent Pd/MeO_x after long-term tests at T_{100} (feed gas consisting of CH_4:O_2:N_2 = 1:18:81, at 22,500 $L \cdot kg^{-1} \cdot h^{-1}$) as well as after being used for exhaust gas treatment (feed consisting of 0.1 vol % CH_4, 5.5 vol % CO_2, 9.0 vol % O_2, 10.5 vol % H_2O balanced in N_2 at 90,000 $L \cdot kg^{-1} \cdot h^{-1}$): (**a**) $1Pd/Fe_2O_3$, (**b**) $1Pd/Co_3O_4$ and (**c**) 1Pd/NiO.

Typical Pd^{2+} peaks at ca. 336.7 eV [38] are detected in all the fresh $1Pd/MeO_x$. After 1 h on stream at T_{100}, for all $1Pd/MeO_x$ catalysts, changes in the oxidation state of Pd were found. In the case of $1Pd/Fe_2O_3$ and 1Pd/NiO, an increasing amount of metallic Pd was observed. Contrary, PdO was the dominant Pd-species in $1Pd/Co_3O_4$. After 70 h on stream at T_{100}, the amount of PdO in $1Pd/Co_3O_4$ is still high as well as that of 1Pd/NiO increased. In $1Pd/Fe_2O_3$, the highest amount of metallic Pd was found. Moreover, in Pd/Co_3O_4 and Pd/NiO, a peak with an electron binding energy at around 336 eV can be observed, which can be correlated to Pd suboxides. In summary, on Fe_2O_3, metallic Pd dominates after the long-term tests, whereas oxidic Pd is more present on NiO and, especially, on Co_3O_4. The reducibility of Pd depends on the support in the order Fe_2O_3 > NiO > Co_3O_4.

In correlation to the catalytic results, $1Pd/Fe_2O_3$ shows a good initial performance in methane combustion, but, in the long-term test over 70 h at T_{100}, deactivation is observed. This behaviour probably attributes to the lower oxidation potential of the Fe_2O_3 particles to form sufficient content of PdO, which is necessary for methane oxidation. A better performance is observed for 1Pd/NiO. It remains stable without any deactivation until the end of the long-term test at T_{100}, possibly due to restructuring accompanied by reoxidation. This process obviously is driven by the nanoscale Kirkendall effect [39,40] between Pd and NiO during the catalytic methane combustion. $1Pd/Co_3O_4$ possesses the lowest T_{100} and, in the long-term test at T_{100}, also no deactivation is observed. Strong interactions between Pd and Co_3O_4 at the metal oxide interface lead to continuously newly formed active species at the catalyst surface.

After catalytic tests with a simulated exhaust gas (EGT), all spent $1Pd/MeO_x$ contained two Pd species with higher binding energy. Obviously, water acts as an inhibitor for the catalytic cycle and can be responsible for the lower activity of $1Pd/Fe_2O_3$ and 1Pd/NiO compared to $1Pd/Co_3O_4$.

3. Materials and Experimental Details

3.1. Catalyst Preparation

Fe_2O_3, Co_3O_4 and NiO were prepared reproducibly using a citrate method more than three times. First, ethylene glycol (2.48 g, >99%, Carl Roth, Karlsruhe, Germany) was added to a solution of citric acid (57.6 g, >99.5%, Carl Roth, Karlsruhe, Germany) in methanol (150 mL, >99%, Carl Roth, Karlsruhe, Germany). Afterwards, the corresponding metal nitrate (>99.9%, Fluka, Steinheim, Germany) precursors (0.01 mol) were added and esterification from ethylene glycol and metal citrate was performed at 130 °C until 2 h. Subsequently, the solid was treated in vacuum at 180 °C for 2 h. Finally, calcination was performed at 500 °C for 3 h with a heating rate of 2 °C/min. The resulting metal oxides were impregnated by the incipient wetness method with aqueous $Pd(NO_3)_2 \cdot 2H_2O$ (~40% Pd, Carl Roth, Karlsruhe, Germany) solution (M adjusted to the pore volume) to obtain 1 wt %, 5 wt % and 10 wt % Pd loading reproducibly more than three times, hereinafter denoted as $1Pd/MeO_x$ (MeO_x = Fe_2O_3, Co_3O_4 and NiO), $5Pd/MeO_x$ and $10Pd/MeO_x$, respectively. The samples were dried at 80 °C for 12 h and calcined at 400 °C in air (heating rate of 2 °C/min) for 2 h.

3.2. Catalysts Characterization

3.2.1. Kr Corption

The BET specific surface area of the catalysts was measured by Krypton adsorption using an ASAP 2020 instrument from Mircomeritics (Norcross, GA, USA). The samples were heated under vacuum for 30 min at 150 °C before the Krypton adsorption isotherms were measured.

3.2.2. X-ray Powder Diffraction (XRD)

XRD profiles were measured using a STADI P transmission diffractometer from STOE (Darmstadt, Germany). The samples were ground and afterwards analysed applying a curved germanium monochromator in the incident beam path, CuK_α radiation (λ = 0.15406 nm) and a 6° linear position sensitive detector (PSD). The crystallite domain sizes were calculated based on the Scherrer equation at representative Fe_2O_3 (012), Co_3O_4 (220) and NiO (111) reflections.

3.2.3. Element Analysis

A Varian 715-ES inductively coupled plasma-optical emission spectrometer (ICP-OES) (Palo Alto, CA, USA) was used for the determination of the elemental composition of the catalysts after complete dissolution in a solution containing 8 mL of aqua regia and 2 mL hydrofluoric acid.

3.2.4. In Situ X-ray Diffraction (In Situ XRD)

The in situ XRD reduction experiments were carried out on an X'Pert Pro (Panalytical, Almelo, The Netherlands) with a Material-Research-Instrument-TC-basic (Physikalische Geraete GmbH, Karlsruhe, Germany) high temperature chamber to perform reduction with hydrogen at different temperatures. Furthermore, 30 mg of the respective powders were heated indirectly by an AlCr-sheet. The X-ray diffraction patterns were measured every 50 °C (heating rate 10 °C/min) and the reduction atmosphere consisted of 5 vol % H_2 in He (5.0, Air Liquide Germany, Düsseldorf, Germany), with a total flow rate of 10 mL/min.

3.2.5. Temperature Programmed Hydrogen Reduction (H_2-TPR)

Prior to the temperature programmed reduction (H_2-TPR) experiments with 10–20 mg of each sample a preheating for 30 min in air (50 mL/min) to 400 °C was performed. After cooling, the measurement was started. For this purpose, the samples were heated to 700 °C in an H_2:Ar = 5:95 flow with a temperature ramp of 10 °C/min, the final temperature was kept for 1 h, hydrogen

consumption was monitored by an online thermal conductivity detector (Mircomeritics ChemiSorb 2920-Instrument, Norcross, GA, USA).

3.2.6. Scanning Electron Microscopy (SEM)

The SEM measurements were performed at 10.0 kV with a JSM-4701 (JEOL) microscope (Akishima, Tokyo, Japan).

3.2.7. Transmission Electron Microscopy (TEM)

The TEM measurements were performed at 200 kV with an aberration-corrected JEM-ARM200F (JEOL, Corrector: CEOS, Tokyo, Japan). The microscope is equipped with a JED-2300 (JEOL) energy-dispersive X-ray-spectrometer (EDXS) (Akishima, Tokyo, Japan). The aberration corrected STEM imaging (High-Angle Annular Dark Field (HAADF) and Annular Bright Field (ABF)) were performed under the following conditions. HAADF and ABF both were done with a spot size of approximately 0.1 nm, a convergence angle of 30–36° and collection semi-angles for HAADF and ABF of 90–170 mrad and 11–22 mrad, respectively. The solid samples were deposed without any pretreatment on a holey carbon supported Cu-grid (mesh 300) and transferred to the microscope.

3.2.8. X-ray Photoelectron Spectroscopy (XPS)

X-ray photoelectron spectroscopy (XPS) experiments were performed by a VG ESCALAB 220iXL system (VG Scientific, Waltham, MA, USA) with monochromatic Al-K_α-radiation (E = 1486.6 eV). As internal reference, for the electron binding energy, adventitious carbon with a C1s binding energy of 284.8 eV was used. The peaks were fitted with mixed Gaussian–Lorentzian curves after subtracting a Shirley background.

3.3. Catalyst Testing for CH_4 Combustion

CH_4 combustion catalytic tests were performed in a vertical fixed-bed plug-flow quartz tubular reactor (inner diameter of 8 mm) at ambient pressure. In addition, 0.2 g of the powder catalyst was placed in the isothermal reactor zone and fixed by quartz wool (>99.9%, Carl Roth, Karlsruhe, Germany) located downstream below the catalyst bed. The catalytic activity was measured starting from 150 °C with a stepwise increase at a temperature of 50 K steps maximum until full conversion of methane was achieved. At each temperature, methane conversion was recorded threefold within 30 min using an online gas chromatograph (Agilent 7890A, Santa Clara, CA, USA) equipped with a methanizer for flame ionization detection and a thermal conductivity detector. The feed components as well as the reaction products were detected, except water. Each experiment of these series was repeated and the deviation of absolute values was always below 2% for each measuring point. In separate experiments, Fe_2O_3, Co_3O_4, NiO as well as 1Pd/Fe_2O_3, 1Pd/Co_3O_4, 1Pd/NiO were tested under isothermal conditions at T_{20}, T_{100} (the specific temperatures necessary for 20 or 100% methane conversion, respectively) over 50 or 70 h on stream. In all tests, the reactant gas stream consisted of methane (2.5, Air Liquide Germany, Düsseldorf, Germany), oxygen (5.0, Linde, Pullach, Germany) and nitrogen (5.0, Linde, Pullach, Germany) in the ratio of 1:18:81 representing a feed of 1.0 vol % CH_4. The gas flows were controlled with mass flow controllers supplied from MKS Instruments (Andover, MA, USA). The total flow rate was 75 $cm^3 \cdot min^{-1}$ corresponding to ~22,500 $L \cdot kg^{-1} \cdot h^{-1}$.

The light off tests with simulated exhaust gas were performed in a temperature range from 150–500 °C with a heating rate of about 2 $°C \cdot min^{-1}$. The temperature was controlled with a thermocouple inside of a quartz capillary in the middle of the catalyst bed. At 500 °C, the reaction was performed for 1 h; afterwards, the reaction temperature was decreased to 460 °C, 430 °C, 410 °C, 390 °C, 370 °C, 360 °C, and 150 °C; at each temperature, the catalytic performance was measured for 30 min, with a feed consisting of 0.1 vol % CH_4, 5.5 vol % CO_2 (4.5, Linde, Pullach, Germany), 9.0 vol % O_2, 10.5 vol % H_2O (LC-MS-Grade, Carl Roth, Karlsruhe, Germany) balanced with N_2 at a total flow of about 300 $cm^3 \cdot mL^{-1}$ corresponding to a modified GHSV of 90,000 $L \cdot kg^{-1} \cdot h^{-1}$.

The gas flows were controlled with mass flow controllers supplied from MKS Instruments (Andover, MA, USA). Admixing of liquid water was controlled by a mini-Cori-Flow mass flow controller (Bronkhorst High-Tech B.V., Ruurlo, The Netherlands) followed by an evaporation chamber heated to 150 °C in which the gaseous steam was mixed with CH_4, O_2, CO_2 and N_2 before the reactor. Product analysis was carried out without any water condensation online at ca. 180 °C by IR spectral analysis and linear combination of bands to fit the measured spectrum using a Gasmet CX4000 device (Gasmet Technologies, Helsinki, Finland).

4. Conclusions

Fe_2O_3, Co_3O_4 and NiO prepared via citrate method were functionalized with Pd yielding highly active catalysts for catalytic methane dry combustion. The interactions between metal and support lead to different catalytic properties under humid exhaust gas conditions and can be roughly correlated with reducibility measured by H_2-TPR. By comparing the XPS and STEM information at different times on stream, we can conclude in greater detail that (i) different Pd oxidation states on stream, accompanied by (ii) a restructuring of the metal-support structure occurr. Obviously, strong dynamic interactions between Pd and the metal oxide take place, e.g., in the case of 1Pd/NiO Pd-hollow structures are formed, whereas, in the case of 1Pd/Co_3O_4, sponge-like structures of the Co_3O_4 support are being built. These interactions lead to a restructuring accompanied by reoxidation of active sites, which is the origin of the long-term stability over 70 h on stream for 1Pd/NiO and 1Pd/Co_3O_4 at T_{100}.

Supplementary Materials: The following are available online at http://www.mdpi.com/2073-4344/8/2/42/s1, Figure S1: Catalytic activity tests for methane combustion, feed gas consisting of CH_4:O_2:N_2 = 1:18:81, catalyst masses: 300, 200 and 50 mg, catalysts: 1Pd/Fe_2O_3, 1Pd/Co_3O_4 and 1Pd/NiO. Figure S2: Catalytic activity tests for methane combustion, feed gas consisting of CH_4:O_2:N_2 = 1:18:81, at 22,500 $L \cdot kg^{-1} \cdot h^{-1}$: (left) 5Pd/$Fe_2O_3$, 5Pd/$Co_3O_4$, 5Pd/NiO (right) 10Pd/$Fe_2O_3$, 10Pd/$Co_3O_4$, 10Pd/NiO. Figure S3: XRD Diffraction patterns of (a) Fe_2O_3, 1Pd/Fe_2O_3, 5Pd/Fe_2O_3, 10Pd/Fe_2O_3, (b) Co_3O_4, 1Pd/Co_3O_4, 5Pd/Co_3O_4, 10Pd/Co_3O_4 and (c) NiO, 1Pd/NiO, 5Pd/NiO, 10Pd/NiO; * PdO reference (ICSD 24692). Figure S4: In situ XRD under H_2 reduction (a) Fe_2O_3 and (b) 1Pd/Fe_2O_3, 5 vol % H_2 in He, 10 $mL \cdot min^{-1}$ with a heating rate of 10 K/min (slightly higher phase transition temperatures are specific for the method). Figure S5: In situ XRD under H_2 reduction (a) Co_3O_4 and (b) 1Pd/Co_3O_4, 5 vol % H_2 in He, 10 $mL \cdot min^{-1}$ with a heating rate of 10 K/min (slightly higher phase transition temperatures are specific for the method). Figure S6: In situ XRD under H_2 reduction (a) NiO and (b) 1Pd/NiO, 5 vol % H_2 in He, 10 mL/min with a heating rate of 10 K/min (slightly higher phase transition temperatures are specific for the method). Figure S7: HAADF-STEM images of fresh and spent samples after long-term tests (at T_{100}, feed gas consisting of CH_4:O_2:N_2 = 1:18:81, at 22,500 $L \cdot kg^{-1} \cdot h^{-1}$): 1Pd/$Fe_2O_3$. Figure S8: HAADF-STEM, FFT and inverse FFT of fresh 1Pd/Fe_2O_3. Figure S9: HAADF-STEM, FFT and inverse FFT of 1Pd/Fe_2O_3 after 1 h on stream. Figure S10: HAADF-STEM, FFT and inverse FFT of 1Pd/Fe_2O_3 after 1 h on stream. Figure S11: HAADF-STEM, FFT and inverse FFT of 1Pd/Fe_2O_3 after 70 h on stream. Figure S12: SEM images of fresh and spent samples after long-term tests (at T_{100}, feed gas consisting of CH_4:O_2:N_2 = 1:18:81, at 22,500 $L \cdot kg^{-1} \cdot h^{-1}$): 1Pd/$Co_3O_4$. Figure S13: HAADF-STEM images of fresh and spent samples after long-term tests (at T_{100}, feed gas consisting of CH_4:O_2:N_2 = 1:18:81, at 22,500 $L \cdot kg^{-1} \cdot h^{-1}$): 1Pd/$Co_3O_4$. Figure S14: HAADF-STEM, FFT and inverse FFT of 1Pd/Co_3O_4 after 1 h on stream. Figure S15: HAADF-STEM, FFT and inverse FFT of 1Pd/Co_3O_4 after 70 h on stream. Figure S16: HAADF-STEM images of fresh and spent samples after long-term tests (at T_{100}, feed gas consisting of CH_4:O_2:N_2 = 1:18:81, at 22,500 $L \cdot kg^{-1} \cdot h^{-1}$): 1Pd/NiO. Figure S17: HAADF-STEM, FFT and inverse FFT of 1Pd/NiO after 1 h on stream. Figure S18. HAADF-STEM, FFT and inverse FFT of 1Pd/NiO after 70 h on stream. Figure S19: 1Pd/Fe_2O_3-XPS spectra of fresh and spent samples, after 1 h, 70 h and after test with exhaust gas (EGT). Figure S20: 1Pd/Co_3O_4-XPS spectra of fresh and spent samples, after 1 h, 70 h and after test with exhaust gas (EGT). Figure S21: 1Pd/NiO-XPS spectra of fresh and spent samples, after 1 h, 70 h and after test with exhaust gas (EGT).

Acknowledgments: This work is partially supported by the CSC (China Scholarship Council) and DAAD (Deutscher Akademischer Austausch Dienst). The authors gratefully acknowledge Ralph Kraehnert (TU Berlin) for SEM analysis. We thank Anja Simmula for analytical support.

Author Contributions: S.W. and A.M. conceived the project. D.S. conceived, designed and performed the experiments; J.R., H.A., M.-M.P. and M.S. characterized the materials (XPS, TPR, TEM and XRD); D.S., D.L., J.R., M.-M.P. and S.W. analyzed the data; and D.S., D.L. and S.W. wrote the paper.

Conflicts of Interest: The authors declare no conflict of interest.

References

1. Götz, M.; Lefebvre, J.; Mörs, F.; McDaniel Koch, A.; Graf, F.; Bajohr, S.; Reimert, R.; Kolb, T. Renewable Power-to-Gas: A technological and economic review. *Renew. Energy* **2016**, *85*, 1371–1390. [CrossRef]
2. Forster, P.; Ramaswamy, V.; Artaxo, P.; Berntsen, T.; Betts, R.; Fahey, D.W.; Haywood, J.; Lean, J.; Lowe, D.C.; Myhre, G.; et al. Climate Change 2007: The Physical Science Basis. In *Contribution of Working Group I to the Fourth Assessment Report of the Intergovernmental Panel on Climate Change*; Solomon, S., Qin, D., Manning, M., Chen, Z., Marquis, M., Averyt, K.B., Tignor, M., Miller, H.L., Eds.; Cambridge University Press: Cambridge, UK; New York, NY, USA, 2007; p. 212.
3. Zanoletti, M.; Klvana, D.; Kirchnerova, J.; Perrier, M.; Guy, C. Auto-cyclic reactor: Design and evaluation for the removal of unburned methane from emissions of natural gas engines. *Chem. Eng. Sci.* **2009**, *64*, 945–954. [CrossRef]
4. Ladavos, A.; Pomonis, P. *Methane Combustion on Perovskites in Perovskites and Related Mixed Oxides: Concepts and Applications*; Wiley: Weinheim, Germany, 2016; Volume 2, pp. 369–388.
5. Li, Z.; Hoflund, G.B. A Review on Complete Oxidation of Methane at Low Temperatures. *J. Nat. Gas Chem.* **2003**, *12*, 153–160.
6. Garbowski, E.; Feumi-Jantou, C.; Mouaddib, N.; Primet, M. Catalytic combustion of methane over palladium supported on alumina catalysts: Evidence for reconstruction of particles. *Appl. Catal. A* **1994**, *109*, 277–291. [CrossRef]
7. Ciuparu, D.; Lyubovsky, M.R.; Altman, E.; Pfefferle, L.D.; Datye, A. Catalytic Combustion of Methane over Palladium-Based Catalysts. *Catal. Rev.* **2002**, *44*, 593–649. [CrossRef]
8. Escandón, L.S.; Ordóñez, S.; Vega, A.; Díez, F.V. Oxidation of methane over palladium catalysts: Effect of the support. *Chemosphere* **2005**, *58*, 9–17. [CrossRef] [PubMed]
9. Van Vegten, N.; Maciejewski, M.; Krumeich, F.; Baiker, A. Structural properties, redox behaviour and methane combustion activity of differently supported flame-made Pd catalysts. *Appl. Catal. B* **2009**, *93*, 38–49. [CrossRef]
10. Eguchi, K.; Arai, H. Low temperature oxidation of methane over Pd-based catalysts—Effect of support oxide on the combustion activity. *Appl. Catal. A* **2001**, *222*, 359–367. [CrossRef]
11. Xiao, L.-H.; Sun, K.-P.; Xu, X.-L.; Li, X.-N. Low-temperature catalytic combustion of methane over Pd/CeO_2 prepared by deposition-precipitation method. *Catal. Commun.* **2005**, *6*, 796–801. [CrossRef]
12. Di Sarli, V.; Landi, G.; Lisi, L.; Saliva, A.; Di Benedetto, A. Catalytic diesel particulate filters with highly dispersed ceria: Effect of the soot-catalyst contact on the regeneration performance. *Appl. Catal. B* **2016**, *197*, 116–124. [CrossRef]
13. Roth, D.; Gélin, P.; Kaddouri, A.; Garbowski, E.; Primet, M.; Tena, E. Oxidation behaviour and catalytic properties of Pd/Al_2O_3 catalysts in the total oxidation of methane. *Catal. Today* **2006**, *112*, 134–138. [CrossRef]
14. Hoffmann, M.; Kreft, S.; Georgi, G.; Fulda, G.; Pohl, M.-M.; Seeburg, D.; Berger-Karin, C.; Kondratenko, E.V.; Wohlrab, S. Improved catalytic methane combustion of Pd/CeO_2 catalysts via porous glass integration. *Appl. Catal. B* **2015**, *179*, 313–320. [CrossRef]
15. Li, Z.; Hoflund, G.B. Catalytic oxidation of methane over Pd/Co_3O_4. *React. Kinet. Catal. Lett.* **1999**, *66*, 367–374. [CrossRef]
16. Ishihara, T.; Shigematsu, H.; Abe, Y.; Takita, Y. Effects of Additives on the Activity of Palladium Catalysts for Methane Combustion. *Chem. Lett.* **1993**, *22*, 407–410. [CrossRef]
17. Chen, J.; Zhang, X.; Arandiyan, H.; Peng, Y.; Chang, H.; Li, J. Low temperature complete combustion of methane over cobalt chromium oxides catalysts. *Catal. Today* **2013**, *201*, 12–18. [CrossRef]
18. Ercolino, G.; Grzybek, G.; Stelmachowski, P.; Specchia, S.; Kotarba, A.; Specchia, V. Pd/Co_3O_4-based catalysts prepared by solution combustion synthesis for residual methane oxidation in lean conditions. *Catal. Today* **2015**, *257*, 66–71. [CrossRef]
19. Lu, N.; Wu, Z.-W.; Lei, L.-J.; Qin, Z.-F.; Zhu, H.-Q.; Luo, L.; Fan, W.-B.; Wang, J.-G. Catalytic combustion of lean methane over a core-shell structured Pd-Co_3O_4@SiO_2 catalyst. *Ranliao Huaxue Xuebao* **2015**, *43*, 1120–1127.
20. Wang, Q.; Peng, Y.; Fu, J.; Kyzas, G.Z.; Billah, S.M.R.; An, S. Synthesis, characterization, and catalytic evaluation of Co_3O_4/γ-Al_2O_3 as methane combustion catalysts: Significance of Co. species and the redox cycle. *Appl. Catal. B* **2015**, *168–169*, 42–50. [CrossRef]

21. Wu, Z.; Deng, J.; Liu, Y.; Xie, S.; Jiang, Y.; Zhao, X.; Yang, J.; Arandiyan, H.; Guo, G.; Dai, H. Three-dimensionally ordered mesoporous Co_3O_4-supported Au-Pd alloy nanoparticles: High-performance catalysts for methane combustion. *J. Catal.* **2015**, *332*, 13–24. [CrossRef]
22. Chen, Z.; Wang, S.; Liu, W.; Gao, X.; Gao, D.; Wang, M.; Wang, S. Morphology-dependent performance of Co_3O_4 via facile and controllable synthesis for methane combustion. *Appl. Catal. A* **2016**, *525*, 94–102. [CrossRef]
23. Hu, W.; Lan, J.; Guo, Y.; Cao, X.-M.; Hu, P. Origin of Efficient Catalytic Combustion of Methane over Co_3O_4: Active Low-Coordination Lattice Oxygen and Cooperation of Multiple Active Sites. *ACS Catal.* **2016**, *6*, 5508–5519. [CrossRef]
24. Sun, Y.; Liu, J.; Song, J.; Huang, S.; Yang, N.; Zhang, J.; Sun, Y.; Zhu, Y. Exploring the Effect of Co_3O_4 Nanocatalysts with Different Dimensional Architectures on Methane Combustion. *ChemCatChem* **2016**, *8*, 540–545. [CrossRef]
25. Wang, F.; Zhang, L.; Xu, L.; Deng, Z.; Shi, W. Low temperature CO oxidation and CH_4 combustion over Co_3O_4 nanosheets. *Fuel* **2017**, *203*, 419–429. [CrossRef]
26. Ercolino, G.; Karimi, S.; Stelmachowski, P.; Specchia, S. Catalytic combustion of residual methane on alumina monoliths and open cell foams coated with Pd/Co_3O_4. *Chem. Eng. J.* **2017**, *326*, 339–349. [CrossRef]
27. Kikuchi, R.; Maeda, S.; Sasaki, K.; Wennerström, S.; Eguchi, K. Low-temperature methane oxidation over oxide-supported Pd catalysts: Inhibitory effect of water vapor. *Appl. Catal. A* **2002**, *232*, 23–28. [CrossRef]
28. Demoulin, O.; Rupprechter, G.; Seunier, I.; Le Clef, B.; Navez, M.; Ruiz, P. Investigation of Parameters Influencing the Activation of a Pd/γ-Alumina Catalyst during Methane Combustion. *J. Phys. Chem. B* **2005**, *109*, 20454–20462. [CrossRef] [PubMed]
29. Kucharczyk, B.; Tylus, W. Effect of washcoat modification with metal oxides on the activity of a monolithic Pd-based catalyst for methane combustion. *Catal. Today* **2008**, *137*, 324–328. [CrossRef]
30. Yang, Z.; Yang, P.; Zhang, L.; Guo, M.; Yan, Y. Investigation of low concentration methane combustion in a fluidized bed with Pd/Al_2O_3 as catalytic particles. *RSC Adv.* **2014**, *4*, 59418–59426. [CrossRef]
31. Gholami, R.; Alyani, M.; Smith, K. Deactivation of Pd Catalysts by Water during Low Temperature Methane Oxidation Relevant to Natural Gas Vehicle Converters. *Catalysts* **2015**, *5*, 561–594. [CrossRef]
32. Lin, Y.H.; Yu, S.C. Synthesis and structural features of a flux–grown hematite. *J. Geol. Soc. China* **1999**, *42*, 349–358.
33. Roth, W.L. The magnetic structure of Co_3O_4. *J. Phys. Chem. Solids* **1964**, *25*, 1–10. [CrossRef]
34. Slack, G.A. Crystallography and Domain Walls in Antiferromagnetic NiO Crystals. *J. Appl. Phys.* **1960**, *31*, 1571–1582. [CrossRef]
35. Scherrer, P. Bestimmung der Größe und der inneren Struktur von Kolloidteilchen mittels Röntgenstrahlen. In *Nachrichten von der Gesellschaft der Wissenschaften zu Göttingen, Mathematisch-Physikalische Klasse*; DigiZeitschriften: Göttingen, Germany, 1918; pp. 98–100.
36. Conner, W.C.; Falconer, J.L. Spillover in Heterogeneous Catalysis. *Chem. Rev.* **1995**, *95*, 759–788. [CrossRef]
37. Ciuparu, D.; Perkins, E.; Pfefferle, L. In situ DR-FTIR investigation of surface hydroxyls on γ-Al_2O_3 supported PdO catalysts during methane combustion. *Appl. Catal. A* **2004**, *263*, 145–153. [CrossRef]
38. Naumkin, A.V.; Kraut-Vass, A.; Gaarenstrom, S.W.; Powell, C.J. NIST X-ray Photoelectron Spectroscopy Database, NIST SRD 20, Version 4.1 (Web Version). Available online: https://srdata.nist.gov/xps/Default.aspx (accessed on 13 December 2017).
39. Yin, Y.; Rioux, R.M.; Erdonmez, C.K.; Hughes, S.; Somorjai, G.A.; Alivisatos, A.P. Formation of Hollow Nanocrystals Through the Nanoscale Kirkendall Effect. *Science* **2004**, *304*, 711–714. [CrossRef] [PubMed]
40. Wang, W.; Dahl, M.; Yin, Y. Hollow Nanocrystals through the Nanoscale Kirkendall Effect. *Chem. Mater.* **2013**, *25*, 1179–1189. [CrossRef]

catalysts

MDPI

Article

Chiral Catalyst Deactivation during the Asymmetric Hydrogenation of Acetophenone

Jose P. Ruelas-Leyva [1,2] and Gustavo A. Fuentes [1,*]

[1] Department of Process Engineering, Universidad Autónoma Metropolitana—Iztapalapa, San Rafael Atlixco # 186, Ciudad de México C.P. 09340, Mexico; jose.ruelas@uas.edu.mx

[2] Facultad de Ciencias Químico Biológicas, Universidad Autónoma de Sinaloa, Josefa Ortiz de Domínguez S/N, Ciudad Universitaria, Culiacán Sinaloa C.P. 80013, Mexico

* Correspondence: gfuentes@xanum.uam.mx; Tel.: +52-55-5804-4648

Academic Editor: Morris D. Argyle
Received: 18 May 2017; Accepted: 20 June 2017; Published: 23 June 2017

Abstract: Asymmetric hydrogenation in solution catalyzed by chiral catalysts is a powerful tool to obtain chiral secondary alcohols. It is possible to reach conversions and enantiomeric excesses close to 99%, but that frequently requires the use of non-optimal amounts of catalysts or long reaction times. That is in part caused by the lack of kinetic information needed for the design of large-scale reactors, including few reported details about catalyst deactivation. In this work, we present a kinetic model for the asymmetric hydrogenation in solution of acetophenone, a prochiral substrate, catalyzed by different bisphosphine-diamine Ru complexes. The experimental data was fitted with a first order model that includes first order deactivation of the catalyst and the presence of residual activity. The fit of the experimental data is very good, and an analysis of the kinetic and deactivation parameters gives further insight into the role of each ligand present in the Ru catalysts. This is the first report of a kinetic analysis of homogenous complexes' catalysis including an analysis of their deactivation.

Keywords: asymmetric hydrogenation; deactivation; Ru complexes; kinetic modeling

1. Introduction

Asymmetric hydrogenation of prochiral ketones is important to obtain chiral secondary alcohols [1], which are intermediates in the production of pharmaceuticals, agrochemicals and perfumes [2]. In the hydrogenation of the carbonyl group it is customary to use a homogeneous chiral catalyst to facilitate the reaction and to avoid the formation of undesired enantiomers [3]. In this area, Noyori and his group [4] have developed a series of chiral Ru complexes used as catalysts that have an excellent performance during the asymmetric hydrogenation of several prochiral substrates. Unfortunately, that is not always the case for all the complexes studied in solution. There are reports of experiments in which the catalyst activity decreased drastically or even ceased completely. In some cases, this can be explained by the inhibition of the catalyst by the product. Another possibility, probably the most common, is that the catalyst deactivates. This may occur by the loss of a ligand, the reduction of the central metal and ripening, or formation of dimers, etc. Despite its relevance, there has not been much interest in the open literature in understanding what occurs to the catalysts [5,6]. The research effort has been focused upon the trial and error development of more efficient catalysts to attain high conversion and/or enantioselectivity.

There are few reports in the literature where a mention is made of deactivation and its possible causes. Grasa et al. [7] stated that deactivation occurred during the hydrogenation of acetophenone with a bisphosphine/diamine-Ru catalyst, and suggested that a Ru-hydride active center was formed initially but that it decomposed during reaction. A limited set of experimental data, conversion and enantiomeric excess (ee), was included, which makes an adequate comparison between catalysts more

difficult. Abdur-Rashid et al. [8] conducted several experiments with the same reaction and observed decay in the activity of the catalyst, also a bisphosphine/diamine-Ru complex. They presented a kinetic model to adjust the experimental data, but there was no attempt to relate it with the structure of the complex.

Deactivation is not limited to the bisphosphine/diamine-Ru catalysts. It has also been documented with other catalysts and reactions in solution, as in the case of a $[Rh(DIPAMP)(MeOH)_2]BF_4$ complex in solution used to catalyze the asymmetric hydrogenations of C–C double bonds [9]. Deactivation has also been reported during C–C coupling with a $[(PtBu_3)\text{-}PdBr]_2$ catalyst [10], and olefin hydroamination catalyzed by $PtBr_2/Br^-$ [11]. A recent study of the dehydrogenation of formic acid catalyzed by a TfDPEN-derived iridium complex explains the conversion-time results in terms of deactivation stemming from the irreversible transformation of the active complex to two inactive iridacycles [12].

As the few references above indicate, in the field of organometallic complex catalysts there has been little use of kinetics models, and much less of models that include deactivation. It is apparent that understanding the nature of the phenomena that cause the loss in activity of the catalysts developed is relevant in order to design more efficient processes. In this work, we present results for a series of Ru complexes used to catalyze the asymmetric hydrogenation of the prochiral ketone acetophenone. During reaction, a loss in the activity of the catalyst was observed and to adjust our data a kinetic model that accounts for deactivation was developed. The conversion-time data was fitted successfully, and by analyzing the kinetic and deactivation parameters we could differentiate the effect of each type of ligand in the Ru complexes used as catalysts.

2. Results and Discussion

2.1. Synthesis of the Complexes

The Ru complexes were synthesized following standard Schlenk techniques. The ligands used were (*R*)-BINAP ((*R*)-2,2′-Bis(diphenylphosphino)-1,1′-binaphthalene), (*R*)-Tol-BINAP ((*R*)-2,2′-Bis(di-*p*-tolylphosphino)-1,1′-binaphthyl), (*R*)-DABN ((*R*)-(+)-1-1′-Bi(2-naphthylamine)) and (*R*)-MAB ((*R*)-6,6′-dimethyl-2,2′-diaminobiphenyl). The details, as well as the spectrocopic characterization of the Ru complexes (^{31}P Nuclear Magnetic Resonance and Infrared) can be found in a previous work [13]. The complex structures are shown in Figure 1.

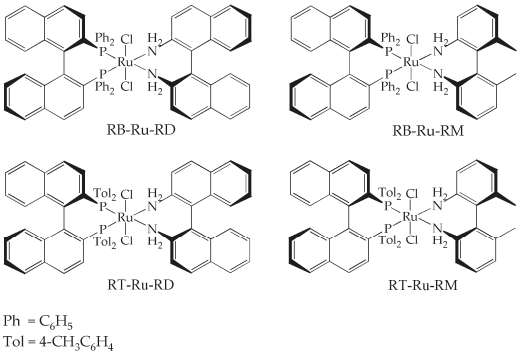

Figure 1. Structure and nomenclature of the complexes used in this work. (*R*)-BINAP-$RuCl_2$-(*R*)-DABN = RB-Ru-RD; (*R*)-BINAP-$RuCl_2$-(*R*)-MAB = RB-Ru-RM; (*R*)-Tol-BINAP-$RuCl_2$-(*R*)-DABN = RT-Ru-RD; (*R*)-Tol-BINAP-$RuCl_2$-(*R*)-MAB = RT-Ru-RM.

2.2. Catalytic Performance

During catalytic experiments in a batch reactor, Figure 2, all the Ru complexes hydrogenated acetophenone asymmetrically. The only product was 1-phenylethanol and (*R*) was the preferred

enantiomer, with ee up to 43%. In all cases, the initial ee was the largest, and then there was decay with time. The conversion (X) vs. time behavior generally consisted of an initial period with fast reaction, followed by a slow rate region. As we discuss later, we attributed the changes to catalyst deactivation.

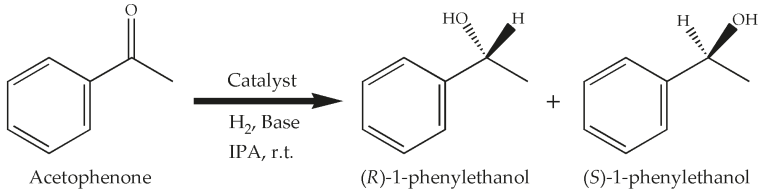

Figure 2. Hydrogenation of acetophenone with the Ru complexes as catalysts.

The conversion and ee (%) vs. time behavior for the different Ru complexes is given in Figures 3 and 4, respectively. The effect of each ligand is different. First, the complexes bearing (*R*)-MAB (RB-Ru-RM and RT-Ru-RM) convert over 80% of the substrate and have a similar trend with time (Figure 3). The complexes having (*R*)-DABN (RB-Ru-RD and RT-Ru-RD) are not as active, with conversions below 60%. This underscores the role of the MAB ligand in favoring a higher activity. As for the bisphosphine ligand, its effect over the performance of the catalyst can be examined on Figure 4. There is at least a 7% difference in the ee between the RT-Ru-RM and the RB-Ru-RM complexes as a result of a difference in the bisphosphine ligand. The difference increases with reaction time. In the case of the RT-Ru-RD and RB-Ru-RD complexes there is also a difference in the ee, about 9%. Hence, a variation in the bisphosphine ligand appears to have a larger effect upon the enantioselectivity.

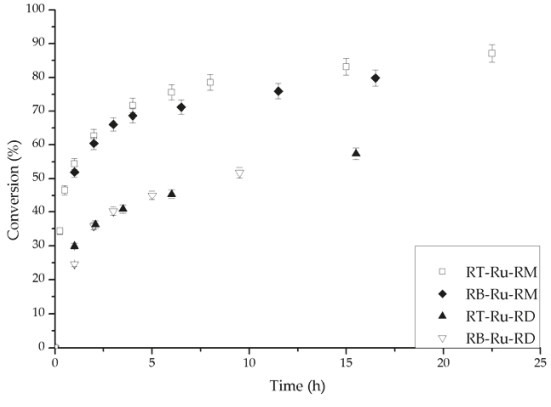

Figure 3. Conversion during the hydrogenation of acetophenone catalyzed by the different Ru-complexes. Conditions: 100 psi of H_2, room temperature, 1 mmol acetophenone, 20 mL isopropanol (IPA), 1.25 mM *t*-BuOK and 0.01 mmol of catalyst.

There is evidence in the literature about the effect of the bisphosphine ligand on the ee, but the role of the diamine ligand is more difficult to understand, although it is essential for these catalysts in order to be functional. Grasa et al. [7] synthesized several Ru complexes with different 1,4-diamine ligands, active in the hydrogenation of acetophenone. The ee reached with (*R*)-P-Phos in the catalyst was 75% for the (*R*) product, but with a more sterically bulky bisphosphine, (*R*)-Xyl-P-Phos and the same diamine, the ee was 55% towards the (*S*) configuration of the product. The conversion reported for each complex was the same. This data supports our conclusions, because the diamine affects the conversion, whereas the bisphosphine ligand modifies the ee.

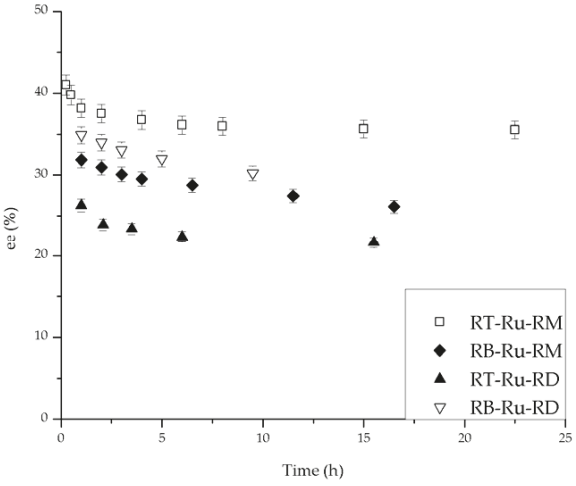

Figure 4. Enantioselectivity during hydrogenation of acetophenone catalyzed by Ru-complexes. Conditions: 100 psi of H_2, room temperature, 1 mmol acetophenone, 20 mL isopropanol (IPA), 1.25 mM *t*-BuOK and 0.01 mmol of catalyst.

After comparing the activity of the complexes under the same conditions, we studied the effect of the base concentration upon the conversion and ee. In these experiments, we used RB-Ru-RM, Figure 5, and RT-Ru-RM, Figure 6, because of their better catalytic performance. With RB-Ru-RM, the largest product yield occurred with a base concentration equal to 1.25 mM, which corresponds to a base/catalyst molar ratio (B/C) of 2.5. With other base concentrations, the production of the secondary alcohol was lower. Interestingly, the initial rates with base concentrations of 0.50 and 1.25 mM were similar, but in the first case the reaction stopped almost completely after about 2 h. The difference between the initial and final ee values increased with the base concentration. It was the largest when 2.50 mM of base were used.

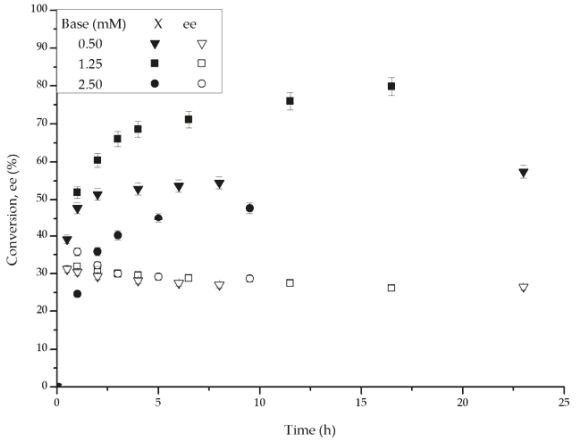

Figure 5. Conversion and ee vs. time plots for different base concentrations with the RB-Ru-RM complex as catalyst. Conditions: 100 psi of H_2, room temperature, 1 mmol acetophenone, 20 mL IPA, base *t*-BuOK and 0.01 mmol of catalyst.

To address the origin of the loss in activity of the catalysts, an additional experiment was conducted. After the last sampling at 23 h with the RB-Ru-RM complex and 1.25 mM of base, acetophenone (1 mmol) was added again to the reactor. After another 5 h of reaction the analysis of the reaction media showed that there had been no further reaction. This result led us to conclude that there was catalyst deactivation rather than product inhibition. If the latter were occurring, there would have been some extra production of the secondary alcohol. An example of product inhibition was reported during the oxidation of alcohol to aldehyde catalyzed by Bis(pyridyl)siloxane Pd(II) complex [14].

With the RT-Ru-RM complex, shown in Figure 6, the effect of the base concentration can be broadly divided in two zones. For reaction times smaller than 20 h, the use of high base concentrations resulted in lower initial reaction rates, but at larger reaction times there was a crossover in the conversion-time behavior, which made the use of higher base concentrations more favorable. As to the ee values, they varied according to the base concentration, the larger the base concentration, the larger the initial ee and its decay. These results stress the importance of doing a full analysis of the time evolution of this type of reaction. Unfortunately, it is customary to reach conclusions based on one-point samplings. In this case, as shown in Figure 6, the opposite conclusions can be derived depending on whether the results are analyzed before or after 20 h of reaction.

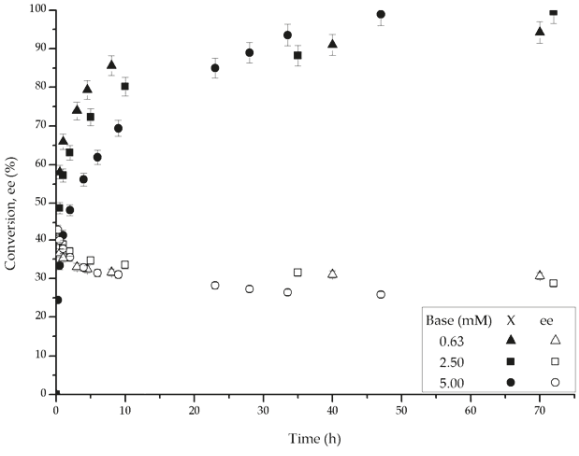

Figure 6. Effect of the base concentration upon conversion and ee with the RR-Ru-RM catalyst. Conditions: 100 psi of H_2, room temperature, 1 mmol acetophenone, 40 mL IPA, base *t*-BuOK and 0.01 mmol of catalyst.

Sandoval et al. [15] report that the initial reaction rate depends on the base concentration and that there is an optimum, but in their case the ee remains constant. In our case, the base concentration seems to influence not only the initial reaction rate but also the final conversion level and the decay in ee. This implies that the deactivation of the catalysts depends upon the base concentration. In a recent review of the enantioselective reduction of ketones catalyzed by Noyori and Noyori-Ikariya bifunctional catalysts [16], it is stated that the base concentration can affect the formation of the major product originated by a diastereomeric transition state that is stabilized either by N-H···π or N-K···π ligand-aromatic ring non-covalent attractive interactions in the catalysts-substrate complex and/or the absence of steric constrains. A dependence of the ee on the base concentration has been reported by other authors. Abdur-Rashid et al. [8] found that by adding *t*-BuOK in excess the ee values increased but no explanation was given. In a more recent work, Abbel et al. [17] conducted several experiments to address the variation in ee observed during reaction. The authors varied the initial proportion of different Ru complex isomers (*t*,*c*-3a, Λ*c*,*c*-3a and Δ*c*,*c*-3a, nomenclature used in their work) in the

asymmetric hydrogenation of acetophenone. They observed that by having a larger proportion of the *t*,*c*-3a isomer, the conversion towards 1-phenylethanol increased and the ee was constant at 63% (*S*). However, if they continued the same experiment for longer times, the additional isomers (Λ*c*,*c*-3a and Δ*c*,*c*-3a) began to contribute to the reaction, and that led to higher conversions of the secondary alcohol but to a decrease in ee values (50–30% (*S*)). This suggests that the Λ*c*,*c*-3a and Δ*c*,*c*-3a isomers were active for the hydrogenation of the substrate, but their capability to do it asymmetrically was lower than that of the *t*,*c*-3a complex.

To rationalize our results, it is plausible to assume there is isomerization of the Ru complex during reaction and that would affect the ee and result in deactivation, providing an explanation of the experimental observations. To test this assumption, the experimental results were fitted to a kinetic + deactivation model in the next section.

2.3. Kinetic Model with Deactivation

There has been much study of deactivation in the case of solid catalysts as shown in recent reviews [18,19], but that is not the case for homogeneous catalysts in solution. In the present study, an analysis of the conversion-time results indicates that there is a different degree of residual activity after the initial fast decay. We tested a kinetic model that includes deactivation with residual activity [20] and found that first order kinetics for the substrate, coupled with first order deactivation, was the best model for fitting our experimental results. The equations representing our experimental setup (batch reactor at constant volume and pressure) are:

$$-\frac{dC_A}{dt} = k_c \cdot a \cdot C_A \tag{1}$$

$$-\frac{da}{dt} = k_d \cdot (a - a_{ss}) \tag{2}$$

Here, C_A is the concentration of acetophenone, k_c is the rate constant, k_d is the deactivation constant, a is the activity of the catalyst and a_{ss} is a residual activity. Equations (1) and (2) are a case of the so-called separable deactivation kinetics and their solution, using as initial conditions that $C_A = C_{Ao}$ and ao = 1 at t = 0, is given as Equation (3):

$$X_A = 1 - \frac{C_A}{C_{Ao}} = 1 - e^{\left[\frac{k_c(e^{-k_d \cdot t}-1)}{k_d} - \frac{a_{ss} \cdot k_c(e^{k_d \cdot t}-1)}{k_d} - a_{ss} \cdot k_c \cdot t\right]} \tag{3}$$

The parameters k_c, k_d and a_{ss} of Equation (3) were determined from a non-linear least squares fit (Mathematica, version 10, Wolfram Research, Champaign, IL, USA). The adjusted curves are plotted against the experimental values in Figure 7. It is evident that there is excellent agreement. The fitted parameters for the different experimental condition are summarized in Table 1. A direct comparison of the fitted parameters under the same experimental conditions for all the catalysts can be analyzed on entries 1, 2, 3 and 4. The complexes bearing the MAB ligand were the best catalysts to produce the secondary alcohol, as their k_c values were the highest. In addition, the dynamics of the main reaction and of the complex deactivation were of the same order of magnitude, as can be appreciated from the k_c and k_d values. On the other hand, the catalysts with the ligand DABN resulted in lower acetophenone conversions, and their k_c values were smaller when compared to the complexes with MAB.

The fitted parameters are a function of the base concentration for the RB-Ru-RM catalyst, as seen in entries 3, 5 and 6. Under entry 3 conditions, there was an optimum base concentration for which k_c was slightly larger than k_d and a_{ss} was the largest. This corresponds to the higher conversion profiles observed in Figure 5. The base concentration affected the performance of the RT-Ru-RM catalyst and that can be concluded from the analysis of the fitted parameters in entries 7, 8 and 9. When the base concentration increased, deactivation was more noticeable, i.e., high k_d and low k_c values. Interestingly,

the presence of higher k_d leads to a faster approach to the residual activity, and since the a_{ss} for the entry 9 was the largest, the conversion reached was the highest at shorter reaction time (Figure 6).

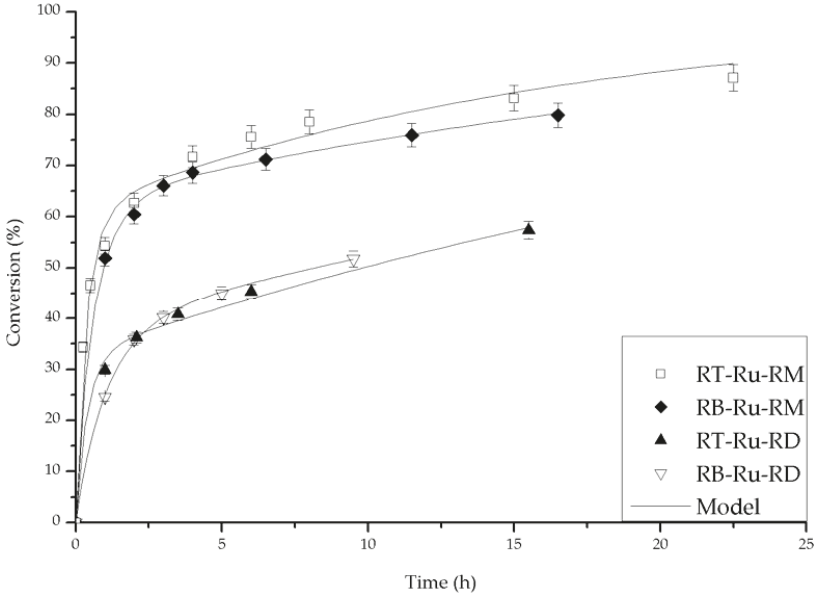

Figure 7. Fit of the experimental data with the deactivation model (Equation (3)). Conditions: 100 psi of H_2, room temperature, 1 mmol acetophenone, 20 mL isopropanol (IPA), 1.25 mM *t*-BuOK and 0.01 mmol of catalyst.

Table 1. Summary of the experimental condition and the resulting parameters for the kinetic model with deactivation.

Entry	Complex	IPA mL	Base (mM)	k_c (h^{-1})	k_d (h^{-1})	a_{ss}	TOF (h^{-1}) [1]
1	RB-Ru-RD	20	1.250	0.402	0.773	0.063	40.2
2	RT-Ru-RD	20	1.250	0.913	2.22	0.033	91.3
3	RB-Ru-RM	20	1.250	1.183	1.151	0.032	118.3
4	RT-Ru-RM	20	1.250	1.935	1.98	0.031	193.5
5	RB-Ru-RM	20	0.500	1.627	2.222	0.003	162.7
6	RB-Ru-RM	20	2.500	0.383	0.644	0.019	38.3
7	RT-Ru-RM	40	0.625	2.422	1.697	0.012	242.2
8	RT-Ru-RM	40	2.500	1.907	1.806	0.021	190.7
9	RT-Ru-RM	40	5.000	1.213	2.047	0.052	121.3

[1] Calculated with TOF initial = $(k_c \cdot N_{A0})/N_{Ru}$; N_{A0} = initial moles of acetophenone and N_{Ru} = initial moles of Ru. In all cases 1 mmol of acetophenone and 0.01 mmol of catalyst were used, together with the proper amount of *t*-BuOK and IPA. a_{ss} is dimensionless.

2.4. Mechanistic Considerations

A representation of the different steps occurring during reaction is shown in Scheme 1 (more details of the catalyzed pathway can be found in reference [21]). Initially, the pre-catalyst **1** is transformed into the catalyst **2**. Then, the catalyst hydrogenates the substrate and is transformed into **3**. The product of the reaction is mainly the *R* enantiomer but as the time of reaction increases, the structure-directing ability of the catalyst to produce the *R* enantiomer decreases. At the end of the reaction cycle, part of the species **3** is regenerated by hydrogen and another fraction is converted to an

inactive species. The species **3** has a square based pyramidal geometry and it can form an isomer with trigonal bipyramidal geometry. The latter species is probably difficult to be regenerated with H_2, hence leading to overall deactivation. Such isomerization can proceed via the Berry pseudorotation [22].

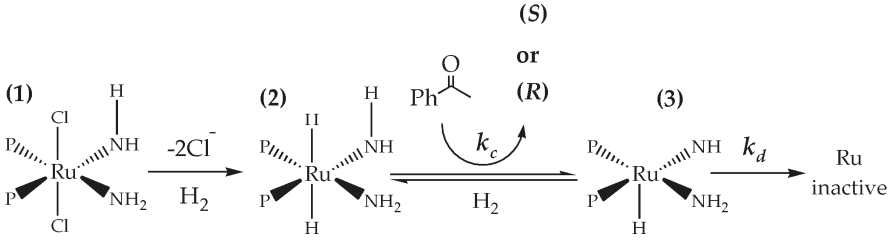

Scheme 1. Proposed steps involved in asymmetric hydrogenation considering one active site and deactivation. For clarity, the complete structure of the ligands is omitted.

Although the mechanism proposed cannot be ascertained based only on kinetics, it is based on reasonably well established ideas in the field. On the other hand, the kinetic model developed here allows to compare the interplay between reaction and deactivation through the analysis of the values for k_c, k_d and a_{ss}. These are sensitive to the structure of the catalyst and to the experimental conditions used. Besides the use of novel complexes as catalysts, this is the first report of the modeling of deactivation for asymmetric hydrogenation catalyzed by Ru complexes in solution.

3. Materials and Methods

All the manipulations of the reagents were carried out using Schlenk techniques inside a glove bag filled several times with N_2. (*R*)-BINAP, (*R*)-Tol-BINAP ((*R*)-2,2′-Bis(di-*p*-tolylphosphino) -1,1′-binaphthyl), $RuCl_2(\eta^6\text{-}C_6H_6)$ dimer, (*R*)-DABN ((*R*)-(+)-1-1′-Bi(2-naphthylamine)), acetophenone, potassium terbutoxide (*t*-BuOK), dimethylformamide (DMF) and anhydrous isopropyl alcohol (IPA) were purchased from Sigma-Aldrich Química (Toluca, MX, Mexico). (*R*)-MAB ((*R*)-6,6′-dimethyl-2,2′-diaminobiphenyl) was synthesized according to previous reports [23,24]. ^{31}P Nuclear Magnetic Resonance in the liquid state ($CDCl_3$ as solvent) was performed in a Bruker spectrometer (Avance III 500, resonance frequency of ^{1}H 500 MHz, Bruker Mexicana, Ciudad de México, Mexico). The IR spectra were acquired in a Bruker FTIR spectrometer (Tensor 27, Bruker Mexicana, Ciudad de México, Mexico) from KBr pellets. The products of reaction were analyzed by Gas Chromatography (HP 5890, Agilent Technologies Mexico, Ciodad de Mexico, Mexico) with a chiral column (cp-chirasildex-cb 7502). The final configuration was determined by comparison with standards ((*R*) and (*S*) 1-phenylethanol also purchased from Sigma-Aldrich Química).

3.1. Synthesis of the Complexes

Preparation of (*R*)-BINAP-Ru-(*R*)-DABN complex (RB-Ru-RD): We followed the procedures reported by Ohkuma et al. [25] and Grasa et al. [7] with some minor modifications. (*R*)-BINAP (0.3 mmol) and of $RuCl_2(\eta^6\text{-}C_6H_6)$ dimer (0.15 mmol) were mixed in a Schlenk flask and DMF (12 mL) was then poured in. The solution was heated to 115 °C during 3 h and then cooled to room temperature. To this mixture (*R*)-DABN (0.3 mmol) was added, and the resulting solution was left under stirring overnight. DMF was removed under vacuum while keeping the temperature constant at 40 °C.

3.2. Procedure for the Hydrogenation of Acetophenone

The model reaction used to test the complexes was the hydrogenation of acetophenone (Figure 2). The expected product, 1-phenylethanol, is employed in the pharmaceutical and fragrances industries [26,27]. Typically, the desired amounts of complex (0.01 mmol) and of *t*-BuOK were poured

in the reactor, followed by IPA (20 or 40 mL) and then acetophenone (1 mmol). The reactor was flushed 5 times with pure H_2 before the pressure was set at 689.5 kPa (100 psi) to begin the reaction at room temperature. Samples were withdrawn during the reaction to obtain the conversion vs. reaction time data.

3.3. Parameter Estimation for the Kinetic Model with Catalyst Deactivation

We used the integral method to analyze the kinetics of acetophenone hydrogenation. As the deactivation Equation (2) is independent, it was first integrated and simplified to give Equation (4) for the activity

$$a = e^{-k_d \cdot t} \cdot (1 - a_{ss}) + a_{ss} \tag{4}$$

Equation (4) was substituted in Equation (1) to give Equation (5):

$$-\frac{dC_A}{dt} = k_c \cdot [e^{-k_d \cdot t} \cdot (1 - a_{ss}) + a_{ss}] \cdot C_A \tag{5}$$

Integration of Equation (5) resulted in:

$$\frac{C_A}{C_{A0}} = e^{\frac{k_c \cdot (e^{-k_d \cdot t} - 1)}{k_d} - \frac{a_{ss} \cdot k_c \cdot (e^{-k_d \cdot t} - 1)}{k_d} - a_{ss} \cdot k_c \cdot t} \tag{6}$$

Applying the definition of conversion, Equation (3) was obtained:

$$X(t) = 1 - \frac{C_A}{C_{A0}} = 1 - e^{\frac{k_c \cdot (e^{-k_d \cdot t} - 1)}{k_d} - \frac{a_{ss} \cdot k_c \cdot (e^{-k_d \cdot t} - 1)}{k_d} - a_{ss} \cdot k_c \cdot t} \tag{7}$$

The k_c, k_d and a_{ss} parameters were determined from a non-linear least-squares fit of Equation (3) using the Levenberg-Marquardt algorithm option in Mathematica (version 10, Wolfram Research). As this involves an iterative process, we used different seed values for the parameters in order to assure that the converged solution was optimal.

4. Conclusions

Four complexes of the type bisphosphine/diamine-Ru were used as catalysts for the asymmetric hydrogenation of acetophenone. The diamine ligands employed have axial chirality similar to the bisphosphine ligands normally employed. The role of each ligand in the catalyst was assigned according to our experimental observations. The diamine ligand had a major influence on the conversion reached, while the bisphosphine ligand affected the ee values. The catalysts behave in a singular way because the base concentration affects the initial reaction rates and subsequent deactivation. A first order kinetic model that includes deactivation was proposed, and it fitted the experimental observations with very good agreement. Deactivation was modeled as a first order process with residual activity. This is one of the few studies where deactivation is modeled using this type of catalyst. A scheme for the structural changes in the complexes during reaction, based on generally accepted knowledge in the field and the deactivation model, is proposed to explain the transient variations in ee and conversion during the asymmetric hydrogenation of acetophenone in solution catalyzed by bisphosphine/diamine Ru complexes.

Acknowledgments: J.P.R.-L. thanks Consejo Nacional de Ciencia y Tecnología (CONACyT) for the graduate scholarships granted. The authors acknowledge the financial support of UAS and UAM-Iztapalapa during the development of this work.

Author Contributions: J.P.R.-L. performed experiments and contributed to the numerical analysis and writing of the manuscript. G.A.F. directed the research and contributed to the modeling and writing of the manuscript. Both authors have approved the final version of the manuscript.

Conflicts of Interest: The authors declare no conflict of interest.

References

1. Noyori, R. Facts are the enemy of truth-reflections on serendipitous discovery and unforeseen developments in asymmetric catalysis. *Angew. Chem. Int. Ed.* **2013**, *52*, 79–92. [CrossRef] [PubMed]
2. Noyori, R.; Ohkuma, T. Asymmetric catalysis by architectural and functional molecular engineering: Pactical chemo- and stereoselective hydrogenation of ketones. *Angew. Chem. Int. Ed.* **2001**, *40*, 40–73. [CrossRef]
3. Hayashi, T.; Yamasaki, K. Rhodium-catalyzed asymmetric 1,4-addition and its related asymmetric reactions. *Chem. Rev.* **2003**, *103*, 2829–2844. [CrossRef] [PubMed]
4. Noyori, R. Asymmetric catalysis: Science and opportunities (Nobel Lecture). *Angew. Chem. Int. Ed.* **2002**, *41*, 2008–2022.
5. Jones, C.W. On the stability and recyclability of supported metal-ligand complex catalysts: Myths, misconceptions and critical research needs. *Top. Catal.* **2010**, *53*, 942–952.
6. Van Leeuwen, P.W.N.M. Decomposition pathways of homogeneous catalysts. *Appl. Catal. A-Gen.* **2001**, *212*, 61–81. [CrossRef]
7. Grasa, G.A.; Zanotti-Gerosa, A.; Medlock, J.A.; Hems, W.P. Asymmetric hydrogenation of isobutyrophenone using a [(diphosphine) $RuCl_2$ (1,4-diamine)] catalyst. *Org. Lett.* **2005**, *7*, 1449–1451. [CrossRef] [PubMed]
8. Abdur-Rashid, K.; Clapham, S.E.; Harvey, J.N.; Lough, A.J.; Morris, R.H. Mechanism of the hydrogenation of ketones catalyzed by *trans*-dihydrido(diamine)ruthenium(II) complexes. *J. Am. Chem. Soc.* **2002**, *124*, 15104–15118. [CrossRef] [PubMed]
9. Schmidt, T.; Baumann, W.; Drexler, H.J.; Heller, D. Unusual deactivation in the asymmetric hydrogenation of itaconic acid. *J. Organomet. Chem.* **2011**, *696*, 1760–1767. [CrossRef]
10. Proutiere, F.; Aufiero, M.; Schoenebeck, F. Reactivity and stability of dinuclear Pd(I) complexes: Studies on the active catalytic species, insights into precatalyst activation and deactivation, and application in highly selective cross-coupling reactions. *J. Am. Chem. Soc.* **2012**, *134*, 606–612. [CrossRef] [PubMed]
11. Dub, P.A.; Béthegnies, A.; Poli, R. DFT and experimental studies on the PtX_2/X–catalyzed olefin hydroamination: Effect of halogen, amine basicity, and olefin on activity, regioselectivity, and catalyst deactivation. *Organometallics* **2012**, *31*, 294–305. [CrossRef]
12. Matsunami, A.; Kuwata, S.; Kayaki, Y. A bifunctional iridium catalyst modified for persistent hydrogen generation from formic acid: Understanding deactivation via cyclometalation of a 1,2-Diphenylethylenediamine motif. *ACS Catal.* **2017**, *7*, 4479–4484. [CrossRef]
13. Rivera, V.M.; Ruelas-Leyva, J.P.; Fuentes, G.A. Pd and Ru complexes bearing axially chiral ligands for the asymmetric hydrogenation of C=C and C=O double bonds. *Catal. Today* **2013**, *213*, 109–114. [CrossRef]
14. Missaghi, M.N.; Galloway, J.M.; Kung, H.H. Bis(pyridyl)siloxane-Pd(II) complex catalyzed oxidation of alcohol to aldehyde: Effect of ligand tethering on catalytic activity and deactivation behavior. *Appl. Catal. A-Gen.* **2011**, *391*, 297–304. [CrossRef]
15. Sandoval, C.A.; Ohkuma, T.; Muñiz, K.; Noyori, R. Mechanism of asymmetric hydrogenation of ketones catalyzed by BINAP/1,2-diamine-Ruthenium(II) complexes. *J. Am. Chem. Soc.* **2003**, *125*, 13490–13503. [CrossRef] [PubMed]
16. Dub, P.A.; Gordon, J.C. The mechanism of enantioselective ketone reduction with Noyori and Noyori-Ikariya bifunctional catalysts. *Dalton Trans.* **2016**, *45*, 6756–6781. [CrossRef] [PubMed]
17. Abbel, R.; Abdur-Rashid, K.; Faatz, M.; Hadzovic, A.; Lough, A.J.; Morris, R.H. A succession of isomers of Ruthenium dihydride complexes. Which one is the ketone hydrogenation catalyst? *J. Am. Chem. Soc.* **2005**, *127*, 1870–1882. [CrossRef] [PubMed]
18. Argyle, M.; Bartholomew, C.H. Heterogeneous catalyst deactivation and regeneration: A review. *Catalysts* **2015**, *5*, 145–269. [CrossRef]
19. Bartholomew, C.H.; Argyle, M. Advances in catalyst deactivation and regeneration. *Catalysts* **2015**, *5*, 949–954. [CrossRef]
20. Fuentes, G.A. Catalyst deactivation and steady state activity: A generalized power-law equation. *Appl. Catal.* **1985**, *15*, 33–40. [CrossRef]
21. Li, L.; Pan, Y.; Lei, M. The enantioselectivity in asymmetric ketone hydrogenation catalyzed by RuH_2(diphosphine)(diamine) complexes: Insights from a 3D-QSSR and DFT study. *Catal. Sci. Technol.* **2016**, *6*, 4450–4457. [CrossRef]

22. Ugi, I.; Marquarding, D.; Klusacek, H.; Gillespie, P.; Ramirez, F. Berry pseudorotation and turnstile rotation. *Acc. Chem. Res.* **1971**, *4*, 288–296. [CrossRef]
23. Pérez, C.; Pérez, S.; Fuentes, G.A.; Corma, A. Preparation and use of a chiral amine Ruthenium hydrogenation catalyst supported on mesoporous silica. *J. Mol. Catal. A-Chem.* **2003**, *197*, 275–281. [CrossRef]
24. Uehara, A.; Kubota, T.; Tsuchiya, R. New atropisomeric chiral bisphosphine, (S)-6-6′-dimethyl-2-2′-bis(diphenylphosphinamino)biphenyl, and asymmetric hydrogenation using the Rh(I) complex thereof. *Chem. Lett.* **1983**, *13*, 441–444. [CrossRef]
25. Ohkuma, T.; Hattori, T.; Hirohito, O.; Inoue, T.; Noyori, R. BINAP/1,4-diamine-Ruthenium(II) complexes for efficient asymmetric hydrogenation of 1-tetralones and analogues. *Org. Lett.* **2004**, *6*, 2681–2683. [CrossRef] [PubMed]
26. Bertero, N.M.; Apesteguía, C.R.; Marchi, A.J. Catalytic and kinetic study of the liquid-phase hydrogenation of acetophenone over Cu/SiO_2 catalysts. *Appl. Catal. A-Gen.* **2008**, *349*, 100–109. [CrossRef]
27. Yadav, G.D.; Mewada, R.K. Selective hydrogenation of acetophenone to 1-phenyl ethanol over nanofibrous Ag-OMS-2 catalysts. *Catal. Today* **2012**, *198*, 330–337. [CrossRef]

MDPI
St. Alban-Anlage 66
4052 Basel
Switzerland
Tel. +41 61 683 77 34
Fax +41 61 302 89 18
www.mdpi.com

Crystals Editorial Office
E-mail: crystals@mdpi.com
www.mdpi.com/journal/crystals

MDPI
St. Alban-Anlage 66
4052 Basel
Switzerland

Tel: +41 61 683 77 34
Fax: +41 61 302 89 18

www.mdpi.com

ISBN 978-3-03897-532-8